Ghosts and bottlenecks in elastic snap-through

Gomez, Michael

Awarding institution:
University of Oxford, Oxford, UK

Ghosts and bottlenecks in elastic snap-through

Michael Gomez

Pembroke College

Oxford
Mathematics

UNIVERSITY OF
OXFORD

Preface

The research described in this thesis was performed in the Mathematical Institute at the University of Oxford between October 2014 and February 2018 and was supervised by Professor Dominic Vella and Professor Derek E. Moulton.

This thesis describes my own work, including the experiments performed in §4.6. However, I am grateful to Jean-Baptiste Gorce for early experiments in a related system.

The results presented in this thesis are original, apart from the results of §2.2 and §2.3.3 which constitute review material, and where reference is made to the work of others. No part of the thesis has been submitted previously for a degree of the University or elsewhere.

At the time of writing, two papers based on the work presented in this thesis have been published, co-authored with D. E. Moulton and D. Vella. A paper based on the pull-in dynamics presented in Chapter 2 has been published in the *Journal of Micromechanics and Microengineering* (Gomez *et al.*, 2018a), and the dynamics of elastic snap-through presented in Chapter 4 has been published in *Nature Physics* (Gomez *et al.*, 2017a). In both publications, I performed the theoretical analysis and experiments (if applicable), while D. E. Moulton and D. Vella supervised the research.

<div align="right">Oxford, February 2018</div>

Since submission, a paper based on the pull-in dynamics presented in Chapter 3 has been published in the *Journal of Micromechanics and Microengineering* (Gomez *et al.*, 2018c) and a preprint of a paper based on the viscoelastic snap-through presented in Chapter 5 is available (Gomez *et al.*, 2018b), both co-authored with D. E. Moulton and D. Vella.

<div align="right">Oxford, September 2018</div>

Acknowledgements

ABSTRACT

Snap-through is a striking instability in which an elastic object rapidly jumps from one state to another. It is seen in the leaves of the Venus flytrap plant and umbrellas flipping on a windy day among many other examples. Similar structures that snap-through are used to generate fast motions in soft robotics, switches in micro-scale electronics and artificial heart valves. Despite the ubiquity of snap-through in nature and engineering, its dynamics is usually only understood qualitatively. In this thesis we develop analytical understanding of this dynamics, focussing on how the mathematical structure underlying the snap-through transition controls the timescale of instability.

We begin by considering the dynamics of 'pull-in' instabilities in microelectromechanical systems (MEMS) — a type of snap-through caused by electrostatic forces in which the motions are dominated by fluid damping. Using a lumped-parameter model, we show that the observed time delay near the pull-in transition is a type of critical slowing down — a so-called 'bottleneck' due to the 'ghost' of a saddle-node bifurcation. We obtain a scaling law describing this slowing down, and, in the process, unify a large range of experiments and simulations that exhibit delay phenomena during pull-in.

We also investigate the pull-in dynamics of MEMS microbeams, extending the lumped-parameter approach to incorporate the details of the beam geometry. This provides a model system in which to understand snap-through of a continuous elastic structure due to external loading. We develop a perturbation method that systematically exploits the proximity to pull-in to reduce the governing equations to a simpler evolution equation, with a structure that highlights the saddle-node bifurcation. This allows us to analyse the bottleneck dynamics in detail, which we compare with previous experimental and numerical data.

The remainder of the thesis is concerned with the dynamics of snap-through in macroscopic systems. In particular, we explore the extent to which dissipation is required to explain anomalously slow snap-through. Considering an elastic arch as an archetype of a snapping system, we use the perturbation method developed earlier to show that two bottleneck regimes are possible, depending delicately on the relative importance of external damping. In particular, we show that critical slowing down occurs even in the absence

of damping, leading to a new scaling law for the snap-through time that is confirmed by elastica simulations and experiments.

In many real systems material viscoelasticity is present to some degree. Finally, we examine how this influences the snap-through dynamics of a simple truss-like structure. We present a regime diagram that characterises when the timescale of snap-through is controlled by viscous, elastic or viscoelastic effects.

Contents

Contents

Introduction

> To the layman buckling is a mysterious,
> perhaps even awe-inspiring, phenomenon
> that transforms objects originally imbued
> with symmetrical beauty into junk.
>
> *(David Bushnell)*

1.1 Motivation

1.1.1 Elastic instability and buckling

Elastic instabilities are familiar from everyday life: umbrellas suddenly flip upwards on a windy day, while children's popper toys resemble rubber spherical caps that rapidly 'pop' and jump after being turned inside-out. On much larger scales, similar instabilities have traditionally been viewed as a type of failure in engineering applications; for example, the collapse of a water tower due to the weight of liquid inside. For this reason, classical work has placed an emphasis on predicting the onset of elastic instabilities, the primary aim being to design structures that avoid such instabilities in reasonable operating conditions (Bushnell, 1981).

A common type of instability is buckling. This is when slender structures suddenly deform out of plane in response to in-plane compression. To have a simple picture in mind, consider compressing an ordinary playing card at its edges: rather than being crushed, experience tells us that the card will deform out of plane to form an arch shape (see figures 1.1a–c). This is an example of the classical Euler buckling instability that
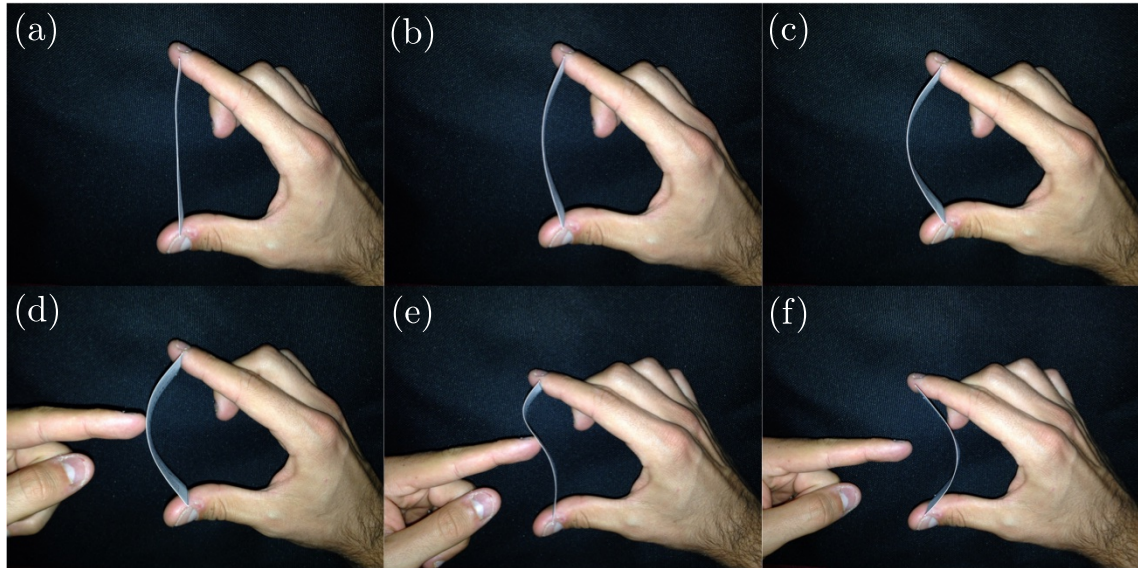
Figure 1.1: *A strip of card can be used to demonstrate two types of buckling. The first is the classical Euler buckling of an axially compressed column, which creates bistable arch shapes that are reflections of each other (a–c). When one of these arches is indented near its midpoint (d,e), another type of buckling is observed: the arch snaps through to the second stable configuration (f).*

has become the paradigm for many structural stability problems (Johnston, 1983). More generally, buckling is characterised by a bifurcation of the equilibrium shape in which a structural element deforms. The post-buckled response is usually difficult to predict due to a high sensitivity to material imperfections, which may lead to a significant reduction in the load-carrying capacity (Jones, 2006). In traditional applications (such as a water tower), this type of behaviour can spell catastrophic failure and so is to be avoided at all costs.

Recently, there has been a shift in perspective to take advantage of elastic instabilities rather than trying to avoid them (Reis, 2015). Because elastic instabilities generally occur quickly and cause large changes in shape, they open up the possibility of generating fast movements with little power (since energy can be stored slowly but released suddenly). This principle has long been exploited in biology, for example by carnivorous plants to catch their prey: the leaf of the Venus flytrap resembles a thin shell (i.e. a structure that is naturally curved in two orthogonal directions) which, upon stimulation of trigger hairs, rapidly snaps to a closed state in around 100 ms (Forterre *et al.*, 2005). Similarly, the beak of the hummingbird snaps through to catch insects mid-flight (Smith *et al.*, 2011).

The same idea has widespread potential for technological applications. A major part of the emerging field of 'extreme mechanics' combines elements of mathematics, physics, materials science, chemistry and biology to harness elastic instabilities for novel functions (Reis, 2015; Hu & Burgueño, 2015). Recent interest in this area has been partly driven by

the availability of soft materials, such as silicone-based elastomers, which can be easily fabricated and undergo large displacements while remaining linearly elastic (Krieger, 2012). A promising use is in morphing structures — continuous devices that seamlessly change shape in response to their environment — in which several discrete parts can be replaced by a flexible component whose instabilities provide the means of shape control. The result is a substantial saving in weight and energy requirements, as well as the capability to withstand larger deflections without damage (Brinkmeyer *et al.*, 2012). This technology is already being used to develop multistable wind turbine blades that change shape to minimise drag forces (Lachenal *et al.*, 2013), as well as adaptive aerofoil structures (Kuder *et al.*, 2013; Gano *et al.*, 2003). To make full use of instabilities in this context requires an understanding of how fast the instability proceeds, i.e. its dynamics, as well as its onset, and how the system behaves when pushed far beyond the threshold of instability.

1.1.2 Snap-through

This thesis is concerned with 'snap-through' buckling or snapping, a type of instability in which an elastic object rapidly jumps from one state to another. Snap-through is observed in many elastic systems that are bistable, i.e. systems that can be in equilibrium in one of two stable configurations. Bistability is often caused by geometric nonlinearity (for example natural curvature) but may also result from residual stress or some sort of material anisotropy (Krylov *et al.*, 2008). When one configuration ceases to exist as a stable equilibrium, for instance due to a change in geometry or external loading, the system rapidly switches to the alternative configuration.

The strip of card in figure 1.1 demonstrates this. The applied compression has buckled the card into one of two possible arch shapes, and if we 'poke' the arch at its midpoint (figure 1.1d,e) we find that eventually it becomes unstable and jumps to the alternative shape (figure 1.1f). The snap-through dynamics is governed by a build up of potential energy that, without further energetic cost, drives the system to the only remaining stable configuration. This example also shows that for macroscopic systems, we can generally expect timescales for snap-through to be on the order of milliseconds for motions over distances comparable to the initial displacement.

Contrast this behaviour to the buckling event pictured in figure 1.1a–c, the classical Euler buckling of a straight column. There, a smooth, *local* progression occurs from the pre-buckled (flat) shape to the post-buckled (arched) shape as a critical amount of compression is reached; a small increase beyond the threshold leads to a small amplitude displacement. Mathematically speaking, this difference exists because the bifurcations causing buckling in these two examples are qualitatively different. Classical Euler buckling is well known to
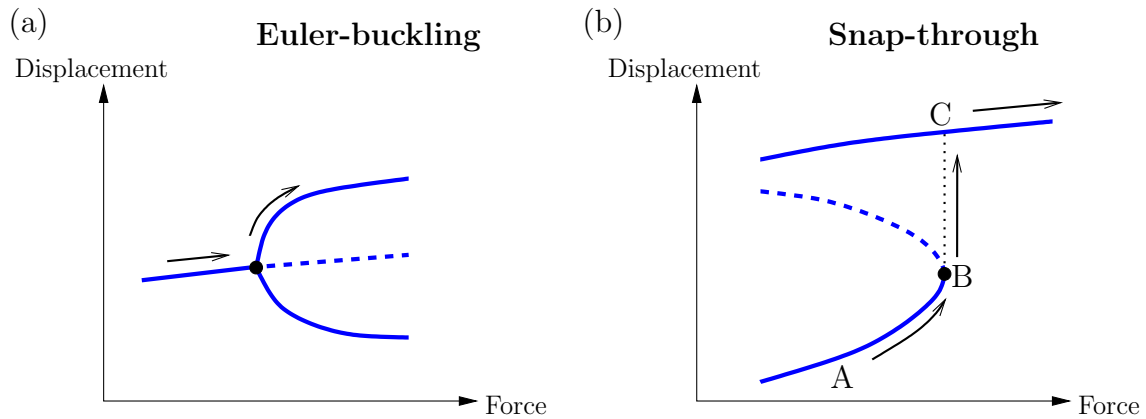
Figure 1.2: *The typical response of an elastic system undergoing (a) Euler buckling and (b) snap-through at a saddle-node bifurcation. In both plots the solid curves correspond to stable equilibrium modes, while the dashed curves correspond to unstable modes; arrows indicate the direction in which deformation takes place.*

be a supercritical pitchfork bifurcation (Howell *et al.*, 2009): the equilibrium loses stability to two stable, neighbouring modes, as illustrated by the force-displacement diagram in figure 1.2a[1]. This type of buckling has been termed bifurcation buckling (Bushnell, 1981).

To reiterate, snap-through is a bifurcation that causes the sudden disappearance of a nearby stable mode (known as a catastrophic bifurcation) — the system must undergo a *global* re-arrangement to find the remaining stable shape. Generically this is a saddle-node/fold bifurcation, in which the stable equilibrium meets another (unstable) mode and disappears. A typical force-displacement diagram for this case is shown in figure 1.2b: loading the system up to snap-through corresponds to (quasi-statically) traversing the branch from the point labelled A to the saddle-node bifurcation at B. Any further increase in the load at this point then causes snap-through to the remote equilibrium at C. Because this is where failure would occur in many traditional applications, this kind of bifurcation has also been called a limit point (Bushnell, 1981).

We can also get some intuition by visualising snap-through using the so-called ball-on-hill analogy (Wiebe, 2012). In this picture we imagine a ball rolling on a hill under the action of gravity — see figure 1.3. The equilibrium positions of the ball are analogous to the equilibrium modes of a generic elastic system. Initially, the profile of the hill is chosen to represent a double-well potential giving rise to bistability: the valleys correspond to two stable equilibria (any perturbation to a ball placed at this point would cause it to roll back), and the hilltop corresponds to an unstable equilibrium which separates the two. If we evolve the profile so that one of the valleys approaches the hilltop, a saddle-node bifurcation occurs in which the stable and unstable equilibria meet at an inflection point.

---

[1]In practice a true pitchfork is never possible, since the presence of geometric imperfections will always select a particular branch (Bushnell, 1981).
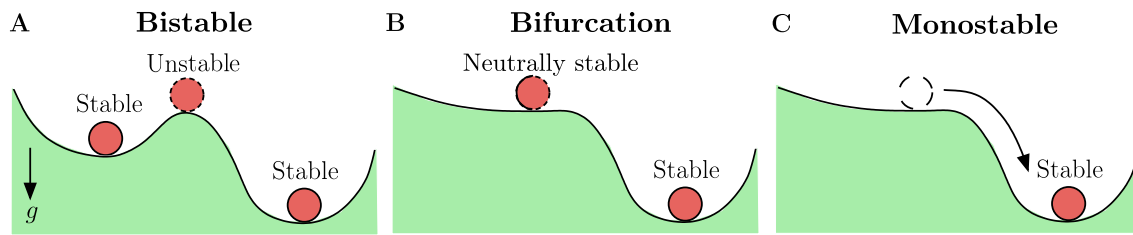
Figure 1.3: *The ball-on-hill analogy: the mechanics of a generic system exhibiting bistability and snap-through can be represented by a ball rolling under the action of gravity.*

Any further change will cause the ball to 'snap' and spontaneously roll down to the only remaining equilibrium. Note that the points labelled A, B and C here can be directly identified with the same points on the force-displacement diagram in figure 1.2b. This analogy is also useful in other ways: for example, it shows that dynamic snap-through is possible, in which snap-through results from a dynamic load such as an initial impulse.

1.1.3 Applications of snap-through

Snap-through has proved to be particularly useful among other elastic instabilities (e.g. wrinkling and crumpling), due to its ability to convert stored energy into fast motions in a highly reproducible way. Classical structures such as arches and shells naturally provide the structural prototypes (Hu & Burgueño, 2015), since their well-studied stability and post-buckled responses can be tuned to the desired application. For example, bistable arches and plates exhibiting snapping instabilities are becoming increasingly popular in the design of switches and actuators in microelectromechanical systems (MEMS) (Go *et al.*, 1996; Krylov & Dick, 2010), for which there is a need to generate large changes in shape while consuming little power. A number of loading types have been explored in this context, such as electrostatic (Krylov *et al.*, 2008), transverse point force (Qiu *et al.*, 2004), piezoelectric (Maurini *et al.*, 2007), electromagnetic (Han *et al.*, 2004), and photomechanical (Shankar *et al.*, 2013).

Other applications have expanded the scope significantly. Boisseau *et al.* (2013) have demonstrated how a bimetallic arch, clamped between a heat source and sink, can act as a 'heat engine' and convert thermal gradients to electrical energy via snap-through. Gonçalves *et al.* (2003) have developed a ventricular assist device that consists of a chamber sealed by a spherical cap, which snaps under a pneumatic load to generate net blood flow. Holmes & Crosby (2007), inspired by the snapping Venus flytrap, have designed an array of pre-stressed shells that snap simultaneously upon local expansion of the material; see figure 1.4a. This expansion can be triggered by a range of environmental factors, thus creating a responsive surface for potential use in sensors, adhesives and on-demand drug
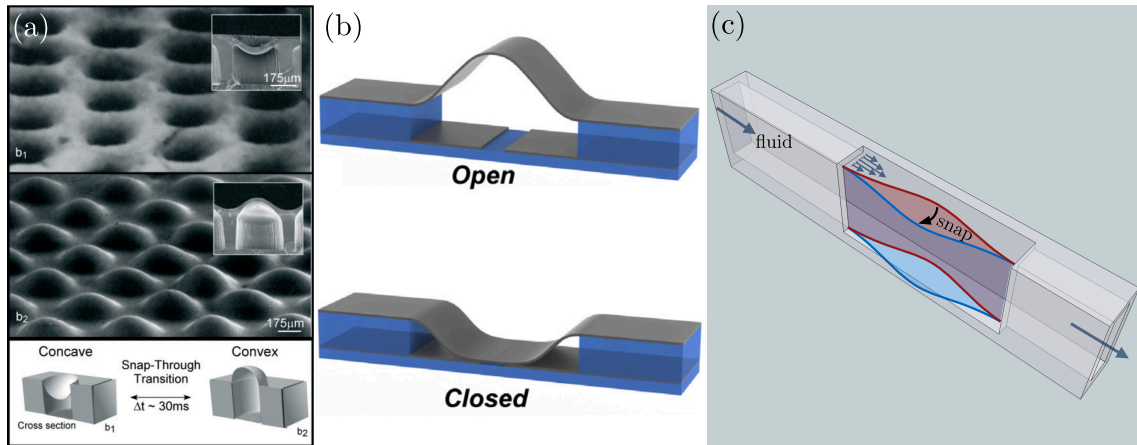
Figure 1.4: *Applications of snap-through instabilities. (a) A responsive surface featuring bio-inspired shells that snap upon swelling of the substrate (reprinted with permission from [D. P. Holmes and A. J. Crosby. Advanced Materials. 19 (21), 3589–3593 (2007). DOI: https://doi.org/10.1002/adma.200700584]. Copyright © 2007 WILEY-VCH Verlag GmbH & Co. KGaA, Weinheim). (b) A flexible switch composed of a ferromagnetic arch that snaps under an external magnetic field (reprinted from [V. Ramachandran, M. D. Bartlett, J. Wissman and C. Majidi. Extreme Mechanics Letters. 9, 282–290 (2016). DOI: https://doi.org/10.1016/j.eml.2016.08.007] under a Creative Commons Attribution-NonCommercial-No Derivatives License [https://creativecommons.org/licenses/by-nc-nd/4.0/]). (c) A passive valve to control viscous flow, which uses snap-through of an embedded elastic arch to rapidly unconstrict a channel and increase its hydraulic conductivity (reprinted from [M. Gomez, D. E. Moulton and D. Vella. Physical Review Letters. 119, 144502 (2017). DOI: https://doi.org/10.1103/PhysRevLett.119.144502]. Copyright 2017 by the American Physical Society).*

delivery. Building on this work, Loukaides *et al.* (2014) have demonstrated that a magnetic field may be used to remotely induce snap-through of a spherical cap, which can be readily scaled down to create micro-scale switches. Figure 1.4b shows a similar design of a switch in soft electronics, based on a ferromagnetic arch that snaps under an applied magnetic force (Ramachandran *et al.*, 2016).

Fargette *et al.* (2014) have shown that snap-through is not restricted to dry systems, but that capillary forces in a water drop, working against gravity, can trigger snap-through in an elastic arch. This can arise due to condensation on the lower side of the arch, and so has been proposed as a passive moisture sensor that snaps at a critical ambient humidity. Overvelde *et al.* (2015) have designed a fluidic actuator to generate fast movements in soft robotics, based on the snap-through of an inflatable segment. Snap-through may also result from bulk fluid flow, just as an umbrella suddenly inverts in fast winds. Gomez *et al.* (2017*b*) have demonstrated that the pressure gradient in a viscous channel flow may cause snap-through of an embedded elastic element (figure 1.4c). This gives the channel a number of properties that are unusual at low Reynolds number, including large and abrupt changes in the channel conductivity and history dependence; in addition, it is believed that these features may be scaled down to control flow in micro-fluidic devices without the need for direct intervention. Snap-through has also been demonstrated in colloidal particles in response to changes in pH (Epstein *et al.*, 2015), and in micro hydrogel devices upon solvent-induced swelling (Lee *et al.*, 2010); in both systems, snap-through enables shape changes that are much faster than changes in external stimulus, which are typically limited by diffusion. Other advances in harnessing snap-through include scaling down to nanoscale systems such as graphene membranes, generalising to multistable systems capable of many different configurations, and developing new structural prototypes such as ribbons and orthotropic shells; for a review see Hu & Burgueño (2015).

1.1.4 Dynamics of snap-through

The initiation of snap-through is often a loss of stability arising from a local bifurcation. As a result, snap-through instabilities in basic structural components (e.g. arches, plates, shells) have been well studied as classical stability problems, with the focus on accurately predicting the onset of instability (Bazant & Cendolin, 1991; Patricìo *et al.*, 1998; Plaut, 2009; Chen & Hung, 2011). More recent studies address the mathematical problems associated with large pre-buckling deformations, material imperfections and inhomogeneities, as well as the effects of dynamic loading (Krylov & Dick, 2010).

Despite the ubiquity of snap-through in nature and engineering, the dynamics of snap-through is much less well understood (Pandey *et al.*, 2014). Typically, only a linear

stability analysis is considered, which analyses small-amplitude oscillations about equilibrium in the equations of motion (in this context this is also known as the vibration method; see Chen & Hung, 2011). Mathematically, this yields a linear eigenvalue problem for the natural frequencies of oscillation (eigenvalues), ω; the corresponding eigenfunctions are simply the modes of oscillation. If one of these frequencies becomes complex as the loading proceeds, then the equilibrium mode has become unstable: any perturbation to its shape will grow exponentially in time. The eigenfunction associated with instability also reveals how the shape initially evolves; for example, an asymmetric eigenfunction will lead to asymmetric deformations during snap-through. It is sometimes possible to go further and use a linear stability analysis to predict the timescale of the snap-through transition. An example is poking an arch at its midpoint, as in figure 1.1, which has been studied in detail by Pandey *et al.* (2014). Here the shape always evolves to an unstable Euler buckling mode before snap-through occurs. A linear stability analysis of the Euler buckling mode then yields an eigenvalue characterising the growth rate of the instability.

However, a simple stability analysis is often not applicable or feasible due to the complexity of the system. In such a case, previous approaches have been mainly numerical or experimental in nature (Santer, 2010; Brinkmeyer *et al.*, 2013; Wiebe, 2012; Loukaides *et al.*, 2014). An important class of problems of this type involve snap-through at a saddle-node bifurcation: if we increase the load slightly beyond the fold point (point B in figure 1.2b), there no longer exists an equilibrium mode to consider the stability of! In particular, we are unable to obtain an eigenvalue that characterises the growth rate in the same way. This raises the fundamental question of how we can analyse the timescale of snap-through in such problems. Do we have to rely on numerically integrating the equations of motion, or is analytical progress feasible? Analytical insight would be of interest both from the perspective of fundamental science and also for applications of snap-through, as it provides a basis to control the dynamic response without relying on direct numerical simulations.

The dynamics near a saddle-node bifurcation has been well studied in low dimensional dynamical systems — those that consist of a few ordinary differential equations (ODEs) — in various physical and biological settings (Strogatz & Westervelt, 1989; Sardanyés & Solé, 2006; Trickey & Virgin, 1998). These studies have shown that, as well as hysteresis, the nonlinearity underlying bifurcation can lead to delay phenomena. An upcoming saddle-node bifurcation is often signalled by the so-called 'critical slowing down', in which the system recovers from perturbations over an increasingly long timescale (Scheffer *et al.*, 2009). Furthermore, the remnant or 'ghost' of a saddle-node bifurcation continues to influence the dynamics in its aftermath: by simply being close to bifurcation in parameter space, the motions are slowed in what is called a 'bottleneck' phase (Strogatz, 2014). For example, consider the trajectory that is just to the right of the fold point in figure 1.2b

(vertical arrow). Because the various forces within the structure are in balance at the fold point (as this is an equilibrium solution), the net force on the structure is very small as it passes near the fold during snap-through, and its motions slow down significantly. The structure therefore appears to feel the attraction of the equilibrium at the fold, even though this no longer exists as a solution at loads beyond the point B. This ghost phenomenon is in fact generic for the dynamics near a saddle-node bifurcation, and has been analysed in various physical settings including first-order phase transitions in condensed matter physics (Chaikin & Lubensky, 1995). One of the key challenges of this thesis is to extend this work to an elastic continuum described by partial differential equations (PDEs), which can be regarded as a dynamical system having infinite degrees of freedom.

1.2 Structure of the thesis

In this thesis we study the dynamics of snap-through. In particular, we determine how the underlying mathematical structure influences the snapping timescale, and the precise role played by energy dissipation. Below we provide a more detailed synopsis of each chapter.

We begin in Chapter 2 by reviewing the concept of a saddle-node ghost, before considering the dynamics of electrostatic 'pull-in' — a type of snap-through under the action of electrostatic forces that is frequently encountered in microelectromechanical systems (MEMS). This occurs when an elastic structure suddenly collapses onto a nearby electrode as an applied voltage exceeds a threshold value, and so provides a context in which to understand the dynamics of overdamped snap-through — the motions during pull-in are dominated by squeeze film damping when the air gap between components becomes very small. To gain insight we study a parallel-plate capacitor — a single-degree-of-freedom structure. Despite its simplicity, this model captures the balance between electrostatic and mechanical restoring forces that underlies pull-in, and provides a first approximation of more complex structures used in MEMS such as microbeams. We show that the slowing down observed near the pull-in transition can be attributed to the ghost of a saddle-node bifurcation, and so is generic for these kind of systems. This allows us to obtain an analytical expression for the time taken to pull-in, unifying a large range of experiments and numerical simulations of pull-in that exhibit delay phenomena.

Continuing our work on pull-in dynamics, in Chapter 3 we analyse the behaviour of MEMS microbeams. We address the problem of how to analyse snap-through of continuous elastic structures due to external loading: rather than using a single-degree-of-freedom model, we now consider the explicit geometry of the device, modelled using beam theory. As the governing equation is now a PDE in space and time, we develop a perturbation method that systematically reduces the dynamics to a much simpler ODE, resembling the

normal form for a saddle-node bifurcation. The method we present depends on the under-lying mathematical structure, rather than the precise physical details, and so provides a framework for analysing the snap-through dynamics in later chapters. For the microbeam we are then able to obtain an asymptotic prediction for the pull-in time, which we compare to numerical simulations and experimental data reported in the literature. In light of these results, we also discuss the validity of other approaches used to analyse the pull-in dynamics of microbeams.

In Chapter 4 we explore whether energy dissipation is needed to obtain bottleneck behaviour during snap-through: what happens in elastic systems where damping is negligible? This is motivated by the anomalously slow dynamics shown by spherical caps which, when turned 'inside-out', may take several seconds to snap back to their natural shape. Rather than dealing with the complications that come with the shell equations, we instead consider an elastic arch as a simpler model system that possesses similar phenomenology. We show that the perturbation method developed in Chapter 3 carries over to this scenario, so that anomalously slow dynamics are still generic when the system is near the snap-through transition — there is no need for dissipation of energy. This has far reaching consequences for applications of snap-through, as it explains what limits the speed of snapping. We also quantify the regimes in which the system is effectively underdamped and overdamped during a bottleneck phase, and confirm our results using numerical simulations of an elastica model and experiments.

In many real systems, internal damping due to material viscosity is present to some degree. In Chapter 5, we consider the dynamics of snap-through when such viscoelastic effects are present. In particular, we analyse how the relaxation timescale of the material interacts with the critical slowing down we have previously studied. Considering a single-degree-of-freedom structure as a model system, we identify the regimes in which each effect dominates. We also show that even a small amount of viscoelasticity can significantly modify the snap-through dynamics. In the process, we uncover an intricate asymptotic structure of the different dynamical regimes, featuring new scaling laws for the snap-through time.

Finally, in Chapter 6, we summarise our findings and highlight some areas that make for interesting further study. We discuss how we might adapt our perturbation method to study the dynamics of other snap-through problems, incorporating the effects of noise and material imperfections, and similar delay phenomena that have been reported in other kinds of mechanical instabilities.

A simple example of snap-through: pull-in

Synopsis

We consider the dynamics of electrostatic MEMS devices undergoing the pull-in instability — an example of snap-through in which the motions are dominated by fluid damping. Numerous experiments and numerical simulations have shown that the time taken to pull-in increases significantly near the pull-in transition, where the transient dynamics slow down during a 'metastable' or 'bottleneck' phase. However, this phenomenon is not well understood quantitatively. Using a lumped parallel-plate capacitor model, we perform a detailed asymptotic analysis of the pull-in dynamics in this regime. We show that the bottleneck phenomenon is a type of critical slowing down arising from the pull-in bifurcation. This allows us to obtain a simple analytical expression for the pull-in time, which obeys an inverse square-root scaling law as the transition is approached. We then compare our prediction to a wide range of pull-in time data reported in the literature, showing that the observed slowing down is well captured by our scaling law. The scaling law therefore appears to be generic for overdamped pull-in. This realisation unifies a large number of previous observations of bottleneck behaviour during pull-in, and provides a useful design rule to tune dynamic response in sensing applications, including high-resolution accelerometers and pressure sensors. We also propose a method to estimate the pull-in voltage based only on data of the pull-in times.

A paper based on the work described in this chapter has been published in the *Journal of Micromechanics and Microengineering* (Gomez *et al.*, 2018*a*).

2.1 Introduction

Local bifurcations play a key role in the behaviour of physical and biological systems, due to their ability to change the system in an abrupt and dramatic way. This is particularly true of saddle-node (fold) bifurcations, which are the generic mechanism by which equilibrium solutions are created and destroyed (Strogatz, 2014). In this way, a saddle-node bifurcation naturally describes a transition from bistability to monostability: there is a sudden collapse of the possible configurations the system can adopt. For example, in climate systems, saddle-node bifurcations are encountered as 'tipping points' where a small change in conditions can cause abrupt shifts (Scheffer *et al.*, 2009). These are of great concern because the sudden collapse is prone to hysteresis, meaning the shift is extremely difficult to reverse.

Saddle-node bifurcations also frequently arise in microelectromechanical systems (MEMS) via the so-called 'pull-in' instability. Pull-in occurs when an elastic structure, under the action of electrostatic forces, suddenly collapses towards a nearby electrode when a critical voltage is exceeded (Pelesko & Bernstein, 2002). While pull-in may seem qualitatively different to traditional snap-through instabilities (such as those discussed in Chapter 1), the instability has a similar mathematical structure: at the critical voltage, the stable equilibrium away from collapse ceases to exist as an equilibrium solution, so that the system abruptly moves to the collapsed state to remain in equilibrium. Nevertheless, unlike traditional snap-through instabilities, the nonlinearity underlying the saddle-node bifurcation stems from the electrostatic force (via Coulomb's law) rather than from geometry. In addition, for devices operating in atmospheric conditions, the motions during pull-in are dominated by fluid damping, arising in the squeeze film when the air gap between components becomes very small (Missoffe *et al.*, 2008). We will therefore study pull-in as a model system in which to understand the dynamics of overdamped snap-through.

Because pull-in can result in failure via short circuit or stiction between components, studies have traditionally focussed on the stability of devices under a combination of electrostatic and mechanical restoring forces, with a view to developing methods that extend the operating range of a device prior to pull-in (Zhang *et al.*, 2014). More recently, pull-in has been identified as a useful instability for smart applications, in a similar way to macroscopic snap-through instabilities. For example, the critical voltage required to pull-in is commonly used in mass sensing applications (Younis & Alsaleem, 2009) and to estimate material parameters such as the elastic modulus (Osterberg & Senturia, 1997).

The dynamics of the pull-in transition is also becoming the basis of many MEMS devices. In these scenarios pull-in is allowed to proceed safely (e.g. by limiting the displacement of the structure to prevent contact between components), enabling fast motions and large
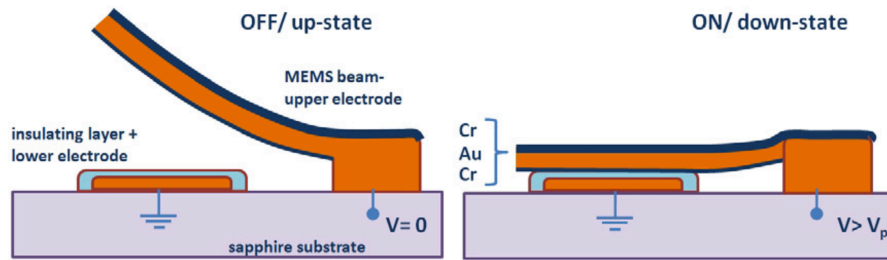
Figure 2.1: *A MEMS cantilever beam that undergoes a pull-in instability when a critical voltage is exceeded, corresponding to a saddle-node bifurcation. This causes the beam to rapidly switch from an 'off' state to an 'on' state as it adheres to the electrode. (Reprinted from [D. Bouyge, A. Crunteanu, M. Durán-Sindreu, A. Pothier, P. Blondy, J. Bonache, J. C. Orlianges and F. Martín. Reconfigurable split rings based on MEMS switches and their application to tunable filters. Journal of Optics. 14 (11), 114001 (2012). DOI: https://doi.org/10.1088/2040-8978/14/11/114001]. Copyright © IOP Publishing. Reproduced with permission. All rights reserved.)*

relative displacements to be generated in a reproducible way. For example, microvalves make use of the collapsed state to block off fluid flow in microchannels (Desai *et al.*, 2012), and microswitches harness pull-in to rapidly switch between two remote configurations, corresponding to distinct 'off' and 'on' states (Nguyen *et al.*, 1998; LaRose & Murphy, 2010; Deng *et al.*, 2017). An example of a microcantilever switch is shown in figure 2.1. In these applications, an understanding of the pull-in dynamics is essential since it determines the switching time of the device.

The time taken to pull-in can itself be used as a sensing mechanism: the relationship between the pull-in time of a microbeam and the ambient air pressure has been proposed as a pressure sensor (Gupta & Senturia, 1997), while high-resolution accelerometers make use of the sensitivity of parallel-plate actuators to external acceleration (Rocha *et al.*, 2004a; Dias *et al.*, 2011; 2015). In these applications, unlike microswitches and other actuators, it is not desirable to simply minimise the pull-in time. Instead, the device is operated at voltages very close to the pull-in transition, where the transient dynamics are observed to slow down significantly. Crucially, this slowing down is highly sensitive to ambient conditions, including external forces, and so has widespread potential to enable high-resolution, low-noise measurements to be made. Using pull-in time as a sensing mechanism also offers the advantage that the device may be integrated in standard circuit technology, so that commercially available micromachining processes can be used (Dias *et al.*, 2011).

The slowing down observed in parallel-plate actuators has been attributed to a 'metastable' or 'bottleneck' phase that dominates the dynamics during pull-in, characterised by a temporary balance between electrostatic and mechanical restoring forces (Rocha *et al.*, 2004a): as the net force on the structure is very small, it evolves slowly and the pull-in time is large. However, a quantitative understanding of this phenomenon is still lacking,

despite the obvious importance of this regime in the operation of many MEMS devices. In particular, it is not clear how the length of the delay (and hence the pull-in time) scales with the applied voltage, the external acceleration, and the material parameters of the system.

2.1.1 Models of pull-in dynamics

Because a standard linear stability analysis cannot be used to study the dynamics of pull-in — beyond the saddle-node bifurcation there is no unstable equilibrium base state from which the system evolves — most studies adopt a purely numerical or experimental approach. A large number of studies have focussed on generating macromodels, i.e. reduced-order models that couple deformations of the structure to realistic models of the squeeze film damping, incorporating compressibility and rarefaction effects. These macromodels are then used to reduce the computational cost of simulating MEMS devices during pull-in (see Batra *et al.*, 2007; Nayfeh *et al.*, 2005, and references therein). Bottleneck phenomena have been described in a number of macromodel simulations of microbeams (Grétillat *et al.*, 1997; Hung & Senturia, 1999; Younis *et al.*, 2003; Nayfeh *et al.*, 2007) as well as parallel-plate actuators (Rocha *et al.*, 2004*a*); slowing down appears to be a generic feature when the system is near the pull-in transition, though this has not been explored further. More recent studies instead address the dynamic stability of MEMS resonators under a combination of AC and DC loads (Nayfeh *et al.*, 2007; Zaitsev *et al.*, 2012), the effects of geometric nonlinearities due to large displacements (Chaterjee & Pohit, 2009), contact bouncing (McCarthy *et al.*, 2002; LaRose & Murphy, 2010), and modelling structures that possess natural curvature where traditional snap-through buckling can occur alongside pull-in (Krylov *et al.*, 2008; Das & Batra, 2009; Krylov & Dick, 2010); for a review see Zhang *et al.* (2014).

Few analytical results concerning pull-in dynamics are available. While general bounds on the pull-in time have been obtained (Flores *et al.*, 2003), these bounds are not very tight and do not give insight into anomalously slow behaviour close to pull-in. In the case of underdamped, inertia-driven systems, some progress has been made. For devices operating at very low ambient pressures, inertial effects can cause the critical voltage at pull-in (known as the dynamic pull-in voltage in this case) to decrease compared to that obtained when the voltage is quasi-statically varied (the static pull-in voltage) (Nielson & Barbastathis, 2006). Using energy methods, scaling laws for the pull-in time have been derived for parallel-plate actuators (Leus & Elata, 2008) and extracted for more complex devices such as microbeams using lumped-parameter models (Joglekar & Pawaskar, 2011). The key result is that the pull-in time, t_{PI}, scales logarithmically with the difference

between the applied voltage and the pull-in voltage, $\Delta V > 0$: we have that

$$t_{\mathrm{PI}} \propto \log(1/\Delta V), \tag{2.1}$$

as $\Delta V \to 0$. As ΔV decreases, the pull-in time therefore increases rapidly, until eventually mechanical noise limits the response.

Due to its simplicity, the scaling law (2.1) offers a useful design rule to tune dynamic response in applications: only a small number of runs are needed to extract the appropriate pre-factor in the scaling law to make further predictions. The need to perform parameter sweeps that at each stage involve detailed simulations can then be eliminated. However, no corresponding scaling law has been found for overdamped systems, despite the fact that (i) many MEMS devices operate in this regime (Rocha *et al.*, 2004*a*) and (ii) there is a clear need for such a design rule as devices continue to scale down and grow in complexity (Loh & Espinosa, 2012). Obtaining such a scaling law analytically is the primary objective of this chapter.

2.1.2 A scaling law for overdamped pull-in

To explore the possibility of a scaling law analogous to (2.1) but applicable to overdamped devices, we have assembled a large range of data for pull-in times reported in the literature. We focus on results for devices operating at (or near) atmospheric pressure only; we do not consider data for pull-in times in vacuum where inertial effects are important. We consider parallel-plate and microbeam devices, incorporating data from both experiments and dynamic simulations. This includes data where the actuation voltage is varying while the external acceleration is zero, as well as data from pull-in time accelerometers where the actuation voltage is fixed but the external acceleration is varied. A summary of the conditions for each data set is provided later in tables 2.1–2.2. In all cases examined, the pull-in times are measured from the point of application of a step DC voltage (stepped from zero), one of the most common types of electrostatic actuation. Where data is only available graphically, we have extracted the values using the WebPlotDigitizer (aro-hatgi.info/WebPlotDigitizer).

For each measurement, we use the reported values of the pull-in voltage to compute the normalised distance to the pull-in transition, which we denote by ϵ. In particular, in the case of zero external acceleration, we have $\epsilon = (V/V_{\mathrm{SPI}})^2 - 1$ with V the applied voltage and V_{SPI} the static pull-in voltage. (When the external acceleration is non-zero, we define ϵ later in §2.4.) The results are shown on logarithmic axes in figure 2.2, where different symbols are used to indicate different data sets (i.e. where the properties of the actuator are varied), and data from different references are distinguished using different colours.
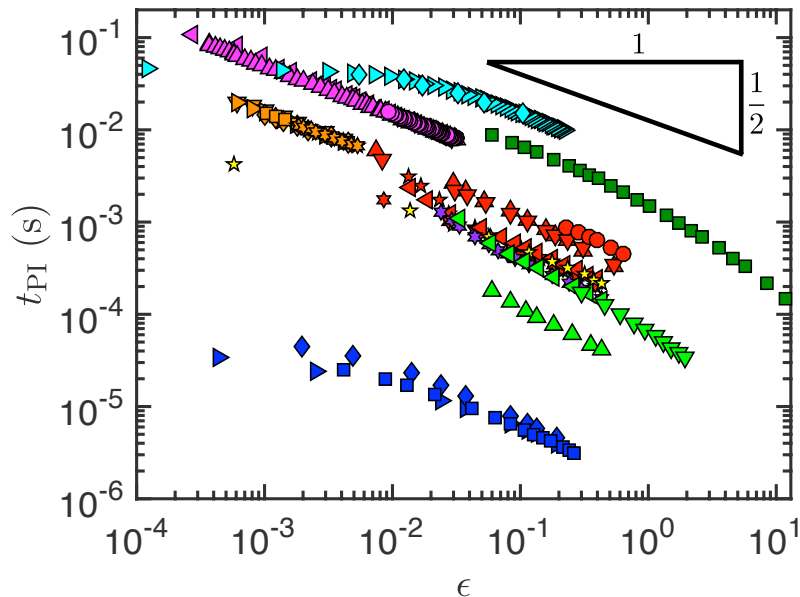
Figure 2.2: *Pull-in times of parallel-plate and microbeam devices under step DC loads reported in the literature. In total, 27 sets of data from 9 different references are included, indicated by different symbol shape and colour; details and legend are provided later in tables 2.1–2.2. (Reprinted from Gomez et al. (2018a), DOI: https://doi.org/10.1088/1361-6439/aa9a70. Copyright © IOP Publishing. Reproduced with permission. All rights reserved.)*

We observe that the pull-in time increases as ϵ decreases in a systematic way. Very close to the pull-in transition, the dynamics become highly sensitive to the precise value of ϵ: the pull-in time may increase by over an order of magnitude within a very narrow range of ϵ. This is the bottleneck regime in which the dynamics of pull-in are dramatically slowed down.

This delay behaviour is reminiscent of the critical slowing down observed near saddle-node bifurcations in a range of physical systems, such as phase transitions (Chaikin & Lubensky, 1995) and the switching of charge density waves (Strogatz & Westervelt, 1989). In these systems, the remnant or 'ghost' of the saddle-node bifurcation continues to attract trajectories that are nearby in parameter space, producing a bottleneck whose duration generically increases with decreasing distance from the bifurcation (Strogatz, 2014). The detailed scaling of the bottleneck duration depends on the importance of inertia: a scaling $\propto \epsilon^{-1/2}$ is characteristic of overdamped motion (reviewed in §2.2 below) while the scaling $\propto \epsilon^{-1/4}$ is characteristic of underdamped motion (we will study this regime in Chapter 4).

The key observation here is that most of the data in figure 2.2 appears to be consistent with the same overdamped scaling law, namely $t_{\mathrm{PI}} \propto \epsilon^{-1/2}$ as $\epsilon \to 0$. More precisely, we have fitted each data set (using least-squares) to a power law of the form $t_{\mathrm{PI}} = \alpha \epsilon^{-\beta}$ where $\beta > 0$; over all 27 data sets considered in figure 2.2, we find a mean value $\beta \approx 0.56$ with a standard deviation of 0.14 in the fitted values. While an $\epsilon^{-1/2}$ scaling law has been

identified as the source of anomalously slow dynamics in microbeam resonators (Zaitsev *et al.*, 2012), we believe this has not yet been properly appreciated as a generic feature of overdamped pull-in under DC loads.

The slowing down observed in figure 2.2 motivates a more careful analysis of the dynamics of overdamped pull-in. In this chapter we focus on the simplest possible electrostatic device: a parallel-plate actuator under a DC load. This single-degree-of-freedom structure captures the balance between electrostatic and mechanical restoring forces that underlies the pull-in instability, without requiring details of the geometry of the device. It has been successfully used as a lumped-parameter model for more complex structures such as microbeams and microplates (Castaner & Senturia, 1999). Our analysis of the parallel-plate actuator therefore allows us to consider a generic MEMS device, upon taking appropriate values of the lumped parameters. Our central result is that the bottleneck behaviour observed near the pull-in transition is a type of saddle-node ghost, and so inherits the expected scaling law, with the pull-in time $t_{\text{PI}} \propto \epsilon^{-1/2}$ as $\epsilon \to 0$. While some data sets in figure 2.2 do not appear to follow this scaling, we suggest that the discrepancy is due to sensitivity to the precise value of the reported pull-in voltage, and propose a method to obtain a more accurate value of the pull-in voltage based only on measured pull-in times.

The remainder of this chapter is organised as follows. We begin in §2.2 by reviewing the concept of a saddle-node ghost, and the origin of the $\epsilon^{-1/2}$ scaling law for the bottleneck duration. We also discuss how the tools of dynamical systems generalises this to higher-order systems of ODEs and PDEs; this material will form the basis behind how we later analyse the dynamics near the pull-in bifurcation. In §2.3 we derive the equations governing the motion of the parallel-plate actuator. In §2.4, we solve the equations numerically when the system is perturbed just beyond the static pull-in transition. In the overdamped limit, we recover the bottleneck phenomenon reported previously (Rocha *et al.*, 2004*a*). We then perform a detailed asymptotic analysis of the solution structure in this regime, allowing us to derive an approximate expression for the pull-in time. In §2.5, we compare our asymptotic prediction to the experimental and numerical data given in figure 2.2. We show that the observed slowing down is well explained by our scaling law, and use our theory to collapse the data presented in figure 2.2 onto a master curve (see figure 2.9). Finally, in §2.6, we summarise and conclude our findings.

2.2 Ghosts and bottlenecks

2.2.1 A simple example

(The notation used in this review section is independent of that used in the rest of the chapter.)
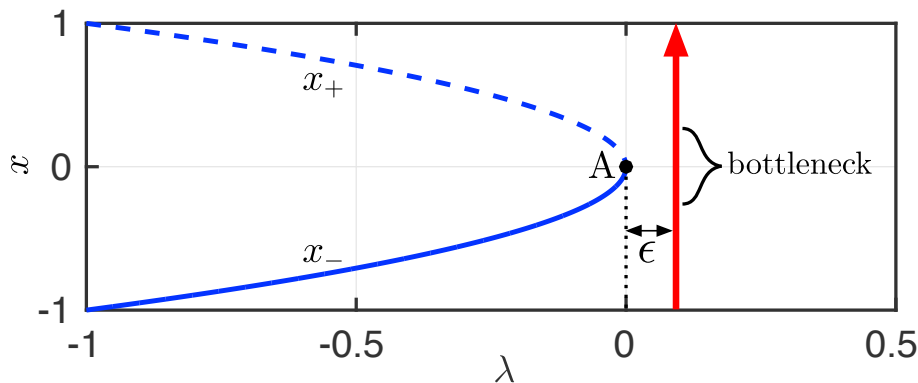
Figure 2.3: *Response diagram for the fixed points $x_\pm$ (solid and dashed curves) of equation (2.2). This exhibits a saddle-node bifurcation at the point A where $\lambda = 0$ and $x_\pm = 0$. A trajectory at fixed λ beyond the bifurcation point is also shown (red arrow).*

To better understand the dynamics near a saddle-node bifurcation, and why a linear stability analysis does not apply, we begin with a simple example. Consider the ODE:

$$\frac{\mathrm{d}x}{\mathrm{d}t} = \lambda + x^2. \tag{2.2}$$

Here $x(t)$ is a (real valued) continuous variable and $\lambda \in \mathbb{R}$ is regarded as a control parameter, i.e. we consider the effect on fixed points of (2.2) upon varying λ. This equation is in fact the normal form for a saddle-node bifurcation: we can think of (2.2) as describing the local behaviour near a generic saddle-node bifurcation, after 'zooming in' on the region near the fold in the bifurcation diagram where it resembles a parabola (Strogatz, 2014). Because of the single time derivative in (2.2), we are also assuming the dynamics are overdamped.

Suppose that $\lambda < 0$. Setting $\mathrm{d}x/\mathrm{d}t = 0$ in (2.2), we see that the equation has the distinct fixed points

$$x_\pm = \pm(-\lambda)^{1/2}.$$

To determine their linear stability, we let $x(t) = x_\pm + \epsilon X(t)$, where $\epsilon \ll 1$ is some small perturbation and $X(t)$ is to be determined. Substituting into (2.2) and linearising in ϵ, we obtain

$$\frac{\mathrm{d}X}{\mathrm{d}t} = 2x_\pm X.$$

Solving gives $X(t) = X(0)e^{2x_\pm t}$. We deduce that for $\lambda < 0$, the point x_- is linearly stable: $x_- < 0$, so perturbations decay exponentially in time. Similarly, x_+ is linearly unstable (perturbations grow exponentially in time). The timescale of this exponential decay/growth is $\sim (-\lambda)^{-1/2}$.

Now suppose that the system is at the stable point x_-, and we quasi-statically increase λ towards zero. Initially, the two equilibria only approach each other and the system lies
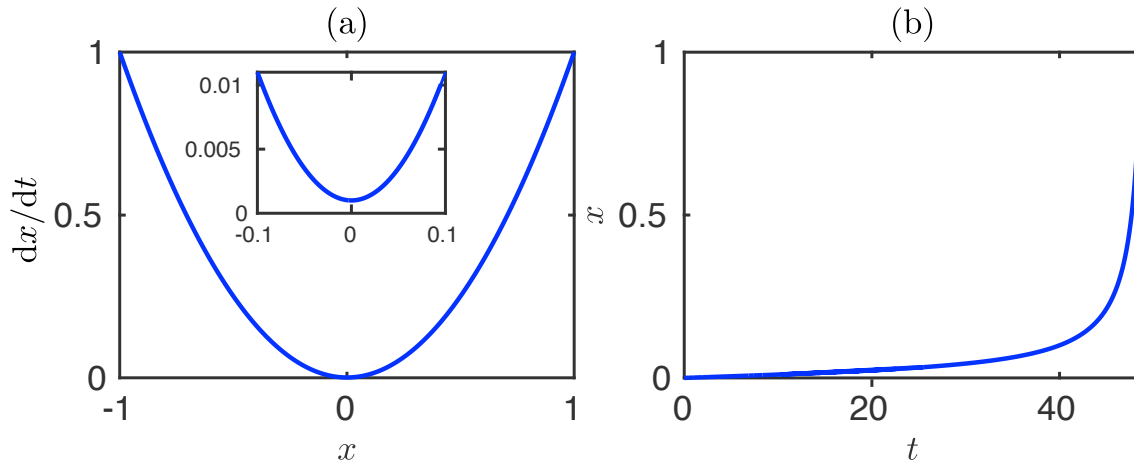
Figure 2.4: *The typical behaviour of (2.2) for values of λ just beyond the saddle-node bifurcation at $\lambda = 0$. (a) The phase plane and a close-up near $x = 0$ (inset). (b) A typical trajectory $x(t)$, displaying a distinctive bottleneck phase as it passes the ghost of the fixed point $x_\pm = 0$. Here we have taken $\epsilon = 10^{-3}$.*

happily at x_- for each value of λ; see figure 2.3, which displays the points as branches on a bifurcation diagram as λ is varied. Eventually, as λ reaches zero, the equilibria merge and disappear at a saddle-node bifurcation with $x_\pm = 0$ (point A on figure 2.3). For values $\lambda > 0$, there are no longer any fixed points of (2.2). It follows that the system must now move away from x_-.

How does the system evolve for values of λ just beyond the fold? Notice that if we try to repeat the linear stability analysis, setting $x(t) = x_\pm + \epsilon X(t)$ etc. with $x_\pm = 0$, we obtain

$$\frac{\mathrm{d}X}{\mathrm{d}t} = 0,$$

which tells us nothing useful. In the language of dynamical systems, the fold at $\lambda = 0$ is a non-hyperbolic fixed point: the associated Jacobian matrix has a simple zero eigenvalue when evaluated at the fixed point $x_\pm = 0$, which does not specify whether perturbations grow or decay in time. In other words, a linear stability analysis gives us no information about the local dynamics.

To explore the local behaviour, we set $\lambda = \epsilon$ in (2.2), where $0 < \epsilon \ll 1$ is again some small quantity. The dependence of the velocity $\mathrm{d}x/\mathrm{d}t$ on x is shown by the phase plane in figure 2.4a: we see that while x is near zero the velocity is very small. The result is a slow phase in trajectories — a dynamical bottleneck — as $x(t)$ passes near zero, before the trajectories rapidly blow up due to the quadratic nonlinearity (in fact, they blow up in finite time). A typical trajectory, taking $x(0) = 0$ (which is where we lost x_- at the saddle-node bifurcation), is displayed in figure 2.4b. The trajectory and bottleneck phase are also illustrated schematically on the response diagram in figure 2.3.

This delay is purely a remnant of the saddle-node bifurcation, and relies on no extra physics than that contained in (2.2). Generally, whenever a saddle-node bifurcation continues to influence a region in the phase space by slowing trajectories, we say that the dynamics is influenced by the 'ghost' of the saddle-node bifurcation (Strogatz, 2014). Figure 2.4a makes the mechanism underlying a ghost clear: we see that the fold point just misses the line $\mathrm{d}x/\mathrm{d}t = 0$, so that the velocity is very small but non-zero there. Thus, the system appears to 'feel' the attraction of the fixed points, even though they no longer exist!

In this example, it is a simple matter to evaluate the time taken for a trajectory to pass through the bottleneck (Kuehn, 2008). Since equation (2.2) is separable, we use standard techniques to find the solution in implicit form:

$$ t = \epsilon^{-1/2} \left\{ \tan^{-1}[\epsilon^{-1/2} x(t)] - \tan^{-1}(\epsilon^{-1/2} x_0) \right\}, \tag{2.3} $$

where we have specified the initial data $x(0) = x_0$. Notice that while x is small, its growth is only linear in time; contrast this to the exponential growth/decay we saw away from the fixed points before bifurcation, when a linear stability analysis was applicable. Using the implicit solution above, the time taken to pass through the fixed interval $[-\delta, \delta]$, centered around zero, is

$$ t_b = 2\epsilon^{-1/2} \tan^{-1}(\epsilon^{-1/2}\delta) \sim \pi\epsilon^{-1/2} \quad \text{as} \quad \epsilon \searrow 0. $$

We could also define the bottleneck duration t_b as the time taken for the solution to blow-up at infinity, starting from zero: if we think of (2.2) as a local rescaling in space, having neglected higher-order terms, then blow-up corresponds to leaving the neighbourhood of the fold as this scaling breaks down. Letting $x_0 = 0$ and $x(t) \to \infty$ in (2.3) yields

$$ t_b = \frac{\pi}{2}\epsilon^{-1/2} = O(\epsilon^{-1/2}) \quad \text{as} \quad \epsilon \searrow 0. \tag{2.4} $$

In either case, the bottleneck duration scales with the distance ϵ from the bifurcation point as an inverse square-root law. The robustness of this scaling is because the time taken to pass through zero dominates any other timescale; only the pre-factor of $\epsilon^{-1/2}$ varies.

2.2.2 Ghosts in higher dimensions

The bottleneck associated with a saddle-node ghost is a very general phenomenon. In fact, it is found generically in dynamical systems near saddle-node bifurcations, regardless of whether the phase space has a very high dimension. For such systems, it is inherently more tricky to analyse the dynamics near a bifurcation compared to equation (2.2). However, we might expect that not all of the dimensions in phase space have equal influence on

the behaviour, and that particular subspaces (or more precisely manifolds) — such as those associated with the bifurcation — play a key role. This means that the asymptotic behaviour can still be extracted from a lower order system. The methods of dimension reduction or reduced-order modelling rigorously justify this expectation, and are based on systematically reducing the order of the system while still capturing its salient features (Rega & Troger, 2005). In this way we can make use of the well-developed theory of low-dimensional systems and their normal forms.

Using these tools, it can be shown that the dynamics in a neighbourhood of a generic saddle-node bifurcation quantitatively resembles the normal form (2.2) (for the precise conditions of one-dimensionality and genericity combined into a compact theorem, see Guckenheimer & Holmes, 2013). As a consequence, the bottleneck duration t_b generically obeys the same inverse square-root scaling law. If λ is the bifurcation parameter, with stability lost as λ increases to λ_c, this becomes

$$t_b = O\left([\lambda - \lambda_c]^{-1/2}\right) \quad \text{as} \quad \lambda \searrow \lambda_c.$$

The square-root scaling law of a ghost has been applied in various physical and biological systems that lose stability at a fold. It occurs in the hypercycle model of self-replicating molecular species (such as RNA), where the bottleneck has been suggested as a favourable — and possibly naturally selected — 'memory effect' in pre-biotic evolution that delays the transition to extinction (Sardanyés & Solé, 2006). In condensed matter physics, models of the delayed switching of charge density waves also exhibit the inverse square-root law (Strogatz & Westervelt, 1989). Other instances include discrete and continuous population models in ecology near extinction points (Fontich & Sardanyés, 2007); the transient dynamics of a Duffing oscillator realised experimentally in an electronic circuit (Trickey & Virgin, 1998); the dynamics of the membrane potential in neurons at the transition to firing (Roa *et al.*, 2007); the slow evolution of a solar flare during magnetic reconnection near the loss of stability (Cassak, 2006); and the evolution of random networks undergoing a pruning process near the threshold of complete collapse (Baxter *et al.*, 2015).

Other scaling laws arise for non-generic bifurcations. This includes bifurcations where certain genericity, transversality or smoothness conditions fail; see Kuehn (2008) for more details. These have been described in other models of the switching of charge density waves (Strogatz & Westervelt, 1989), hypercycle models incorporating a higher number of molecular species (Sardanyés & Solé, 2007), and pendulums whose lengths have a non-smooth angular dependence (Kuehn, 2008). Moreover, in underdamped systems where inertial forces dominate damping, the normal form (2.2) instead has a second-order time derivative. A similar analysis then shows that the bottleneck duration obeys the scaling
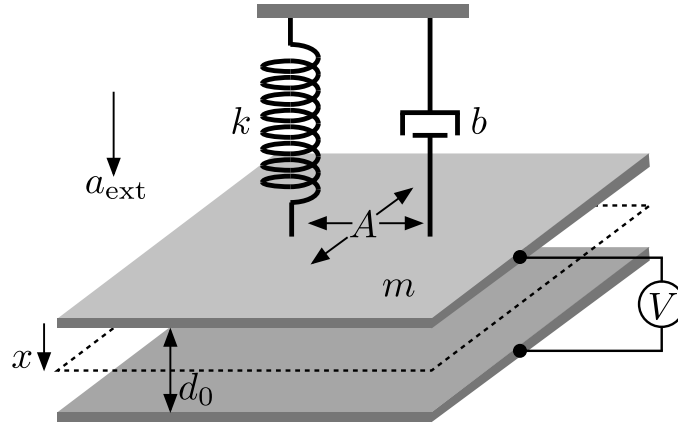
Figure 2.5: *Schematic of the mass-spring parallel-plate capacitor. Fluid between the plates is represented by a linear dashpot of constant damping coefficient b. (Reprinted from Gomez et al. (2018a), DOI: https://doi.org/10.1088/1361-6439/aa9a70. Copyright © IOP Publishing. Reproduced with permission. All rights reserved.)*

law

$$t_b = O\left([\lambda - \lambda_c]^{-1/4}\right) \quad \text{as} \quad \lambda \searrow \lambda_c,$$

i.e. the exponent of slowing down is 1/4 rather than 1/2. Later, in Chapter 4, we will show that this modified scaling law applies to underdamped snap-through instabilities.

2.3 Theoretical formulation

2.3.1 Governing equations

With the above discussion in mind, we now wish to understand the bottleneck dynamics of a generic MEMS device near the pull-in bifurcation. As the bottleneck is characterised by slow motions, and occurs well before the device comes into close contact with the actuating electrode (Rocha *et al.*, 2004a), we neglect compressibility and rarefaction effects in the squeeze film — the fluid damping is assumed to be purely viscous (Veijola *et al.*, 1995). This is justified by numerical simulations (Missoffe *et al.*, 2008) that show compressibility has very little effect on the pull-in time very close to the transition. Moreover, we assume a constant damping coefficient, denoted by b, taken to be the effective value of the damping coefficient in the bottleneck. Here b is regarded as a lumped parameter that characterises the properties of the squeeze film, including the thickness of the air gap, the ambient pressure, the fluid viscosity, and finite-width (border) effects, as well as any additional material damping that may be present.

As the geometry of the device is also slowly varying when its motions are slow, the elastic restoring forces can be approximated to leading order as a linear spring with constant stiffness (LaRose & Murphy, 2010). We denote the effective spring constant by k,

which combines properties of the mechanical restoring force, such as the dimensions of the actuator, the material stiffness and any residual stress built into the elastic structure. In addition, we use a parallel-plate approximation of the electrostatic force; this is valid provided the aspect ratio of the air gap and the slopes of deformation are small (Batra *et al.*, 2007). In this way, our model becomes a single-degree-of-freedom mass-spring model (Pelesko & Bernstein, 2002). Physically, it is equivalent to a parallel-plate capacitor, in which one plate is fixed while the other is attached to a linear spring and damper; see figure 2.5.

The assumptions made above are not valid outside of the bottleneck phase, where the speed of the device is increased and the details of its geometry may become important. However, by choosing suitable values for the lumped parameters b and k, we expect to correctly account for the length of the slow phase and hence approximate the total pull-in time, which is dominated by the time spent passing through the bottleneck. In particular, we discuss how a variable damping coefficient should be accounted for at the end of §2.4 and in Appendix 2.A.

As shown in figure 2.5, the properties of the moving plate are its mass m, area A and displacement x. The applied DC voltage is V, and d_0 is the gap thickness in the absence of any displacement ($x = 0$). We also account for an external acceleration a_{ext} of the whole device, which we assume is constant. This approximation is valid provided that a_{ext} varies over a timescale much longer than the timescale of pull-in (typically $1 - 10$ ms).

Under these assumptions, the displacement of the moving plate, $x(t)$, obeys the equation of motion

$$m\frac{\mathrm{d}^2 x}{\mathrm{d}t^2} + b\frac{\mathrm{d}x}{\mathrm{d}t} + kx = \frac{1}{2}\frac{\epsilon_0 A V^2}{(d_0 - x)^2} + m a_{\text{ext}}. \tag{2.5}$$

Here the first term on the right-hand side is the electrostatic force in the parallel-plate approximation (ϵ_0 is the permittivity of air), neglecting corrections due to fringing fields (Pelesko & Bernstein, 2002). As initial conditions, we consider the case of a suddenly applied (step function) voltage with the plate initially at rest at the zero voltage state, i.e. $x(0) = m a_{\text{ext}}/k$ and $\dot{x}(0) = 0$ (here and throughout $\dot{}$ denotes $\mathrm{d}/\mathrm{d}t$). These initial conditions are commonly used in applications of pull-in time in pressure sensors and accelerometers (Gupta *et al.*, 1996; Rocha *et al.*, 2004a; Dias *et al.*, 2011; 2015).

2.3.2 Non-dimensionalisation

To make the problem dimensionless, we note that a balance between viscous and spring forces in equation (2.5) leads to the timescale $[t] = b/k$. It is natural to scale the displacement away from the zero voltage state with the maximum allowed displacement before

contact occurs. This motivates introducing the dimensionless variables

$$T = \frac{t}{[t]}, \quad X = \frac{x - ma_{\text{ext}}/k}{d_0 - ma_{\text{ext}}/k}, \quad A_{\text{ext}} = \frac{ma_{\text{ext}}}{kd_0}.$$

Equation (2.5) can then be written as

$$Q^2 \frac{\mathrm{d}^2 X}{\mathrm{d}T^2} + \frac{\mathrm{d}X}{\mathrm{d}T} + X = \frac{\lambda}{(1 - X)^2}, \quad (2.6)$$

where the importance of inertia is measured by the quality factor $Q = \sqrt{mk}/b$, and we have introduced the normalised voltage

$$\lambda = \frac{1}{2} \frac{\epsilon_0 A V^2}{kd_0^3 (1 - A_{\text{ext}})^3}. \quad (2.7)$$

The initial conditions become

$$X(0) = \dot{X}(0) = 0, \quad (2.8)$$

and we note that, with this non-dimensionalisation, contact between the electrodes occurs at $X = 1$, with physical solutions requiring $X < 1$.

The dimensionless parameter λ is the key control parameter and may be interpreted as the ratio of the typical electrostatic force ($\sim \epsilon_0 A V^2 / [2d_0^2]$) to the spring force ($\sim kd_0$) (Pelesko & Bernstein, 2002), together with an additional factor that depends on the acceleration of the device. For realistic MEMS devices we have $|A_{\text{ext}}| \ll 1$, owing mainly to the small value of the mass m; for example, in the accelerometer reported by Rocha *et al.* (2004a), the range of accelerations encountered is $a_{\text{ext}} \leq 80$ mg, corresponding to $A_{\text{ext}} = O(10^{-3})$ for their experimental parameters. We therefore consider only the case $\lambda \geq 0$ here.

2.3.3 Steady solutions

The behaviour of the steady-state solutions of equation (2.6) is well-known (see Pelesko & Bernstein, 2002, for example). Here we only summarise the main results. For $0 \leq \lambda < \lambda_{\text{fold}} = 4/27$, there are two real solutions with $0 < X < 1$, one of which is linearly stable and the other linearly unstable. At $\lambda = \lambda_{\text{fold}}$, these two solutions coincide and disappear at a saddle-node (fold) bifurcation with $X = X_{\text{fold}} = 1/3$. For $\lambda > \lambda_{\text{fold}}$, no physical solutions exist. This is illustrated by the response diagram shown in figure 2.6a.

Under quasi-static conditions, the fold point corresponds to where pull-in is observed experimentally (no equilibrium solution away from collapse exists for $\lambda > \lambda_{\text{fold}}$), giving
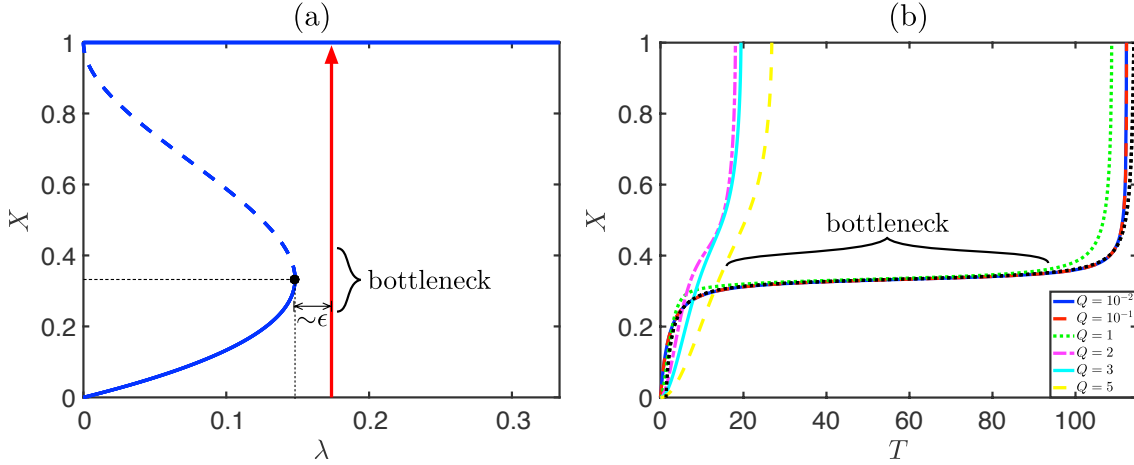
Figure 2.6: *(a) Response diagram for the steady-state solutions of (2.6) (blue curves), which satisfy $X = \lambda/(1-X)^2$, as the dimensionless voltage λ varies. At $\lambda = 4/27$ the stable equilibrium away from pull-in (lower solid curve) intersects an unstable solution (dashed curve) and disappears at a saddle-node bifurcation. A typical trajectory at fixed λ beyond the pull-in transition is also shown (red arrow). (b) Dimensionless trajectories $X(T)$ satisfying (2.6) and (2.8) for $\epsilon = 10^{-3}$ and different quality factor Q (coloured curves; see legend). For later comparison, the asymptotic trajectory predicted by (2.16) is also shown (black dotted curve). (Reprinted from Gomez et al. (2018a), DOI: https://doi.org/10.1088/1361-6439/aa9a70. Copyright © IOP Publishing. Reproduced with permission. All rights reserved.)*

the static pull-in voltage and pull-in displacement in terms of the external acceleration as

$$V_{\mathrm{PI}} = \sqrt{\frac{8kd_0^3(1-A_{\mathrm{ext}})^3}{27\epsilon_0 A}}, \quad x_{\mathrm{PI}} = \frac{d_0}{3}\left(1 + 2A_{\mathrm{ext}}\right).$$

In the case of zero external acceleration, this reduces to the classic (static) pull-in voltage and pull-in displacement of a parallel-plate capacitor, widely reported in the literature (Zhang *et al.*, 2014); we label these as V_{SPI} and x_{SPI} respectively.

2.4 Pull-in dynamics

We now consider the case when the system is perturbed just beyond the static pull-in transition, i.e. we set

$$\lambda = \lambda_{\mathrm{fold}}(1 + \epsilon),$$

where $0 < \epsilon \ll 1$ is a small parameter capturing the distance beyond the pull-in transition (ϵ is shown schematically in figure 2.6a). Using the expression (2.7) and the fact that

$$\lambda_{\mathrm{fold}} = \frac{1}{2}\frac{\epsilon_0 A V_{\mathrm{SPI}}^2}{kd_0^3},$$

we may write ϵ as

$$\epsilon = \frac{\lambda}{\lambda_{\text{fold}}} - 1 = \frac{(V/V_{\text{SPI}})^2}{(1 - A_{\text{ext}})^3} - 1. \tag{2.9}$$

We see that for a fixed actuation voltage $V > V_{\text{SPI}}$, the external acceleration changes the effective perturbation ϵ, with ϵ increasing as A_{ext} increases. The result will be an associated change in the pull-in time. This is the basis on which pull-in time accelerometers operate: by repeatedly inducing pull-in and measuring the resulting pull-in times, the external acceleration can be determined after a suitable calibration is performed (Dias *et al.*, 2011). In practice, pull-in times can be measured extremely accurately and with low noise by sensing large changes in capacitance using a high frequency clock. The sensitivity of the pull-in time to changes in ϵ is therefore the primary factor that limits the sensitivity of the accelerometer.

The key observation, first reported by Rocha *et al.* (2004a), is that for quality factors Q smaller than unity (i.e. overdamped devices) the motion of the plate is slowed in a bottleneck as it passes the static pull-in displacement, $X_{\text{fold}} = 1/3$. This behaviour is confirmed in figure 2.6b, which displays the dimensionless trajectories $X(T)$ during pull-in for different values of Q. We have obtained these trajectories by integrating equation (2.6) numerically with initial conditions (2.8) in MATLAB. As the ODE is singular in the limit $Q \to 0$ (the second-order derivative needed to satisfy the initial conditions disappears when $Q = 0$, but remains important at early times for small, but finite, Q), we use the MATLAB routine `ode15s`, which employs a stiff solver to capture transients in which the inertia of the plate cannot be neglected.

We see from figure 2.6b that for $Q \ll 1$, the bottleneck phase dominates the transient dynamics, and hence the total time taken to pull-in. The phase becomes highly dependent on the damping as Q is increased past unity, with virtually no bottleneck present for $Q \geq 2$. The duration of the bottleneck is also sensitive to the perturbation ϵ, and appears to increase without bound as $\epsilon \to 0$. We now perform a detailed asymptotic analysis of equation (2.6) in the limit $Q \ll 1$, showing that the bottleneck phenomenon is an instance of a saddle-node ghost whose duration scales as $\epsilon^{-1/2}$ as $\epsilon \to 0$.

2.4.1 Solution structure for $Q \ll 1$

We begin by considering the different leading order balances the solution passes through during pull-in. This analysis will confirm that the bottleneck phase does indeed dominate the pull-in dynamics, as expected from figure 2.6b: the bottleneck duration is much longer than any other timescale in the problem, including any intervals for which plate inertia is important. This will enable us to approximate the total pull-in time based on the duration of the bottleneck alone.

Early times

At early times, the initial conditions (2.8) imply that the displacement X is small. Linearising equation (2.6) then gives

$$Q^2 \frac{\mathrm{d}^2 X}{\mathrm{d}T^2} + \frac{\mathrm{d}X}{\mathrm{d}T} + X \sim \lambda(1 + 2X).$$

The solution satisfying $X(0) = \dot{X}(0) = 0$ is

$$X = \frac{\lambda}{1 - 2\lambda}\left(1 + \frac{\alpha_-}{\alpha_+ - \alpha_-}e^{\alpha_+ T} - \frac{\alpha_+}{\alpha_+ - \alpha_-}e^{\alpha_- T}\right), \tag{2.10}$$

where

$$\alpha_\pm = \frac{-1 \pm \sqrt{1 - 4Q^2(1 - 2\lambda)}}{2Q^2}.$$

When $Q \ll 1$, we expand to find

$$\alpha_+ = -(1 - 2\lambda) + O(Q^2), \quad \alpha_- = -\frac{1}{Q^2} + O(1).$$

This shows that inertia may only be neglected for $T \gg Q^2$, when $e^{\alpha_- T}$ is exponentially small and the leading order terms in (2.10) become independent of Q. In this case the solution simplifies to

$$X = \frac{\lambda}{1 - 2\lambda}\left[1 - e^{-(1 - 2\lambda)T}\right].$$

It follows that the terms we neglected in linearising equation (2.6), of size $O(X^2)$, only remain small provided $T \ll 1$ (as $\lambda \approx \lambda_{\mathrm{fold}} = 4/27$ is order unity). As T reaches $O(1)$, this solution therefore breaks down and a different leading order balance emerges.

Later times, $T \gtrsim 1$

Using the previous solution to evaluate the size of terms for $T = O(1)$ yields the updated balance

$$\frac{\mathrm{d}X}{\mathrm{d}T} + X \sim \frac{\lambda}{(1 - X)^2}, \tag{2.11}$$

with inertia now negligible. This equation can be solved to give the displacement implicitly in terms of time (e.g. Gupta & Senturia, 1997):

$$T = \int_0^X \frac{(1 - \xi)^2}{\lambda - \xi(1 - \xi)^2} \, \mathrm{d}\xi. \tag{2.12}$$

(Here matching into $T \ll 1$ requires the constant of integration to be zero.)

This solution is not uniformly valid during pull-in: close to contact the electrostatic force will grow very large, leading to fast motions where inertia becomes important again. We can use equation (2.11) directly to determine when this first occurs. Differentiating, we obtain

$$\frac{\mathrm{d}^2 X}{\mathrm{d}T^2} + \frac{\mathrm{d}X}{\mathrm{d}T} \sim \frac{2\lambda}{(1-X)^3}\frac{\mathrm{d}X}{\mathrm{d}T}.$$

The ratio of the neglected inertia term to the damping term can then be evaluated as

$$\frac{Q^2 \ddot{X}}{\dot{X}} \sim Q^2 \left[\frac{2\lambda}{(1-X)^3} - 1\right].$$

Away from $X = 1$, the term in square brackets is $O(1)$ and so inertia is unimportant when $Q \ll 1$. This first breaks down when $X = 1 - O(Q^{2/3})$, at which point we have $\dot{X} = O(Q^{-4/3})$ (using (2.11)) and $Q^2\ddot{X} = O(Q^{-4/3})$. Note that these updated scalings must hold close to the pull-in time, which we denote $T = T_{\mathrm{PI}}$, as X is close to 1. Setting $T = T_{\mathrm{PI}} - O(Q^\gamma)$ and seeking a balance between these terms shows that $\gamma = 2$, i.e. these scalings hold inside the interval $T = T_{\mathrm{PI}} - O(Q^2)$.

In summary, for $Q \ll 1$ we have shown that inertia of the plate remains negligible for

$$Q^2 \ll T \ll T_{\mathrm{PI}} - O(Q^2), \quad Q^2 \ll X \ll 1 - O(Q^{2/3}).$$

In particular, we conclude that the dynamics are first order when X passes the static pull-in displacement $X_{\mathrm{fold}} = 1/3$. Because λ is close to its value at the fold, where the spring force exactly balances the electrostatic force, it follows that the difference between these two forces will be very small around X_{fold}. This explains the previous observation that the bottleneck is a type of meta-stable interval characterised by a balance of forces (Rocha *et al.*, 2004*a*). In fact, when $X = X_{\mathrm{fold}}$ we have

$$\left.\frac{\mathrm{d}X}{\mathrm{d}T}\right|_{X=X_{\mathrm{fold}}} \sim \left.\left[\frac{\lambda}{(1-X)^2} - X\right]\right|_{X=X_{\mathrm{fold}}} = \frac{\epsilon}{3}.$$

As the velocity is very small but non-zero in the bottleneck, the system appears to 'feel' the attraction of the equilibrium at the saddle-node bifurcation, similar to the example discussed in §2.2.

Note that for larger quality factors, $Q = O(1)$, this conclusion is not valid: as the dynamics are no longer first order, a small net force does not imply slow dynamics. The inertia of the plate 'carries' it through the bottleneck without significant slow down, as is evident from the trajectories in figure 2.6b for $Q \geq 2$. It can also be observed that the pull-in time does not simply decrease monotonically in this regime as Q is increased (e.g. the pull-in for $Q = 2$ is faster than that for $Q = 5$ in figure 2.6b). While high inertia

carries the plate quickly through the bottleneck, it also slows down the initial dynamics, as the plate must be accelerated from its rest position.

Bottleneck analysis

We now consider the solution inside the bottleneck phase. While we can make progress using the implicit solution (2.12), we instead analyse equation (2.11) directly. The method we present is more general as it can be applied to systems for which no analytical solution is available.

When the solution is close to the static pull-in displacement we have

$$X = X_{\text{fold}}\left[1 + \tilde{X}(T)\right],$$

where $|\tilde{X}| \ll 1$. Using $\lambda = \lambda_{\text{fold}}(1 + \epsilon)$, the electrostatic force can then be expanded as

$$\frac{\lambda}{(1 - X)^2} = X_{\text{fold}}\left[1 + \epsilon + \tilde{X} + \frac{3}{4}\tilde{X}^2\right] + O(\epsilon\tilde{X}, \tilde{X}^3).$$

Substituting into (2.11) and neglecting terms of $O(\epsilon\tilde{X}, \tilde{X}^3)$, we obtain

$$\frac{\mathrm{d}\tilde{X}}{\mathrm{d}T} \sim \epsilon + \frac{3}{4}\tilde{X}^2. \tag{2.13}$$

Equation (2.13) is valid in the regime $\epsilon \ll |\tilde{X}| \ll 1$, i.e. the neglected terms of $O(\epsilon\tilde{X}, \tilde{X}^3)$ are smaller than the retained terms. In particular, we note the importance of retaining the quadratic term. This term is neglected in the approach taken by Rocha *et al.* (2004*b*); an analysis of their solution shows that it incorrectly predicts the pull-in time scales as ϵ^{-1} as $\epsilon \to 0$.

Up to numerical pre-factors, equation (2.13) is the normal form (2.2) for a saddle-node bifurcation discussed in §2.2. This reflects the bifurcation structure underlying the pull-in transition: the first term on the right-hand side of (2.13) is the normalised perturbation to the bifurcation parameter (either due to a change in voltage or external acceleration), and the quadratic term is the nonlinearity that characterises the bifurcation as being of saddle-node type (locally parabolic near the fold). In this way, equation (2.13) is generic for the dynamics of overdamped MEMS devices close to the pull-in transition. Similar evolution equations have been obtained using a single-degree-of-freedom approximation for a microbeam (Krylov & Maimon, 2004), and in a MEMS resonator modelled as a Duffing-like oscillator (Zaitsev *et al.*, 2012). However, our approach here offers new insight into why this equation should apply more generally.

The solution of (2.13) is

$$\tilde{X} \sim \frac{2}{3}\sqrt{3\epsilon}\tan\left[\frac{1}{2}\sqrt{3\epsilon}(T-T_0)\right],\tag{2.14}$$

for some constant T_0. In the immediate vicinity of the static pull-in displacement, where $|\tilde{X}| \ll \epsilon^{1/2}$, the term in square brackets in (2.14) is much smaller than unity. Here the solution simplifies to

$$\tilde{X} \sim \epsilon(T-T_0),$$

so that the displacement evolves linearly in time in the middle of the bottleneck. Outside of this interval, the tangent function captures how the plate begins to accelerate away from the static pull-in displacement. We note that as this linear behaviour is precisely the solution of equation (2.13) upon neglecting the quadratic term in favour of the term in ϵ, we deduce that (2.14) is asymptotically valid for all $|\tilde{X}| \ll 1$ (rather than just for $\epsilon \ll |\tilde{X}| \ll 1$).

The solution (2.14) appears to undergo finite-time blow-up as the term in square brackets approaches $\pm\pi/2$. However, as soon as $\tilde{X}$ grows comparable to $O(1)$, our original assumption $|\tilde{X}| \ll 1$ is no longer valid and the solution breaks down. In terms of the diagram in figure 2.6a, this means that the displacement has left the vicinity of the fold point and a local analysis can no longer be applied. Upon making use of the expansion $\tan x \sim \pm(\pi/2 \mp x)^{-1}$ as $x \to \pm\pi/2$, it follows that the solution accelerates according to the power law

$$\tilde{X} \sim \frac{\pm 4/3}{\pi/\sqrt{3\epsilon} \mp (T-T_0)}.$$

Here the minus sign corresponds to initially entering the bottleneck ($\tilde{X} < 0$), while the plus sign corresponds to leaving the bottleneck towards pull-in ($\tilde{X} > 0$). We deduce that $\tilde{X} = O(1)$ when

$$T - T_0 = \pm\frac{\pi}{\sqrt{3\epsilon}} + O(1).$$

The duration of the bottleneck, denoted T_{bot}, is simply the difference between these two values and so we have $T_{\mathrm{bot}} = 2\pi/\sqrt{3\epsilon} + O(1)$.

The bottleneck dominates the time spent in the regime where the dynamics are first order. Moreover, we showed that inertia is only important in intervals of duration $O(Q^2)$ ($\ll 1$) around $T = 0$ and $T = T_{\mathrm{PI}}$. It follows that the total pull-in time is equal to the bottleneck duration to leading-order:

$$T_{\mathrm{PI}} = \frac{2\pi}{\sqrt{3\epsilon}} + O(1).\tag{2.15}$$
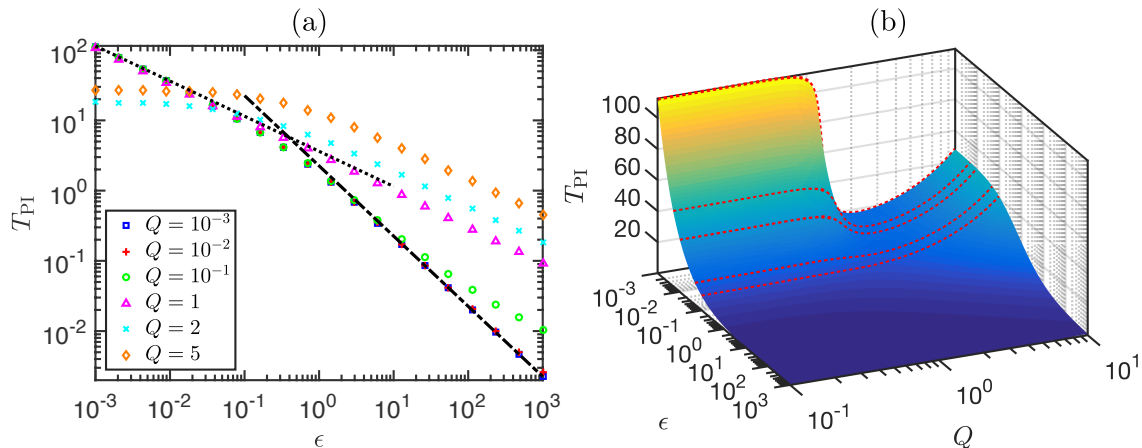
Figure 2.7: *Pull-in times T_{PI} determined from the numerical solution of (2.6) with initial conditions (2.8). (a) Numerical results for fixed Q and variable ϵ (symbols, see legend), together with the asymptotic prediction $T_{\mathrm{PI}} \sim 2\pi/\sqrt{3\epsilon}$ valid for $\epsilon \ll 1$ and $Q \ll 1$ (dotted line), and the prediction $T_{\mathrm{PI}} \sim 9/(4\epsilon)$ valid for $\epsilon \gg 1$ and $Q \ll 1$ (dashed-dotted line) (Gupta & Senturia, 1997). (b) Surface plot of T_{PI} as a function of ϵ and Q. Also shown are slices through the surface at values $\epsilon \in \{10^{-3}, 5 \times 10^{-3}, 10^{-2}, 5 \times 10^{-2}, 10^{-1}\}$ (red dotted curves). (Reprinted from Gomez et al. (2018a), DOI: https://doi.org/10.1088/1361-6439/aa9a70. Copyright © IOP Publishing. Reproduced with permission. All rights reserved.)*

To validate the prediction (2.15), we numerically determine the pull-in time by integrating the full ODE (2.6) with initial conditions (2.8). As equation (2.6) is singular at $X = 1$, we use event location to stop integration as soon as $(1 - X) < \mathrm{tol}$ for some tolerance tol, and the corresponding time at this point then gives the pull-in time. The accuracy of this method can be justified by analysing the behaviour of (2.6) very close to pull-in, where a power law solution can be extracted; we use $\mathrm{tol} = 10^{-5}$, which guarantees an accuracy of $O(10^{-6})$ in the computed pull-in time when we restrict to $Q \le 10$. In figure 2.7a we plot the computed times as a function of the normalised perturbation ϵ. We conclude that the asymptotic prediction (2.15) approximates the pull-in time extremely well for moderately small quality factors $Q \lesssim 1$ and perturbations $\epsilon \lesssim 10^{-1}$.

Figure 2.7b shows a surface plot of the computed pull-in times for a range of values of ϵ and Q. As well as showing that the dynamics become very slow as $\epsilon \to 0$ with Q fixed, we observe that, with ϵ fixed, the dependence of the pull-in time on the quality factor Q is non-monotonic. In particular, when we fix $\epsilon \lesssim 10^{-2}$, a minimum in T_{PI} is obtained at $Q \approx 2$; within a narrow range of Q close to this value, T_{PI} varies significantly. While this minimum may seem surprising at first, it is the result of inertia being small enough for the plate to be rapidly accelerated from its rest position but large enough that it passes the pull-in displacement without significant slowing down in a bottleneck. If we imagine fixing the actuation voltage V near V_{SPI} and varying the plate mass m, so that Q is varied while all other parameters are fixed, then this corresponds to a value of m that minimises the pull-in time. This may be relevant to switching applications where the pull-in time

needs to be minimised without increasing the voltage significantly (Castaner & Senturia, 1999) (since increasing the voltage would increase the total energy consumed).

Currently, the constant T_0 appearing in the bottleneck solution (2.14) remains undetermined. This corresponds to the time at which $\tilde{X} = 0$ (when the displacement is equal to the static pull-in displacement X_{fold}). However, we can find the value of T_0 by a symmetry argument. From the solution (2.14), we see that the displacement about the static pull-in displacement is antisymmetric, i.e. we have $\tilde{X} \to -\tilde{X}$ as $(T - T_0) \to -(T - T_0)$. (This is a consequence of the dynamics being first order, and the symmetry of the quadratic nonlinearity in equation (2.13).) As the bottleneck phase dominates the entire motion in the limit $\epsilon \ll 1$, it follows that, to leading order in ϵ, the value of T_0 is simply half of the bottleneck time: $T_0 \sim \pi/\sqrt{3\epsilon}$. The rescaled displacement in the bottleneck, (2.14), can then be written as

$$\tilde{X} \sim \frac{2\sqrt{3\epsilon}}{3} \tan\left[\frac{\sqrt{3\epsilon}}{2}T - \frac{\pi}{2}\right].$$

The unscaled displacement, X, then becomes

$$X \sim \frac{1}{3} + \frac{2\sqrt{3\epsilon}}{9} \tan\left[\frac{\sqrt{3\epsilon}}{2}T - \frac{\pi}{2}\right]. \tag{2.16}$$

This compares well to the trajectories obtained by numerical integration of the full system; see figure 2.6b, where the analytical prediction is almost indistinguishable from numerical results with $Q \ll 1$. As the motions are so fast outside the bottleneck, we see that (2.16) also provides a good description of the global dynamics (restricting X to the interval $[0, 1]$), despite the fact that the assumptions made in deriving (2.16) are only strictly valid in the bottleneck phase.

We note that some caution is needed when using a constant damping coefficient, as in our approach here: in reality the damping coefficient may itself depend on the current gap thickness. Indeed, simulations that use a constant damping coefficient corresponding to the initial gap thickness have been shown to give large errors (Rocha *et al.*, 2004*a*). However, using the damping coefficient appropriate in the bottleneck phase of the motion correctly accounts for the duration of the bottleneck, and hence provides a good approximation of the total time taken to pull-in (see Appendix 2.A).

2.5 Data comparison

In §2.4 we derived a scaling law for the slowing down of a parallel-plate actuator close to the pull-in transition. In dimensional form, this predicts that the pull-in time increases as

$$t_{\mathrm{PI}} \sim \frac{b}{k} \frac{2\pi}{\sqrt{3\epsilon}} \quad \text{where} \quad \epsilon = \frac{(V/V_{\mathrm{SPI}})^2}{(1 - A_{\mathrm{ext}})^3} - 1. \tag{2.17}$$

This result is valid for $0 < \epsilon \ll 1$ and small quality factor, $Q \ll 1$. As discussed at the start of §2.3, we expect that this result also describes the dynamics of a generic MEMS device operating in overdamped conditions; here we regard the damping coefficient b and spring constant k as lumped parameters that encapsulate the properties of the squeeze film and the mechanical restoring force during the bottleneck phase, respectively.

We now compare our prediction to pull-in data reported in the literature, both from experiments and numerical simulations. The details of each data set are summarised in table 2.1 for parallel-plate devices, and in table 2.2 for microbeam devices. These provide the relevant parameter values in each study, and the type of model used (for numerical simulations). We have separated the data so that only the actuation voltage or the acceleration is varying within each data set, corresponding to a particular row in the tables. Where the properties of the actuator or the squeeze film have changed within a single reference, the data have therefore been separated into different rows in the tables.

For data on parallel-plate actuators (table 2.1), the relevant parameters are the ratio of the actuation voltage to the pull-in voltage V/V_{SPI}, external acceleration a_{ext}, initial gap thickness d_0, plate mass m, spring constant k, pull-in voltage V_{SPI}, and the damping coefficient in the bottleneck phase, b. For the data on microbeams (table 2.2), the parameters are the initial gap thickness d_0, beam length L, beam thickness h, beam width w, Young's modulus E, and pull-in voltage V_{SPI}. (In both tables, blank entries indicate that no value is provided in the reference.) A wide range of values are exhibited in these parameters across the studies. We also report any additional effects that may be present in experiments and simulations; these include residual stress, rarefaction effects, partial field screening, varying ambient pressures, and different boundary conditions for microbeams.

The reported pull-in times were shown on logarithmic axes in figure 2.2 (as a function of the corresponding values of ϵ). As well as generally confirming the expected scaling law that $t_{\mathrm{PI}} \propto \epsilon^{-1/2}$ as $\epsilon \to 0$, we see that this rescaling collapses data from accelerometers, where the acceleration is variable and the actuation voltage varies between each data set (all other parameters fixed); see the data of Rocha *et al.* (2004*a*), orange symbols. We also see a collapse in data over a single experimental system where the actuation mechanism changes, between varying the voltage (with zero acceleration) or varying the acceleration

Table 2.1: *Summary of previous data for the pull-in times of parallel-plate actuators reported in the literature (reprinted from Gomez et al. (2018a), DOI: https://doi.org/10.1088/1361-6439/aa9a70. Copyright © IOP Publishing. Reproduced with permission. All rights reserved).*

Reference	Data type	V/V_{SPI}	a_{ext}	d_0 (μm)	m (μg)	k (Nm^{-1})	V_{SPI} (V)	Reported b (gs^{-1})	Model	Additional effects	Fitted b (gs^{-1})	Fitted Q	Legend
Gupta *et al.* (1996)	Simulation	Variable	0	2.07	0.114	6.33	8.76	0.35	MS, LD		0.330	0.0813	red star
Gupta *et al.* (1996)	Simulation	Variable	0	2.07	0.132	2.94	5.54	0.35	MS, LD		0.296	0.0668	red left triangle
Nijhuis *et al.* (1999)†	Simulation	Variable	0	25	1000	40	72.3		MS, CSQFD	SBC	21.4	0.296	green square
Rocha *et al.* (2004a)	Experiment	1.0009	Variable	2.25	4.27	1.2930	2.931	0.192	N/A		0.182	0.408	orange diamond
Rocha *et al.* (2004a)	Experiment	1.0005	Variable	2.25	4.27	1.2930	2.931	0.192	N/A		0.182	0.408	orange left triangle
Rocha *et al.* (2004a)	Experiment	1.0003	Variable	2.25	4.27	1.2930	2.931	0.192	N/A		0.182	0.408	orange star (outline)
Rocha *et al.* (2004a)	Simulation	1.0009	Variable	2.25	4.27	1.2930	2.931	0.192	MS, CSQFD	SBC	0.182	0.408	orange inverted triangle
Rocha *et al.* (2004a)	Simulation	1.0005	Variable	2.25	4.27	1.2930	2.931	0.192	MS, CSQFD	SBC	0.182	0.408	orange square
Rocha *et al.* (2004a)	Simulation	1.0003	Variable	2.25	4.27	1.2930	2.931	0.192	MS, CSQFD	SBC	0.182	0.408	orange star (filled)
Dias *et al.* (2011)	Experiment	1.01	Variable	2.25*	249*	3.33*	2.931*	2.88*	N/A		1.40	0.651	magenta left triangle
Dias *et al.* (2011)	Experiment	Variable	0	2.25*	249*	3.33*	2.931*	2.88*	N/A		1.40	0.651	magenta up triangle
Dias *et al.* (2011)	Simulation	1.01	Variable	2.25	249	3.33	2.916	2.88	MS, CSQFD	SBC, BE	1.40	0.651	magenta circle
Dias *et al.* (2011)	Simulation	Variable	0	2.25	249	3.33	2.916	2.88	MS, CSQFD	SBC, BE	1.40	0.651	magenta right triangle
Dias *et al.* (2015)	Experiment	1.05	Variable	3.00	497*	2.40	2.94	4.80	N/A	N/A	2.91	0.375	cyan inverted triangle
Dias *et al.* (2015)	Experiment	Variable	0	3.00	497*	2.40	2.94	4.80	N/A	N/A	2.91	0.375	cyan diamond

MS, single-degree-of-freedom mass-spring model; LD, linear damping with constant coefficient; CSQFD, compressible squeeze film damping (Reynolds equation); SBC, corrections due to slip boundary conditions (rarefaction effects); RS, residual stress; BE, border (finite-width) effects; N/A, not applicable

*Experimental parameter reported as being obtained by modelling/estimated

†Electromagnetic force; data has been converted to equivalent DC voltage in electrostatic-electromagnetic analogy

Table 2.2: *Summary of previous data for the pull-in times of microbeam actuators reported in the literature (reprinted from Gomez et al. (2018a), DOI: https://doi.org/10.1088/1361-6439/aa9a70. Copyright © IOP Publishing. Reproduced with permission.).*

Reference	Data type	d_0 (μm)	L (μm)	h (μm)	w (μm)	E (GPa)	V_{SPI} (V)	Model	Additional effects	Fitted [t] (μs)	Legend
Gupta et al. (1996)	Experiment	2.07	610	2.12	40	164	8.76	N/A		52.1	★
Gupta et al. (1996)	Experiment	2.07	710	2.12	40	164	5.54	N/A		101	◀
Gupta et al. (1996)	Simulation	2.07	610	2.12	40	164	8.76	PE, CC, CSQFD	RS	52.1	▼
Gupta et al. (1996)	Simulation	2.07	710	2.12	40	164	5.54	PE, CC, CSQFD	RS	101	●
Grétillat et al. (1997)	Experiment		300			200*	48.7	N/A	FS	0.444	▲
Grétillat et al. (1997)	Simulation		300			200	48.7	BE, CC, CSQFD	RS, FS	0.444	◆
Grétillat et al. (1997)	Simulation		300			200	48.5	BE, SE, CSQFD	RS, FS	0.444	■
Hung & Senturia (1999)	Simulation	2.3	610	2.2	40	149	8.76	BE, CC, CSQFD	SBC, RS	36.8	✦
Younis et al. (2003)	Simulation	2.3	610	2.015	40	166	8.76	BE, CC, LD	SS	41.2	★
Missoffe et al. (2008)	Simulation	2.3	610	2.2	40	149	8.76	BE, CC, CSQFD	0.1013 bar‡, SBC, RS	9.38	◀
Missoffe et al. (2008)	Simulation	2.3	610	2.2	40	149	8.76	BE, CC, CSQFD	1.013 bar‡, SBC, RS	34.2	▼
Missoffe et al. (2008)	Simulation	2.3	610	2.2	70	149	8.76	BE, CC, CSQFD	0.1013 bar‡, SBC, RS	21.9	▶

BE, dynamic beam equation; PE, dynamic (2D) plate equation; CC, clamped-clamped boundary conditions; SE, stepped-up boundary conditions; LD, linear damping with constant coefficient; CSQFD, compressible squeeze film damping (Reynolds equation); SBC, corrections due to slip boundary conditions (rarefaction effects); RS, residual stress; FS, partial field screening; SS, strain-stiffening; N/A, not applicable

* Experimental parameter reported as being obtained by modelling/estimated

‡ Ambient pressure
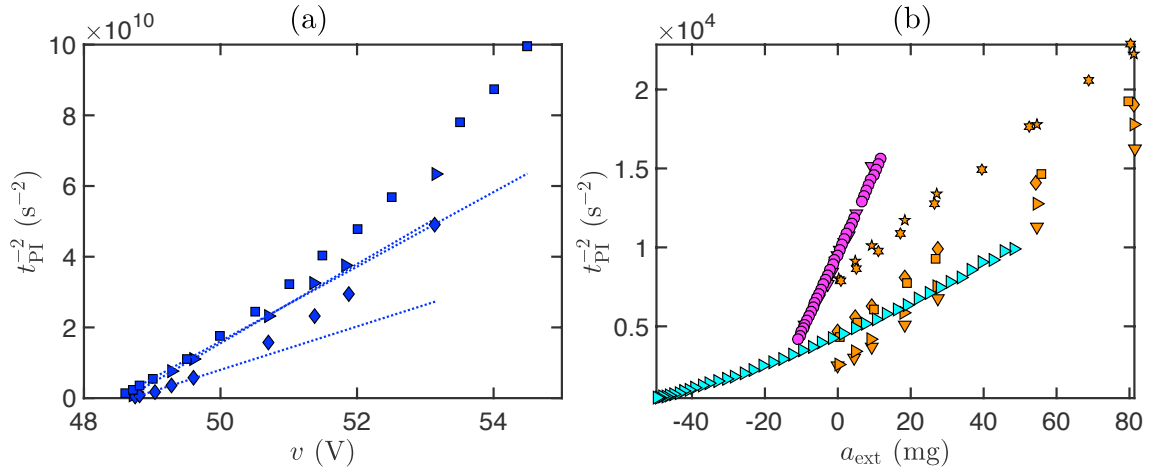
Figure 2.8: *Re-scaling the pull-in times according to the scaling law $t_{\mathrm{PI}} = O(\epsilon^{-1/2})$ as $\epsilon \to 0$ for (a) the data of Grétillat* et al. *(1997) and (b) all accelerometer data. (Reprinted from Gomez* et al. *(2018a), DOI: https://doi.org/10.1088/1361-6439/aa9a70. Copyright © IOP Publishing. Reproduced with permission. All rights reserved.)*

(with fixed voltage); see the data of Dias *et al.* (2011), magenta symbols. This verifies that ϵ is the correct dimensionless parameter to capture both variations in the voltage and external acceleration near the pull-in transition.

Some data sets plotted in figure 2.2 do not appear to follow the expected $\epsilon^{-1/2}$ scaling, curving downward slightly for small ϵ. These include the experiments/simulations of Grétillat *et al.* (1997) (blue symbols) and the experiments of Dias *et al.* (2015) (cyan symbols). However, we believe that this may be due to sensitivity to the reported value of the pull-in voltage: a small error introduces shifts in the computed values of ϵ, which can cause large variations when plotted on logarithmic axes. Another way to test the scaling law, which eliminates this sensitivity, is to plot t_{PI}^{-2} as a function of voltage/external acceleration on linear axes. This is shown in figure 2.8a for the data of Grétillat *et al.* (1997) (blue symbols), and in figure 2.8b for all accelerometer data. (Due to the large range of pull-in times under varying voltage, figure 2.8a shows only a subset of the data, for clarity.) In all cases a linear relationship is observed close to the pull-in transition, i.e. as $t_{\mathrm{PI}}^{-2} \to 0$. A linear relationship here implies the expected $\epsilon^{-1/2}$ scaling, because ϵ is linear in the voltage/acceleration close to the pull-in transition. For example, in the case of zero external acceleration, we have from (2.17):

$$\epsilon = \left(\frac{V}{V_{\mathrm{SPI}}}\right)^2 - 1 \approx \frac{2}{V_{\mathrm{SPI}}} \left(V - V_{\mathrm{SPI}}\right),$$

when $V \approx V_{\mathrm{SPI}}$, and similarly in the case when the acceleration is varied.

2.5.1 Estimating the pull-in voltage

The above analysis highlights the sensitivity of the pull-in time to the actual pull-in voltage, which can be quite difficult to measure precisely — for instance, quasi-statically increasing the voltage until pull-in occurs is subject to mechanical noise as well as imprecision in voltage measurements. There may also be rounding error in the reported pull-in voltage. Hence, we suggest an alternative approach. For the data of Grétillat *et al.* (1997), we have determined the best-fit (least-squares) line over the five data points that are closest to the pull-in transition (dotted lines on figure 2.8a). By finding the intercept of each best-fit line with the horizontal axis, we are able to compute 'corrected' values of the pull-in voltage. These are $\{48.615, 48.697, 48.477\}$ V, which are in good agreement with the reported values of $\{48.7, 48.7, 48.5\}$ V respectively. This procedure may be applied more generally as a way to estimate the pull-in voltage based only on data for the pull-in times, rather than using the static behaviour of the system prior to pull-in.

2.5.2 Estimating the pre-factor

Finally, we show that it is possible to obtain good quantitative agreement with the predicted pre-factor in the scaling of (2.17), when we use realistic values of the lumped parameters b and k. We make the pull-in times shown in figure 2.2 dimensionless using the timescale $[t] = b/k$. We can then use $[t]$ as a single fitting parameter to fit each data set to the dimensionless prediction $T_{\mathrm{PI}} \sim 2\pi/\sqrt{3\epsilon}$. This is consistent with the way we have separated each data set: as the properties of the squeeze film (e.g. plate area, ambient pressure) and the mechanical restoring force (e.g. material stiffness, beam length) entering b and k do not vary in each data set, the timescale $[t]$ is fixed. Many of the references in tables 2.1–2.2 have multiple data sets with the same timescale $[t]$; for example, when the actuation mechanism changes over a single experimental system (e.g. the data of Dias *et al.*, 2011, magenta symbols), and when numerical simulations use the same parameter values as experiments (e.g. the data of Rocha *et al.*, 2004*a*, orange symbols). In these cases we fit $[t]$ to only one set of experimental data and use this value to non-dimensionalise all of the data sets.

The best-fit (least-squares) timescales $[t]$ are given in table 2.2 for the data on microbeams. For the data on parallel-plate actuators, the spring constant k is usually a known design parameter, and so we use the reported value of k to give the corresponding best-fit damping coefficient b. These compare reasonably well to approximate values obtained in numerical simulations of squeeze film damping (table 2.1). The corresponding quality factors $Q = \sqrt{mk}/b$ are all smaller than unity, so that the fitting performed here is consistent with our assumption that the devices are overdamped.
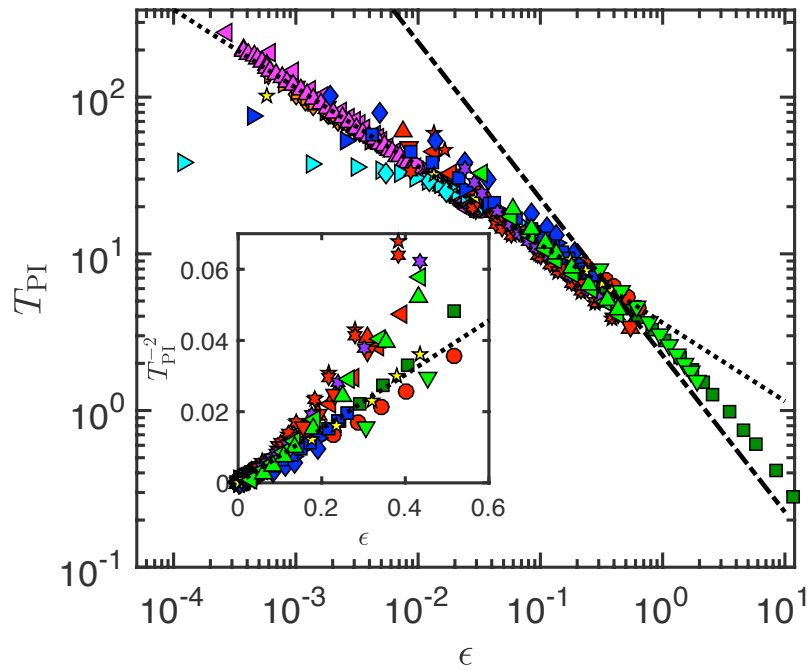
Figure 2.9: *Main plot: Dimensionless pull-in times obtained by fitting the overdamped timescale* $[t] = b/k$. *Plotted for comparison is the prediction* $T_{\mathrm{PI}} \sim 2\pi/\sqrt{3\epsilon}$ *valid for* $\epsilon \ll 1$ *(black dotted line), as well as the large-ϵ prediction* $T_{\mathrm{PI}} \sim 9/(4\epsilon)$ *(black dashed-dotted line) (Gupta & Senturia, 1997). Inset: The same data, re-scaled according to the scaling law* $T_{\mathrm{PI}} = O(\epsilon^{-1/2})$ *as* $\epsilon \to 0$. *(Reprinted from Gomez* et al. *(2018a), DOI: https://doi.org/10.1088/1361-6439/aa9a70. Copyright © IOP Publishing. Reproduced with permission. All rights reserved.)*

With the fitted values of $[t]$, we obtain excellent collapse over all data sets considered, up to the sensitivity to the value of the pull-in voltage used; see the main panel of figure 2.9. In the inset of figure 2.9 we plot T_{PI}^{-2} as a function of ϵ on linear axes, which demonstrates the collapse for small ϵ without this sensitivity.

2.6 Summary and discussion

In this chapter we have considered the pull-in dynamics of MEMS devices, an example of overdamped snap-through. When the system is near the static pull-in voltage/acceleration, the motion is known to slow down considerably during a meta-stable or bottleneck phase. By considering a lumped parallel-plate model, we have shown that the bottleneck be-haviour is an instance of a saddle-node ghost; the duration of the bottleneck increases $\propto \epsilon^{-1/2}$, where ϵ is the normalised distance of the system beyond the pull-in transition (defined in equation (2.9)). A detailed asymptotic analysis then allowed us to evaluate the pre-factor in this scaling law. The result is a simple analytical prediction for the total pull-in time: $t_{\mathrm{PI}} \sim (b/k)2\pi/\sqrt{3\epsilon}$, in which b is the effective damping coefficient and k is the lumped mechanical stiffness applicable to the bottleneck phase. This result complements previous studies that have calculated a similar asymptotic pull-in time for underdamped devices (Leus & Elata, 2008; Joglekar & Pawaskar, 2011).

The $\epsilon^{-1/2}$ scaling law explains the high sensitivity of the pull-in time observed in pre-vious experiments and numerical simulations. Moreover, because the bottleneck phase dominates the dynamics during pull-in, the resulting pull-in time is relatively insensitive to what happens outside of the bottleneck region; this includes the precise geometry of the device, the effects of compressibility and air rarefaction, and the way in which stoppers limit the displacement before contact occurs. The implication is that a simple parallel-plate model, using lumped values for the damping coefficient and spring constant, is an effective means of capturing the behaviour of a complex MEMS device. Indeed, the wide range of available data collapsed onto a single master curve (figure 2.9), despite the number of additional effects that are present in the range of experiments and simulations analysed (summarised in tables 2.1–2.2). Moreover, while the assumption of a constant damping coefficient is often stated to give large errors (Hung & Senturia, 1999; Rocha *et al.*, 2004*a*), we have shown that, in the bottleneck regime, this assumption is sufficient to correctly predict the pull-in time.

The sensitivity of the bottleneck to external perturbations is the basis of using pull-in time as a sensing mechanism, as in some pressure sensors (Gupta *et al.*, 1996; Gupta & Senturia, 1997) and accelerometers (Rocha *et al.*, 2004*a*; Dias *et al.*, 2011; 2015). Cur-rently, the lack of linearity in the response is considered to be the main disadvantage of

these devices, and it has been suggested that the voltage/pull-in time curve might be linearised by the introduction of extra forces (Dias *et al.*, 2011). Our expression for the pull-in time partly resolves the issue, as it provides a simple power law that can be used to calibrate a device. In addition, our introduction of the dimensionless parameter ϵ, equation (2.9), captures both variations in the voltage and external acceleration near the pull-in transition. When plotted in terms of this parameter, we observe a collapse of data over experiments where either the voltage or the acceleration was varied.

Finally, we discuss the conditions under which our analysis holds. We have considered only devices with low quality factors, so that inertia of the moving electrode can be neglected during the bottleneck phase. We also focussed on DC loads that are stepped from zero, since this loading type is commonly used in applications of the pull-in time. Nevertheless, our analysis may be adapted to other types of loading, provided the behaviour before pull-in remains quasi-static; for example, if the voltage is instead stepped from a positive value. However, in the case of a voltage sweep (e.g. triangular wave), the quasi-static condition is not met and the $\epsilon^{-1/2}$ scaling law will not apply. Similarly, extremely close to the pull-in transition, mechanical noise will eventually become important and limit the system response. Nevertheless, we hope that the unifying perspective we have presented here will lead to new insights in the application of dynamic pull-in instabilities.

Appendix 2.A Assumption of a constant damping coefficient

The assumption of a constant damping coefficient has often been reported to give large errors compared to simulations that incorporate a variable damping coefficient (Rocha *et al.*, 2004*a*; Hung & Senturia, 1999); based on this, it is argued that a variable damping coefficient should always be used when predicting the pull-in time for MEMS applications. For example, Rocha *et al.* (2004*a*) consider the pull-in dynamics of a parallel-plate actuator, showing that a constant damping coefficient approximation leads to errors of up to 40%. However, Rocha *et al.* (2004*a*) use the value of the damping coefficient when the plate is in the zero voltage state, which we denote b_{init}. This damping is much smaller than the value when the plate is near the static pull-in displacement, labelled b_{PI} (where the thickness of the air gap is around 2/3 of the zero-voltage thickness). Because the pull-in timescale $[t]$ depends linearly on the damping coefficient (for overdamped devices), and the system spends most of its time close to the pull-in displacement during the bottleneck phase, using b_{init} will significantly underpredict the pull-in time. Here, we show that using b_{PI} (our approach throughout this chapter) is sufficient to correctly predict the pull-in time.

We modify our spring-mass model to consider a variable damping coefficient $b(x)$:

$$m\frac{\mathrm{d}^2 x}{\mathrm{d}t^2} + b(x)\frac{\mathrm{d}x}{\mathrm{d}t} + kx = \frac{1}{2}\frac{\epsilon_0 A V^2}{(d_0 - x)^2} + m a_{\text{ext}}. \tag{2.18}$$

Ignoring compressibility and rarefaction effects, the incompressible Reynolds equation may be solved approximately in the parallel-plate geometry to give (Veijola *et al.*, 1995)

$$b(x) = \frac{\mu C}{(d_0 - x)^3},$$

where μ is the air viscosity and C is a constant that depends on the dimensions of the moving plate. The damping coefficient corresponding to the zero voltage state, $x = m a_{\text{ext}}/k$, is then

$$b_{\text{init}} = \frac{\mu C}{d_0^3 (1 - A_{\text{ext}})^3}.$$

Since a variable damping coefficient does not change the steady solutions, the static pull-in displacement is $x_{\text{PI}} = (d_0/3)\,(1 + 2A_{\text{ext}})$, as before. The damping coefficient during the bottleneck phase is then

$$b_{\text{PI}} = \frac{27}{8}\frac{\mu C}{d_0^3 (1 - A_{\text{ext}})^3},$$

so that

$$\frac{b_{\text{init}}}{b_{\text{PI}}} = \frac{8}{27}.$$

We non-dimensionalise in a similar way to §2.3, though now we set

$$T = \frac{t}{b_{\mathrm{init}}/k}, \quad Q = \frac{\sqrt{mk}}{b_{\mathrm{init}}}.$$

Equation (2.18) then becomes

$$Q^2 \frac{\mathrm{d}^2 X}{\mathrm{d}T^2} + \frac{1}{(1-X)^3} \frac{\mathrm{d}X}{\mathrm{d}T} + X = \frac{\lambda}{(1-X)^2}, \tag{2.19}$$

and the initial conditions remain $X(0) = \dot{X}(0) = 0$. We may then perform a local analysis of equation (2.19) when the solution is in the bottleneck phase, along similar lines to §2.4.1 (where now we Taylor expand the $(1-X)^{-3}$ term about $X = X_{\mathrm{fold}} = 1/3$). This shows that the dimensional pull-in time, t_{PI}, is given by

$$t_{\mathrm{PI}} \sim \frac{b_{\mathrm{PI}}}{k} \frac{2\pi}{\sqrt{3\epsilon}},$$

valid for $0 < \epsilon \ll 1$. We conclude that setting $b = b_{\mathrm{PI}}$ in our constant damping model (as done in the main text) yields the correct asymptotic expression for the pull-in time (see equation 2.17), while setting $b = b_{\mathrm{init}}$ will lead to a prediction of t_{PI} that is a fraction $8/27$ (approximately 30%) of the true value.

This is illustrated in figure 2.10, which compares the numerical solution of the full equation (2.19) with two approximate approaches: (i) the solution in which we instead assume a constant damping coefficient $b(x) = b_{\mathrm{PI}}$ (corresponding to setting $X = X_{\mathrm{fold}}$ in the $(1-X)^{-3}$ term) and (ii) the solution with a constant coefficient $b(x) = b_{\mathrm{init}}$ (setting $X = 0$ in the $(1-X)^{-3}$ term). We see that the constant coefficient b_{PI} successfully captures the duration of the bottleneck phase, and hence the total time taken to pull-in, while using b_{init} leads to large errors.

Rocha *et al.* (2004*a*) report that using a constant coefficient b_{init} yields a pull-in time that is 60% of that obtained using a variable damping coefficient. This is larger than the $\approx 30\%$ that we predict here. However, the simulations reported by Rocha *et al.* (2004*a*) also incorporate compressibility and rarefaction effects in the squeeze film, which may account for this discrepancy.
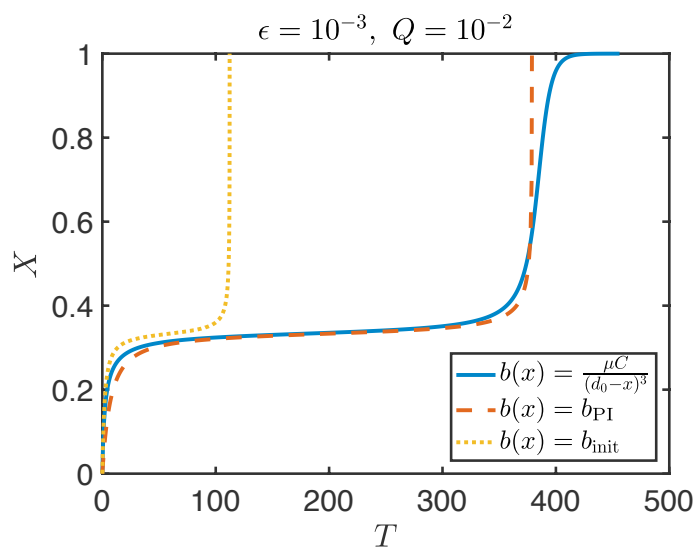
Figure 2.10: *Trajectories obtained by numerical integration of equation (2.18) with different damping models $b(x)$ (see legend). Here dimensionless quantities are defined as in §2.3, but now we set $T = t/(b_{\text{init}}/k)$ and $Q = \sqrt{mk}/b_{\text{init}}$. (Reprinted from Gomez et al. (2018a), DOI: https://doi.org/10.1088/1361-6439/aa9a70. Copyright © IOP Publishing. Reproduced with permission. All rights reserved.)*

Overdamped snap-through: pull-in of microbeams

Synopsis

We study the pull-in dynamics of MEMS microbeams — a model of a continuous elastic structure that snaps in response to an externally applied field. We extend the parallel-plate model of Chapter 2 to now incorporate the beam geometry. Starting from the dynamic beam equation, we develop a perturbation method that systematically reduces the dynamics near the pull-in transition to the normal form for a saddle-node bifurcation. Focussing on the overdamped limit, this allows us to attribute bottleneck behaviour observed in microbeams to a saddle-node ghost, and we obtain a simple expression for the pull-in time in terms of the beam parameters and external damping coefficient. This expression is found to agree well with experiments and numerical simulations that incorporate more realistic models of squeeze film damping, and so will be useful in applications that use pull-in time as a sensing mechanism. We also consider the accuracy of a single-mode approximation of the microbeam equations — an approach that is commonly used to make analytical progress, though no systematic investigation of its accuracy has been attempted. By comparing to our bottleneck analysis, we identify the factors that control the error of this approach, and we demonstrate that this error can be very small.

A paper based on the work described in this chapter has been published in the *Journal of Micromechanics and Microengineering* (Gomez *et al.*, 2018*c*).
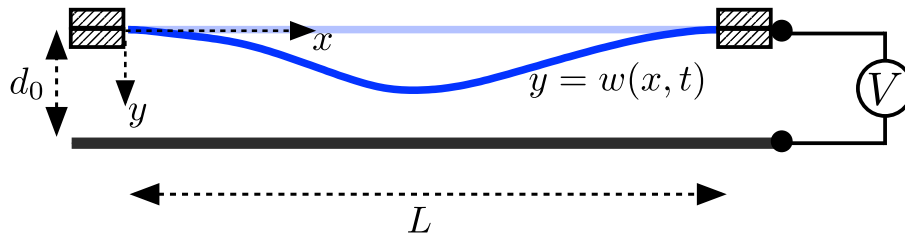
Figure 3.1: *Schematic of a microbeam in its undeformed state (light blue) and deforming under a DC load (dark blue). Here the ends of the beam are assumed to be clamped parallel to the lower electrode (shown as a thick black line), so that stretching effects are important during deformation. (Reprinted from Gomez* et al. *(2018c), DOI: https://doi.org/10.1088/1361-6439/aad72f. Copyright © IOP Publishing. Reproduced with permission. All rights reserved.)*

3.1 Introduction

Microbeams are a widely used element of microelectromechanical systems (MEMS) (Pelesko & Bernstein, 2002): they are a basic structural prototype that forms the building blocks for more complex devices (Lin & Wang, 2006). In these applications they are subject to a range of loading types including magnetic, thermal and piezoelectric, though electrostatic forcing is the most commonly used (Das & Batra, 2009). In a typical electrostatic device, the microbeam acts as a deformable electrode that is separated from a fixed electrode by a thin air gap; an example is shown schematically in figure 3.1. A potential difference is then applied between the electrodes. When the applied voltage exceeds a critical value, the microbeam abruptly collapses onto the fixed electrode — another example of a snap-through instability referred to as 'pull-in' (Batra *et al.*, 2007).

Microbeams are commonly used as microresonators in radio frequency (RF) applications, where a combination of AC and DC voltages drive the beam near its natural frequencies. In this context pull-in generally corresponds to failure of the device (Nayfeh *et al.*, 2007). In switching applications, pull-in is instead exploited to generate large changes in shape between 'off' and 'on' states. Here it is important to understand the transient dynamics upon pull-in, as this governs the switching time of the device and hence the energy consumed during each cycle (Castaner & Senturia, 1999). At voltages just beyond the pull-in voltage, a number of experiments and numerical simulations have also reported bottleneck behaviour in microbeams, specifically when the dynamics are dominated by squeeze film damping in the air gap (Gupta *et al.*, 1996; Gupta & Senturia, 1997; Grétillat *et al.*, 1997; Hung & Senturia, 1999; Younis *et al.*, 2003; Missoffe *et al.*, 2008). In this regime, the time taken to pull-in may increase by over an order of magnitude within a very narrow range of the applied voltage, and its sensitivity to ambient conditions is exploited in sensing applications (Gupta & Senturia, 1997). However, a detailed analysis of this slowing down has only been attempted for parallel-plate devices (Rocha *et al.*, 2004a;b) so that many features of the bottleneck remain poorly understood.

In Chapter 2, using a lumped mass-spring model similar to Rocha *et al.* (2004*a*), we showed that the bottleneck phenomenon is a type of critical slowing down near the pull-in transition — the 'ghost' of the saddle-node bifurcation. Accordingly, the pull-in time, t_{PI}, increases according to an inverse square-root scaling law, i.e. we have $t_{\mathrm{PI}} \propto \epsilon^{-1/2}$ as $\epsilon \to 0$, where ϵ is the normalised difference between the applied voltage and the pull-in voltage. In addition, we determined an analytical expression for this pull-in time in terms of a lumped mechanical stiffness and effective damping coefficient appropriate to the bottleneck phase, which can then be used as fitting parameters to obtain good agreement with experiments and simulations of microbeams reported in the literature. However, this lumped-parameter approach does not show how the pull-in time depends on the various physical parameters of the beam (e.g. its thickness and Young's modulus); such information will be useful when using the scaling law as a design rule in applications, as it eliminates the need for further simulations to predict the dynamic response if these parameters change. While it is possible to obtain equivalent stiffnesses under simple loading types (see LaRose & Murphy, 2010, for example), these do not account for effects such as a variable residual stress and different boundary conditions applied to the beam. We would therefore like to extend the lumped-parameter approach of Chapter 2 to incorporate the beam geometry.

The key challenge we address in this chapter is how to analyse the timescale of snap-through for continuous elastic structures. Unlike lumped mass-spring models, it is much more difficult to make analytical progress with the equations governing structures such as beams and shells, which typically consist of partial differential equations (PDEs) in space and time. For this reason, previous studies mainly rely on detailed numerical simulations or *ad hoc* single-mode approximations, such as those discussed below. In this chapter we show that the underlying bifurcation structure governs the bottleneck dynamics, rather than the precise physical details of the system, and we obtain analytical results in the process. This work then provides a framework for analysing snap-through of continuous structures, which we adapt later in Chapter 4 when we consider systems that may be underdamped and in which snap-through is caused by geometric nonlinearity (rather than an external field).

3.1.1 Models of pull-in dynamics

A variety of numerical methods have been developed to study the pull-in dynamics of microbeams, including finite difference methods (Gupta *et al.*, 1996; McCarthy *et al.*, 2002), finite element methods (Rochus *et al.*, 2005) and reduced-order models (macromodels) (Nayfeh *et al.*, 2005). Macromodels typically apply a Galerkin procedure: the solution is expanded as a truncated series of known functions of the spatial variables (the basis functions), whose coefficients are unknown and depend on time. Commonly, the undamped

vibrational modes about the undeformed beam are used as basis functions (Younis *et al.*, 2003). This yields a finite set of ordinary differential equations (ODEs) that can be integrated efficiently using pre-existing ODE solvers.

When only the first term in the Galerkin expansion is kept, this procedure results in a single-mode or single-degree-of-freedom (SDOF) approximation of the microbeam equations. Despite its simplicity, this approximation is often effective at capturing the leading-order dynamic phenomena — for example the pull-in transition, the phase-plane portrait, and the influence of different parameter values and loading types have all been qualitatively explained using the SDOF method (Krylov & Maimon, 2004; Krylov, 2007; Krylov & Dick, 2010). Moreover, Joglekar & Pawaskar (2011) have used the SDOF approximation to obtain an analytical expression for the pull-in time of an undamped microbeam. They found that using two different basis functions gives very similar results, suggesting that such approximations are reasonable. However, a comparison with numerical solutions indicated that the error in this approach grows larger near the pull-in transition. Based on this, Joglekar & Pawaskar (2011) conclude that a SDOF approximation is insufficient to model the dynamics near the pull-in transition, and that it is necessary to retain higher modes in a macromodel. However, no systematic investigation of this error is provided. Elsewhere, the accuracy of the SDOF method has only been validated by computing the natural frequencies of the beam and the equilibrium shapes (Ijntema & Tilmans, 1992; Kacem *et al.*, 2009; Batra *et al.*, 2008). It therefore remains unclear how valid the SDOF method is when analysing the transient dynamics of pull-in.

This motivates a more careful analysis of the pull-in dynamics of a microbeam. In this chapter we model the beam geometry using the dynamic beam equation, accounting for the effects of midplane stretching, residual stress and strain-stiffening. However, similar to Chapter 2, we will use a lumped damping coefficient to model the squeeze film damping. While we could use a more complex damping model, this assumption enables us to make significant analytical progress. (The assumption of a constant damping coefficient can also be justified during the bottleneck phase, for reasons we discuss in §3.2.) In particular, we develop a perturbation method that reduces the governing PDE to a simpler ODE resembling the normal form for a saddle-node bifurcation. The key feature of this method is that the reduction is systematic and results in a SDOF-like approximation, but in which the appropriate basis function naturally emerges as part of the analysis. In light of this, we are then able to check the validity of a SDOF approximation in which the basis function is chosen *a priori*, as is standard in the literature.

The rest of this chapter is organised as follows. We begin in §3.2 by describing the equations governing the microbeam dynamics and their non-dimensionalisation. In §3.3, we consider the equilibrium behaviour as the voltage is quasi-statically varied. In §3.4, we

analyse the dynamics when the voltage is just beyond the static pull-in transition. Using direct numerical solutions, we demonstrate bottleneck behaviour in the overdamped limit. We then perform a detailed asymptotic analysis of the bottleneck phase. We confirm the expected scaling $t_{\mathrm{PI}} \propto \epsilon^{-1/2}$ as $\epsilon \to 0$, and we calculate the pre-factor in this relationship in terms of the beam parameters. This is compared to experiments and numerical simulations that incorporate more realistic models of squeeze film damping. In §3.5 we consider the accuracy of a standard SDOF approximation. We demonstrate that the error of this approach can be small and we derive criteria that a 'good' choice of basis function should satisfy. Finally, we summarise our findings and conclude in §3.6.

3.2 Theoretical formulation

3.2.1 Governing equations

A schematic of the microbeam is shown in figure 3.1. The properties of the beam are its density ρ_s, thickness h, width b and bending stiffness $B = Ebh^3/12$, with E the Young's modulus. (Note that we are using the bending stiffness appropriate for a narrow strip of material rather than an infinite plate, so that the Poisson ratio does not appear in the expression for B; see Audoly & Pomeau, 2010, for example.) We suppose that the ends of the beam are clamped parallel to the lower electrode a distance L apart (also called fixed–fixed ends). These boundary conditions are commonly used in applications of microbeams in pressure sensors and microswitches (Joglekar & Pawaskar, 2011), and have been widely studied as a 'benchmark problem' (Krylov *et al.*, 2008). Because the natural length of the fabricated beam may differ slightly from L (Lin & Wang, 2006), we also account for a possible (constant) residual tension P_0 when the beam is flat (P_0 may also be negative, corresponding to residual compression). We choose coordinates so that x measures the horizontal distance from the left end of the beam, and $y = w(x,t)$ is the transverse displacement (with t denoting time). The applied DC voltage is V, and d_0 is the thickness of the air gap between the beam and the lower electrode in the absence of any displacement, $w = 0$ (figure 3.1).

When the microbeam passes through a bottleneck phase, the motions are dramatically slowed and so we can neglect compressibility and rarefaction effects in the squeeze film — the damping is purely viscous (Missoffe *et al.*, 2008). As the geometry of the microbeam is also slowly varying in the bottleneck, we assume a constant damping coefficient, η. While it is possible to obtain an approximate expression for the damping coefficient, starting from the incompressible Reynolds equation (Blech, 1983; Veijola *et al.*, 1995; Krylov & Maimon, 2004), we do not consider the precise form of the damping coefficient η here, and

instead treat η as a lumped parameter for simplicity. This also means that we are able to parameterise additional effects such as material damping and different venting conditions at the beam edges. This approach is similar to Chapter 2 except now we no longer lump the beam elasticity into a spring constant.

We assume the beam thickness is small compared to its length (i.e. $h \ll L$) and its shape remains shallow; if the beam does not contact the lower electrode ($w < d_0$), this assumption is valid provided the aspect ratio of the air gap is also small, $d_0 \ll L$. Under the above assumptions, a vertical force balance on the beam yields the dynamic beam equation (Pelesko & Bernstein, 2002)

$$\rho_s bh \frac{\partial^2 w}{\partial t^2} + \eta \frac{\partial w}{\partial t} + B \frac{\partial^4 w}{\partial x^4} - P \frac{\partial^2 w}{\partial x^2} = \frac{1}{2} \frac{\epsilon_0 b V^2}{(d_0 - w)^2}, \quad 0 < x < L, \tag{3.1}$$

where P is the (unknown) tension in the beam and ϵ_0 is the permittivity of air. Here we are using a parallel-plate approximation of the electrostatic force, consistent with our assumption $d_0 \ll L$; for simplicity we neglect the effects of fringing fields (this requires $d_0 \ll b$) and we do not consider partial field screening between the beam and lower electrode.

As the beam deforms, Hooke's law implies the compressive strain is given by $\epsilon_{xx} = (P - P_0)/(Ebh)$. Incorporating the lowest-order geometric nonlinearity in the beam slope, the compressive strain is given in terms of the horizontal displacement u and transverse displacement w by the von Kármán strain (see for example Howell *et al.*, 2009):

$$\epsilon_{xx} = \frac{\partial u}{\partial x} + \frac{1}{2} \left(\frac{\partial w}{\partial x} \right)^2.$$

Integrating from $x = 0$ to $x = L$, and using the clamped boundary conditions $u(0, t) = u(L, t) = 0$, we eliminate the horizontal displacement to obtain

$$\frac{(P - P_0)L}{Ebh} = \frac{1}{2} \int_0^L \left(\frac{\partial w}{\partial x} \right)^2 \, \mathrm{d}x. \tag{3.2}$$

Physically, this equation states that the tension changes in response to changes in the length of the centreline (i.e. midplane stretching). We refer to (3.2) as the Hooke's law constraint.

The remaining boundary conditions at the clamped ends are (subscripts here and throughout denoting partial differentiation)

$$w(0, t) = w_x(0, t) = w(L, t) = w_x(L, t) = 0.$$

As in Chapter 2, for initial conditions we suppose the beam is at rest when the voltage is suddenly stepped from zero, i.e. $w(x,0) = w_t(x,0) = 0$. With these initial conditions, our model is equivalent to that used by Younis *et al.* (2003), who focus on solving the equations numerically using a reduced-order model based on a Galerkin procedure. Here we will instead use the system to gain analytical understanding of the pull-in dynamics, including the bottleneck phenomenon. We will then use our own numerical solutions, together with those of Younis *et al.* (2003), to validate our results.

3.2.2 Non-dimensionalisation

It is convenient to scale the horizontal coordinate with the length L between the two clamps, and to scale the vertical displacement with the initial gap thickness d_0. As we are interested in overdamped devices, a natural timescale $[t]$ comes from balancing damping and bending forces in the beam equation (3.1), giving $[t] = L^4\eta/B$. We therefore introduce the dimensionless variables

$$X = \frac{x}{L}, \quad W = \frac{w}{d_0}, \quad T = \frac{t}{[t]}.$$

With these re-scalings, the beam equation (3.1) becomes

$$Q^2\frac{\partial^2 W}{\partial T^2} + \frac{\partial W}{\partial T} + \frac{\partial^4 W}{\partial X^4} - \tau\frac{\partial^2 W}{\partial X^2} = \frac{\lambda}{(1-W)^2}, \quad 0 < X < 1, \tag{3.3}$$

where we have introduced the dimensionless parameters

$$Q = \frac{\sqrt{\rho_s b h B/L^4}}{\eta}, \quad \tau = \frac{PL^2}{B}, \quad \lambda = \frac{1}{2}\frac{\epsilon_0 bL^4V^2}{Bd_0^3}. \tag{3.4}$$

These correspond to the quality factor (measuring the importance of inertia compared to damping forces), the dimensionless tension in the beam, and the dimensionless voltage, respectively. We may interpret λ as the ratio of the typical electrostatic force per unit length ($\sim \epsilon_0 bV^2/[2d_0^2]$) to the typical force per unit length required to bend the beam by an amount comparable to d_0 ($\sim Bd_0/L^4$).

Re-scaling the Hooke's law constraint (3.2), the dimensionless tension τ is given by

$$\mathcal{S}(\tau - \tau_0) = \frac{1}{2}\int_0^1 \left(\frac{\partial W}{\partial X}\right)^2 \mathrm{d}X, \tag{3.5}$$

where

$$\tau_0 = \frac{P_0 L^2}{B}, \quad \mathcal{S} = \frac{h^2}{12d_0^2},$$

are the dimensionless residual tension and 'stretchability' of the beam (Pandey *et al.*, 2014). Here $\mathcal{S}$ acts as a dimensionless membrane stiffness. In real devices the beam thickness h is often comparable to the initial gap thickness d_0 (Gupta *et al.*, 1996; Gupta & Senturia, 1997), so that $\mathcal{S}$ typically lies in the range $(10^{-2}, 10^{-1})$. Finally, the boundary conditions at the clamped ends become

$$W(0, T) = W_X(0, T) = W(1, T) = W_X(1, T) = 0, \qquad (3.6)$$

and the initial conditions are

$$W(X, 0) = W_T(X, 0) = 0. \qquad (3.7)$$

3.3 Equilibrium behaviour

We briefly review the equilibrium behaviour as the dimensionless voltage λ is quasi-statically varied. We solve the steady version of the beam equation (3.3) together with the Hooke's law constraint (3.5) and clamped boundary conditions (3.6) numerically in MATLAB using the routine `bvp4c`. We write the beam equation as a first-order system in W and its derivatives, and we impose (3.5) by introducing the additional variable $I(X) = \frac{1}{2} \int_0^X [W'(\xi)]^2 \, \mathrm{d}\xi$ with boundary conditions $I(0) = 0$ and $I(1) = \mathcal{S}(\tau - \tau_0)$ (writing $'$ for $\mathrm{d}/\mathrm{d}X$). Because pull-in corresponds to a saddle-node bifurcation, near which the system becomes highly sensitive to λ, we avoid convergence issues (Younis *et al.*, 2003) by instead controlling the tension τ and solving for λ as part of the solution (such unknown parameters are easily incorporated into the `bvp4c` solver). For each stretchability $\mathcal{S}$ and residual tension τ_0, we implement a simple continuation algorithm that follows equilibrium branches as τ is increased in small steps. The fold point then simply corresponds to a local maximum in the value of λ, which we can numerically continue past without any convergence issues. To begin the continuation, we use an asymptotic solution valid at small voltages, when the beam is nearly flat and $\tau \approx \tau_0$ (for details see Appendix 3.A).

When plotted back in terms of λ, the resulting bifurcation diagram confirms that for small λ, two distinct equilibrium branches exist that are physical (i.e. $W < 1$). As λ increases, both branches approach each other, before they eventually meet at a saddle-node bifurcation when $\lambda = \lambda_{\text{fold}}$: no equilibrium shape exists away from collapse for $\lambda > \lambda_{\text{fold}}$ (we are unable to numerically find further solutions). This is shown in figure 3.2a, where we plot the midpoint displacement, $W(1/2)$, as a function of λ. The critical value λ_{fold} evidently increases as $\mathcal{S}$ decreases (corresponding to a larger membrane stiffness), growing rapidly for values $\mathcal{S} \lesssim 10^{-1}$. At small stretchabilities typical of realistic devices, the dependence of λ_{fold} on the residual tension τ_0 is much weaker; see figure 3.2b. (In both
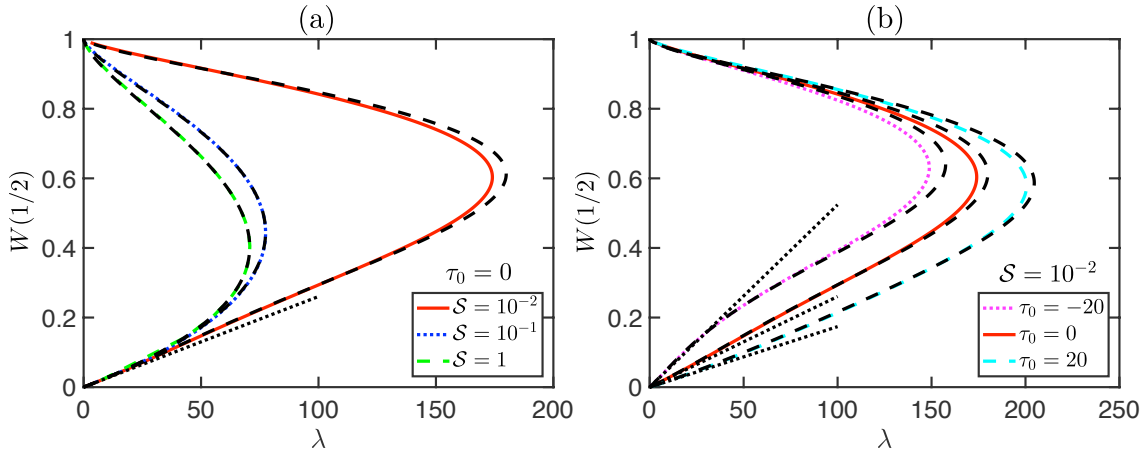
Figure 3.2: *Response diagram for steady solutions of the beam equation (3.3) subject to (3.5)–(3.6) as the dimensionless voltage λ varies. Numerical results are shown for (a) zero residual tension ($\tau_0 = 0$) and varying stretchability $\mathcal{S}$ and (b) fixed stretchability $\mathcal{S} = 10^{-2}$ and varying residual tension τ_0 (coloured curves; see legends). For later comparison, predictions from the SDOF approximation computed using (3.30) are shown (black dashed curves), as well as the asymptotic behaviour valid for $\lambda \ll 1$ derived in Appendix 3.A (black dotted lines). (Reprinted from Gomez et al. (2018c), DOI: https://doi.org/10.1088/1361-6439/aad72f. Copyright © IOP Publishing. Reproduced with permission. All rights reserved.)*

plots we have also shown the asymptotic behaviour when $\lambda \ll 1$, derived in Appendix 3.A, and, for later reference, the predictions of the SDOF approximation computed in §3.5.)

Using a standard linear stability analysis, it has been shown (Younis *et al.*, 2003) that the equilibrium branches below the fold point in figures 3.2a–b (i.e. with $W(1/2) \to 0$ as $\lambda \to 0$) are linearly stable and correspond to the shapes observed experimentally. The upper branches are linearly unstable, so the fold point corresponds to a standard 'exchange of stability' (Maddocks, 1987) in which both branches become neutrally stable as they meet. For later reference, we note that only the fundamental natural frequency of the beam equals zero at the fold. More specifically, suppose we set $W = W_b(X) + \delta W_p(X)e^{i\omega T}$ where $W_b(X)$ is an equilibrium shape and $\delta \ll 1$ is a fixed perturbation (and similarly for the tension τ). Inserting into (3.3), (3.5)–(3.6) and considering terms of $O(\delta)$, we obtain a linear eigenvalue problem for the unknown natural frequency (eigenvalue) ω and eigenfunction W_p; at the saddle-node bifurcation, there is then a simple zero eigenvalue $\omega = 0$ (i.e. the associated eigenspace is of dimension one).

We deduce that the critical value λ_{fold} corresponds to where pull-in *first* occurs if λ is increased quasi-statically. In dimensional terms, this gives the static pull-in voltage, V_{SPI}, and the pull-in displacement, $w_{\text{SPI}}(x)$, as

$$V_{\text{SPI}} = \sqrt{\frac{2Bd_0^3\lambda_{\text{fold}}}{\epsilon_0 bL^4}}, \quad w_{\text{SPI}}(x) = d_0 W_{\text{fold}}(X),$$

where we write $W_{\text{fold}}(X)$ for the dimensionless equilibrium shape at the fold point (with associated tension τ_{fold}).

3.4 Pull-in dynamics

We now explore the dynamics at voltages just beyond the static pull-in transition, setting

$$\lambda = \lambda_{\text{fold}}(1 + \epsilon),$$

where $0 < \epsilon \ll 1$ is a small perturbation. If all parameters except the voltage are fixed, combining the definition of λ in (3.4) with the fact that

$$\lambda_{\text{fold}} = \frac{1}{2} \frac{\epsilon_0 b L^4 V_{\text{SPI}}^2}{B d_0^3},$$

shows that ϵ is simply the normalised voltage difference:

$$\epsilon = \frac{\lambda}{\lambda_{\text{fold}}} - 1 = \left(\frac{V}{V_{\text{SPI}}}\right)^2 - 1 \approx \frac{2}{V_{\text{SPI}}}\left(V - V_{\text{SPI}}\right).$$

3.4.1 Numerical solution

We solve the dynamic beam equation (3.3) subject to (3.5)–(3.7) numerically using the method of lines. This involves discretising the equations in space so that the system reduces to a finite set of ODEs in time. We obtain second-order accuracy in the convergence of our scheme; for details see Appendix 3.B. For each combination of Q, λ, $\mathcal{S}$ and τ_0, we integrate the ODEs numerically in MATLAB (routine `ode23t`) to compute the trajectory of each grid point in the discretisation. To avoid the singularity at $W = 1$, we use event location to stop integration as soon as $(1 - W) < \text{tol}$ at any grid point, for some specified tolerance tol. The corresponding time at this event is then the reported pull-in time, labelled T_{PI}. For all simulations reported in this chapter we use $N = 100$ grid points and $\text{tol} = 10^{-4}$; we also specify relative and absolute error tolerances of 10^{-8} in `ode23t` and we limit the maximum time step of the solver to 10^{-6}. We have checked that our results are insensitive to further increasing N and decreasing these tolerances/maximum time step.

Numerical trajectories of the beam midpoint, $W(1/2, T)$, are plotted in figure 3.3 for various values of ϵ (here $Q = 10^{-2}$ corresponding to an overdamped beam). We observe that the microbeam slows down significantly in a bottleneck phase. This is similar to the bottleneck behaviour of a parallel-plate capacitor (Chapter 2), in that (i) the bottleneck dominates the total time taken to pull-in; (ii) the duration of the bottleneck is highly
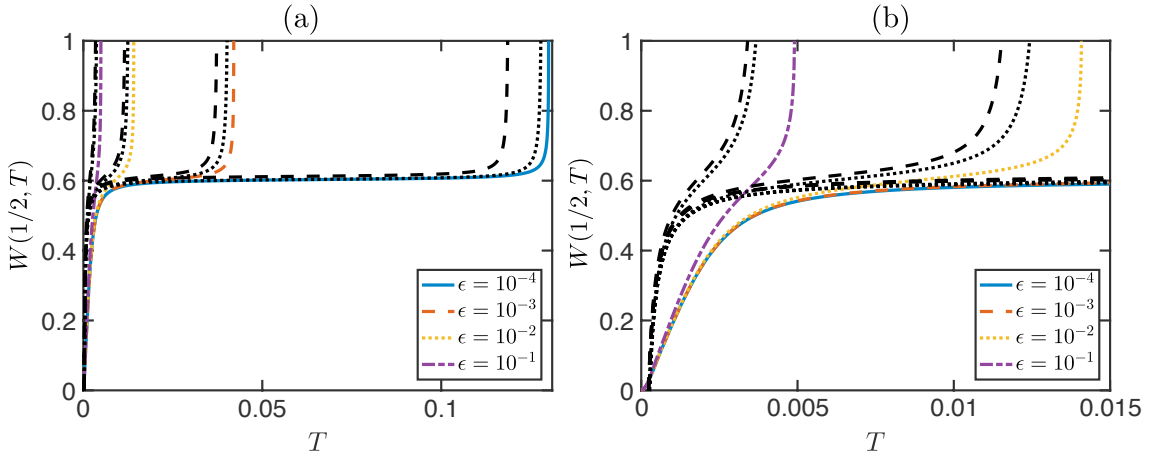
Figure 3.3: *Bottleneck behaviour at voltages close to the pull-in transition ($Q = 10^{-2}$, $\mathcal{S} = 10^{-2}$, $\tau_0 = 0$, $N = 100$). (a) Dimensionless midpoint trajectories obtained by integrating the dynamic beam equation (3.3) subject to (3.5)–(3.7) numerically (coloured curves; see legends). These exhibit a bottleneck as $W(1/2, T)$ passes $W_{\rm fold}(1/2) \approx 0.6036$, which increases in duration as ϵ decreases. For later comparison, also shown are the predictions (3.22) of the bottleneck analysis (black dotted curves) and the predictions (3.35) of the SDOF approximation (black dashed curves). (b) A close up of the trajectories in (a) at early times. (Reprinted from Gomez et al. (2018c), DOI: https://doi.org/10.1088/1361-6439/aad72f. Copyright © IOP Publishing. Reproduced with permission. All rights reserved.)*

sensitive to the value of ϵ, increasing apparently without bound as $\epsilon \to 0$; and (iii) the bottleneck always seems to occur close to a well-defined displacement. Indeed, this displacement is precisely the static pull-in displacement; see figure 3.4, which shows that the beam 'waits' near the fold shape, $W_{\rm fold}(X)$ (black dotted curve), before rapidly accelerating towards the lower electrode, as seen by the shapes (plotted at equally spaced times) becoming closely packed together.

These similarities suggest that the bottleneck here is also a saddle-node ghost: as the beam passes the static pull-in displacement, the net force becomes very small (since $\epsilon \ll 1$ and the forces balance exactly at the pull-in displacement with $\epsilon = 0$), so that the motions slow down considerably. Hence, we expect that inertia of the beam does not play a role. We now perform a detailed analysis of the solution during the bottleneck phase. We use a similar method to Chapter 2: we expand the solution about the pull-in displacement, and solve the governing equations asymptotically. However, the system here is infinite dimensional and the pull-in displacement is the function $W_{\rm fold}(X)$ rather than a lumped scalar value. It turns out that the 'extra' degrees of freedom mean we need to proceed to higher order to obtain a simple equation that characterises the bottleneck dynamics. This will allow us to obtain the expected $\epsilon^{-1/2}$ scaling for the bottleneck duration, and to calculate the corresponding pre-factor.
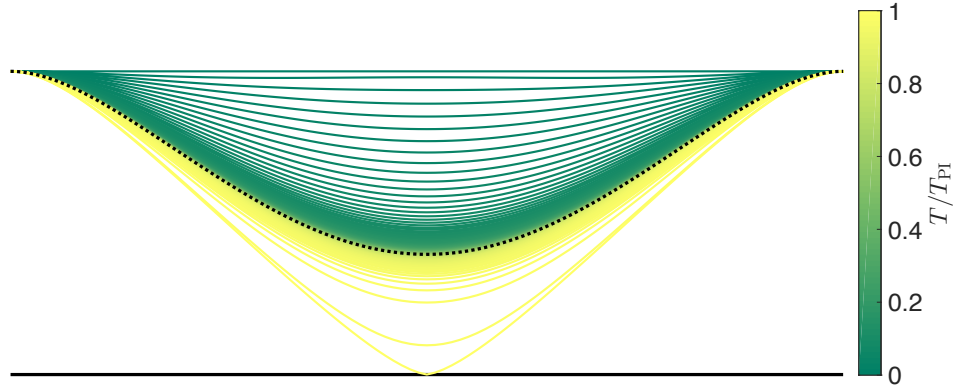
Figure 3.4: *Sequence of beam shapes during pull-in ($\epsilon = 10^{-3}$, $Q = 10^{-2}$, $\mathcal{S} = 10^{-2}$, $\tau_0 = 0$, $N = 100$). In total, 212 profiles at equally spaced time steps between $T = 0$ and contact with the lower electrode (shown as a black line) at $T = T_{\mathrm{PI}}$ are displayed (coloured curves; see colourbar), as well as the pull-in displacement $W_{\mathrm{fold}}(X)$ (black dotted curve). (Reprinted from Gomez et al. (2018c), DOI: https://doi.org/10.1088/1361-6439/aad72f. Copyright © IOP Publishing. Reproduced with permission. All rights reserved.)*

3.4.2 Bottleneck analysis

When the solution is close to the static pull-in displacement, we have

$$
\begin{aligned}
W(X, T) &= W_{\mathrm{fold}}(X) + \tilde{W}(X, T), \\
\tau(T) &= \tau_{\mathrm{fold}} + \tilde{\tau}(T),
\end{aligned}
\tag{3.8}
$$

where $|\tilde{W}| \ll 1$ and $|\tilde{\tau}| \ll 1$. It follows that the electrostatic force can be expanded as

$$
\frac{\lambda}{(1 - W)^2} = \frac{\lambda_{\mathrm{fold}}}{(1 - W_{\mathrm{fold}})^2} (1 + \epsilon) + \frac{2\lambda_{\mathrm{fold}}}{(1 - W_{\mathrm{fold}})^3} \tilde{W} + \frac{3\lambda_{\mathrm{fold}}}{(1 - W_{\mathrm{fold}})^4} \tilde{W}^2 + O(\epsilon\tilde{W}, \tilde{W}^3). \tag{3.9}
$$

(The reason why we retain the $O(\tilde{W}^2)$ term but neglect the $O(\epsilon\tilde{W}, \tilde{W}^3)$ terms will be discussed below.) Inserting these expansions into the dynamic beam equation (3.3), and neglecting the inertia term (which from the above discussion is not expected to be important in the bottleneck), we obtain

$$
L(\tilde{W}, \tilde{\tau}) = -\frac{\partial \tilde{W}}{\partial T} + \tilde{\tau} \frac{\partial^2 \tilde{W}}{\partial X^2} + \frac{\lambda_{\mathrm{fold}}}{(1 - W_{\mathrm{fold}})^2} \epsilon + \frac{3\lambda_{\mathrm{fold}}}{(1 - W_{\mathrm{fold}})^4} \tilde{W}^2 + O(\epsilon\tilde{W}, \tilde{W}^3), \tag{3.10}
$$

where we have introduced the linear operator

$$
L(U, V) \equiv \frac{\partial^4 U}{\partial X^4} - \tau_{\mathrm{fold}} \frac{\partial^2 U}{\partial X^2} - V \frac{\mathrm{d}^2 W_{\mathrm{fold}}}{\mathrm{d}X^2} - \frac{2\lambda_{\mathrm{fold}}}{(1 - W_{\mathrm{fold}})^3} U. \tag{3.11}
$$

The Hooke's law constraint (3.5) becomes

$$\mathcal{S}\tilde{\tau} = \int_0^1 \frac{\mathrm{d}W_{\mathrm{fold}}}{\mathrm{d}X} \frac{\partial \tilde{W}}{\partial X} \, \mathrm{d}X + \frac{1}{2} \int_0^1 \left(\frac{\partial \tilde{W}}{\partial X} \right)^2 \, \mathrm{d}X, \tag{3.12}$$

and the boundary conditions (3.6) imply that

$$\tilde{W}(0,T) = \tilde{W}_X(0,T) = \tilde{W}(1,T) = \tilde{W}_X(1,T) = 0. \tag{3.13}$$

We now make two important assumptions that we will check at the end of our analysis:

(i) For small perturbations $\epsilon \ll 1$ the bottleneck timescale satisfies $T \gg 1$.

(ii) In the bottleneck, we must account for changes in the solution that are much larger than ϵ but remain small compared to unity, i.e. we have $\epsilon \ll |\tilde{W}| \ll 1$ and $\epsilon \ll |\tilde{\tau}| \ll 1$.

These assumptions are partly justified by the analysis in Chapter 2, which showed that (i) and (ii) hold for a parallel-plate capacitor. The idea is that while $\tilde{W}$ is $O(\epsilon)$ on smaller, inner, timescales, these assumptions will allow us to correctly predict the total bottleneck duration, when we later compare the results to numerics. In particular, these assumptions imply that the right-hand side of (3.10) remains small: the time derivative is small by virtue of the slow bottleneck timescale, while the remaining terms are either quadratic in the small quantities $(\tilde{W}, \tilde{\tau})$, or are $O(\epsilon)$. The left-hand side is linear in $(\tilde{W}, \tilde{\tau})$ and hence dominates these terms (from assumption (ii)). We now use this property to solve the problem asymptotically.

Leading order

We expand

$$\begin{aligned} \tilde{W}(X,T) &\sim \tilde{W}_0(X,T) + \tilde{W}_1(X,T), \\ \tilde{\tau}(T) &\sim \tilde{\tau}_0(T) + \tilde{\tau}_1(T), \end{aligned} \tag{3.14}$$

where $|\tilde{W}_1| \ll |\tilde{W}_0|$ and $|\tilde{\tau}_1| \ll |\tilde{\tau}_0|$ are first-order corrections. From the above discussion, at leading order we then have the homogeneous problem

$$L(\tilde{W}_0, \tilde{\tau}_0) = 0.$$

The constraint (3.12) at leading order is

$$\mathcal{S}\tilde{\tau}_0 = \int_0^1 \frac{\mathrm{d}W_{\mathrm{fold}}}{\mathrm{d}X} \frac{\partial \tilde{W}_0}{\partial X} \, \mathrm{d}X,$$

while the clamped conditions (3.13) remain unchanged in terms of $\tilde{W}_0$. These leading order equations are precisely the homogeneous, linearised versions of the full system (3.10)–(3.13) in $(\tilde{W}, \tilde{\tau})$. Hence, the leading order equations are equivalent to the equations governing linear stability of the fold shape $(W_{\text{fold}}, \tau_{\text{fold}})$, but — crucially — restricted to neutrally-stable modes (eigenfunctions) whose natural frequency (eigenvalue) is zero: we would have obtained similar equations upon setting $W = W_{\text{fold}}(X) + \delta W_p(X)e^{i\omega T}$ and $\tau = \tau_{\text{fold}} + \delta \tau_p e^{i\omega T}$ in the original beam equations, after considering terms of $O(\delta)$ and setting $\omega = 0$. We note these modes are also referred to as 'slow' modes (Rega & Troger, 2005)

Recall from our earlier discussion in §3.3 that there is a single eigenvalue that equals zero at the fold bifurcation. The homogeneous problem in $L(\cdot, \cdot)$ therefore has a one-dimensional solution space, spanned by the pair (W_p, τ_p) satisfying

$$L(W_p, \tau_p) = 0, \quad \mathcal{S}\tau_p = \int_0^1 \frac{\mathrm{d}W_{\text{fold}}}{\mathrm{d}X} \frac{\mathrm{d}W_p}{\mathrm{d}X} \, \mathrm{d}X,$$

$$W_p(0) = W_p'(0) = W_p(1) = W_p'(1) = 0, \quad \int_0^1 W_p^2 \, \mathrm{d}X = 1. \tag{3.15}$$

(The final equation here is a normalisation condition required to uniquely specify W_p, since the other equations are linear and homogeneous in (W_p, τ_p)). While this seems to over-determine the eigenfunction W_p (notice that $L(\cdot, \cdot)$ is fourth order and τ_p is unknown, but we have six constraints), we can be confident we are guaranteed a solution when W_{fold} is specifically the equilibrium shape evaluated at the fold.

From the above discussion, we deduce that the solution for $(\tilde{W}_0, \tilde{\tau}_0)$ must be a multiple of the pair (W_p, τ_p):

$$(\tilde{W}_0, \tilde{\tau}_0) = A(T)(W_p, \tau_p),$$

for some variable $A(T)$. The variable $A(T)$ plays a key role in the pull-in dynamics: re-arranging the original series expansion in (3.8) shows that

$$A(T) = \frac{\tilde{W}_0(X, T)}{W_p(X)} \sim \frac{W(X, T) - W_{\text{fold}}(X)}{W_p(X)}, \tag{3.16}$$

so that $A(T)$ characterises how the beam evolves away from the pull-in displacement during the bottleneck. Equation (3.16) also shows how we have performed a SDOF-type approximation: the solution is projected onto the neutrally-stable eigenfunction W_p associated with the loss of stability. The behaviour on this eigenspace is what limits the dynamics and hence the duration of the bottleneck: as all other eigenfunctions are linearly stable, the component of the solution in these directions decays exponentially fast.

We have arrived at this solution by assuming that $\epsilon \ll |\tilde{W}_0| \ll 1$ and $\epsilon \ll |\tilde{\tau}_0| \ll 1$. It appears that this leading-order part does not directly 'feel' the perturbation ϵ — how,

then, does the system know that it is beyond the fold and has to pull-in? Notice that we have not yet determined the amplitude $A(T)$. As with other problems in elasticity, such as Euler buckling of a straight beam (Howell *et al.*, 2009), we expect to determine $A(T)$ using a solvability condition on a higher order problem. It is here that the dependence on ϵ enters.

First order

To obtain the first-order problem, we substitute the expansions (3.14) into (3.10) and neglect higher-order terms in favour of those involving the leading-order terms $(\tilde{W}_0, \tilde{\tau}_0)$. The result is the same operator $L(\cdot, \cdot)$ as in the leading-order problem, though now applied to $(\tilde{W}_1, \tilde{\tau}_1)$, together with an inhomogeneous right-hand side forced by the leading-order terms. To obtain dynamics at leading order that aren't trivial, i.e. $A(T) \neq$ constant, it is also necessary to include both the time derivative and $O(\epsilon)$ terms at this order. Substituting $(\tilde{W}_0, \tilde{\tau}_0) = A(T)(W_p, \tau_p)$ then gives

$$L(\tilde{W}_1, \tilde{\tau}_1) = -W_p \frac{\mathrm{d}A}{\mathrm{d}T} + \frac{\lambda_{\mathrm{fold}}}{(1 - W_{\mathrm{fold}})^2}\epsilon + \left[\tau_p \frac{\mathrm{d}^2 W_p}{\mathrm{d}X^2} + \frac{3\lambda_{\mathrm{fold}}}{(1 - W_{\mathrm{fold}})^4}W_p^2\right]A^2. \qquad (3.17)$$

(Assumption (ii) above guarantees that the neglected terms of $O(\epsilon\tilde{W}_0, \tilde{W}_0^3)$ in (3.9) are small compared to the terms retained here.) Similarly, the Hooke's law constraint (3.12) at first order can be written as

$$\mathcal{S}\tilde{\tau}_1 - \int_0^1 \frac{\mathrm{d}W_{\mathrm{fold}}}{\mathrm{d}X}\frac{\partial \tilde{W}_1}{\partial X} \, \mathrm{d}X = \frac{A^2}{2}\int_0^1 \left(\frac{\mathrm{d}W_p}{\mathrm{d}X}\right)^2 \, \mathrm{d}X,$$

while the clamped boundary conditions (3.13) remain unchanged in terms of $\tilde{W}_1$.

The first-order problem is of the form $L\mathbf{y} = f$, where $\mathbf{y} \equiv (\tilde{W}_1, \tilde{\tau}_1)$, with linear boundary conditions/constraints in the components of $\mathbf{y}$. Because the homogeneous problem $L\mathbf{y} = 0$ has the non-trivial solution (W_p, τ_p), the Fredholm Alternative Theorem (Keener, 1988) states that solutions to the inhomogeneous problem can only exist for a certain function f (specifically we need $f \in \mathrm{Im}\, L$). This yields a solvability condition that takes the form of an ODE for $A(T)$. We formulate this condition in the usual way: we multiply (3.17) by a solution of the homogeneous adjoint problem, integrate over the domain, and use integration by parts to shift the operator onto the adjoint solution. Here, the operator $L(\cdot, \cdot)$ is self-adjoint (it contains only even-order derivatives), and so a solution of the homogeneous adjoint problem is simply (W_p, τ_p). Performing the above steps in (3.17) and simplifying using $L(W_p, \tau_p) = 0$, the clamped boundary conditions and Hooke's law

constraints satisfied by $\tilde{W}_1$, W_p, W_{fold}, and the normalisation $\int_0^1 W_p^2 \, dX = 1$, we arrive at

$$\frac{dA}{dT} = c_1 \epsilon + c_2 A^2, \tag{3.18}$$

where

$$c_1 = \lambda_{\text{fold}} \int_0^1 \frac{W_p}{(1 - W_{\text{fold}})^2} \, dX,$$

$$c_2 = 3\lambda_{\text{fold}} \int_0^1 \frac{W_p^3}{(1 - W_{\text{fold}})^4} \, dX - \frac{3}{2\mathcal{S}} \left[\int_0^1 \frac{dW_{\text{fold}}}{dX} \frac{dW_p}{dX} dX \right] \left[\int_0^1 \left(\frac{dW_p}{dX} \right)^2 dX \right].$$

$$\tag{3.19}$$

We have therefore reduced the leading-order dynamics in the bottleneck to the normal form for a saddle-node bifurcation (up to numerical constants). This represents a great simplification: the dynamic beam equation we started with — a PDE in space and time — has been reduced to a single family of ODEs parameterised by ϵ. Note that if we had not included the time derivative and the $O(\epsilon)$ term in (3.17), but left these to a higher-order problem, we would have obtained trivial dynamics at this stage with (3.18) instead giving $A = 0$. We also note that ϵ can be scaled out of the normal form by setting $A = \epsilon^{1/2}\mathcal{A}$ and $T = \epsilon^{-1/2}\mathcal{T}$. Retracing our steps above, this implies that the leading-order and first-order problems are obtained at $O(\epsilon^{1/2})$ and $O(\epsilon)$ respectively. With much less effort, we could have obtained the same equations by simply posing a regular expansion of the solution in powers of $\epsilon^{1/2}$. This is essentially the approach taken by Aranson *et al.* (2000) in their analysis of the Swift-Hohenberg equation (a PDE that describes the dynamics of localised structures just beyond the threshold of a pattern forming instability, which also corresponds to a saddle-node bifurcation). Our analysis here explains why this is the correct expansion sequence to use.

The normal form (3.18) also resembles the equation we derived in our analysis of the parallel-plate capacitor — we identify A with the change in the lumped displacement away from the pull-in displacement. This provides further evidence that (3.18) is generic for the dynamics of pull-in in overdamped devices. We see that the precise form of the boundary conditions applied to the microbeam enters only through the constants c_1 and c_2 (as the boundary conditions determine the eigenfunction W_p and fold shape W_{fold}). For each stretchability $\mathcal{S}$ and residual tension τ_0, we evaluate these by solving the neutral stability problem (3.15) numerically (using `bvp4c`) and using quadrature to evaluate the integrals appearing in c_1 and c_2.

Solution for $A(T)$

The solution of (3.18) is

$$A = \sqrt{\frac{c_1\epsilon}{c_2}} \tan\left[\sqrt{c_1 c_2 \epsilon}(T - T_0)\right], \tag{3.20}$$

for some constant T_0. At this stage, we can check when our original assumption (ii) holds, i.e. when the leading-order solution satisfies $\epsilon \ll |\tilde{W}_0| \ll 1$ and $\epsilon \ll |\tilde{\tau}_0| \ll 1$. From the expression $\tilde{W} \sim \tilde{W}_0 = W_p(X)A(T)$, this requires $\epsilon \ll |A| \ll 1$ (since W_p is $O(1)$). However, further analysis (given in Appendix 3.C) shows that the solution (3.20) also applies when $A = O(\epsilon)$. We therefore only require $|A| \ll 1$, i.e.

$$\left|\tan\left[\sqrt{c_1 c_2 \epsilon}(T - T_0)\right]\right| \ll \epsilon^{-1/2}.$$

This breaks down when the tan function is very large; the expansion $\tan x \sim \pm(\pi/2 \mp x)^{-1}$ as $x \to \pm\pi/2$ implies that this occurs when

$$T - T_0 \sim \pm\frac{\pi}{2\sqrt{c_1 c_2 \epsilon}}.$$

At this point, the amplitude A reaches $O(1)$ and our asymptotic analysis breaks down. Because A is growing rapidly by this stage (according to the tan function), the beam is no longer in the bottleneck phase. The minus sign here therefore corresponds to initially entering the bottleneck, while the plus sign corresponds to exiting the bottleneck towards pull-in. The duration of the bottleneck is thus

$$T_{\text{bot}} \sim \frac{\pi}{\sqrt{c_1 c_2 \epsilon}}.$$

(This validates our earlier assumption (i) that the bottleneck timescale satisfies $T \gg 1$ when $\epsilon \ll 1$.) The trajectories shown in figure 3.3 suggest that the bottleneck dominates all other timescales in the problem; this includes transients around $T = 0$ and just before contact where inertia is important. The dimensionless pull-in time, T_{PI}, to leading order is then the bottleneck duration,

$$T_{\text{PI}} \sim \frac{\pi}{\sqrt{c_1 c_2 \epsilon}}. \tag{3.21}$$

Because the solution for A is antisymmetric about T_0, it also follows that T_0 is simply half of the bottleneck duration: $T_0 \sim \pi/(2\sqrt{c_1 c_2 \epsilon})$. The solution (3.20) can then be written as

$$A \sim \sqrt{\frac{c_1\epsilon}{c_2}} \tan\left[\sqrt{c_1 c_2 \epsilon}\, T - \frac{\pi}{2}\right].$$

Writing this back in terms of the dimensionless displacement W (see (3.16)), we therefore have

$$W(X,T) \sim W_{\text{fold}}(X) + \sqrt{\frac{c_1\epsilon}{c_2}} W_p(X) \tan\left[\sqrt{c_1 c_2 \epsilon}\, T - \frac{\pi}{2}\right]. \tag{3.22}$$

3.4.3 Comparison with numerical results

To compare our predictions to direct numerical solutions, we consider the case $\mathcal{S} = 10^{-2}$ and zero residual tension, $\tau_0 = 0$. We compute

$$\lambda_{\text{fold}} \approx 174.0343, \quad W_{\text{fold}}(1/2) \approx 0.6036, \quad W_p(1/2) \approx 1.571, \quad c_1 \approx 601.2, \quad c_2 \approx 9985. \tag{3.23}$$

Using these values, for a specified ϵ we determine the midpoint displacement in the bottleneck using (3.22). The predicted behaviour is superimposed (as black dotted curves) onto numerical trajectories in figures 3.3a–b. We see that for $\epsilon \lesssim 10^{-3}$ the agreement is excellent during the bottleneck phase, i.e. while $W(1/2, T)$ remains close to $W_{\text{fold}}(1/2) \approx 0.6036$; outside of this interval, the agreement breaks down as the bottleneck analysis is no longer asymptotically valid. In particular, very close to $T = 0$ and $T = T_{\text{PI}}$, the asymptotic predictions become unbounded and diverge from the numerics.

In figure 3.5a we compare the simulated pull-in times to the asymptotic prediction (3.21), evaluated using the above values of c_1 and c_2. The asymptotic prediction provides an excellent approximation provided $Q \lesssim 10^{-2}$ and $\epsilon \lesssim 1$, with the numerics clearly following the predicted $\epsilon^{-1/2}$ scaling law. The accuracy of the asymptotics is remarkable: even though the result (3.21) is based on our earlier assumption that $T_{\text{PI}} \gg 1$, the computed times for $\epsilon \lesssim 1$ lie in the range $(10^{-3}, 10^{-1})$. For values $Q \gtrsim 10^{-1}$, inertial effects are important when the beam reaches the pull-in displacement, and a bottleneck phase evidently does not occur (figure 3.5a). Unfortunately, without an analytical solution of the dynamic beam equation (3.3), we are unable to predict a threshold value of Q below which bottleneck behaviour occurs, since this requires knowledge of the solution before it reaches the fold shape. We also note that the requirement $Q \lesssim 10^{-2}$ needed to obtain good agreement is more restrictive than what we saw in Chapter 2, where the asymptotic prediction was in good agreement for moderately small $Q \lesssim 1$. However, because the beam equation (3.3) is phrased per unit length (as opposed to the parallel-plate model), it is not meaningful to make a direct comparison between the quality factors.

When we fix $\epsilon \lesssim 10^{-2}$, the pull-in time is a non-monotonic function of Q (figure 3.5a): pull-in occurs more quickly when $Q = 10^{-1}$ (green circles) compared to $Q = 10^{-2}$ (red diamonds), but is slower when $Q = 1$ (magenta triangles). This feature is illustrated more clearly in figure 3.5b, which shows a surface plot of the computed pull-in times as
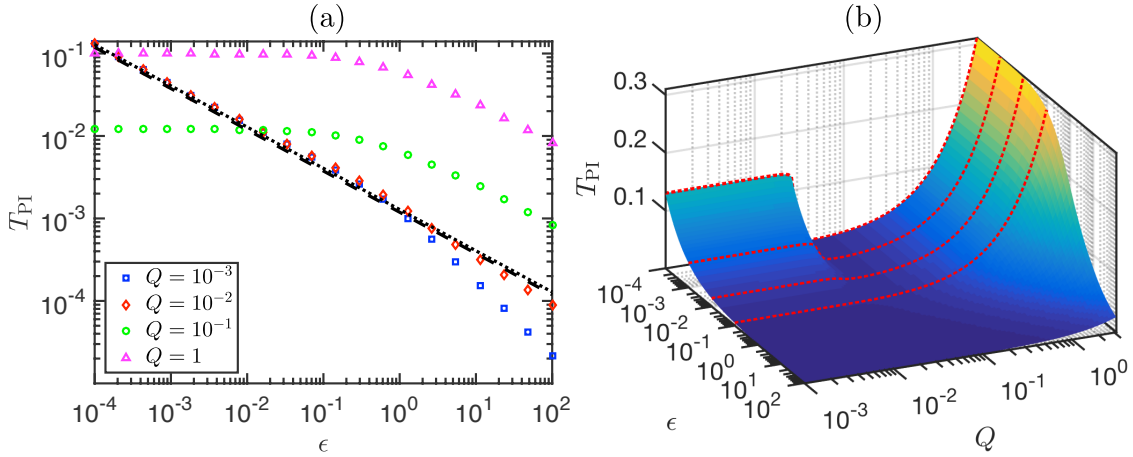
Figure 3.5: *Pull-in times at voltages close to the pull-in transition ($\mathcal{S} = 10^{-2}$, $\tau_0 = 0$, $N = 100$). (a) Numerical results for fixed Q and variable ϵ (symbols; see legend). Also shown is the asymptotic prediction* (3.21) *from the bottleneck analysis (black dotted line), and, for later comparison, the prediction* (3.34) *from the SDOF approximation (black dashed line) which is almost indistinguishable. (b) Surface plot of the numerical pull-in times. Slices through the surface (red dotted curves) are shown at $\epsilon \in \left\{ 10^{-4}, 10^{-3}, 10^{-2}, 10^{-1} \right\}$. (Reprinted from Gomez* et al. *(2018c), DOI: https://doi.org/10.1088/1361-6439/aad72f. Copyright © IOP Publishing. Reproduced with permission. All rights reserved.)*

a function of ϵ and Q. In particular, when $\epsilon \lesssim 10^{-2}$ a minimum pull-in time is obtained when $Q \approx 0.04$. This minimum corresponds to a delicate balance between beam inertia and critical slowing down: inertia is large enough to prevent much slowing down in a bottleneck, but still small enough for the beam to be rapidly accelerated from its rest position. We observed very similar behaviour for a parallel-plate capacitor: compare figure 3.5 to figure 2.7 in Chapter 2.

To validate our numerics, we compare our results to numerical solutions reported by Younis *et al.* (2003), who solve the dynamic beam equation (3.3) subject to (3.5)–(3.7) using a reduced-order model constructed by a Galerkin procedure (with the undamped eigenfunctions about the flat beam as basis functions). The parameter values in their study are

$$d_0 = 2.3 \ \mu\mathrm{m}, \quad L = 610 \ \mu\mathrm{m}, \quad h = 2.015 \ \mu\mathrm{m}, \quad b = 40 \ \mu\mathrm{m}, \quad E = 149 \ \mathrm{GPa},$$

$$\rho_s = 2.33 \ \mathrm{g \ cm^{-3}}, \quad \frac{P_0}{bh} = -3.7 \ \mathrm{MPa}, \quad V_{\mathrm{SPI}} = 8.76 \ \mathrm{V}, \quad \frac{\eta}{\sqrt{\rho_s bhB/L^4}} = Q^{-1} = 260,$$

which correspond to

$$[t] \approx 20.80 \ \mathrm{ms}, \quad \mathcal{S} \approx 0.06396, \quad \tau_0 \approx -27.31, \quad Q \approx 0.003846.$$

We have extracted the pull-in times reported by Younis *et al.* (2003), as a function of the applied voltage V, using the WebPlotDigitizer (arohatgi.info/WebPlotDigitizer). We
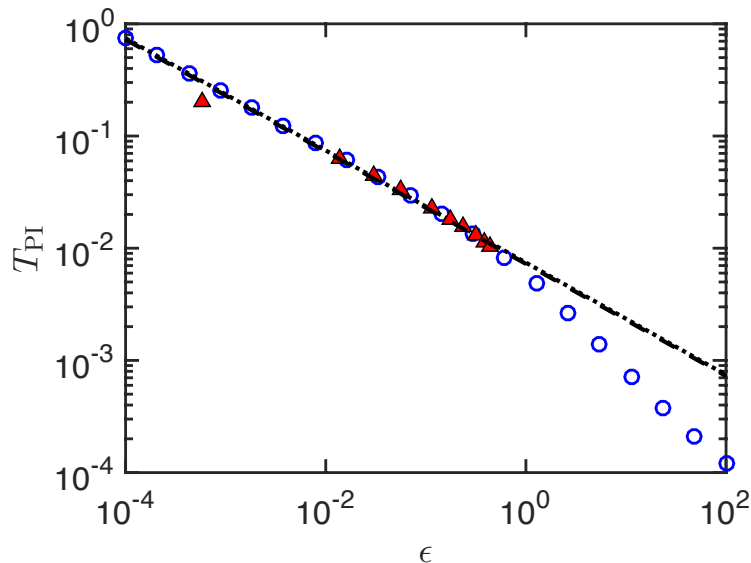
Figure 3.6: *Pull-in times simulated by Younis* et al. *(2003) using a reduced-order model (red triangles), and here using the method of lines with $N = 100$ grid points (blue circles) ($\mathcal{S} \approx 0.06396$, $\tau_0 \approx -27.31$, $Q \approx 0.003846$). Also shown is the asymptotic prediction (3.21) from the bottleneck analysis (black dotted line), and, for later comparison, the prediction (3.34) from the SDOF approximation (black dashed line). (Reprinted from Gomez* et al. *(2018c), DOI: https://doi.org/10.1088/1361-6439/aad72f. Copyright © IOP Publishing. Reproduced with permission. All rights reserved.)*

then use the reported pull-in voltage V_{SPI} to determine the corresponding values of $\epsilon = (V/V_{\mathrm{SPI}})^2 - 1$, and non-dimensionalise the pull-in times using the overdamped timescale $[t]$. The results are in excellent agreement with our numerical simulations; see figure 3.6. (The discrepancy at the smallest value of ϵ is likely due to the error in extracting the point graphically using WebPlotDigitizer, or a possible rounding error in the reported pull-in voltage; either introduces a slight shift in the computed values of ϵ, which is exaggerated for small values on log–log axes.) For the above parameter values we also compute

$$\lambda_{\mathrm{fold}} \approx 38.0173, \quad c_1 \approx 111.5, \quad c_2 \approx 1601. \tag{3.24}$$

The predicted pull-in time (3.21) is also plotted in figure 3.6 (black dotted line) and fits well the numerical data without any adjustable parameters.

3.4.4 Comparison with other data

We have shown that near the static pull-in transition, the dimensional pull-in time is

$$t_{\mathrm{PI}} \sim \frac{L^4 \eta}{B} \frac{\pi}{\sqrt{c_1 c_2 \epsilon}} \quad \text{where} \quad \epsilon = \left(\frac{V}{V_{\mathrm{SPI}}}\right)^2 - 1. \tag{3.25}$$
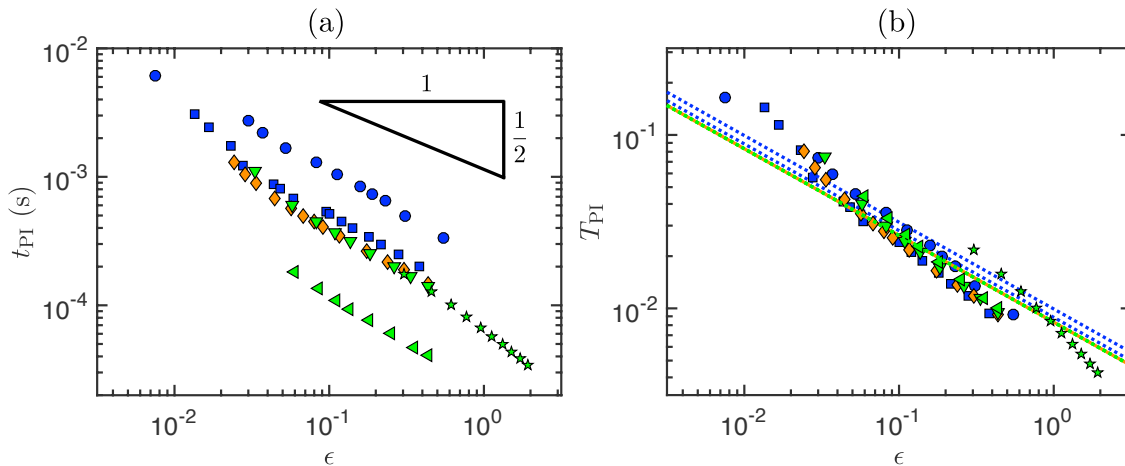
Figure 3.7: *(a) Experimental and numerical pull-in times of overdamped microbeams reported in the literature, plotted as a function of the normalised voltage difference ϵ. For a legend and the parameter values used in each data set, see table 3.1. (b) The data from (a), made dimensionless using the overdamped timescale $[t] = L^4\eta/B$; here η is fitted to match the values with the asymptotic prediction (3.25) (dotted lines). (Reprinted from Gomez et al. (2018c), DOI: https://doi.org/10.1088/1361-6439/aad72f. Copyright © IOP Publishing. Reproduced with permission. All rights reserved.)*

This result is valid for $0 < \epsilon \ll 1$ and $Q \ll 1$. We note that the beam length L and bending stiffness B are quantities that are measurable in experiments. However, as discussed at the start of §3.2, the damping coefficient η is a lumped constant that parameterises the properties of the squeeze film, specifically during the bottleneck phase. We now show that this damping model, despite its simplicity, is able to approximate well experiments and numerical simulations of microbeams that incorporate compressible squeeze film damping.

We consider experiments performed by Gupta *et al.* (1996) in air at atmospheric pressure. As in our model, the beams have clamped ends and are subject to step DC voltages. We also consider numerical simulations that model these experiments, which couple the dynamic beam equation to the compressible Reynolds equation in the squeeze film. The parameter values used in each study are summarised in table 3.1. We have separated the data into rows so that within each data set only the actuation voltage changes: the properties of the beam and the squeeze film do not vary. We also report any additional effects that are incorporated in the simulations. The dimensional pull-in times are plotted as a function of $\epsilon = (V/V_{\mathrm{SPI}})^2 - 1$ in figure 3.7a. Here symbols are used to indicate different data sets, and colours are used to distinguish references, as specified by the 'Legend' column in table 3.1. In all cases the slowing down near the pull-in transition approximately obeys an $\epsilon^{-1/2}$ scaling law.

We make the pull-in times dimensionless using the following procedure. For each data set, we calculate the stretchability $\mathcal{S}$ and residual tension τ_0. By solving the corresponding

Table 3.1: *Summary of data for the pull-in time of microbeams reported in the literature (reprinted from Gomez et al. (2018c), DOI: https://doi.org/10.1088/1361-6439/aad72f. Copyright © IOP Publishing. Reproduced with permission. All rights reserved).*

Reference	Data type	d_0 (μm)	L (μm)	h (μm)	b (μm)	E (GPa)	V_{SPI} (V)	ρ_s (g cm^{-3})	P_0/bh (MPa)	Model	Fitted η (Pa s)	Predicted η (Pa s)	Legend
Gupta et al. (1996)	Experiment	2.07	610	2.12	40	164	8.76	2.2	-3.5	N/A		1.10	■
Gupta et al. (1996)	Experiment	2.07	710	2.12	40	164	5.54	2.2	-3.5	N/A	0.754	1.48	
Hung & Senturia (1999)	Simulation	2.3	610	2.2	40	149	8.76	2.33	-3.7	BE, CC, CSQFD, SBC	0.613	0.908	●
Missoffe et al. (2008)	Simulation	2.3	610	2.2	40	149	8.76	2.33	-3.7	BE, CC, CSQFD, 1.013 bar‡, SBC	0.569	0.908	◆
Missoffe et al. (2008)	Simulation	2.3	610	2.2	40	149	8.76	2.33	-3.7	BE, CC, CSQFD, 0.1013 bar‡, SBC	0.156	0.908	◀
Missoffe et al. (2008)	Simulation	2.3	610	2.2	40	149	8.76	2.33	-3.7	BE, CC, CSQFD, 0.1013 bar‡, SBC	0.536	0.908	▲
Missoffe et al. (2008)	Simulation	2.3	610	2.2	70	149	8.76	2.33	-3.7	BE, CC, CSQFD, 0.1013 bar‡, SBC	0.802	4.87	★

BE, dynamic beam equation; CC, clamped-clamped boundary conditions; CSQFD, compressible squeeze film damping (Reynolds equation); SBC, corrections due to slip boundary conditions (rarefaction effects); N/A, not applicable
‡Ambient pressure

neutral stability problem (3.15) at the saddle-node bifurcation, we numerically compute the dimensionless constants c_1 and c_2. We then compare the dimensional pull-in times with the prediction (3.25), and determine η using a least-squares fit. The resulting pull-in times, made dimensionless using the overdamped timescale $[t] = L^4 \eta / B$, are shown in figure 3.7b. In all cases we obtain good agreement with the dimensionless prediction (3.21) (dotted lines). Moreover, because the values of $\mathcal{S}$ and τ_0 are so similar between the data sets, the non-dimensionalisation also collapses the data well.

We note that this fitting is very similar to that performed in Chapter 2, when we collapsed a large range of data by fitting the overdamped timescale $[t]$ (recall figure 2.9). However, the approach here has the advantage that the parameters of the beam are explicitly accounted for in the timescale $[t]$ and constants c_1 and c_2. Hence, once the damping coefficient has been fitted for one data set, it is possible to use equation (3.25) to make further predictions if the parameters of the beam then change. For example, if the residual tension is varied, it is only necessary to compute the updated values of c_1 and c_2.

We also check that the fitted values of η are realistic by comparing to an approximate analytical solution. Because the beam is shallow, when viewed on the length scale of the squeeze film, it approximately acts as an infinitely long and flat rectangular plate that moves in the perpendicular direction only. The incompressible Reynolds equation may be solved approximately in this geometry (Krylov & Maimon, 2004) to give the damping coefficient $\eta \approx \mu b^3 / d^3$, where μ is the air viscosity and d is the local gap width. For the microbeam considered here, the dimensionless displacement during the bottleneck phase is $W \approx W_{\text{fold}}$. In dimensional terms, the gap width is therefore $d_0[1 - W_{\text{fold}}(X)]$, giving the damping coefficient

$$\eta(X) \approx \frac{\mu b^3}{d_0^3 [1 - W_{\text{fold}}(X)]^3}.$$

This varies along the length of the beam so we cannot compare it directly to our fitted values. As the minimum gap width is attained at $X = 1/2$ (see the shapes in figure 3.4), an upper bound on the damping coefficient is

$$\eta \lesssim \frac{\mu b^3}{d_0^3 [1 - W_{\text{fold}}(1/2)]^3}. \tag{3.26}$$

(Averaging $\eta(X)$ over the beam length instead does not give a useful estimate.) In table 3.1 we compare this prediction to the values obtained by fitting the pull-in times (for all data sets the air viscosity $\mu = 18.2~\mu\text{Pa s}$). The values are of comparable size for all data sets, with (3.26) indeed providing an upper bound. The fitting here is therefore consistent with the damping being dominated by viscous dissipation rather than air compressibility. The discrepancy between the values may also be due to additional effects present in the experiments and numerical simulations, which are not captured by the expression (3.26).

These include finite-length effects (i.e. venting conditions at the clamped boundaries) and rarefaction effects. (This explains why the discrepancy is largest for the data of Missoffe *et al.*, 2008, at reduced ambient pressure 0.1013 bar, i.e. the final two rows in table 3.1; here we expect rarefaction effects to be more significant.) In experiments, material damping may also be present. Finally, we also note that with the fitted values of η, the corresponding quality factors Q are all small compared to unity, consistent with our assumption that the microbeams are overdamped.

3.5 Single-mode approximation

In this final section, we consider the error in the pull-in time calculated using a standard SDOF approximation. We assume *a priori* that the displacement can be written in the separable form

$$W(X, T) = U(T)\Phi(X), \tag{3.27}$$

where $U(T)$ is an unknown amplitude and $\Phi(X)$ is a known spatial function. We focus on the commonly used choice of $\Phi(X)$ as the first eigenfunction about the flat beam, i.e. the fundamental vibrational mode when the applied voltage is zero; this is computed in Appendix 3.D. In this way, equation (3.27) may be interpreted as keeping only the first term in a standard Galerkin expansion that uses these eigenfunctions as basis functions (Younis *et al.*, 2003; Krylov, 2007; Joglekar & Pawaskar, 2011).

We insert the separated ansatz (3.27) into the dynamic beam equation (3.3) to obtain

$$\Phi\left(Q^2\frac{\mathrm{d}^2U}{\mathrm{d}T^2} + \frac{\mathrm{d}U}{\mathrm{d}T}\right) + \left(\frac{\mathrm{d}^4\Phi}{\mathrm{d}X^4} - \tau\frac{\mathrm{d}^2\Phi}{\mathrm{d}X^2}\right)U = \frac{\lambda}{(1 - \Phi U)^2}. \tag{3.28}$$

The Hooke's law constraint (3.5) becomes

$$\tau = \tau_0 + \frac{U^2}{2\mathcal{S}}\int_0^1\left(\frac{\mathrm{d}\Phi}{\mathrm{d}X}\right)^2\mathrm{d}X.$$

Combining this with the ODE satisfied by $\Phi(X)$ (equation (3.44) in Appendix 3.D), the spatial derivatives appearing in the beam equation (3.28) can be written as

$$\frac{\mathrm{d}^4\Phi}{\mathrm{d}X^4} - \tau\frac{\mathrm{d}^2\Phi}{\mathrm{d}X^2} = \Omega^2\Phi - \frac{U^2}{2\mathcal{S}}\frac{\mathrm{d}^2\Phi}{\mathrm{d}X^2}\int_0^1\left(\frac{\mathrm{d}\Phi}{\mathrm{d}X}\right)^2\mathrm{d}X,$$

where Ω is related to the natural frequency of the beam. Multiplying (3.28) by Φ and integrating from $X = 0$ to $X = 1$ (simplifying using integration by parts and the boundary

conditions/normalisation satisfied by Φ; see Appendix 3.D), we obtain an ODE for U:

$$Q^2 \frac{\mathrm{d}^2 U}{\mathrm{d}T^2} + \frac{\mathrm{d}U}{\mathrm{d}T} + \Omega^2 U + \frac{1}{2\mathcal{S}} \left[\int_0^1 \left(\frac{\mathrm{d}\Phi}{\mathrm{d}X} \right)^2 \, \mathrm{d}X \right]^2 U^3 = \lambda \int_0^1 \frac{\Phi}{(1 - \Phi U)^2} \, \mathrm{d}X. \qquad (3.29)$$

It is not clear how to write the integral on the right-hand side as a simple function of U. While this could be avoided by multiplying equation (3.28) by $(1 - \Phi U)^2$ before integrating, the form here is more convenient and makes the physical nature of each term apparent. In particular, the linear term on the left-hand side represents the effective spring force due to the bending stiffness of the beam, while the cubic correction represents additional stiffening due to stretching (known as strain-stiffening).

3.5.1 Steady solutions

Steady solutions of (3.29) satisfy

$$\lambda = \frac{\Omega^2 U + \left[\int_0^1 (\mathrm{d}\Phi/\mathrm{d}X)^2 \, \mathrm{d}X \right]^2 U^3/(2\mathcal{S})}{\int_0^1 \Phi (1 - \Phi U)^{-2} \, \mathrm{d}X}. \qquad (3.30)$$

For given $\mathcal{S}$ and τ_0, the above relation allows us to compute the corresponding values of λ as U varies (using quadrature to evaluate the integrals). At each stage, the midpoint displacement is given in terms of U by

$$W(1/2) = \Phi(1/2)U.$$

Response diagrams of $W(1/2)$ as a function of λ obtained in this way are superimposed (as black dashed curves) on figures 3.2a–b. These show that the SDOF method provides a remarkably good approximation of the numerically computed bifurcation diagrams. The disagreement is largest in the neighbourhood of the fold point, where the solution becomes highly sensitive to changes in λ; similar behaviour has been reported by Younis *et al.* (2003) and Krylov *et al.* (2008).

We write $\lambda_{\mathrm{fold}}^{\mathrm{SDOF}}$ for the value of λ at the fold, which corresponds to $U = U_{\mathrm{fold}}$ in this approximation; the SDOF superscript on λ is to distinguish its value to that obtained in §3.3, when we solved the full beam equation using `bvp4c`. We now obtain two identities that will be useful in the dynamic analysis. Because the fold point is a steady solution, we have from (3.30)

$$\lambda_{\mathrm{fold}}^{\mathrm{SDOF}} = \frac{\Omega^2 U_{\mathrm{fold}} + \left[\int_0^1 (\mathrm{d}\Phi/\mathrm{d}X)^2 \, \mathrm{d}X \right]^2 U_{\mathrm{fold}}^3/(2\mathcal{S})}{\int_0^1 \Phi (1 - \Phi U_{\mathrm{fold}})^{-2} \, \mathrm{d}X}. \qquad (3.31)$$

In addition, the fact that this is a fold gives that

$$\frac{\partial \lambda}{\partial U}\bigg|_{U=U_{\text{fold}},\ \lambda=\lambda_{\text{fold}}^{\text{SDOF}}} = 0,$$

which, using (3.31), can be simplified to

$$2\lambda_{\text{fold}}^{\text{SDOF}} \int_0^1 \frac{\Phi^2}{(1-\Phi U_{\text{fold}})^3}\ \mathrm{d}X = \Omega^2 + \frac{3U_{\text{fold}}^2}{2\mathcal{S}} \left[\int_0^1 \left(\frac{\mathrm{d}\Phi}{\mathrm{d}X} \right)^2 \mathrm{d}X \right]^2. \qquad (3.32)$$

3.5.2 Pull-in dynamics

Using the SDOF approximation, we would like to calculate the pull-in time when

$$\lambda = \lambda_{\text{fold}}^{\text{SDOF}}(1+\epsilon),$$

for $0 < \epsilon \ll 1$. From §3.4, we know that the dynamics are highly sensitive in this regime, with a small change in ϵ producing a large change in pull-in time. Because of the error between $\lambda_{\text{fold}}^{\text{SDOF}}$ and the 'true' bifurcation value λ_{fold} (i.e. from solving the full beam model without making a SDOF approximation), replacing $\lambda_{\text{fold}}^{\text{SDOF}}$ by λ_{fold} above will lead to large errors in the pull-in time: any difference in estimates of λ_{fold} changes the effective value of ϵ. (We also discuss this sensitivity in Appendix 3.B in the context of solving the PDE numerically.) A similar issue has been described by Joglekar & Pawaskar (2011) in their analysis of an underdamped microbeam, who found that the error in the SDOF approximation is very large at voltages near the dynamic pull-in voltage. We now show that it is possible to obtain excellent agreement when using a SDOF approach, provided one uses the bifurcation value $\lambda_{\text{fold}}^{\text{SDOF}}$, i.e. the value consistent with the SDOF equations.

When the solution is close to the pull-in displacement we have

$$U(T) = U_{\text{fold}} + \tilde{U}(T),$$

where $|\tilde{U}| \ll 1$. We expand the electrostatic force in (3.29) as

$$\lambda \int_0^1 \frac{\Phi}{(1-\Phi U)^2}\ \mathrm{d}X = \lambda_{\text{fold}}^{\text{SDOF}}(1+\epsilon)I_1 + 2\lambda_{\text{fold}}^{\text{SDOF}} I_2 \tilde{U} + 3\lambda_{\text{fold}}^{\text{SDOF}} I_3 \tilde{U}^2 + O(\epsilon\tilde{U}, \tilde{U}^3),$$

where we define

$$I_m(\Phi, U_{\text{fold}}) = \int_0^1 \frac{\Phi^m}{(1-\Phi U_{\text{fold}})^{m+1}}\ \mathrm{d}X.$$

We substitute into (3.29) and simplify using the identities (3.31)–(3.32). Neglecting the inertia term and terms of $O(\epsilon \tilde{U}, \tilde{U}^3)$, we obtain at leading order

$$\frac{\mathrm{d}\tilde{U}}{\mathrm{d}T} = d_1 \epsilon + d_2 \tilde{U}^2,$$

where

$$
\begin{aligned}
d_1 &= \lambda_{\mathrm{fold}}^{\mathrm{SDOF}} I_1, \\
d_2 &= 3\lambda_{\mathrm{fold}}^{\mathrm{SDOF}} I_3 - \frac{3U_{\mathrm{fold}}}{2\mathcal{S}} \left[\int_0^1 \left(\frac{\mathrm{d}\Phi}{\mathrm{d}X} \right)^2 \mathrm{d}X \right]^2.
\end{aligned}
$$

These equations are precisely equations (3.18)–(3.19), derived in the bottleneck analysis of the full PDE in §3.4, provided that we identify

$$A \to \tilde{U}, \quad (c_1, c_2) \to (d_1, d_2), \quad \lambda_{\mathrm{fold}} \to \lambda_{\mathrm{fold}}^{\mathrm{SDOF}}, \quad W_p \to \Phi, \quad W_{\mathrm{fold}} \to U_{\mathrm{fold}}\Phi. \qquad (3.33)$$

The pull-in time to leading order is then similarly found to be

$$T_{\mathrm{PI}} \sim \frac{\pi}{\sqrt{d_1 d_2 \epsilon}}, \qquad (3.34)$$

and the displacement in the bottleneck is

$$W(X, T) = U_{\mathrm{fold}}\Phi(X) + \sqrt{\frac{d_1 \epsilon}{d_2}} \Phi(X) \tan\left[\sqrt{d_1 d_2 \epsilon} \; T - \frac{\pi}{2} \right]. \qquad (3.35)$$

This analogy with our analysis of the PDE model may not be so unexpected. In §3.4 we first expanded the solution about the equilibrium shape at the fold, before performing a SDOF-like approximation (using the neutrally-stable eigenfunction W_p as a basis function). In this section we essentially performed these steps in the reverse order: we first used a SDOF approximation to reduce the beam equation to an ODE, and then expanded about the fold solution. It is perhaps not so surprising that these operations 'commute'. The analogy in (3.33) also allows us to deduce that the error in the second approach is governed by three quantities. These are (i) the error between λ_{fold} and $\lambda_{\mathrm{fold}}^{\mathrm{SDOF}}$; (ii) the error between W_p and the basis function Φ, here chosen as the eigenfunction about the flat beam; and (iii) the error between the fold shape W_{fold} and the approximation $U_{\mathrm{fold}}\Phi$. Together, these errors govern the difference between the constants (c_1, c_2) and (d_1, d_2) and hence the discrepancy in the predicted pull-in time and bottleneck displacement.

To quantify these errors, we again consider the case $\mathcal{S} = 10^{-2}$ and $\tau_0 = 0$. For the SDOF

system we calculate

$$\lambda_{\text{fold}}^{\text{SDOF}} \approx 179.9184, \quad U_{\text{fold}}\Phi(1/2) \approx 0.6123, \quad \Phi(1/2) \approx 1.588, \quad d_1 \approx 626.6, \quad d_2 \approx 11135.$$

These values agree well with the corresponding quantities obtained in §3.4; compare to equation (3.23). In figures 3.3a–b, we have superimposed the midpoint displacement predicted by equation (3.35) (as black dashed curves), which consistently under-predicts the duration of the bottleneck phase compared to the bottleneck analysis of the PDE model. Nevertheless, the SDOF approximation closely captures the dependence of the pull-in time on ϵ — the relative error in the pre-factor of $\epsilon^{-1/2}$ between the two approaches is around 7%. This is evident in figure 3.5a, where the predictions of the bottleneck analysis and SDOF approximation are almost indistinguishable.

A similar picture is seen for the parameter values used by Younis *et al.* (2003). We now calculate for the SDOF system

$$\lambda_{\text{fold}}^{\text{SDOF}} \approx 38.3153, \quad U_{\text{fold}}\Phi(1/2) \approx 0.5720, \quad \Phi(1/2) \approx 1.6165, \quad d_1 \approx 112.9, \quad d_2 \approx 1664,$$

which closely match the quantities (3.24) obtained in §3.4. Again, we find that the pre-factors are in very good agreement between the two approaches, with a relative error of around 3% in this case (figure 3.6).

3.6 Summary and discussion

In this chapter, we have analysed the pull-in dynamics of overdamped microbeams. Rather than using a one-dimensional parallel-plate model, we explicitly considered the beam geometry, modelled using the dynamic beam equation. Using direct numerical solutions, we demonstrated that at voltages just beyond the static pull-in transition, the dynamics slow down considerably in a bottleneck phase. This phase is similar to the metastable interval first described by Rocha *et al.* (2004*a*) for a parallel-plate actuator, which we analysed in detail in Chapter 2: the bottleneck depends sensitively on the applied voltage, it dominates the total time taken to pull-in, and occurs when the solution passes the static pull-in displacement.

We analysed the bottleneck dynamics using two approaches. In the first approach we worked with the dynamic beam equation directly. Because a linear stability analysis is not applicable (there is no unstable base state from which the system evolves), we used a perturbation method based on two small quantities: the proximity of the solution to the pull-in displacement, and the small time derivative resulting from the slow bottleneck

timescale. This allowed us to systematically reduce the leading-order dynamics to a simple amplitude equation — the normal form for a saddle-node bifurcation. As a result, the microbeam dynamics inherit the critical slowing down due to the 'ghost' of the saddle-node bifurcation and the displacement grows linearly rather than exponentially. We obtained a simple approximation to the total pull-in time:

$$ t_{\mathrm{PI}} \sim \frac{L^4 \eta}{B} \frac{\pi}{\sqrt{c_1 c_2 \epsilon}}, $$

where L is the beam length, η is the effective damping coefficient during the bottleneck phase, B is the bending stiffness, c_1 and c_2 are dimensionless constants, and ϵ is the normalised difference between the applied voltage and the pull-in voltage. To compute c_1 and c_2 requires some effort: it is necessary to solve for the equilibrium shape at the fold, $W_{\mathrm{fold}}(X)$ (e.g. using a continuation algorithm), as well as the neutrally-stable eigenfunction about the fold shape, $W_p(X)$. These problems depend on the beam stretchability, residual stress and the boundary conditions applied to the beam.

At its heart, this approach shows how the bottleneck dynamics are driven by the neutrally stable or 'slow' eigenfunction (the small-amplitude vibrational mode) associated with the loss of stability. Since its eigenvalue equals zero at the saddle-node bifurcation, this naturally leads to a separation of timescales that we were able to exploit in our asymptotic analysis. All other eigenfunctions are 'fast', associated with linearly stable modes of oscillation, so that trajectories in phase space quickly decay in these directions. In fact, this is a very general feature of dynamical systems near non-hyperbolic fixed points. The theory of centre manifold reduction is based on systematically representing or 'slaving' the fast modes by the slow modes. Generically, the result is a set of evolution equations for the amplitude of the slow modes, resembling a finite system of ODEs in time. For more details of the theory, see Wiggins (2003) (for finite-dimensional systems) or Carr (2012) (for infinite-dimensional systems). This theory could potentially be used to provide a more rigorous grounding for our perturbation approach.

In the second approach, we first applied a SDOF approximation, assuming that the solution can be written in the separable form $W(X, T) = U(T)\Phi(X)$. By reducing the dynamic beam equation to an ODE, we were able to analyse the behaviour near the pull-in transition in a similar way to Chapter 2. Comparing this approach to the bottleneck analysis of the PDE model revealed that three factors control the error of the SDOF approximation:

(i) The error in the computed pull-in voltage.

(ii) The error between the basis function $\Phi(X)$ and the neutrally-stable eigenfunction $W_p(X)$.

(iii) The error in the computed pull-in displacement.

We found that choosing $\Phi(X)$ to be the fundamental vibrational mode about the undeformed beam closely matches $W_p(X)$ (the same eigenfunction when evaluated at the pull-in voltage), so that the error (ii) is small. Moreover, it may be verified that $\Phi(X)$ is left-right symmetric about the beam midpoint $X = 1/2$. Because the pull-in displacement is also left-right symmetric, it turns out that the errors (i) and (iii) above are also small. As a consequence, we could obtain accurate predictions for the pull-in time with much less effort. This result is in direct contrast to previous studies, which conclude that the error in the SDOF approximation grows unacceptably large near pull-in (Joglekar & Pawaskar, 2011) – the apparent discrepancy is because our approach accounts for the shift in the pull-in voltage when using the SDOF system, and so is consistent with its bifurcation behaviour (recall the discussion at the start of §3.5.2). However, in other scenarios (e.g. different boundary conditions) it is possible that the errors (i)–(iii) could be large, meaning the SDOF approximation is no longer valid. In such cases W_p should instead be used as the basis function, provided that the error in the pull-in displacement is verified to be small.

Finally, we discuss the various assumptions we have made in our analysis. We assumed that the quality factor Q is small, so that inertial effects can be neglected. This is necessary to obtain bottleneck behaviour near the static pull-in transition. We focussed on the case of a clamped-clamped beam under step DC loads, though our analysis may be adapted to other boundary conditions and loading types. In addition, we neglected spatial variations in the damping coefficient, and used a lumped constant in our study. Because the bottleneck dominates the transient dynamics, and the beam geometry is roughly constant in the bottleneck, we found that this is sufficient to accurately predict the pull-in time — we were able to collapse data from experiments and simulations that incorporate compressible squeeze film damping (figure 3.7). Nevertheless, the framework we have presented here shows that it is the underlying bifurcation structure that governs the bottleneck dynamics, so that more realistic damping models could also be incorporated. This framework will also guide our analysis in the next chapter, when we consider the dynamics of snap-through in systems such as spherical caps and arches; unlike electrostatic pull-in, these systems snap-through in response to a change in geometrical confinement rather than an externally applied load.

Appendix 3.A Equilibrium behaviour for small voltages, $\lambda \ll 1$

In this appendix we determine the equilibrium shape in the limit of small voltages, $\lambda \ll 1$. Focussing on the solution in which the beam is nearly flat ($W \ll 1$) and the tension is close to the residual value ($\tau \approx \tau_0$), the steady version of the beam equation (3.3) at leading order becomes

$$\frac{\mathrm{d}^4W}{\mathrm{d}X^4} - \tau_0 \frac{\mathrm{d}^2W}{\mathrm{d}X^2} \sim \lambda.$$

The solution of this equation subject to the clamped boundary conditions (3.6) is

$$W \sim \begin{cases} \frac{\lambda}{2\tau_0^{3/2}} \left[\sqrt{\tau_0} X(1-X) + (\cosh X\sqrt{\tau_0} - 1) \coth \frac{\sqrt{\tau_0}}{2} - \sinh X\sqrt{\tau_0} \right] & \tau_0 > 0, \\ \frac{\lambda}{24} X^2 (1-X)^2 & \tau_0 = 0, \\ \frac{\lambda}{2(-\tau_0)^{3/2}} \left[\sqrt{-\tau_0} X(X-1) + (\cos X\sqrt{-\tau_0} - 1) \cot \frac{\sqrt{-\tau_0}}{2} + \sin X\sqrt{-\tau_0} \right] & \tau_0 < 0. \end{cases}$$

Setting $X = 1/2$, the corresponding midpoint displacement simplifies to

$$W(1/2) \sim \begin{cases} \frac{\lambda}{8\tau_0^{3/2}} \left(\sqrt{\tau_0} - 4\tanh \frac{\sqrt{\tau_0}}{4} \right) & \tau_0 > 0, \\ \frac{\lambda}{384} & \tau_0 = 0, \\ -\frac{\lambda}{8(-\tau_0)^{3/2}} \left(\sqrt{-\tau_0} - 4\tan \frac{\sqrt{-\tau_0}}{4} \right) & \tau_0 < 0. \end{cases}$$

These expressions compare well with numerical solutions of the original system; see figures 3.2a–b, where the asymptotic predictions are shown as black dotted lines. These provide a good approximation for $\lambda \lesssim 50$, well beyond the interval where they are strictly asymptotically valid.

The relationship between λ and the tension τ is found from the Hooke's law constraint (3.5), which gives

$$\mathcal{S}(\tau - \tau_0) \sim \begin{cases} \frac{\lambda^2 \mathrm{cosech}^2 \frac{\sqrt{\tau_0}}{2}}{48\tau_0^3} \left[-4(\tau_0 + 6) + (24 + \tau_0)\cosh\sqrt{\tau_0} - 9\sqrt{\tau_0}\sinh\sqrt{\tau_0} \right] & \tau_0 > 0, \\ \frac{\lambda^2}{60480} & \tau_0 = 0, \\ -\frac{\lambda^2 \mathrm{cosec}^2 \frac{\sqrt{-\tau_0}}{2}}{48\tau_0^3} \left[-4(\tau_0 + 6) + (24 + \tau_0)\cos\sqrt{-\tau_0} + 9\sqrt{-\tau_0}\sin\sqrt{-\tau_0} \right] & \tau_0 < 0. \end{cases}$$

Re-arranging to solve for λ, this provides an initial guess (valid for $\tau \approx \tau_0$) that can be used in our numerical continuation in τ.

Appendix 3.B Details of the numerical scheme

To solve the dynamic beam equation, we introduce a uniform mesh on the interval $[0, 1]$ with spacing $\Delta X = 1/N$, where $N \geq 2$ is an integer. We label the grid points as $X_i = i\Delta X$

$(i = 0, 1, 2, \ldots, N)$ and write W_i for the numerical approximation of W at the grid point X_i. We approximate the spatial derivatives appearing in the beam equation (3.3) and boundary conditions (3.6) using centered differences with second-order accuracy. To do this at all interior points in the mesh without losing accuracy, we introduce the ghost points X_{-1} and X_{N+1} (with associated displacement W_{-1} and W_{N+1}) outside of the interval $[0, 1]$. With this scheme, (3.3) becomes, for $i = 1, 2, \ldots, N-1$,

$$Q^2 \frac{\mathrm{d}^2 W_i}{\mathrm{d}T^2} + \frac{\mathrm{d}W_i}{\mathrm{d}T} + \frac{W_{i+2} - 4W_{i+1} + 6W_i - 4W_{i-1} + W_{i-2}}{\Delta X^4} - \tau \frac{W_{i+1} - 2W_i + W_{i-1}}{\Delta X^2} = \frac{\lambda}{(1 - W_i)^2}. \tag{3.36}$$

The clamped boundary conditions (3.6) are approximated by

$$W_0 = 0, \quad \frac{W_1 - W_{-1}}{2\Delta X} = 0, \quad W_N = 0, \quad \frac{W_{N+1} - W_{N-1}}{2\Delta X} = 0. \tag{3.37}$$

To approximate the integral appearing in the Hooke's law constraint (3.5), we use a centered difference to discretise the derivative and apply the trapezium rule for the quadrature. We obtain

$$
\begin{aligned}
\mathcal{S}(\tau - \tau_0) &= \frac{\Delta X}{4} \sum_{k=0}^{N-1} \left[\left(\frac{W_{k+2} - W_k}{2\Delta X} \right)^2 + \left(\frac{W_{k+1} - W_{k-1}}{2\Delta X} \right)^2 \right], \\
&= \frac{1}{8\Delta X} \sum_{k=1}^{N-1} (W_{k+1} - W_{k-1})^2,
\end{aligned} \tag{3.38}
$$

where in the second equality we have shifted the index of the first part of the sum and made use of the clamped boundary conditions above.

To write the scheme in matrix form, we introduce the column vectors of length $(N-1)$

$$\mathbf{W} = (W_1, W_2, \ldots, W_{N-1})^{\mathrm{T}}, \tag{3.39}$$

$$\mathbf{F} = \left(\frac{1}{(1 - W_1)^2}, \frac{1}{(1 - W_2)^2}, \ldots, \frac{1}{(1 - W_{N-1})^2} \right)^{\mathrm{T}}, \tag{3.40}$$

and the $(N-1) \times (N-1)$ matrices

$$\mathcal{A} = \frac{1}{\Delta X^4} \begin{pmatrix} 7 & -4 & 1 & & & & & \\ -4 & 6 & -4 & 1 & & & & \\ 1 & -4 & 6 & -4 & 1 & & & \\ & \ddots & \ddots & \ddots & \ddots & \ddots & & \\ & & 1 & -4 & 6 & -4 & 1 & \\ & & & 1 & -4 & 6 & -4 & \\ & & & & 1 & -4 & 7 & \end{pmatrix},$$

$$\mathcal{B} = \frac{1}{\Delta X^2} \begin{pmatrix} -2 & 1 & & & \\ 1 & -2 & 1 & & \\ & \ddots & \ddots & \ddots & \\ & & 1 & -2 & 1 \\ & & & 1 & -2 \end{pmatrix}, \quad \mathcal{C} = \frac{1}{2\Delta X} \begin{pmatrix} 0 & 1 & & & \\ -1 & 0 & 1 & & \\ & \ddots & \ddots & \ddots & \\ & & -1 & 0 & 1 \\ & & & -1 & 0 \end{pmatrix}.$$

The system of equations (3.36)–(3.37) is then equivalent to

$$Q^2 \frac{\mathrm{d}^2 \mathbf{W}}{\mathrm{d}T^2} + \frac{\mathrm{d}\mathbf{W}}{\mathrm{d}T} + (\mathcal{A} - \tau \mathcal{B}) \mathbf{W} = \lambda \mathbf{F}. \tag{3.41}$$

The Hooke's law constraint (3.38) can be written as

$$\mathcal{S}(\tau - \tau_0) = \frac{\Delta X}{2} \mathbf{W}^{\mathrm{T}} \mathcal{C}^{\mathrm{T}} \mathcal{C} \mathbf{W}. \tag{3.42}$$

Finally, we have the initial data

$$\mathbf{W}(0) = \dot{\mathbf{W}}(0) = \mathbf{0}.$$

These equations can then readily be written as a first-order system in $\mathbf{W}$ and $\dot{\mathbf{W}}$ needed for the MATLAB ODE solvers. We found that the integration can be achieved efficiently using the routine `ode23t`, when we exploit the sparsity pattern of the matrices $\mathcal{A}$, $\mathcal{B}$, $\mathcal{C}$ and provide the corresponding Jacobian matrix of the first-order system. The routine `ode23t` also employs a stiff solver to efficiently integrate the system when $Q \ll 1$ (here the equations are stiff due to transients around $T = 0$ and immediately before contact in which inertia cannot be neglected).

When we set $\lambda = \lambda_{\mathrm{fold}}(1 + \epsilon)$, we anticipate that the dynamics depend sensitively on the value of ϵ as $\epsilon \to 0$. An important point is that due to the error in our numerical scheme, there will also be an error in the bifurcation value λ_{fold}. If we use the value of λ_{fold} predicted by the solution of the 'continuous' problem (i.e. from solving the beam equation

using `bvp4c`) in our simulations, we therefore need to ensure that the relative error in λ_{fold} is much smaller than ϵ: this error acts as an 'extra' perturbation that shortens the pull-in time. For example, we find that taking $N = 600$ ensures a relative error that is typically $O(10^{-5})$, which is sufficient provided we restrict to $\epsilon \gtrsim 10^{-3}$. An alternative approach is to use the value of λ_{fold} predicted from the discretised system (see below), which is consistent with its bifurcation behaviour and so eliminates this sensitivity. This allows us to use fewer grid points, e.g. $N = 100$, to obtain quantitatively similar results with much less computing time. We use this latter approach for all simulations reported in this chapter.

3.B.1 Equilibrium solutions

The steady solutions of the discretised equations (3.41) satisfy

$$(\mathcal{A} - \tau \mathcal{B})\,\mathbf{W} = \lambda \mathbf{F},$$

together with (3.42). We solve these equations in MATLAB using the `fsolve` routine (error tolerances 10^{-10}), using a simple continuation algorithm to trace the bifurcation diagram and compute λ_{fold}. Similar to the way we solved the steady beam equation in §3.3, we control the tension τ and determine λ as part of the solution. To begin the continuation, we use the asymptotic solution when $\tau \approx \tau_0$ (Appendix 3.A), now evaluated on the mesh in our numerical scheme.

3.B.2 Convergence plots

We first check that the equilibrium solutions of the discretised system converge to the solution of the steady beam equation (obtained using `bvp4c`). We label the discretised solution obtained using N grid points by $\mathbf{W}_N$, and the solution obtained using `bvp4c` (evaluated on our numerical mesh) by $\mathbf{W}_\infty$. Figure 3.8a shows a typical plot of the relative error between $\mathbf{W}_N$ and $\mathbf{W}_\infty$, where we vary N while keeping all other parameters constant. This indicates that

$$\frac{||\mathbf{W}_N - \mathbf{W}_\infty||_2}{||\mathbf{W}_\infty||_2} = O(N^{-2}) \quad \text{as} \quad N \to \infty,$$

i.e. we obtain second-order accuracy in the convergence of our scheme.

We also verify that solutions of the unsteady discretised equations converge as N increases. Because we do not have an 'exact' solution of the dynamic problem, we consider
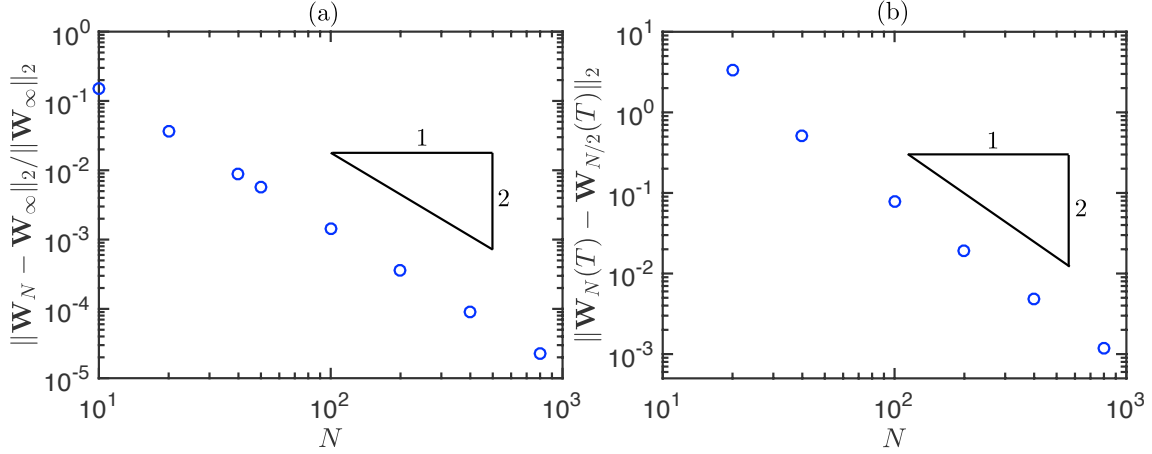
Figure 3.8: *(a) Relative error between the steady solution of the discretised system for N grid points, $\mathbf{W}_N$, and the solution $\mathbf{W}_\infty$ of the steady beam equation ($\lambda = 100$, $\mathcal{S} = 10^{-2}$, $\tau_0 = 0$). (b) Difference between successive solutions of the unsteady equations as N increases ($\lambda = 200$, $T = 3 \times 10^{-3}$, $Q = 10^{-2}$, $\mathcal{S} = 10^{-2}$, $\tau_0 = 0$).*

the difference between successive approximations, integrated up to a fixed time, as N increases. Writing $\mathbf{W}_N(T)$ for the numerical solution with N grid points evaluated at time T, a typical plot of the difference between $\mathbf{W}_N(T)$ and $\mathbf{W}_{N/2}(T)$ is shown in figure 3.8b (here λ is large enough to ensure pull-in occurs, and we have specified a time T before contact). This confirms that

$$||\mathbf{W}_N(T) - \mathbf{W}_{N/2}(T)||_2 = O(N^{-2}) \quad \text{as} \quad N \to \infty.$$

Appendix 3.C   Bottleneck analysis when $A = O(\epsilon)$

In this appendix we show that the solution (3.20) for the amplitude variable $A(T)$ also holds when $A = O(\epsilon)$; using the expansion $\tan x \sim x$ for $|x| \ll 1$, this corresponds to times $|T - T_0| = O(1)$. Because the leading-order solution in the bottleneck is $O(\epsilon)$, our original assumption (ii) (made at the start of §3.4.2) is no longer valid.

Returning to the beam equation (3.10), we see that the left-hand side no longer dominates when $(\tilde{W}_0, \tilde{\tau}_0) = O(\epsilon)$ and $|T - T_0| = O(1)$. We must now keep the time derivative and the $O(\epsilon)$ term on the right-hand side to obtain

$$L(\tilde{W}_0, \tilde{\tau}_0) = -\frac{\partial \tilde{W}_0}{\partial T} + \frac{\lambda_{\text{fold}}}{(1 - W_{\text{fold}})^2}\epsilon. \tag{3.43}$$

Because $|\tilde{W}_0| \ll 1$, the Hooke's law constraint (3.12) remains unchanged at leading order:

$$\mathcal{S}\tilde{\tau}_0 = \int_0^1 \frac{\mathrm{d}W_{\text{fold}}}{\mathrm{d}X} \frac{\partial \tilde{W}_0}{\partial X} \, \mathrm{d}X.$$

Again, we have an inhomogeneous problem and so the Fredholm Alternative Theorem applies. Integrating by parts (making use of the clamped boundary conditions and the Hooke's law constraints satisfied by W_p and $\tilde{W}_0$) shows that

$$\int_0^1 W_p L(\tilde{W}_0, \tilde{\tau}_0) \, \mathrm{d}X = 0.$$

(This follows more generally from the fact that the operator $L(\cdot, \cdot)$, defined in (3.11), is self-adjoint and the boundary conditions/constraints satisfied by (W_p, τ_p) and $(\tilde{W}_0, \tilde{\tau}_0)$ are all homogeneous.) Multiplying (3.43) by W_p and integrating over $(0, 1)$ then gives

$$0 = -\int_0^1 W_p \frac{\partial \tilde{W}_0}{\partial T} \, \mathrm{d}X + \epsilon \lambda_{\mathrm{fold}} \int_0^1 \frac{W_p}{(1 - W_{\mathrm{fold}})^2} \, \mathrm{d}X.$$

From the normalisation $\int_0^1 W_p^2 \, \mathrm{d}X = 1$ (recall equation (3.15)), it follows that $\tilde{W}_0 = A(T) W_p$ with

$$\frac{\mathrm{d}A}{\mathrm{d}T} = \epsilon \lambda_{\mathrm{fold}} \int_0^1 \frac{W_p}{(1 - W_{\mathrm{fold}})^2} \, \mathrm{d}X = c_1 \epsilon.$$

The solution is

$$A(T) = c_1 \epsilon (T - T_0),$$

where the constant of integration is chosen to match into the solution (3.20) when $A \gg \epsilon$. This solution is precisely (3.20) when we expand the tan function for small arguments. We deduce that (3.20) is asymptotically valid for all $|A| \ll 1$.

Appendix 3.D   Linear stability at zero voltage

In this appendix we determine the small-amplitude (flexural) vibrational modes about the flat beam when $\lambda = 0$, and the tension is close to the residual value ($\tau \approx \tau_0$). We set $W = \delta \Phi(X) e^{i\omega T}$ where $\delta \ll 1$ is a fixed quantity and ω is the (unknown) natural frequency. Inserting into the dynamic beam equation (3.3) and considering terms of $O(\delta)$, we obtain (assuming the real part of complex quantities)

$$\frac{\mathrm{d}^4 \Phi}{\mathrm{d}X^4} - \tau_0 \frac{\mathrm{d}^2 \Phi}{\mathrm{d}X^2} - \Omega^2 \Phi = 0, \tag{3.44}$$

where $\Omega^2 = Q^2 \omega^2 - i\omega$. In the absence of any damping, i.e. as $Q \to \infty$, we see that Ω is simply proportional to the natural frequency of the beam. The clamped boundary conditions (3.6) imply that

$$\Phi(0) = \Phi'(0) = \Phi(1) = \Phi'(1) = 0.$$

The solution to (3.44) satisfying the boundary conditions at $X = 0$ is (Neukirch *et al.*, 2012)

$$\Phi = A_1\Big(\cosh\alpha_+ X - \cos\alpha_- X \Big) + A_2\Big(\alpha_- \sinh\alpha_+ X - \alpha_+ \sin\alpha_- X \Big), \qquad (3.45)$$

where A_1 and A_2 are constants and we have introduced

$$\alpha_\pm = \sqrt{\sqrt{\left(\frac{\tau_0}{2}\right)^2 + \Omega^2} \pm \frac{\tau_0}{2}}.$$

The remaining boundary conditions, at $X = 1$, then imply that

$$\Big(\cosh\alpha_+ - \cos\alpha_- \Big) A_1 + \Big(\alpha_- \sinh\alpha_+ - \alpha_+ \sin\alpha_- \Big) A_2 = 0,$$
$$\Big(\alpha_+ \sinh\alpha_+ + \alpha_- \sin\alpha_- \Big) A_1 + \alpha_+\alpha_- \Big(\cosh\alpha_+ - \cos\alpha_- \Big) A_2 = 0. \qquad (3.46)$$

This is a second-order, homogeneous linear system in the two unknowns A_1 and A_2. To determine eigenfunctions, we are only interested in non-trivial solutions. These exist if and only if the corresponding determinant vanishes, which can be re-arranged to

$$\frac{\tau_0}{2\Omega} = \frac{\cosh\alpha_+ \cos\alpha_- - 1}{\sinh\alpha_+ \sin\alpha_-}.$$

For each value of τ_0, the roots of this transcendental equation give the eigenvalues Ω. The smallest positive root then corresponds to the fundamental eigenfunction $\Phi(X)$ used in §3.5. Combining equations (3.45) and (3.46), this can be written as

$$\Phi = A_1 \left[\cosh\alpha_+ X - \cos\alpha_- X - \frac{\alpha_+ \sinh\alpha_+ + \alpha_- \sin\alpha_-}{\alpha_+\alpha_- \left(\cosh\alpha_+ - \cos\alpha_- \right)} \Big(\alpha_- \sinh\alpha_+ X - \alpha_+ \sin\alpha_- X \Big) \right].$$

To determine the constant A_1 we specify the normalisation condition

$$\int_0^1 \Phi^2 \, \mathrm{d}X = 1.$$

Geometrically-constrained snap-through

Synopsis

We study the dynamics of snap-though in macroscopic systems caused by varying geometric confinement (no external loading). In particular, we investigate the extent to which dissipation is required to explain the anomalously slow snap-through reported in various previous works, as opposed to the overdamped dynamics considered in Chapters 2 and 3. We study an elastic arch as a simple model system which transitions between bistable states via snap-through. We show that, for shallow arch shapes, the steady deformation can be described by a single dimensionless parameter that depends only on the geometry. When the system is near the snap-through transition, we then demonstrate that the perturbation method we previously developed for electrostatic pull-in carries over to this scenario. This allows us to show that critical slowing down still occurs in the absence of energy dissipation, and we identify a dimensionless parameter characterising the importance of damping in the bottleneck phase. In the underdamped limit this leads to a new scaling law for the snap-through time, which we confirm using numerical simulations of an elastica model and experiments. This realisation has important consequences for applications of snap-through ranging from soft robotics to morphing devices.

A paper based on the work described in this chapter has been published in *Nature Physics* (Gomez *et al.*, 2017*a*).
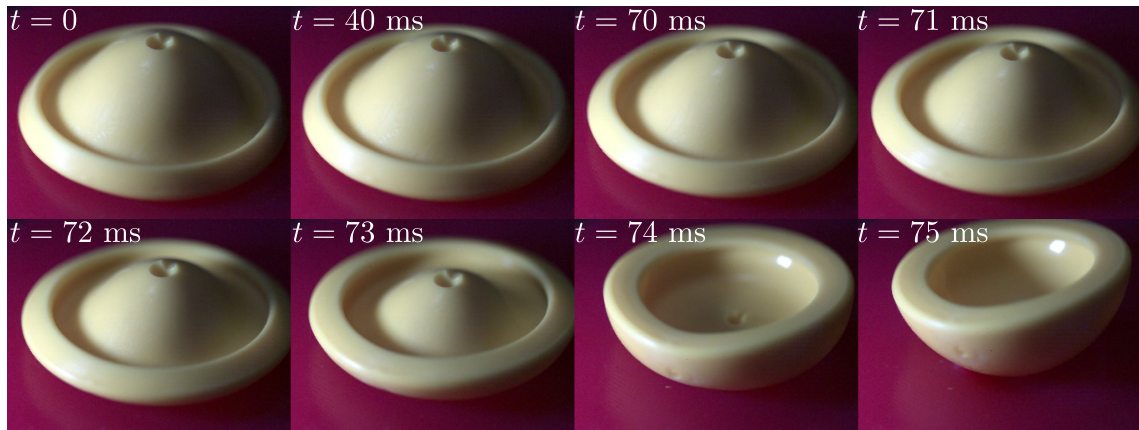
Figure 4.1: *A jumping popper toy can be turned inside-out and released on a surface. It becomes unstable, and after a time delay (≈ 70 ms here) the popper rapidly snaps (in under 5 ms) back to its natural shape and leaps from the surface.*

4.1 Introduction

Many elastic structures have two possible equilibrium states (Bazant & Cendolin, 1991): from bistable hair clips, to nano-electromechanical switches (Loh & Espinosa, 2012; Xu *et al.*, 2014) and origami patterns (Silverberg *et al.*, 2015; Dudte *et al.*, 2016). These systems typically transition from one state to the other via a rapid snap-through. While many studies have focussed on classifying *when* snap-through occurs in simple elastic objects (Patricìo *et al.*, 1998; Plaut, 2009; Seffen & Vidoli, 2016; Sobota & Seffen, 2017), *how fast* snapping happens remains much less well understood.

Indeed, estimates of the speed of snap-through often suggest that it should occur more quickly than is observed. This is illustrated by rubber 'jumping popper' toys that are essentially snapping spherical caps; see figure 4.1. These can be turned 'inside-out' to create an alternative configuration, which remains stable while the cap is held at its edges. Upon leaving the popper on a surface, it becomes unstable, and leaps upwards as it snaps back to its natural shape. However, the snap back is not immediate: a time delay is observed where the popper moves slowly, apparently close to equilibrium, before it rapidly accelerates. The delay can be several tens of seconds in duration — much slower than what is generally expected for an elastic instability. This behaviour, known as pseudo-bistability, has been proposed as a way of creating morphing devices that self-recover after a time delay to reduce energy consumption (Brinkmeyer *et al.*, 2012).

To get a sense of how 'anomalous' these dynamics are, we now estimate how fast a popper should snap if it were purely elastic. The inertia force in a spherical cap scales as $\rho_s h w / t^2$, where ρ_s is the material density, h is the thickness, w is the normal displacement and t is time. As the cap must change its curvature as it snaps, we expect that bending

forces are important. From linear shell theory, these scale as Bw/L_{base}^4 where B is the bending stiffness and L_{base} is the base diameter of the cap (Ventsel & Krauthammer, 2001). Balancing these forces gives the timescale $t^* \sim (\rho_s h L_{\text{base}}^4 / B)^{1/2}$. Using typical values for a commercially available popper toy (Pandey *et al.*, 2014), we find that $t^* \approx 1$ ms — from this estimate, it should not even be possible to place the popper onto a table before it snaps!

Pseudo-bistability has been analysed in single-degree-of-freedom systems, elastic arches (Brinkmeyer *et al.*, 2013) and spherical caps like the jumping popper (Santer, 2010; Brinkmeyer *et al.*, 2012), using a combination of experiments and finite element simulations. The conventional wisdom is that material viscoelasticity must be present, so that the observed delay is in fact the relaxation timescale of the material, similar to the phenomenon of creep buckling (Santer, 2010). (It is also easily demonstrated that holding the shell for longer in its inside-out state causes a slower snap-back, consistent with the importance of viscoelastic effects.) Similar dynamics have also been observed in the Venus flytrap: here the estimated inertial timescale t^* is orders of magnitude faster than the observed snap-through time, and air damping is not enough to account for the discrepancy (Forterre *et al.*, 2005). In this example the proposed mechanism is poroelasticity due to fluid in the leaf tissue.

A natural question to ask is whether a dissipation mechanism is always needed to obtain delay behaviour: can snap-through be both underdamped and much slower than the corresponding inertial timescale t^*? In Chapters 2 and 3, we showed that pull-in instabilities — a type of snap-through under electrostatic forces — may show anomalously slow dynamics due to the 'ghost' of the saddle-node bifurcation. In essence, close to snap-through this introduces a large pre-factor that multiplies the timescale of snapping. While the systems we studied were overdamped, the damping forces were not relevant in determining this pre-factor. In this chapter, we will explore whether a similar mechanism is possible in systems with minimal energy dissipation. To answer this question, we need to understand how the mathematical structure underlying snap-through influences the observed timescale.

4.1.1 Elastic arches

While we are motivated by the jumping popper toy and the Venus flytrap, a spherical cap presents a modelling challenge: it has non-zero Gaussian curvature (i.e. is curved in two orthogonal directions), and this 'two-dimensionality' leads to a strong coupling between geometry and mechanics, in which Poisson effects and isometric transformations play a key role in the deformation (Audoly & Pomeau, 2010; Gomez *et al.*, 2016). In addition, there
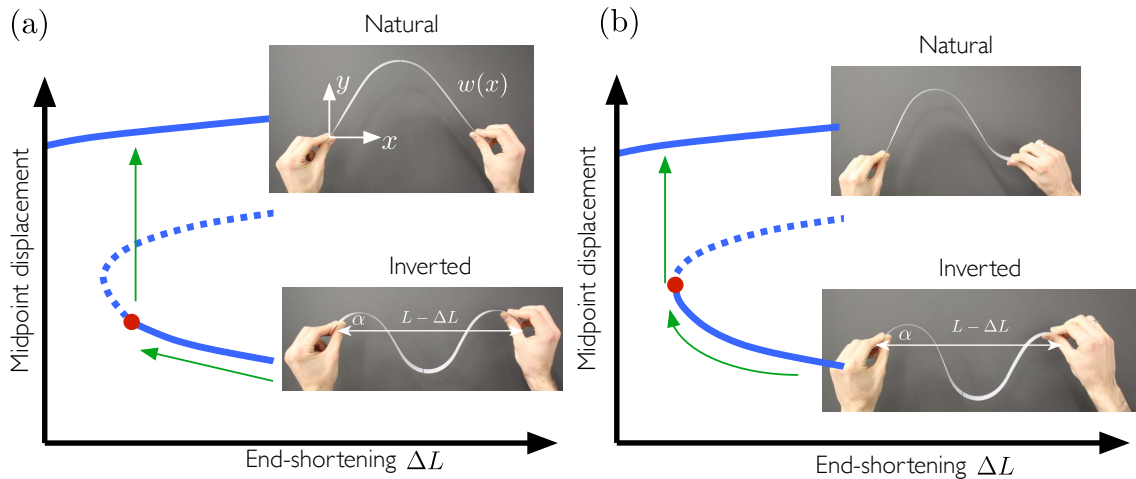
Figure 4.2: *Exploring snap-through instabilities in a simple elastic system. (a) Bringing the edges of a strip of plastic together, while also holding them at a non-zero angle α to the horizontal, creates bistable 'inverted' (bottom) and 'natural' (top) arch shapes. Under smaller end-shortenings ΔL, the arch snaps from the inverted to the natural shape at a subcritical pitchfork bifurcation: the inverted mode (lower solid curve) intersects an unstable asymmetric mode (not drawn) and becomes linearly unstable (dashed curve). (b) Introducing asymmetry in the boundary conditions, by holding the right end horizontally, still creates a bistable system. However, the destabilising effect of the asymmetric mode is removed and the inverted mode remains stable up to a fold: the snap-through bifurcation is now a saddle-node/fold bifurcation. (Reprinted from Gomez et al. (2017a), DOI: https://doi.org/10.1038/nphys3915.)*

is the possibility of non-axisymmetric deformations during snap-through (Seffen & Vidoli, 2016). We therefore consider a much simpler system: an elastic arch. This simplification allows us to make a large amount of analytical progress, so that we can gain insight into what controls the dynamics of a generic elastic system and reveal the precise role played by dissipation.

Despite their simplicity, elastic arches illustrate many features of snap-through that are present in more complex systems such as shells (Harvey & Virgin, 2015). For example, they show how the qualitative behaviour is governed by the relative importance of bending and stretching effects, which depends on the geometry rather than the material properties. Sufficiently thick/shallow arches typically snap-through in an entirely symmetric manner: stretching effects dominate in this case, and it is favourable for the arch to compress along its length rather than bend. Meanwhile, thinner/deeper arches prefer to bend into asymmetric shapes to accommodate the applied load. This same picture is seen in the poking example discussed in Chapter 1 (figure 1.1), as well as in spherical caps under point indentation (Fitch, 1968) and uniform pressure (Huang, 1964).

While arches can be stress-free if they have natural curvature (e.g. circular or sinusoidal in shape), we will focus on arches that are formed by buckling a planar strip of material.

This will allow us to easily vary the geometry of the arch and hence its stability characteristics in a single experiment. We consider a set-up that resembles a 'one-dimensional' snapping cap: we buckle a strip into an arch shape by clamping its ends at a non-zero angle α to the horizontal, and bringing the ends a controlled distance ΔL closer. As figure 4.2a illustrates, two equilibrium shapes are possible — an 'inverted' shape and a 'natural' shape. However, as a simple experiment demonstrates (e.g. using an ordinary strip of plastic), the inverted state needs a sufficiently large ΔL to be stable: at small end-shortenings, if the arch is placed in the inverted shape, it snaps back to the natural one when released. This is evocative of the behaviour of a spherical cap, which snaps from an inside-out state to its original shape.

An analysis of the bifurcation diagram for this system shows that snapping is caused by a subcritical pitchfork bifurcation: as ΔL is decreased, the inverted mode intersects an unstable asymmetric mode and becomes linearly unstable, before ceasing to exist at still smaller ΔL. (Because the asymmetric mode is unstable it is not observed in practice.) Hence, the snap-through dynamics may be understood using a standard linear stability analysis (Pandey *et al.*, 2014; Fargette *et al.*, 2014): the displacement of each point on the arch evolves in time as $\sim e^{\sigma t}$ for some growth rate σ. This behaviour is qualitatively different from spherical caps in which the inside-out state first loses stability at a saddle-node/fold bifurcation (Brodland & Cohen, 1987). However, this type of snap-through can be obtained within our arch setup by simply holding one end of the strip horizontally, while the other remains clamped at the angle α; see figure 4.2b. This situation is more dynamically interesting because a linear stability analysis no longer applies — finding the timescale of the transition is now a non-trivial problem from the outset.

We note that the set-up in figure 4.2a has been explored by Brinkmeyer *et al.* (2013), who were also motivated by the pseudo-bistability shown by spherical caps. Using a combination of finite element analysis and experiments, they found that a delayed snap-through may occur in this system. Moreover, the amount of delay is highly sensitive to the boundary conditions, i.e. the angle at the clamp and the imposed end-shortening, while the Young's modulus and Poisson ratio have a negligible effect. Brinkmeyer *et al.* (2013) implicitly attribute this delay to the viscoelasticity of the arch: in their numerics a viscoelastic model is used. Crucially, the possibility of a delay without viscoelastic effects is not explored. A very similar experiment has also been analysed by Plaut (2009), though only the stability of the arch was considered.

The remainder of this chapter is dedicated to understanding the dynamics of the arch setup shown in figure 4.2b. To elucidate the precise role played by energy dissipation, we account for both inertial and external (viscous) damping forces in our model. In §4.2 we formulate the equations governing the motion of the arch, focussing on shallow shapes that
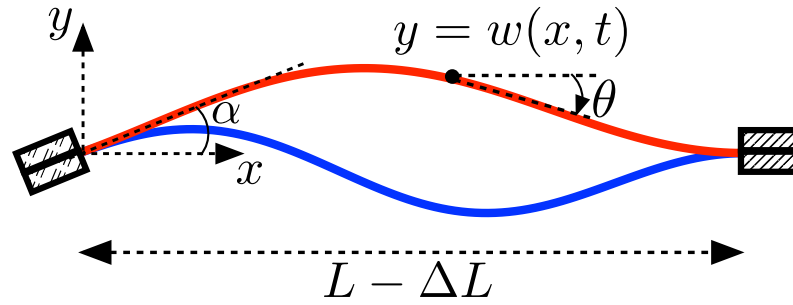
Figure 4.3: Cross-section of the current/deformed configuration of the arch showing the notation used (reprinted from Gomez et al. (2017a), DOI: https://doi.org/10.1038/nphys3915).

are well-approximated by beam theory. We identify a single dimensionless parameter μ that characterises the stability of the arch. In §4.3, we consider the equilibrium shapes and onset of snap-through as μ is varied. In §4.4 we then analyse the dynamics when the system is placed just beyond the snap-through transition. We show that critical slowing down occurs in the underdamped limit, causing a bottleneck phase in which the displacement grows quadratically in time rather than exponentially, and we obtain a scaling law for the snap-through time. We also analyse the overdamped limit, showing that in this case the dynamics is similar to the overdamped pull-in studied in Chapter 3. We then compare our asymptotic analysis to elastica simulations in §4.5, which incorporate the effects of geometric nonlinearities, showing that the scaling laws for the snap-through time hold even for arches that are not shallow in shape. We present experimental results for underdamped arches in §4.6, before discussing our findings in §4.7.

4.2 Theoretical formulation

Consider a thin strip of linearly elastic material with Young's modulus E and constant density ρ_s. In its undeformed state, the strip is flat and has constant thickness h, width b and length L. The ends of the strip are subject to an end-shortening ΔL in the horizontal direction, with one end clamped at an angle α to the horizontal and the other end clamped horizontally. This causes the strip to buckle into one of two possible arch shapes, as shown schematically in figure 4.3.

4.2.1 Beam theory

We assume that the dimensions of the cross-section are much smaller than the length, i.e. $h, b \ll L$, so that the strip remains within the limit of small strains as it deforms (later we will be more precise about when this holds). We also suppose that the strip undergoes

pure bending in the vertical plane perpendicular to its width, i.e. we ignore bending out of this plane and twist about the axis of the strip. Note that this is partly justified by specifying $h \ll b$, corresponding to a relatively flat cross-section, since this yields a high rigidity to out-of-plane bending and twist compared to a square cross-section (Patricìo *et al.*, 1998). We neglect the effects of gravity (experiments are performed on their side to minimise the effects of gravity).

In our first analysis we assume that the shape of the arch is shallow, so that geometric nonlinearities can be neglected. This allows us to make significant analytical progress, and cleanly reveal the underlying mathematical structure without added complications. In §4.5, we will account for geometric nonlinearities by solving an elastica model numerically; we shall see that our conclusions from the shallow arch case are quantitatively accurate for deep arches. Furthermore, we neglect the effects of extensibility, considering only arches that are well beyond the buckling threshold under the imposed end-shortening ΔL. In practice, this is satisfied simultaneously with the requirement of a shallow shape by having a small thickness $h \ll L$ (see Pandey *et al.*, 2014, for a discussion of this point in a related problem). (We note that this situation is very different to the microbeam problem we studied in Chapter 3: because the beam was clamped in its flat state, stretching of the beam centreline could not be ignored during deformation.)

Under the above assumptions, the transverse displacement, $w(x,t)$, satisfies the dynamic beam equation (Howell *et al.*, 2009)

$$\rho_s h \frac{\partial^2 w}{\partial t^2} + \Upsilon \frac{\partial w}{\partial t} + B \frac{\partial^4 w}{\partial x^4} + P_c \frac{\partial^2 w}{\partial x^2} = 0, \qquad 0 < x < L. \tag{4.1}$$

Here x is the horizontal coordinate measured from the left end (labelled in figure 4.3), t is time, $B = Eh^3/12$ is the bending stiffness and $P_c(t)$ is the (unknown) compressive force applied to the arch (note these quantities are phrased per unit width, and, as in Chapter 3, we are using the form of B appropriate for a narrow strip rather than an infinite plate; see Audoly & Pomeau, 2010, for example). Here we are also including possible viscous damping due to the environment; since we are interested in the case when the motions are slowed near the snap-through transition, it is reasonable to assume this damping is linear in the velocity with constant coefficient Υ (per unit width).

The boundary conditions at the clamped ends are (using subscripts to denote partial derivatives here and throughout)

$$w(0,t) = 0, \quad w_x(0,t) = \alpha, \quad w(L,t) = w_x(L,t) = 0. \tag{4.2}$$

(The boundary conditions at the right clamp are imposed at $x = L$ because we identify $s \sim x$ in beam theory, where s is arclength along the beam centreline.) Under the assumption

of inextensibility, the imposed end-shortening becomes

$$\int_0^L \cos\theta \ \mathrm{d}s = L - \Delta L,$$

where θ is the angle between the strip and the x-direction (figure 4.3) and s is the arclength. In beam theory we have $s \approx x$ and $\theta \approx \partial w/\partial x \ll 1$ so that this constraint may be approximated as

$$\int_0^L \left(\frac{\partial w}{\partial x}\right)^2 \ \mathrm{d}x = 2\Delta L, \tag{4.3}$$

representing how the amplitude of the arch must accommodate the imposed end-shortening. Equation (4.1) with boundary conditions (4.2), the constraint (4.3) and appropriate initial conditions (to be specified later) then fully specify the problem. We expect that the assumption of a shallow shape is valid provided $\alpha \ll 1$ and $\Delta L \ll L$, which agrees with the fact that the solution for $\alpha = \Delta L = 0$ is simply a flat strip, $w = 0$.

4.2.2 Non-dimensionalisation

To make the problem dimensionless, we scale the horizontal coordinate by the length L of the strip, i.e. we set $X = x/L$. Balancing terms in the inextensibility constraint (4.3) shows that a typical slope $w_x \sim (\Delta L/L)^{1/2}$, giving the natural vertical lengthscale $w \sim (L\Delta L)^{1/2}$. We therefore introduce the dimensionless displacement $W = w/(L\Delta L)^{1/2}$. Time is scaled as $T = t/t^*$ where $t^* = (\rho_s h L^4/B)^{1/2}$ is the inertial timescale obtained by balancing inertial and bending forces in (4.1) (this is analogous to the inertial timescale for a spherical shell in the qualitative discussion of §4.1). Substituting the expression for B, this can be written as $t^* = 2\sqrt{3}L^2/(hc)$ where $c = (E/\rho_s)^{1/2}$ is the speed of sound in the material — typically, t^* is very short due to the factor of c in the denominator. The key idea of this chapter is that the dimensional snap-through time may differ significantly from t^*, even in the absence of damping, depending on how close the system is to the snap-through transition.

Inserting the above scalings into the beam equation (4.1), we obtain

$$\frac{\partial^2 W}{\partial T^2} + \upsilon\frac{\partial W}{\partial T} + \frac{\partial^4 W}{\partial X^4} + \tau^2\frac{\partial^2 W}{\partial X^2} = 0, \qquad 0 < X < 1, \tag{4.4}$$

where $\tau(T)^2 = P_c L^2/B$ is the dimensionless compressive force and the importance of damping is measured by the dimensionless parameter

$$\upsilon = \frac{L^2\Upsilon}{\sqrt{\rho_s h B}}.$$

Specifically, v is the ratio of viscous forces per unit length ($\sim \Upsilon w/t^*$) to bending forces ($\sim Bw/L^4$) over the inertial timescale t^*. The boundary conditions (4.2) are modified to

$$W_X(0,T) = \mu, \quad W(0,T) = W(1,T) = W_X(1,T) = 0, \qquad (4.5)$$

where we have introduced the parameter

$$\mu = \alpha \left(\frac{\Delta L}{L} \right)^{-1/2}. \qquad (4.6)$$

The constraint (4.3) becomes

$$\int_0^1 \left(\frac{\partial W}{\partial X} \right)^2 \, \mathrm{d}X = 2. \qquad (4.7)$$

Together with appropriate initial conditions for W and W_T, these equations provide a closed system to determine the profile $W(X,T)$ and compressive force $\tau(T)^2$.

By non-dimensionalising the problem, we have reduced the control parameters α and ΔL to the single parameter μ, which enters the problem as a normalised inclination angle (the dimensionless compressive force τ^2 acts as a Lagrange multiplier and is determined as part of the solution). The parameter μ measures the ratio of the angle imposed by clamping, α, to that due to the imposed end-shortening, $(\Delta L/L)^{1/2}$, and so is entirely geometric in nature; it is independent of the material parameters of the system, notably ρ_s and E (and also the thickness h). This means that we can use μ to characterise the equilibrium shapes and their stability entirely in terms of the geometry. We focus on the case $\mu > 0$ throughout ($\mu < 0$ follows similarly).

We also note that μ may be interpreted as the ratio of bending energy to stretching (membrane) energy in the arch. To see this, note that the slope w_x decreases from α to 0 along the length of the arch by (4.2). The typical curvature associated with this is $\kappa \approx w_{xx} \sim \alpha/L$, implying a bending energy per unit length of $\mathcal{E}_B = Bb\kappa^2/2 \sim Bb\alpha^2/L^2$ ignoring numerical pre-factors (see Audoly & Pomeau, 2010, for example). Meanwhile, the end-shortening condition (4.3) dictates that the slope is of order $(\Delta L/L)^{1/2}$. Since we identify arclength with the horizontal coordinate in beam theory, any vertical deflection is an extension, leading to a local strain also of order $(\Delta L/L)^{1/2}$. The stretching energy per unit length, denoted $\mathcal{E}_S$, is then $\mathcal{E}_S = Ehb \cdot (\text{strain})^2 \sim Ehb\Delta L/L$. The ratio of these two energies is

$$\frac{\mathcal{E}_B}{\mathcal{E}_S} \sim \left(\frac{h\mu}{L} \right)^2.$$

This argument shows that μ is the analogue of the Föppl-von-Kármán number, which measures the ratio of bending to stretching energy for complete spherical shells (Knoche,

2014) and spherical caps (Brodland & Cohen, 1987). In addition, we see that the assumption of small strains is valid precisely when $h\mu/L \ll 1$: in this limit stretching effects are extremely expensive so that the arch will remain inextensible. Note that this remains true even when $\mu = O(1)$ because we have assumed $h \ll L$.

4.3 Equilibrium shapes

At this stage we can understand the snap-through behaviour of the arch. When $\mu = 0$, the inverted and natural shapes are simply reflections of each other and correspond to the fundamental Euler-buckling mode of a horizontally-clamped beam. For $\mu \neq 0$, the up-down symmetry is broken and the inverted shape features an edge effect: near $X = 0$ there is a region of enhanced curvature due to the non-zero clamp angle. This costs more bending energy compared to the natural shape (figure 4.3). While μ is small, this effect remains small and both configurations should remain stable. For larger values of μ, we expect that the bending stiffness is sufficient to 'roll' the arch back to the natural shape in a snap-through motion, qualitatively similar to the snap-through of a spherical cap.

To confirm this intuition, we solve the steady version of the dimensionless beam equation (4.4) subject to the boundary conditions (4.5) to obtain

$$W(X) = \mu \frac{\tau X(\cos\tau - 1) + \tau\{\cos[\tau(1-X)] - \cos\tau\} - \sin\tau X - \sin[\tau(1-X)] + \sin\tau}{\tau(2\cos\tau + \tau\sin\tau - 2)}.$$
$$(4.8)$$

To determine the dimensionless compressive force τ^2 in terms of the control parameter μ, we substitute this solution into the end-shortening constraint (4.7) and rearrange to find

$$\mu^2 = \frac{8\tau(2\cos\tau + \tau\sin\tau - 2)^2}{2\tau^3 - \tau^2(\sin 2\tau + 4\sin\tau) + 4\tau(\cos\tau - \cos 2\tau) + 2(\sin 2\tau - 2\sin\tau)}. \quad (4.9)$$

For each value of μ, the allowed values of $\tau(\mu)$ may be found numerically (e.g. using the MATLAB routine `fzero`). Because it is easier to measure the midpoint displacement $W(1/2)$ rather than τ in experiments, we plot the resulting bifurcation diagram in terms of $W(1/2)$ and μ using the relation

$$W(1/2) = \mu \frac{\tan(\tau/4)}{2\tau}, \quad (4.10)$$

which follows from (4.8). This result is shown in figure 4.4, and confirms that for small μ, both inverted and natural equilibrium shapes exist. The inverted shape undergoes a saddle-node bifurcation at

$$\mu = \mu_{\text{fold}} \approx 1.7818, \quad W(1/2) = W_{\text{fold}}(1/2) \approx -0.3476, \quad \tau = \tau_{\text{fold}} \approx 7.5864.$$
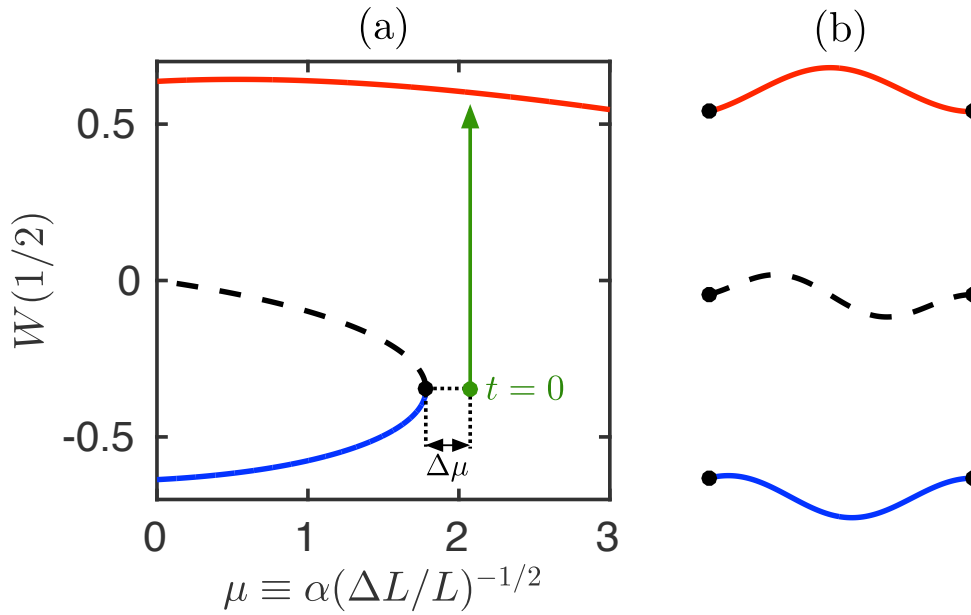
Figure 4.4: *The equilibrium behaviour of the strip, as predicted by beam theory. (a) Bifurcation diagram: plotting the dimensionless midpoint displacement as a function of $\mu = \alpha(\Delta L/L)^{-1/2}$. The upper branch (solid red curve) corresponds to the natural shape, while the lower branch (solid blue curve) corresponds to the inverted shape that disappears at the saddle-node (fold) bifurcation at $\mu_{\mathrm{fold}} \approx 1.7818$ (the black dashed curve corresponds to an unstable mode that is not observed experimentally). A typical trajectory at fixed μ beyond the snap-through transition is also shown (green arrow). (b) The corresponding arch shapes for each of the three modes when $\mu = 1$. (Reprinted from Gomez et al. (2017a), DOI: https://doi.org/10.1038/nphys3915.)*

Here we refer to the equilibrium shape at the fold as $W_{\mathrm{fold}}(X)$ with corresponding compressive force τ_{fold}^2. Using standard techniques (Maddocks, 1987), it may be shown that the inverted shape remains stable until the fold point, while the natural shape is always stable (all other modes are unstable).

4.4 Snap-through dynamics

We now analyse the dynamics when the system is just beyond the saddle-node bifurcation. We set $\mu = \mu_{\mathrm{fold}} + \Delta\mu$ with $0 < \Delta\mu \ll 1$, a small perturbation measuring the 'distance' to the snap-through transition. Because no inverted equilibrium exists for $\Delta\mu > 0$ (i.e. we are to the right of the fold point in the bifurcation diagram of figure 4.4a), it follows that for the strip to reach an equilibrium, it must snap upwards to the natural shape.

To give a physical interpretation of $\Delta\mu$, suppose that α_{fold} and ΔL_{fold} are values of α and ΔL at the fold point — so that $\mu_{\mathrm{fold}} = \alpha_{\mathrm{fold}}(\Delta L_{\mathrm{fold}}/L)^{-1/2}$ — and set

$$\alpha = \alpha_{\mathrm{fold}}(1 + \delta), \quad \Delta L = \Delta L_{\mathrm{fold}}(1 - \epsilon),$$

where $|\delta| \ll 1$ and $|\epsilon| \ll 1$. Inserting these into the expression (4.6) for μ shows that $\Delta\mu$ is equivalent to perturbing the angle α and end-shortening ΔL where

$$
\begin{aligned}
\frac{\Delta\mu}{\mu_{\text{fold}}} &= (1+\delta)(1-\epsilon)^{-1/2} - 1, \\
&\sim \delta + \frac{\epsilon}{2}.
\end{aligned}
\tag{4.11}
$$

It follows that $\Delta\mu$ is positive, i.e. we are beyond the fold, provided $\delta + \epsilon/2 > 0$. If α is held fixed and we only vary ΔL, this reduces to $\epsilon > 0$.

We re-emphasise that we cannot perform a linear stability analysis at this stage: for $\Delta\mu > 0$ there is no equilibrium base state from which the system evolves during snap-through. We faced this same issue in Chapter 3 when we analysed the behaviour of a microbeam near the pull-in transition, which also corresponds to a saddle-node bifurcation. Recall that we made progress via a perturbation approach, using the closeness of the solution to the equilibrium shape at the fold as a small parameter. Here, the perturbation $\Delta\mu$ is analogous to the normalised difference between the applied voltage and the pull-in voltage. We now adapt the approach of Chapter 3 to study the snap-through dynamics of the elastic arch, showing that the perturbation method still applies despite crucial differences here: unlike the microbeam, the arch is not necessarily overdamped, and the snap-through is driven by a change in geometry (according to (4.11)) rather than an external field. This will allow us to obtain our key result: slow dynamics can be the consequence of the ghost of a saddle-node bifurcation, and dissipation need not play a part at all. This can contribute to a pseudo-bistable response, where the system appears to be in equilibrium before accelerating to a remote state.

For initial conditions, we suppose that the arch starts at rest in a shape that is 'close' to the shape at the fold bifurcation, i.e.

$$
W(X,0) \approx W_{\text{fold}}(X), \quad W_T(X,0) = 0.
\tag{4.12}
$$

In practice, we achieve this with an indenter that 'pushes' the shape to be close to $W_{\text{fold}}(X)$, by imposing the midpoint displacement $W(1/2,0) = W_{\text{fold}}(1/2)$; away from the midpoint, $W(X,0) \approx W_{\text{fold}}(X)$ then holds because $\Delta L \approx \Delta L_{\text{fold}}$ for $\Delta\mu \ll 1$. (More precisely, the steady indentation problem can be solved to obtain the shape of the beam, $W_{\text{indent}}(X)$; comparing this with the bifurcation shape confirms that $|W_{\text{indent}}(X) - W_{\text{fold}}(X)| = O(\Delta\mu)$.) When the indenter is removed, the arch then snaps from rest to the natural configuration (figure 4.4a).

The initial conditions (4.12) are different from the pull-in instabilities we studied in Chapters 2 and 3: there we assumed the system starts in the zero voltage state, rather

than near the displacement at the saddle-node bifurcation. This meant that when the damping was small, the electrode was moving rapidly by the time it passed the pull-in displacement, and there was no bottleneck phase. Here, the arch is forced to start at rest near the fold shape, so that such inertial effects are no longer relevant. For $\Delta\mu$ sufficiently small, we then expect that the arch will only evolve away from $W_{\text{fold}}(X)$ on a timescale that is much slower than the inertial timescale — we have that $W(X,T) \approx W_{\text{fold}}(X)$ (and also $\tau \approx \tau_{\text{fold}}$) up to some dimensionless time $T \gg 1$.

To capture this explicitly we rescale time as $T = \Delta\mu^{-\eta}\mathcal{T}$, where $\eta > 0$ characterises the duration of this slow bottleneck phase and will be determined as part of the analysis. In terms of re-scaled time, the beam equation (4.4) reads

$$\Delta\mu^{2\eta}\frac{\partial^2 W}{\partial \mathcal{T}^2} + \upsilon\Delta\mu^{\eta}\frac{\partial W}{\partial \mathcal{T}} + \frac{\partial^4 W}{\partial X^4} + \tau^2\frac{\partial^2 W}{\partial X^2} = 0, \qquad 0 < X < 1. \tag{4.13}$$

Interestingly, this shows that the importance of damping depends on the perturbation $\Delta\mu$, with two regimes possible. For sufficiently large υ/small $\Delta\mu$, we expect that viscous damping dominates the inertia term, so that the dynamics are overdamped to leading order. However, for sufficiently small υ, inertial forces will dominate: in other words, the limiting effect is now how fast the arch can be accelerated from rest, rather than how much it is slowed by damping.

We now make these considerations more precise. Recall that in Chapter 3, we showed that the bottleneck analysis is equivalent to an expansion in powers of $O(\Delta\mu^{1/2})$ ($\Delta\mu$ being analogous to the normalised voltage difference). We therefore seek an asymptotic expansion about the fold shape of the form

$$W(X,\mathcal{T}) = W_{\text{fold}}(X) + \Delta\mu^{1/2}\tilde{W}_0(X,\mathcal{T}) + \Delta\mu\tilde{W}_1(X,\mathcal{T}) + \dots, \tag{4.14}$$

$$\tau(\mathcal{T}) = \tau_{\text{fold}} + \Delta\mu^{1/2}\tilde{\tau}_0(\mathcal{T}) + \Delta\mu\tilde{\tau}_1(\mathcal{T}) + \dots. \tag{4.15}$$

The choice of powers of $\Delta\mu^{1/2}$ can also be justified *a posteriori* and reflects the fact that the displacement (away from the bifurcation shape) in the bottleneck may grow larger than the original perturbation to the system, $\Delta\mu$, though still remain small compared to unity.

4.4.1 Leading-order problem

Inserting (4.14)–(4.15) into (4.13) and considering terms of $O(\Delta\mu^{1/2})$, we obtain the homogeneous equation

$$L(\tilde{W}_0, \tilde{\tau}_0) \equiv \frac{\partial^4 \tilde{W}_0}{\partial X^4} + \tau_{\text{fold}}^2\frac{\partial^2 \tilde{W}_0}{\partial X^2} + 2\tau_{\text{fold}}\tilde{\tau}_0\frac{\mathrm{d}^2 W_{\text{fold}}}{\mathrm{d}X^2} = 0. \tag{4.16}$$

The end-shortening constraint (4.7) and boundary conditions (4.5) are also homogeneous at $O(\Delta\mu^{1/2})$:

$$\int_0^1 \frac{\mathrm{d}W_{\mathrm{fold}}}{\mathrm{d}X} \frac{\partial \tilde{W}_0}{\partial X} \mathrm{d}X = 0, \quad \tilde{W}_0(0, \mathcal{T}) = \tilde{W}_{0_X}(0, \mathcal{T}) = \tilde{W}_0(1, \mathcal{T}) = \tilde{W}_{0_X}(1, \mathcal{T}) = 0.$$

Because the leading-order problem is homogeneous, it is equivalent to the equations governing small-amplitude oscillations about $(W_{\mathrm{fold}}, \tau_{\mathrm{fold}})$, restricting to the neutrally-stable ('slow') eigenfunctions whose natural frequency (eigenvalue) is zero.

Using linearity of the operator $L(\cdot, \cdot)$, we may scale $\tilde{\tau}_0$ out from (4.16) (since $\tilde{\tau}_0$ is independent of X) so that

$$(\tilde{W}_0, \tilde{\tau}_0) = A(\mathcal{T})(W_p(X), 1). \tag{4.17}$$

Here $A(\mathcal{T})$ is an (undetermined) amplitude and $W_p(X)$ is the eigenfunction satisfying equation (4.16) with $\tilde{\tau}_0 = 1$, i.e.

$$L(W_p, 1) = 0, \quad \int_0^1 \frac{\mathrm{d}W_{\mathrm{fold}}}{\mathrm{d}X} \frac{\mathrm{d}W_p}{\mathrm{d}X} \mathrm{d}X = 0, \tag{4.18}$$

$$W_p(0) = W_p'(0) = W_p(1) = W_p'(1) = 0, \tag{4.19}$$

where $' = \mathrm{d}/\mathrm{d}X$. While this system appears to over-determine $W_p(X)$ (there are four derivatives but five constraints), there is in fact a unique solution

$$W_p(X) = \frac{1}{\tau_{\mathrm{fold}}} \left(X \frac{\mathrm{d}W_{\mathrm{fold}}}{\mathrm{d}X} - \mu_{\mathrm{fold}} X \right) + a_1 \left(\sin \tau_{\mathrm{fold}} X - \tau_{\mathrm{fold}} X \right) + a_2 \left(\cos \tau_{\mathrm{fold}} X - 1 \right), \tag{4.20}$$

where

$$a_1 = -2\mu_{\mathrm{fold}} \frac{\sin^2(\tau_{\mathrm{fold}}/2) \left[(\tau_{\mathrm{fold}}^2 - 2) \cos \tau_{\mathrm{fold}} - 2\tau_{\mathrm{fold}} \sin \tau_{\mathrm{fold}} + 2 \right]}{\tau_{\mathrm{fold}}^2 \left(2 \cos \tau_{\mathrm{fold}} + \tau_{\mathrm{fold}} \sin \tau_{\mathrm{fold}} - 2 \right)^2},$$

and

$$a_2 = -\mu_{\mathrm{fold}} \frac{\tau_{\mathrm{fold}}^3 + \tau_{\mathrm{fold}}^2 \sin \tau_{\mathrm{fold}} (\cos \tau_{\mathrm{fold}} - 2) + 2(\tau_{\mathrm{fold}} \cos \tau_{\mathrm{fold}} - \sin \tau_{\mathrm{fold}})(\cos \tau_{\mathrm{fold}} - 1)}{\tau_{\mathrm{fold}}^2 \left(2 \cos \tau_{\mathrm{fold}} + \tau_{\mathrm{fold}} \sin \tau_{\mathrm{fold}} - 2 \right)^2}.$$

(This solution is found by applying the boundary conditions (4.19), but also satisfies the integral constraint in (4.18) when τ_{fold} is specifically the value of τ taken at the fold.) Subsequently, we shall need two integrals associated with (4.20). We record the values of these integrals here:

$$I_1 = \int_0^1 W_p^2 \, \mathrm{d}X \approx 0.0518, \quad I_2 = \int_0^1 \left(\frac{\mathrm{d}W_p}{\mathrm{d}X} \right)^2 \mathrm{d}X \approx 0.950. \tag{4.21}$$

The variable $A(\mathcal{T})$ appearing in (4.17) plays a key role in the snapping dynamics, and is analogous to the variable used in Chapter 3: re-arranging the expansion in (4.14) shows that it acts as an amplitude of the leading-order solution (and also its compressive force) via

$$A(\mathcal{T}) = \frac{\tilde{W}_0(X,\mathcal{T})}{W_p(X)} \sim \Delta\mu^{-1/2}\frac{W(X,\mathcal{T}) - W_{\text{fold}}(X)}{W_p(X)}. \tag{4.22}$$

Currently, $A(\mathcal{T})$ is undetermined. We proceed to the next order problem to determine $A(\mathcal{T})$.

4.4.2 First-order problem

The amplitude $A(\mathcal{T})$ will be determined by a solvability condition on the first-order problem. To obtain dynamics at leading order, i.e. for A to be a non-constant function of time, either the inertia term or the damping term must come into play at $O(\Delta\mu)$. Assuming that the inertia term enters at this order, we require $\eta = 1/4$. With this choice, at $O(\Delta\mu)$ the beam equation (4.13) becomes

$$L(\tilde{W}_1, \tilde{\tau}_1) = -W_p\left(\frac{\mathrm{d}^2 A}{\mathrm{d}\mathcal{T}^2} + \Lambda\frac{\mathrm{d}A}{\mathrm{d}\mathcal{T}}\right) - A^2\left(2\tau_{\text{fold}}\frac{\mathrm{d}^2 W_p}{\mathrm{d}X^2} + \frac{\mathrm{d}^2 W_{\text{fold}}}{\mathrm{d}X^2}\right), \tag{4.23}$$

where the importance of damping is measured by

$$\Lambda = \upsilon\Delta\mu^{-1/4}.$$

The reason for retaining the damping term at this order will be discussed below. The end-shortening constraint and clamped boundary conditions at $O(\Delta\mu)$ have the form

$$\int_0^1 \frac{\mathrm{d}W_{\text{fold}}}{\mathrm{d}X}\frac{\partial\tilde{W}_1}{\partial X}\mathrm{d}X = -\tfrac{1}{2}A^2\int_0^1\left(\frac{\mathrm{d}W_p}{\mathrm{d}X}\right)^2\mathrm{d}X = -\tfrac{1}{2}I_2 A^2,$$
$$\tilde{W}_{1_X}(0,\mathcal{T}) = 1, \quad \tilde{W}_1(0,\mathcal{T}) = \tilde{W}_1(1,\mathcal{T}) = \tilde{W}_{1_X}(1,\mathcal{T}) = 0,$$

where I_2 was defined in (4.21).

Equation (4.23) features the same linear operator $L(\cdot,\cdot)$ as in the leading-order problem, but now with an inhomogeneous right-hand side. The Fredholm Alternative Theorem (Keener, 1988) implies that solutions exist only for a certain right-hand side, yielding a solvability condition that takes the form of an ODE for $A(\mathcal{T})$. We formulate this condition by multiplying (4.23) by the solution of the homogeneous adjoint problem (which from (4.18)–(4.19) is simply $W_p(X)$ as $L(\cdot,\cdot)$ is self-adjoint), integrating over the domain, and using integration by parts to shift the operator onto the adjoint solution. After applying

the various boundary conditions satisfied by W_{fold}, W_p and $\tilde{W}_1$, we arrive at

$$\frac{\mathrm{d}^2 A}{\mathrm{d}\mathcal{T}^2} + \Lambda \frac{\mathrm{d}A}{\mathrm{d}\mathcal{T}} = C_1 + C_2 A^2, \tag{4.24}$$

where

$$C_1 = \frac{4\tau_{\text{fold}}}{\mu_{\text{fold}}I_1} \approx 329.0, \quad C_2 = \frac{3\tau_{\text{fold}}I_2}{I_1} \approx 417.8, \tag{4.25}$$

and the integrals I_1 and I_2 are as defined in (4.21).

By including the damping term in the first-order problem, it appears that we have implicitly assumed $\Lambda = O(1)$. In the case where damping dominates inertia, we can instead balance the damping term at $O(\Delta\mu)$ (i.e. we choose $\eta = 1/2$ instead of $\eta = 1/4$ prior to (4.23)). This leads to the same equation for A though with only a first-order derivative (and time re-scaled by a factor of $\Delta\mu^{-1/4}$), which is exactly the behaviour of (4.24) in the limit $\Lambda \gg 1$. Similarly, equation (4.24) also holds asymptotically when $\Lambda \ll 1$: the leading order solution in this case is precisely the solution if we neglect the damping term. Hence, equation (4.24) is in fact asymptotically valid for any Λ.

We have now reduced the leading-order dynamics in the bottleneck to the normal form for a saddle-node bifurcation (up to numerical constants), in a similar way to our analysis in Chapter 3. However, the normal form now has a second-order time derivative arising from the beam inertia. We see that the precise form of the boundary conditions applied to the beam again enters only through the dimensionless constants appearing in the normal form, i.e. C_1 and C_2 (as the boundary conditions determine the eigenfunction W_p and fold shape W_{fold}); we therefore expect equation (4.24) to be generic for the dynamics of snap-through.

When $\Lambda \gg 1$, equation (4.24) at leading order reduces to the amplitude equation we studied in Chapter 3, upon re-scaling $\mathcal{T}$ by a factor of Λ (and identifying A with the change in displacement away from the pull-in displacement). Because all terms become $O(1)$ after this re-scaling, the bottleneck duration in this case is $\mathcal{T}_b = O(\Lambda)$. In original dimensionless time, $T = t/t^* = \Delta\mu^{-1/4}\mathcal{T}$, we therefore expect the scaling law

$$T_b = O(v\Delta\mu^{-1/2}),$$

for the duration of the bottleneck, i.e. we inherit the usual inverse square-root scaling. On the other hand if $\Lambda \ll 1$, we expect the bottleneck time is $\mathcal{T}_b = O(1)$, and so we have

$$T_b = O(\Delta\mu^{-1/4}).$$

Hence, the underdamped dynamics changes the exponent typically seen for the slowing

down due to a saddle-node ghost. As expected, the overdamped timescale is always slower, and in either case the timescale satisfies $T_b \gg 1$ provided that $\Delta \mu \ll 1$.

Another important feature of (4.24), regardless of the size of Λ, is that solutions undergo finite-time blow up. This is due to the quadratic forcing term. In fact, as $A \to \infty$, the equation ultimately reduces to a balance between inertia and this nonlinearity:

$$\frac{\mathrm{d}^2 A}{\mathrm{d}\mathcal{T}^2} \sim C_2 A^2,$$

which can be solved (with appropriate matching conditions) to demonstrate blow-up at $\mathcal{T} = \mathcal{T}_\infty < \infty$. Of course, the motions of the strip actually remain bounded during snap-through. Returning to our original asymptotic expansion (4.14), we see that asymptotic validity requires $\tilde{W}_0 \ll \Delta \mu^{-1/2}$ or equivalently $A \ll \Delta \mu^{-1/2}$. As soon as A grows comparable to $\Delta \mu^{-1/2}$ ($\gg 1$), the local analysis presented above breaks down: in terms of the picture in figure 4.4a, this means that the strip has left the vicinity of the fold and is accelerating rapidly towards the natural shape. Nevertheless, our treatment here will allow us to obtain the key quantity of interest, the snapping time, which is dominated by the time spent getting through the bottleneck.

To solve (4.24), we need initial conditions for A and $A_\mathcal{T}$. Recall from the discussion after (4.12) that we impose $|W(X, 0) - W_{\text{fold}}(X)| = O(\Delta \mu)$ and $W_T(X, 0) = 0$. Because the leading-order component enters the asymptotic expansion in (4.14) at $O(\Delta \mu^{1/2})$ ($\gg \Delta \mu$), the initial conditions on A are homogeneous, i.e.

$$A(0) = A_\mathcal{T}(0) = 0. \tag{4.26}$$

With these initial data, we now analyse the solution in the two regimes $\Lambda \ll 1$ and $\Lambda \gg 1$.

4.4.3 Underdamped snap-through: $\Lambda \ll 1$

When $\Lambda \ll 1$, the amplitude equation (4.24) at leading order becomes

$$\frac{\mathrm{d}^2 A}{\mathrm{d}\mathcal{T}^2} = C_1 + C_2 A^2.$$

Multiplying by $A_\mathcal{T}$ and integrating twice with initial conditions (4.26) (taking the positive root for $A_\mathcal{T}$) we obtain the solution in implicit form:

$$\mathcal{T} = \sqrt{\frac{3}{2}} \int_0^{A(\mathcal{T})} \frac{\mathrm{d}\xi}{(3C_1 \xi + C_2 \xi^3)^{1/2}}. \tag{4.27}$$

The right-hand side can be written in terms of elliptic integrals of the first kind, though we do not pursue this here. We check that this solution remains uniformly valid while $A \ll \Delta\mu^{-1/2}$: the ratio of the neglected damping term to the inertia term is

$$\frac{\Lambda A_{\mathcal{T}}}{A_{\mathcal{T}\mathcal{T}}} \sim \sqrt{\frac{2}{3}} \Lambda \left(\frac{\sqrt{3C_1 A + C_2 A^3}}{C_1 + C_2 A^2} \right),$$

and as the bracketed term is bounded for all $A \geq 0$, this remains small when $\Lambda \ll 1$.

At early times when $A \ll 1$, the integrand in (4.27) is dominated by the $3C_1\xi$ term. The solution therefore simplifies to

$$A \sim \frac{C_1}{2}\mathcal{T}^2.$$

(This may also be obtained directly from the ODE). Since $A(\mathcal{T})$ acts as an amplitude of the motions of the strip, we see that the displacement initially grows *quadratically* in time, in contrast to the linear growth we have seen for overdamped systems. At later times when $A \gg 1$, the integrand is dominated by the $C_2\xi^3$ term for large ξ. We then have

$$
\begin{aligned}
\mathcal{T} &= \sqrt{\frac{3}{2}} \int_0^\infty \frac{\mathrm{d}\xi}{(3C_1\xi + C_2\xi^3)^{1/2}} - \sqrt{\frac{3}{2}} \int_{A(\mathcal{T})}^\infty \frac{\mathrm{d}\xi}{(3C_1\xi + C_2\xi^3)^{1/2}}, \\
&\sim \sqrt{\frac{3}{2}} \int_0^\infty \frac{\mathrm{d}\xi}{(3C_1\xi + C_2\xi^3)^{1/2}} - \sqrt{\frac{6}{C_2}} A^{-1/2}.
\end{aligned}
\tag{4.28}
$$

We deduce that $A = O(\Delta\mu^{-1/2})$ when

$$\mathcal{T} = \sqrt{\frac{3}{2}} \int_0^\infty \frac{\mathrm{d}\xi}{(3C_1\xi + C_2\xi^3)^{1/2}} + O(\Delta\mu^{1/4}).$$

Evaluating the integral gives the bottleneck time

$$\mathcal{T}_b \sim \left(\frac{64\pi^2 C_1 C_2}{3} \right)^{-1/4} \Gamma\left(\tfrac{1}{4}\right)^2 \approx 0.179. \tag{4.29}$$

Re-arranging (4.28) also shows that the solution accelerates out of the bottleneck according to the power law

$$A \sim \frac{6}{C_2}(\mathcal{T}_b - \mathcal{T})^{-2}.$$

For comparison, we have solved the full amplitude equation (4.24) with the initial data $A(0) = A_{\mathcal{T}}(0) = 0$ in MATLAB using the routine `ode15s` (relative and absolute error tolerances of size 10^{-10}). The trajectories $A(\mathcal{T})$ at the values $\Lambda = 10^{-3}$, 10^{-2} and 10^{-1} are plotted on log–log axes in figure 4.5; also shown is the asymptotic blow-up time (4.29) (for later reference, trajectories at larger values of Λ are also displayed). We see that the
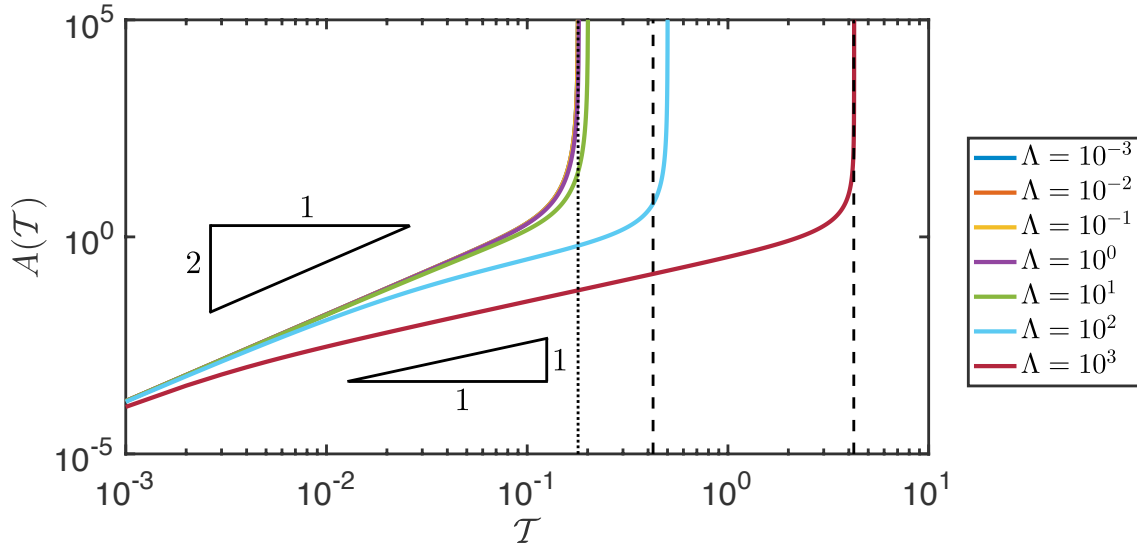
Figure 4.5: *Trajectories $A(\mathcal{T})$ satisfying the amplitude equation (4.24) with initial conditions $A(0) = A_{\mathcal{T}}(0) = 0$ (coloured curves; see legend). Also shown is the predicted bottleneck time (4.29) for $\Lambda \ll 1$ (vertical black dotted line) and the corresponding bottleneck times (4.32) valid for $\Lambda \gg 1$ (vertical black dashed lines).*

curves collapse well for $\Lambda \ll 1$, being indistinguishable on the figure, and clearly show quadratic behaviour at early times.

4.4.4 Overdamped snap-through: $\Lambda \gg 1$

For completeness, we also consider the overdamped limit $\Lambda \gg 1$. We neglect the inertia term in (4.24) to obtain

$$\Lambda \frac{\mathrm{d}A}{\mathrm{d}\mathcal{T}} = C_1 + C_2 A^2. \tag{4.30}$$

(This is equivalent to re-scaling $\mathcal{T}$ by Λ and neglecting terms of $O(\Lambda^{-2})$.) Ignoring the transient around $\mathcal{T} = 0$ where inertia is important (needed to satisfy the initial conditions (4.26)), the solution satisfying $A \to 0$ as $\mathcal{T} \to 0$ is

$$A = \sqrt{\frac{C_1}{C_2}} \tan\left(\frac{\sqrt{C_1 C_2}}{\Lambda}\mathcal{T}\right).$$

As well as showing that A initially grows linearly in time (after the inertial transient), this solution implies that when $A \gg 1$ we have

$$A \sim \frac{\Lambda}{C_2}\left(\frac{\pi}{2\sqrt{C_1 C_2}}\Lambda - \mathcal{T}\right)^{-1}, \tag{4.31}$$

where we have used the expansion $\tan x \sim (\pi/2 - x)^{-1}$ as $x \to \pi/2$.

However, this solution is not uniformly valid. Differentiating (4.30) shows that the corresponding acceleration is $A_{\mathcal{T}\mathcal{T}} = (2C_2/\Lambda)AA_{\mathcal{T}}$. The ratio of the neglected inertia term to the damping term is then

$$\frac{A_{\mathcal{T}\mathcal{T}}}{\Lambda A_{\mathcal{T}}} \sim \frac{2C_2}{\Lambda^2}A.$$

When $A = O(\Lambda^2)$, this ratio becomes $O(1)$ and the solution breaks down. Because $\Lambda \gg 1$, we have that $A \gg 1$ at this point and so (4.31) implies that this occurs when

$$\mathcal{T} = \frac{\pi}{2\sqrt{C_1 C_2}}\Lambda - O(\Lambda^{-1}).$$

Further analysis shows that the solution always blows up inside this interval. Hence, as $A = O(\Delta\mu^{-1/2})$ whenever $\mathcal{T} \sim \pi/(2\sqrt{C_1 C_2})\Lambda$, regardless of the relative sizes of $\Delta\mu^{-1/2}$ and Λ, the bottleneck time to leading order is

$$\mathcal{T}_b \sim \frac{\pi}{2\sqrt{C_1 C_2}}\Lambda. \tag{4.32}$$

The behaviour as the strip leaves the bottleneck is more delicate. If $\Delta\mu^{-1/2} \ll \Lambda^2$, then $A = O(\Delta\mu^{-1/2})$ while the solution (4.31) is still valid, so that

$$A \sim \frac{\Lambda}{C_2}\left(\mathcal{T}_b - \mathcal{T}\right)^{-1}.$$

However, if $\Delta\mu^{-1/2} \gtrsim \Lambda^2$, then the solution leaves the bottleneck when inertia is important again. In particular, if $\Delta\mu^{-1/2} \gg \Lambda^2$, scaling arguments show that the inertia term dominates the damping term at this stage. The power law behaviour is then similar to the underdamped case, i.e.

$$A \sim \frac{6}{C_2}(\mathcal{T}_b - \mathcal{T})^{-2}.$$

The trajectories in the regime $\Lambda \gg 1$ are also shown in figure 4.5, obtained by numerical integration of the amplitude equation (4.24). Because we have not re-scaled time by a factor of Λ, these do not collapse onto a master curve. However, figure 4.5 confirms the linear growth of solutions, and that the blow-up time of trajectories closely follows the leading-order prediction (4.32) (vertical black dashed lines).

4.4.5 Summary

We have shown that while the arch remains close to the equilibrium shape at the fold, its leading-order behaviour obeys

$$W(X,T) \sim W_{\text{fold}}(X) + \Delta\mu^{1/2}A(\mathcal{T})W_p(X),$$

where $W_p(X)$ is the neutrally-stable eigenfunction given by (4.20) and the amplitude $A(\mathcal{T})$ satisfies the ODE (4.24) parameterised by $\Lambda = v\Delta\mu^{-1/4}$. This predicts that the duration of the bottleneck scales as $\mathcal{T}_b = O(1)$ for $\Lambda \ll 1$ (underdamped dynamics) and $\mathcal{T}_b = O(\Lambda)$ for $\Lambda \gg 1$ (overdamped dynamics). In the case when the system is initially at rest near the fold shape, we obtained the bottleneck times (given here in original dimensionless time)

$$
T_b = \frac{t_b}{t^*} \sim \begin{cases} \left(\frac{64\pi^2 C_1 C_2}{3}\right)^{-1/4} \Gamma\left(\tfrac{1}{4}\right)^2 \Delta\mu^{-1/4} \approx 0.179\Delta\mu^{-1/4} & v \ll \Delta\mu^{1/4} \ll 1, \\ \frac{\pi}{2\sqrt{C_1 C_2}} v\Delta\mu^{-1/2} \approx 0.00424\, v\Delta\mu^{-1/2} & \Delta\mu^{1/4} \ll v. \end{cases} \tag{4.33}
$$

We also compute the bottleneck time directly from equation (4.24) for each value of Λ. The power law behaviour as $A \to \infty$ is used to compute $\mathcal{T}_b$ to a relative accuracy Tol by integrating until A has grown sufficiently large to ensure $(\mathcal{T}_b - \mathcal{T})/\mathcal{T}_b <$ Tol. The dependence of $\mathcal{T}_b$ on Λ is plotted on log–log axes in figure 4.6, and for comparison the leading-order predictions in (4.33) are shown. We conclude that the asymptotic analysis captures the behaviour of the amplitude equation (4.24) extremely well for $\Lambda \lesssim 10^{-1}$ and $\Lambda \gtrsim 10^2$. Combining the asymptotic results for $\Lambda \ll 1$ and $\Lambda \gg 1$, we can also form a composite expansion that approximates the behaviour of $\mathcal{T}_b$ for intermediate values of Λ. In this case, we apply an *ad hoc* additive expansion to obtain

$$
\mathcal{T}_b \approx \left(\frac{64\pi^2 C_1 C_2}{3}\right)^{-1/4} \Gamma\left(\tfrac{1}{4}\right)^2 + \frac{\pi}{2\sqrt{C_1 C_2}}\Lambda \approx 0.179 + 0.00424\,\Lambda. \tag{4.34}
$$

As well as yielding the correct behaviour in the limits $\Lambda \ll 1$ and $\Lambda \gg 1$, this approximation is accurate to within 23% when $\Lambda = O(1)$. This is plotted as the red curve in figure 4.6.

4.5 Simulations of the dynamic elastica

The above analysis is based on classical beam theory, and so is formally valid only for arches that are shallow in shape. We now investigate the behaviour of deeper arches using the dynamic elastica equations. These extend beam theory to account for geometrically large displacements, while remaining in the limit of small mechanical strains; this is possible because the cross-section of the strip has dimensions much smaller than its length, i.e. $h, b \ll L$.

4.5.1 Theoretical formulation

To formulate the elastica equations, we parameterise the deformed centreline of the arch as $\mathbf{r}(s,t) = x(s,t)\mathbf{e}_x + y(s,t)\mathbf{e}_y$, where $\mathbf{e}_x$ and $\mathbf{e}_y$ are unit vectors in the x and y directions,
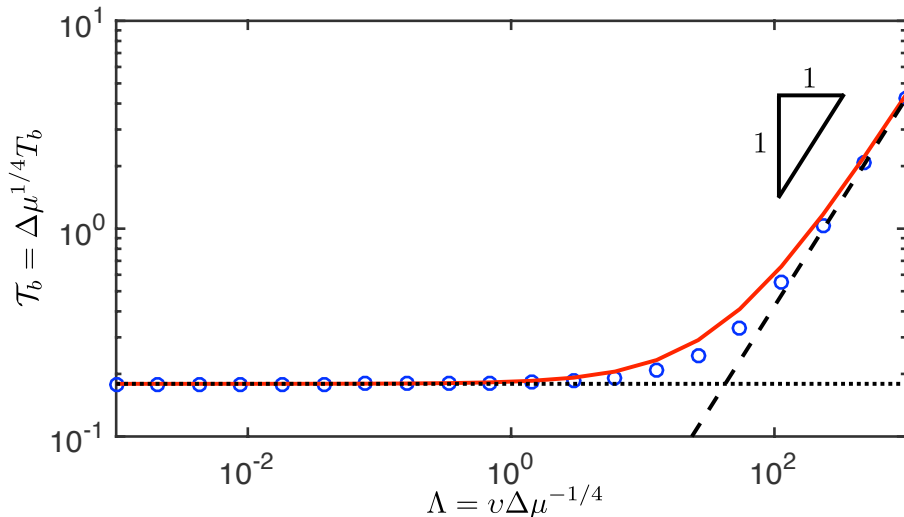
Figure 4.6: *The bottleneck time obtained by numerical integration of* (4.24) *(with initial conditions* $A(0) = A_{\mathcal{T}}(0) = 0$*) until the point when* $(\mathcal{T}_b - \mathcal{T})/\mathcal{T}_b < 10^{-3}$ *(blue circles). The asymptotic results predicted by* (4.33) *in the underdamped regime* $\Lambda \ll 1$ *(black dotted line) and the overdamped regime* $\Lambda \gg 1$ *(black dashed line) are also shown, together with their composite expansion* (4.34) *(red curve).*

and s is arclength measured along the centreline from the left clamp. Modelling the strip as an inextensible, unshearable elastica, the arclength s is then viewed as a Lagrangian coordinate fixed in the deforming strip (Howell *et al.*, 2009). If we again neglect out-of-plane bending and twist about the axis of the strip, its local orientation is completely characterised by the angle $\theta(s, t)$ between the tangent to the centreline and the horizontal; see figure 4.3. In terms of Cartesian components, we have the geometric relation

$$\frac{\partial \mathbf{r}}{\partial s} = \cos \theta \, \mathbf{e}_x + \sin \theta \, \mathbf{e}_y. \tag{4.35}$$

Let $\mathbf{n}(s, t)$ be the resultant force and $\mathbf{m}(s, t)$ be the resultant moment (per unit width) attached to the centreline, obtained by averaging the internal force/moment over the cross-section. The dynamic elastica equations can be derived using a variational approach (see Patricìo *et al.*, 1998, for example), or, alternatively, we can follow McMillen & Goriely (2003) and directly balance linear and angular momentum to yield

$$\frac{\partial \mathbf{n}}{\partial s} = \rho_s h \frac{\partial^2 \mathbf{r}}{\partial t^2} + \Upsilon \frac{\partial \mathbf{r}}{\partial t}, \tag{4.36}$$

$$\frac{\partial \mathbf{m}}{\partial s} + \frac{\partial \mathbf{r}}{\partial s} \times \mathbf{n} = \rho_s I \frac{\partial^2 \theta}{\partial t^2} \mathbf{e}_z. \tag{4.37}$$

Here $I = h^3/12$ is the second moment of area (per unit width) of the rectangular cross-section (Landau & Lifshitz, 1986) and the other quantities are defined as in §4.2. Equations (4.36)–(4.37) are supplemented with the Euler-Bernoulli constitutive law, which states that

the bending moment is proportional to the curvature of the centreline:

$$\mathbf{m} = B\frac{\partial \theta}{\partial s}\mathbf{e}_z, \tag{4.38}$$

where the bending stiffness is $B = EI$.

Non-dimensionalisation

For convenience we now scale all lengths by the length L of the strip, i.e. we set $s = LS$, $\mathbf{r} = L\mathbf{R}$ (so that $x = LX$ and $y = LY$). In addition, we introduce the dimensionless forces $\mathbf{n} = \frac{B}{L^2}\mathbf{N}$. As in §4.2, time is scaled as $t = t^*T$ where $t^* = (\rho_s hL^4/B)^{1/2}$ is the inertial timescale. We insert these scalings into equations (4.36)–(4.37) and the geometric relation (4.35), re-writing the bending moment using the Euler-Bernoulli law (4.38). We also decompose the force resultant as $\mathbf{N} = N_X\mathbf{e}_X + N_Y\mathbf{e}_Y$. In Cartesian components, the full system of dimensionless equations becomes

$$\frac{\partial X}{\partial S} = \cos\theta, \tag{4.39}$$

$$\frac{\partial Y}{\partial S} = \sin\theta, \tag{4.40}$$

$$\frac{\partial N_X}{\partial S} = \frac{\partial^2 X}{\partial T^2} + \upsilon\frac{\partial X}{\partial T}, \tag{4.41}$$

$$\frac{\partial N_Y}{\partial S} = \frac{\partial^2 Y}{\partial T^2} + \upsilon\frac{\partial Y}{\partial T}, \tag{4.42}$$

$$\frac{\partial^2\theta}{\partial S^2} - N_X\sin\theta + N_Y\cos\theta = \mathcal{S}\frac{\partial^2\theta}{\partial T^2},$$

where the dimensionless damping υ is defined as in §4.2, and the importance of rotational inertia is measured by the 'stretchability' parameter (Neukirch *et al.*, 2012; Pandey *et al.*, 2014)

$$\mathcal{S} = \frac{h^2}{12L^2}.$$

Consistent with the small-strain assumption, valid for $h \ll L$, we neglect this term so that the moment balance simplifies to

$$\frac{\partial^2\theta}{\partial S^2} = N_X\sin\theta - N_Y\cos\theta. \tag{4.43}$$

The imposed angles at the clamped ends (figure 4.3) are

$$\theta(0,T) = \alpha, \quad \theta(1,T) = 0. \tag{4.44}$$

The applied end-shortening gives the re-scaled boundary conditions

$$X(0,T) = 0, \quad Y(0,T) = 0,$$
$$X(1,T) = 1 - \frac{\Delta L}{L}, \quad Y(1,T) = 0. \tag{4.45}$$

Note that the geometric relations (4.39)–(4.40) allow the dimensionless displacement of the centreline to be written in terms of $\theta(S,T)$ as

$$\mathbf{R}(S,T) = \left[\int_0^S \cos\theta(\xi,T)\mathrm{d}\xi \right] \mathbf{e}_X + \left[\int_0^S \sin\theta(\xi,T)\mathrm{d}\xi \right] \mathbf{e}_Y. \tag{4.46}$$

Setting $S = 1$, the final two conditions in (4.45) can instead be written as integral constraints on $\theta(S,T)$, namely

$$\int_0^1 \cos\theta(S,T) \, \mathrm{d}S = 1 - \frac{\Delta L}{L}, \quad \int_0^1 \sin\theta(S,T) \, \mathrm{d}S = 0. \tag{4.47}$$

The problem is closed with initial conditions for θ and θ_T, which will be specified later.

Relationship to beam theory

Because the elastica generalises classical beam theory to geometrically large displacements, we recover the beam equations derived in §4.2 to leading order when $\theta \ll 1$. The details of this reduction are provided in Appendix 4.A, which shows that in this limit we can identify

$$S \sim X, \quad \theta \sim \frac{\partial Y}{\partial X}, \quad Y \sim \left(\frac{\Delta L}{L} \right)^{1/2} W, \quad N_X \sim -\tau^2, \quad N_Y \sim N_x \frac{\partial Y}{\partial X} - \frac{\partial^3 Y}{\partial X^3}, \tag{4.48}$$

where W is the dimensionless displacement of the shallow arch with corresponding compressive force τ (defined in §4.2.2). The factor of $(\Delta L/L)^{1/2}$ necessary to relate W and Y is because of the different vertical lengthscale used in the non-dimensionalisation in this section.

4.5.2 Equilibrium shapes

We first consider the equilibrium solutions of the elastica equations. Neglecting the time derivatives in (4.41)–(4.42) shows that the force components N_X and N_Y are constant along the length of the arch. We then solve the moment balance (4.43) subject to the boundary conditions (4.44) and integral constraints (4.47). Unfortunately, we cannot scale the end-shortening ΔL out of these equations, as we did with the beam model in

§4.2; the behaviour of the arch now depends on the individual values of α and $\Delta L/L$, rather than the combination $\mu = \alpha(\Delta L/L)^{-1/2}$. Nevertheless, we shall still talk of varying μ in this case, though of course solutions with the same μ will not, in general, map to one another. Throughout this section we focus on the scenario in which $\alpha > 0$ is fixed while the dimensionless end-shortening $\Delta L/L$ is quasi-statically varied; the opposite case may be treated in a similar way.

While it may be possible to make analytical progress using elliptic functions, we do not pursue this here. For each value of α and $\Delta L/L$, we instead solve the boundary-value problem numerically by discretising in S and solving the resulting set of algebraic equations (we later use this technique to solve the dynamic equations; for details of the discretisation scheme see §4.5.3 below and also Appendix 4.B). The result is a similar response diagram to that predicted by beam theory. Crucially, the bifurcation structure is preserved: at large end-shortenings $\Delta L/L$ (corresponding to small values of μ), both inverted and natural equilibrium shapes exist, while the inverted equilibrium disappears at a saddle-node bifurcation as $\Delta L/L$ is decreased (larger μ). This is shown in figure 4.7a, where we have plotted the equilibrium modes in terms of the vertical midpoint displacement $Y(1/2)$ (for clarity only results for values of $\Delta L/L$ in a neighbourhood of the bifurcation point are plotted). In figure 4.7b we re-scale the data to plot the corresponding values of $W(1/2) = (\Delta L/L)^{-1/2}Y(1/2)$ as a function of μ. With this re-scaling, and for sufficiently small clamp angles $\alpha \lesssim \pi/6$, the branches collapse onto the predictions of beam theory (obtained in §4.3) as expected. At larger values $\alpha \gtrsim \pi/4$, we observe a small shift in the branches and the location of the saddle-node bifurcation.

4.5.3 Dynamics

Numerical solution

To solve the dynamic elastica equations (4.39)–(4.45) we use the method of lines. More specifically, we discretise the arclength S on a uniform mesh composed of $(N + 1)$ grid points in the interval $[0, 1]$. We use a second-order centered difference to approximate the derivative appearing in (4.43), and we apply the trapezium rule to compute the integrals appearing in (4.46) and (4.47). In this way, the problem reduces to a system of differential algebraic equations (DAEs), consisting of $(N - 1)$ ODEs in time and algebraic constraints that enforce the boundary conditions $X(1, T) = 1 - \Delta L/L$ and $Y(1, T) = 0$. We are able to demonstrate second-order accuracy in the convergence of our numerical scheme as N is increased; further details of the scheme and convergence plots are provided in Appendix 4.B.
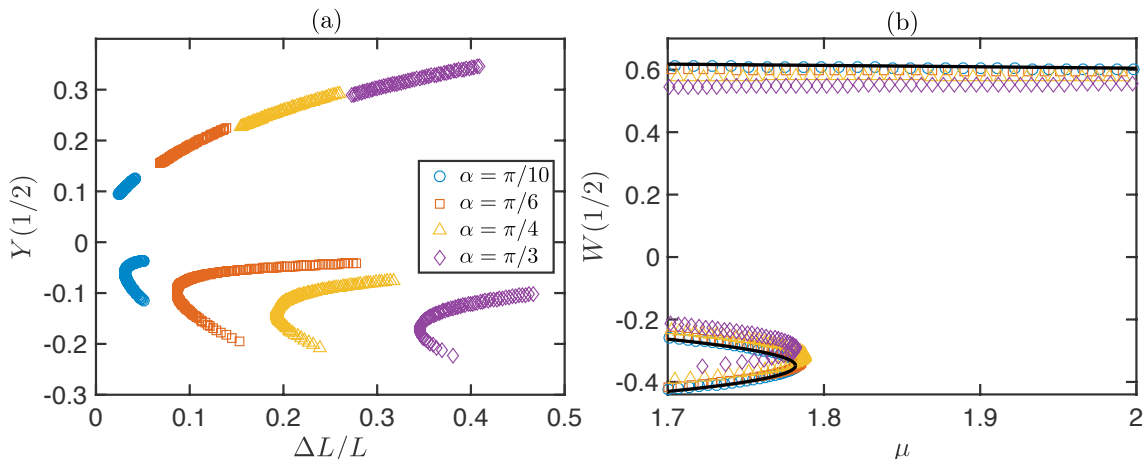
Figure 4.7: *(a) Response diagram of the equilibrium solutions of* (4.43) *subject to* (4.44) *and* (4.47)*, plotted in terms of the dimensionless midpoint height* $Y(1/2)$*. Numerical results are shown when* α *is fixed while the end-shortening* $\Delta L/L$ *is varied quasi-statically (symbols; see legend), obtained by solving the discretised equations (with* $N = 100$*; see §4.5.3). The upper branches* $(Y(1/2) > 0)$ *correspond to the natural shape, while the lower branches* $(Y(1/2) < 0)$ *correspond to the inverted shape; the connected branches above each fold point are unstable. (b) Re-scaling the data in terms of* $W(1/2) = (\Delta L/L)^{-1/2}Y(1/2)$ *as a function of* $\mu = \alpha(\Delta L/L)^{-1/2}$*. Also shown for comparison are the predictions from beam theory using equations* (4.9)–(4.10) *(solid black curves).*

We use the same initial conditions considered for the shallow arch in §4.4: the arch starts at rest in a shape that is near the equilibrium shape at the fold, using an indenter to impose the midpoint displacement $W(1/2, 0) = W_{\mathrm{fold}}(1/2)$. When the indenter is removed at $T = 0$, the arch then snaps to the natural shape. This is achieved within our numerical scheme by the following procedure. We first determine the location of the fold point, and the corresponding equilibrium solution, using the continuation algorithm described in Appendix 4.B. Because we fix the clamp angle $\alpha > 0$, this corresponds to a critical end-shortening $\Delta L_{\mathrm{fold}}/L$ and associated midpoint height $Y_{\mathrm{fold}}(1/2)$. We perturb the system beyond the fold, i.e. we set

$$\Delta L = \Delta L_{\mathrm{fold}}(1 - \epsilon),$$

where $0 < \epsilon \ll 1$. We then solve for the indented shape (and the associated force components) using a modified form of our steady equations, accounting for an (unknown) transverse point force at the arch midpoint needed to satisfy the additional constraint $Y(1/2) = Y_{\mathrm{fold}}(1/2)$ (see §4.B.3 in Appendix 4.B). The corresponding solution then serves as the initial data. We use the indented shape and bifurcation value ΔL_{fold} from the discretised system, rather than solving the steady elastica equations directly (e.g. using `bvp4c` in MATLAB); this eliminates the sensitivity of the bottleneck dynamics to errors in these quantities (we discussed a similar point in Chapter 3 in the context of solving the dynamic microbeam equations; see Appendix 3.B there).

The system of DAEs are integrated numerically for each damping coefficient v using the routine `ode15s`, to output the trajectory at each grid point in the discretisation scheme. For all simulations reported in this chapter we specify $N = 100$, a relative error tolerance of 10^{-8} and an absolute error tolerance of 10^{-3} in `ode15s`. We also limit the maximum time step of the solver to 10^{-4}. We have checked that our results are insensitive to further increasing N, decreasing these tolerances or decreasing the maximum time step.

To allow us to relate the solutions to those obtained by beam theory, we note that the above perturbation to ΔL is equivalent to setting (recall equation (4.11))

$$\frac{\Delta \mu}{\mu_{\text{fold}}} = (1 - \epsilon)^{-1/2} - 1 \approx \frac{\epsilon}{2}.$$

Using $\mu_{\text{fold}} \approx 1.7818$, the corresponding value of Λ, measuring the importance of damping during the bottleneck phase, is then

$$\Lambda = v \Delta \mu^{-1/4} \approx 0.8655 \, v \left[(1 - \epsilon)^{-1/2} - 1 \right]^{-1/4} \approx 1.0293 \, v \epsilon^{-1/4}.$$

Underdamped snap-through: $\Lambda \ll 1$

Typical trajectories of the arch midpoint height, $Y(1/2, T)$, when the system is underdamped are shown in figure 4.8a. Here we have varied the perturbation ϵ, while choosing the dimensionless damping v to ensure that $\Lambda = 10^{-2}$; results are shown for a relatively shallow clamp angle $\alpha = \pi/6$ ($30°$), and a much deeper angle $\alpha = \pi/3$ ($60°$). We see that the arch passes through a slow bottleneck phase before accelerating upwards, with the duration of the bottleneck increasing as ϵ decreases. The midpoint then reaches a turning point before undergoing underdamped oscillations about the natural shape (these are prolonged due to the small amount of damping; for clarity only the start of these oscillations is plotted).

We re-scale the trajectories in terms of the amplitude variable $A(\mathcal{T})$ as a function of re-scaled time $\mathcal{T} = \Delta \mu^{1/4} T$; recall from §4.4.1 that A characterises the growth of the displacement during the bottleneck phase. Combining equations (4.22) and (4.48) (setting $X = 1/2$), the variable A is related to $Y(1/2, \mathcal{T})$ via

$$A(\mathcal{T}) = \Delta \mu^{-1/2} \left(\frac{\Delta L}{L} \right)^{-1/2} \frac{Y(1/2, \mathcal{T}) - Y_{\text{fold}}(1/2)}{W_p(1/2)}, \tag{4.49}$$

where $W_p(1/2) \approx 0.3324$ follows from (4.20). This re-scaling is shown in figure 4.8b, and shows that the different trajectories collapse onto the prediction from beam theory over a large portion of the bottleneck phase. In particular, we are able to collapse trajectories

Figure 4.8: *Dynamics of underdamped snap-through* ($\Lambda = 10^{-2}$). *(a) Midpoint trajectories obtained by numerical integration of the elastica equations (coloured curves; see legend). (b) Rescaling the trajectories to plot the amplitude variable $A(\mathcal{T})$ (defined in (4.49)) as a function of re-scaled time $\mathcal{T} = \Delta\mu^{1/4}T$. For comparison, the trajectory predicted by the amplitude equation (4.24) is shown (black dotted curve).*

at the larger clamp angle $\alpha = \pi/3$ and for moderately small perturbations $\epsilon \lesssim 10^{-1}$. The quadratic growth is also evident and is well captured by the leading-order dynamics predicted by the amplitude equation (4.24).

At later times, when the solution to (4.24) undergoes finite-time blow up, the numerical trajectories no longer collapse (see the inset of figure 4.8b); this corresponds to the loss of asymptotic validity as soon as A reaches $O(\Delta\mu^{-1/2})$. Nevertheless, since the growth by this point is rapid anyway (due to the quadratic nonlinearity in (4.24)), we see that the blow-up time will lead to an accurate prediction of the bottleneck duration. At very early times ($\mathcal{T} \lesssim 10^{-2}$) the trajectories also do not collapse and differ from the asymptotic solution. This is because equation (4.24) is only asymptotically valid when $A \gg \Delta\mu^{1/2}$: at smaller values, the higher-order terms of $O(\Delta\mu)$ in the asymptotic expansions we made during the bottleneck analysis (recall (4.14)–(4.15)) must be considered.

Overdamped snap-through: $\Lambda \gg 1$

The corresponding trajectories in the overdamped limit, $\Lambda \gg 1$, are shown in figure 4.9a. In this case the arch displays a more pronounced bottleneck phase, due to the additional (external) damping in the system. Figure 4.9b shows that excellent agreement with the asymptotic prediction (4.24) may again be obtained, which confirms that the growth throughout the bulk of the bottleneck is linear in time (the quadratic behaviour at early times, which occurs due to an initial transient where inertia is important, is exaggerated due to the log–log axes). Outside of this interval, where asymptotic validity is lost, we see
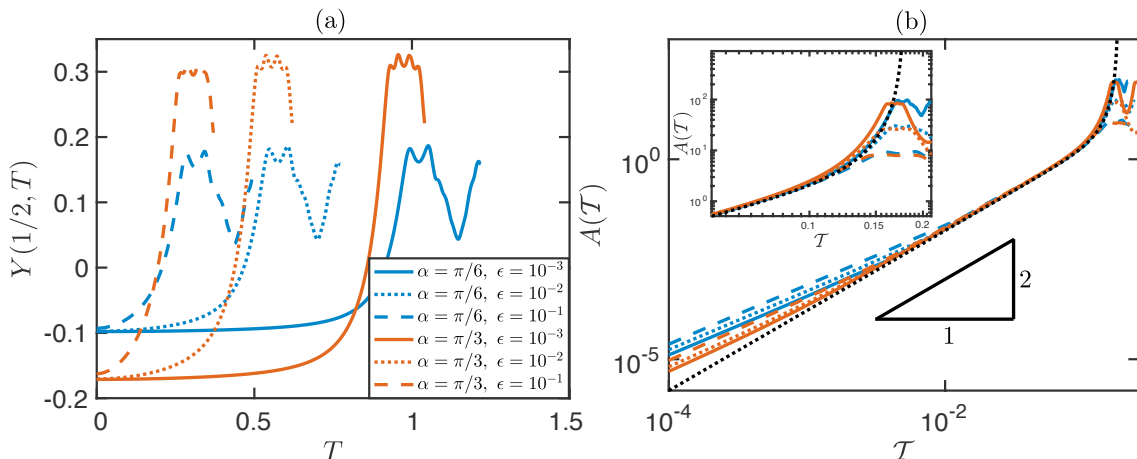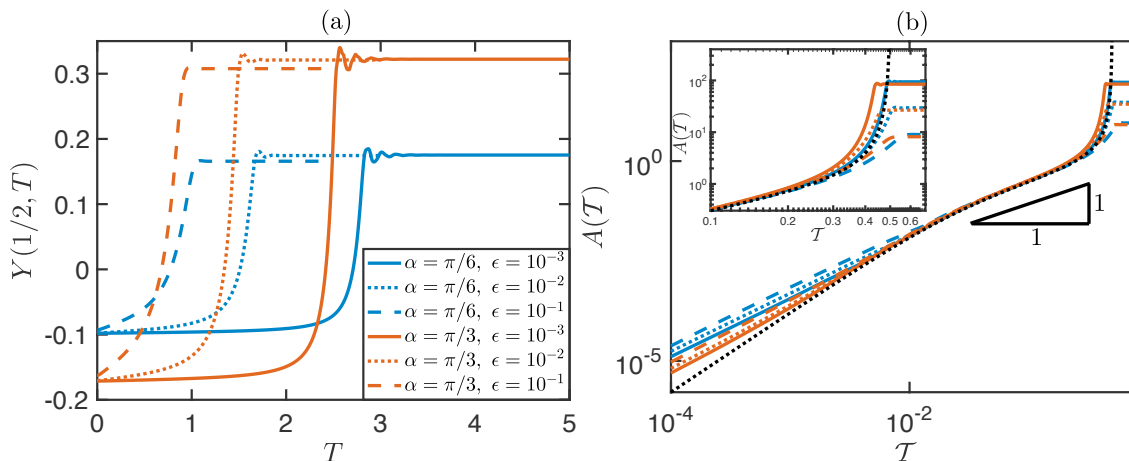
Figure 4.9: *Dynamics of overdamped snap-through ($\Lambda = 10^2$). (a) Midpoint trajectories obtained by numerical integration of the dynamic elastica equations for different clamp angle α and perturbation ϵ beyond the snap-through bifurcation (coloured curves; see legend). (b) Re-scaling the trajectories to plot the amplitude variable $A(\mathcal{T})$ (defined in (4.49)) as a function of re-scaled time $\mathcal{T} = \Delta\mu^{1/4}T$, the data collapse onto the solution of the amplitude equation (4.24) (black dotted curve).*

a similar picture as in the underdamped regime, though now the arch rapidly comes to rest in the natural state without prolonged oscillations.

Comparison of snap-through times

We define the snap-through time T_{snap} to be the time when the velocity of the midpoint equals zero, i.e. the point at which the arch begins to reverse its motion and oscillate about the natural shape. (When the arch is overdamped and instead relaxes to equilibrium without oscillating, we define T_{snap} to be the time at which the midpoint velocity decreases below 10^{-3}.) This allows us to measure the duration of the bottleneck in a consistent way, though we note that the value is relatively insensitive to the precise definition of T_{snap}, since the snap-through time is always dominated by the duration of the bottleneck.

The re-scaled snap-through times, $\mathcal{T}_{\mathrm{snap}} = \Delta\mu^{1/4}T_{\mathrm{snap}}$, are shown in figure 4.10 for a range of numerical simulations. We see that the snap-through time is in good agreement with the prediction of beam theory, both for non-shallow arches and for moderately small perturbations ϵ, consistent with the agreement observed for the trajectories. We expect that it is possible to perform a similar bottleneck analysis in the full elastica equations, since the asymptotic method we presented relies only on the underlying bifurcation structure; hence it is not so surprising that our asymptotics also captures the scaling behaviour of non-shallow arches. However, what is remarkable is that the pre-factors are also well approximated by beam theory, despite the fact that this is formally valid only for $\alpha \ll 1$.
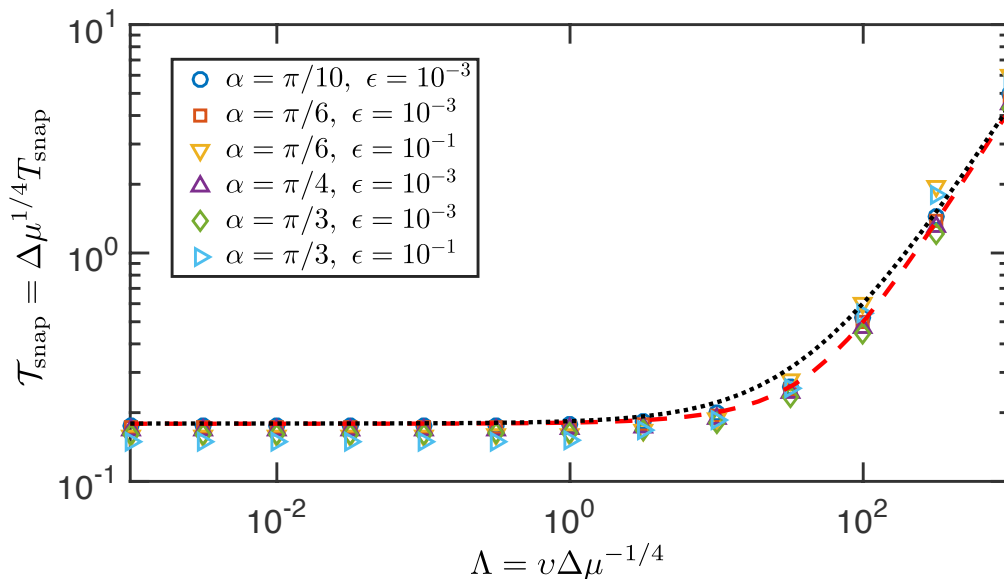
Figure 4.10: *The snap-through time obtained by simulations of the dynamic elastica (symbols; see legend); for each data set, Λ has been varied by changing the damping υ. For comparison the bottleneck time obtained by numerical integration of the amplitude equation (4.24) is shown (red dashed curve), together with the composite asymptotic expansion (4.34) (black dotted curve).*

4.6 Experiments

We have shown that near the snap-through transition, the dimensional snap-through time increases according to

$$t_b \approx \left(0.179\,\Delta\mu^{-1/4} + 0.00424\,\upsilon\Delta\mu^{-1/2}\right) t^*,$$

valid for shallow arches with $0 < \Delta\mu \ll 1$; here $\Delta\mu$ measures the normalised 'distance' to the snap-through bifurcation, υ is the dimensionless damping coefficient, and t^* is the inertial timescale. In §4.5, we also showed that this prediction approximates well the behaviour of arches that are not shallow in shape. In particular, for underdamped dynamics where $\upsilon \ll \Delta\mu^{1/4}$, critical slowing down still occurs, albeit with a modified exponent (1/4 rather than 1/2 for overdamped dynamics). As $\Delta\mu \to 0$, this means that the inertial timescale will significantly underestimate the observed snap-through time. To test this scaling law, and the extent to which t^* fails to predict the snap-through time for realistic values of $\Delta\mu$, we now consider experiments on real samples.

4.6.1 Experimental methods

To obtain dynamics that were effectively underdamped, we used arches composed of bi-axially oriented polyethylene terephthalate (PET) film (Goodfellow, Cambridge, $\rho_s =$
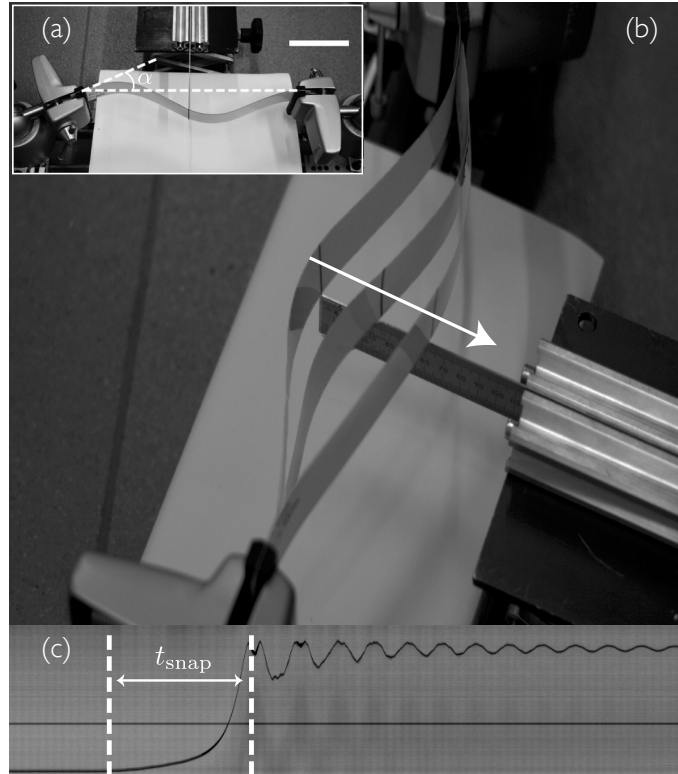
Figure 4.11: *Experimental setup used to investigate the snap-through dynamics of the arch system. (a) Top view showing the strip buckled into an unstable inverted state with an end-shortening past the snapping transition, $\Delta L < \Delta L_{\text{fold}}$; a metal indenter prevents the strip from snapping by making contact at its midpoint and imposes $w(L/2, 0) = w_{\text{fold}}(L/2)$. Scale bar 10 cm. (b) The indenter is then lowered allowing the arch to snap (three successive stages superimposed). (c) A spatio-temporal plot of the midpoint reveals its trajectory during snapping (PET, $L = 240$ mm, $\alpha = 21.34°$, $\Delta L_{\text{fold}} = 10.41$ mm, $w_{\text{fold}}(L/2) = -16.75$ mm, $\Delta L = 10.20$ mm). The montage begins before the point when the indenter loses contact with the strip, and ends as the arch oscillates about the natural shape (the horizontal line is at zero displacement). Slices through a total of 828 frames (separated by 1 ms) are shown. (Reprinted from Gomez et al. (2017a), DOI: https://doi.org/10.1038/nphys3915.)*

1.337 g cm^{-3}, $h = 0.35$ mm, $E = 5.707$ GPa). As experiments were conducted at room temperature, well below the glass transition temperature of PET, this material acts as a glassy polymer, showing little viscous creep and dynamic dissipation (Demirel *et al.*, 2011; Yilmazer *et al.*, 2000). To study the effect of different material properties, we also performed experiments on stainless steel rolled shim (304 grade, RS components, $\rho_s = 7.881 \text{ g cm}^{-3}$, $h = 0.1$ mm, $E = 203.8$ GPa). The value of the Young's modulus E for each material was determined by analysing the frequency of small-amplitude vibrations of the arch. The timescale of snapping was varied by changing the natural length of the strip: for PET we used lengths $L \in \{240, 290, 430\}$ mm while for steel we used $L \in \{140, 280\}$ mm.

The ends of each strip were clamped into vice clamps (PanaVise 301) which were

mounted onto a linear track so that the strip deformed in one plane only. To minimise the effect of gravity, the strip was oriented sideways so its width was along the vertical direction; see figure 4.11a. The right clamp was fixed parallel to the track, while the left clamp held the strip at an angle $\alpha \neq 0$ (constant throughout each experiment) and could be moved along the track to vary the applied end-shortening ΔL. We note that finer control could be obtained using this method, rather than the alternative case in which ΔL is fixed and α is varied. A digital camera mounted above the left clamp allowed α to be determined to an accuracy of $\pm 2°$, and changes in ΔL to be measured to an accuracy of ± 200 μm (by measuring displacement of the clamp from a known reference state).

In each experiment, the strip was first placed in the inverted equilibrium shape with a large enough end-shortening, ΔL, so that the system was bistable. We then decreased ΔL quasi-statically in small steps, measuring the steady midpoint displacement, $w(L/2)$, until the strip snapped. The bifurcation value ΔL_{fold}, and the corresponding midpoint displacement, $w_{\text{fold}}(L/2)$, was determined experimentally (further details are provided in Appendix 4.C).

For values $\Delta L < \Delta L_{\text{fold}}$, the strip then snaps upwards to the natural shape. To enforce the initial condition that the arch starts at rest close to the fold shape, we used a metal ruler (tip width 1 mm) to impose the midpoint displacement $w(L/2, 0) = w_{\text{fold}}(L/2)$. The ruler was attached to a laboratory jack that was lowered vertically out of contact with the strip to allow snapping to proceed (figure 4.11b). The snapping dynamics were filmed using a high speed camera (Phantom Miro 310) at a frame rate of 1000 fps. The camera was placed vertically above the strip, allowing the midpoint position (marked on the edge) to be recorded when the strip was in motion. For each movie, we crop around the midpoint position and convert the movie to a spatio-temporal plot (montage) of the midpoint trajectory using ImageJ (NIH); a typical plot is shown in figure 4.11c. This shows how the arch passes through an initial bottleneck phase before accelerating to the natural shape, after which the arch undergoes prolonged underdamped oscillations. While it is not clear from the montage when the indenter is lowered and snapping begins, this can be determined using a fitting procedure (described in Appendix 4.D), from which the midpoint trajectory can be extracted.

4.6.2 Experimental results

With the start of the snap determined (and set to be $t = 0$), typical plots of the midpoint trajectories are shown in figure 4.12a. This confirms that the displacement of the midpoint initially grows quadratically in time, in contrast to the exponential growth that is
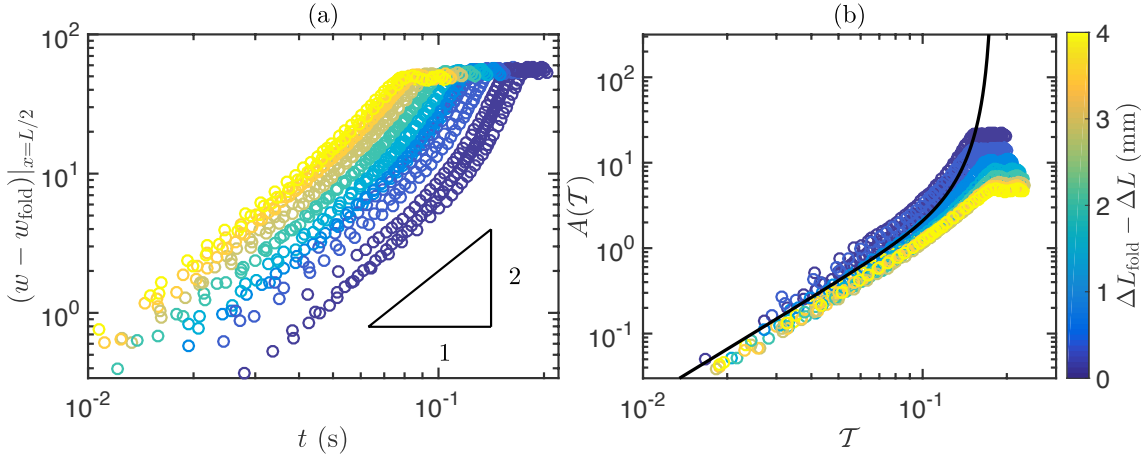
Figure 4.12: *Midpoint trajectories during snapping. (a) Evolution of the midpoint position, $w(L/2, t)$, away from the initial value $w_{\mathrm{fold}}(L/2)$ (PET, $L = 290$ mm, $\alpha = 19.85°$, $\Delta L_{\mathrm{fold}} = 9.20$ mm, $w_{\mathrm{fold}}(L/2) = -20.95$ mm). For each value of $\Delta L_{\mathrm{fold}} - \Delta L$ (given by the colourbar), three runs are recorded and shown here (circles). (Data is plotted only until the strip begins to oscillate about the natural shape.) (b) The data of (a), rescaled in terms of the amplitude variable $A(\mathcal{T})$ (defined in (4.50)) as a function of dimensionless time $\mathcal{T} = \Delta\mu^{1/4}t/t^*$, collapse onto the predicted asymptotic behaviour (4.27) (solid black curve) while A is small. (Reprinted from Gomez et al. (2017a), DOI: https://doi.org/10.1038/nphys3915.)*

commonly observed in systems at the onset of instability (Pandey *et al.*, 2014). In addition, the dynamics slow down systematically as the system approaches the snap-through transition, with the trajectories shifted further to the right as $\Delta L \nearrow \Delta L_{\mathrm{fold}}$.

In figure 4.12b, we re-scale the experimental trajectories in terms of the amplitude variable $A(\mathcal{T})$, defined in equation (4.22) above but now setting $X = 1/2$:

$$A(\mathcal{T}) = \Delta\mu^{-1/2}(L\Delta L)^{-1/2}\frac{w(L/2, \mathcal{T}) - w_{\mathrm{fold}}(L/2)}{W_p(1/2)}. \tag{4.50}$$

Here we compute $\Delta\mu$ using the experimentally determined value of ΔL_{fold} rather than the theoretical value, since this is consistent with the behaviour of the strip prior to snap-through (Appendix 4.C). We see that this rescaling collapses the trajectories onto a single master curve reasonably well. We have also superimposed the solution (4.27) predicted by the bottleneck analysis in the underdamped limit, which compares favourably to the experimental trajectories while $A \lesssim 1$ (note that data is not available at very early times $\mathcal{T} \lesssim 10^{-2}$, when we observed a deviation from the asymptotic solution for the elastica simulations reported in §4.5). For $A \gg 1$, the asymptotic analysis breaks down and fails to predict how the arch approaches the natural equilibrium and oscillates.

We note that there is some dispersion of the data in figure 4.12b about the numerically predicted $A(\mathcal{T})$. We attribute this dispersion to uncertainty in the measured value of ΔL (± 200 μm), which increases the relative error in $\Delta\mu$ as ΔL approaches ΔL_{fold}. Figure
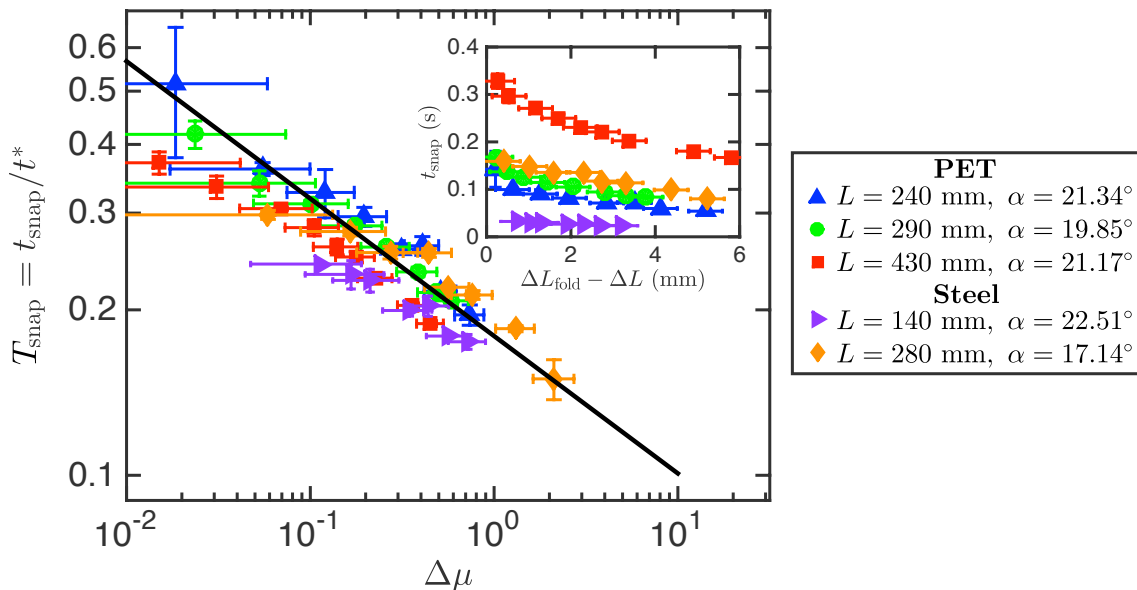
Figure 4.13: *Slowing down of snapping dynamics. Inset: Experimentally measured snapping times, t_{snap}, as the end-shortening ΔL approaches ΔL_{fold} (symbols; see legend). Main plot: Snapping times, re-scaled by the inertial timescale t^*, as a function of the normalised distance to bifurcation $\Delta\mu = \mu - \mu_{fold}$. The data collapse onto the asymptotic prediction $T_{snap} \approx 0.179\Delta\mu^{-1/4}$ from beam theory (solid black line). Horizontal error bars correspond to the uncertainties in measurements of α ($\pm 2°$) and ΔL (± 200 μm); vertical error bars correspond to the standard deviation of the measured snapping times over three runs. (Reprinted from Gomez et al. (2017a), DOI: https://doi.org/10.1038/nphys3915.)*

4.17 in Appendix 4.D shows the experimentally determined $A(\mathcal{T})$ that were not shown in figure 4.12b; these experiments were performed with other lengths L and strips made of either PET or steel, and show that a better collapse can be obtained.

As in §4.5, for each experiment we define the snap-through time, t_{snap}, to be the time when the arch reaches the first peak of vibrations and its velocity is zero (labelled in figure 4.11c); here we average the value over three runs. The measured times obtained in this way are shown in the inset of figure 4.13, which confirms the systematic slowing down near the snap-through transition. In the main panel of the figure, we show that the underdamped bottleneck prediction $T_b \approx 0.179\Delta\mu^{-1/4}$ leads to a collapse of the data for strips composed of different materials and natural lengths L, and predicts the dependence on $\Delta\mu$ well; in particular, the data are consistent with the $\Delta\mu^{-1/4}$ scaling law even up to values $\Delta\mu = O(1)$ where our asymptotic analysis is no longer strictly valid.

The data in figure 4.13 and the expression for the snap-through time, $T_b \approx 0.179\Delta\mu^{-1/4}$, show that as the system approaches the snap-through transition the dynamics slow down significantly. However, we note that the pre-factor (≈ 0.179) is small, meaning that the snap-through time is comparable to the characteristic elastic timescale t^* for experimentally attainable $\Delta\mu$, which here is on the order of 0.1 s. In other systems the appropriate

pre-factor may be substantially larger and finer control of the distance to bifurcation $\Delta\mu$ may be possible; in such circumstances we expect that a substantial disparity between the observed snap-through time and the characteristic elastic timescale t^* may then emerge.

4.7 Summary and discussion

In various areas of physics, delay phenomena have been shown to be a consequence of being close to a critical transition — a phenomenon often referred to as critical slowing down (Scheffer *et al.*, 2009; Chaikin & Lubensky, 1995). In this chapter, we have shown that macroscopic snap-through instabilities exhibit a very similar phenomenology. Our central result is that a delay in the dynamics can be due to the ghost of a saddle-node bifurcation, and that this behaviour should be generically expected near the loss of stability. This can occur over purely elastic timescales and requires no additional physics. In such scenarios, the timescale of the delay is not necessarily the relaxation timescale of the material, as has often been assumed in the literature (Forterre *et al.*, 2005; Santer, 2010).

We have studied an elastic arch as a simple model system to gain insight. Using beam theory (which is valid for shallow arches), we identified the parameter $\mu = \alpha(\Delta L/L)^{-1/2}$ that arises naturally as the only control parameter in the (steady) problem. This is the first time the parameter has been identified in the context of pre-stressed arches, i.e. those that are formed by buckling a planar strip (see the discussion in Brinkmeyer *et al.*, 2013). By interpreting μ as the ratio of bending and stretching energies, we see that the mechanism underlying snap-through is the system finding a shape with lower bending energy. This is similar to the situation seen in shallow spherical caps, which are characterised by an analogous geometric parameter (Fitch, 1968; Brodland & Cohen, 1987).

Because a linear stability analysis was not applicable, we analysed the snapping dynamics using the perturbation method we developed in Chapter 3 for electrostatic pull-in. The key difference here is that bistability and snap-through behaviour arises from geometric nonlinearity (due to the end-shortening applied to the arch) rather than from an external field, and inertial forces were considered as well as external damping. Nevertheless, we were able to adapt the perturbation method and reduce the leading-order dynamics to the normal form for a saddle-node bifurcation, now with a second-order time derivative due to beam inertia. As a result, the snapping dynamics inherit the critical slowing down near a saddle-node bifurcation and the displacement grows ballistically rather than exponentially. A detailed analysis of the amplitude equation revealed two possible regimes depending on the importance of damping compared to the 'distance' to the snap-through transition in parameter space, with different scaling laws for the snap-through time. In particular, in the underdamped limit ($\Lambda \ll 1$), the displacement grows quadratically

and the bottleneck time $T_b = O(\Delta\mu^{-1/4})$, a different exponent to that typically seen in critical slowing down; if damping dominates ($\Lambda \gg 1$), the displacement grows linearly and we recover the well-known inverse square-root law $T_b = O(\upsilon\Delta\mu^{-1/2})$. These regimes were confirmed by numerical simulations of the dynamic elastica and experiments in the underdamped case, extending our conclusions to arches that are not necessarily shallow in shape.

The importance of critical slowing down in elastic instabilities such as snap-through has not been appreciated previously, despite numerous experiments showing signs of diverging timescales as the threshold is approached (Hung & Senturia, 1999; Brinkmeyer *et al.*, 2012; 2013; Urbach & Efrati, 2017). We note that biological systems such as the Venus flytrap may be particularly prone to such a slowing down, as approach to snap-through is often controlled by slow processes such as swelling or growth of tissues; hence we expect that the analogue of $\Delta\mu$ may attain very small values. However, such processes also introduce dynamic effects so that the above analysis does not apply (we assume the system is quasi-statically placed beyond the snap-through transition). It would be interesting to understand how this affects the snap-through dynamics, and if the scaling laws for the snap-through time change as a result. In particular, dynamic effects may cause a delayed bifurcation, as has been observed in other physical systems such as a semiconductor laser (Tredicce *et al.*, 2004) and phase transitions in liquid crystals (Majumdar *et al.*, 2013).

In both biological and engineering settings, snap-through would seem to require a trade-off between the speed of snapping (a faster snap requiring larger $\Delta\mu$) and the time/energy taken to attain a large $\Delta\mu$. Our analysis, combined with techniques for controlling snap-through such as solvent-induced swelling (Holmes & Crosby, 2007) or photo-initiation (Shankar *et al.*, 2013), may offer the possibility to tune the timescale of snap-through from fast to slow by controlling how far beyond the transition one takes the system.

Critical slowing down may also mean that very close to the snap-through transition the system becomes overdamped (rather than inertial), so that the precise nature of the damping present needs to be considered, for example viscoelasticity in man-made applications (Brinkmeyer *et al.*, 2013) or poroelasticity in biological systems (Forterre *et al.*, 2005; Skotheim & Mahadevan, 2005). However, unlike external damping which we considered in this chapter, stress relaxation associated with viscoelasticity can change the effective stiffness of a structure, and hence modify when snap-through occurs. It therefore remains unclear how viscoelasticity influences the snap-through dynamics, and what role material relaxation plays in obtaining anomalously slow dynamics, as opposed to the purely elastic slowing down studied here. We turn to these questions in the next chapter.

Appendix 4.A   Reducing the elastica equations to classical beam theory

Assuming $\theta \ll 1$, we may approximate $\cos\theta \sim 1$ and $\sin\theta \sim \theta$ ignoring terms of $O(\theta^2)$. The geometrical relations (4.39)–(4.40) then simplify to

$$\frac{\partial X}{\partial S} = 1, \quad \frac{\partial Y}{\partial S} = \theta. \tag{4.51}$$

Using $X(0,T) = 0$, we can integrate the first relation to give that $X(S,T) = S$. Hence for a shallow arch, the arclength at a point along the centreline can be identified with its horizontal coordinate, and since the centreline is inextensible there is no horizontal displacement to leading order. Returning to the horizontal momentum balance (4.41), we see that the component N_X of the force resultant cannot vary along the length of the strip, i.e. $N_X = N_X(T)$. Differentiating the moment balance (4.43) once with respect to S, and making use of the vertical momentum balance (4.42) and the second relation in (4.51), we obtain the usual beam equation in terms of the vertical displacement Y:

$$\frac{\partial^2 Y}{\partial T^2} + \upsilon \frac{\partial Y}{\partial T} + \frac{\partial^4 Y}{\partial X^4} - N_X \frac{\partial^2 Y}{\partial X^2} = 0.$$

The boundary conditions (4.44)–(4.45) become (subscripts denoting differentiation)

$$Y_X(0,T) = \alpha, \quad Y(0,T) = Y(1,T) = Y_X(1,T) = 0.$$

Observe that to apply the end-shortening (4.47) we must *globally* retain terms of $O(\theta^2)$: neglecting these terms would lead to the statement $0 = \Delta L/L$. Note that this is consistent with our linear equations above, since the $O(\theta^2)$ terms there were neglected on a *local* basis. Ignoring only higher-order terms of $O(\theta^4)$, this reduces to

$$\frac{1}{2} \int_0^1 \left(\frac{\partial Y}{\partial X} \right)^2 \, \mathrm{d}X = \frac{\Delta L}{L}.$$

Finally, we recover the dimensionless beam equations given in §4.2 upon re-scaling

$$Y = \left(\frac{\Delta L}{L} \right)^{1/2} W, \quad N_X = -\tau^2.$$

Appendix 4.B   Details of the numerical scheme

To solve the dynamic elastica equations, we discretise the interval $[0,1]$ using a uniform mesh with spacing $\Delta S = 1/N$ ($N \geq 2$ is a fixed integer). We write $S_i = i\Delta S$ ($i =$

$0, 1, 2, \ldots, N$) for the ith grid point, with corresponding position vector $\mathbf{r}_i = (X_i, Y_i)^{\mathrm{T}}$. We also let $\theta_i(T)$ be the numerical approximation to $\theta(S, T)$ at the grid point S_i. We use the angles θ_i as generalised coordinates here, i.e. we write the discretised system of equations in terms of θ_i rather than the position vectors $\mathbf{r}_i$; this approach avoids having to introduce N constraints to enforce inextensibility of the centreline on each interval (S_i, S_{i+1}).

To obtain explicit equations for each θ_i, we first integrate (4.41)–(4.42) to write the force components as

$$
N_X(S, T) = P(T) + \int_0^S \frac{\partial^2 X}{\partial T^2} + v \frac{\partial X}{\partial T} \mathrm{d}\xi, \tag{4.52}
$$

$$
N_Y(S, T) = Q(T) + \int_0^S \frac{\partial^2 Y}{\partial T^2} + v \frac{\partial Y}{\partial T} \mathrm{d}\xi, \tag{4.53}
$$

where $P(T)$ and $Q(T)$ are unknown (these act as Lagrange multipliers to enforce the end-shortening constraints). To achieve second-order accuracy in the convergence of our numerical scheme, we use the trapezium rule for quadrature. For a general function $f(S, T)$, we then have that for each $i = 1, 2, \ldots, N-1$

$$
\int_0^{S_i} f(S, T) \, \mathrm{d}S \approx \frac{\Delta S}{2} \sum_{k=0}^{i-1} \left[f(S_{k+1}, T) + f(S_k, T) \right],
$$

$$
= \frac{\Delta S}{2} \left[f(0, T) + \sum_{k=1}^{N-1} U_{ik} f(S_k, T) \right],
$$

where in the last equality we have introduced the $(N-1) \times (N-1)$ upper triangular matrix $U = (U_{ij})$ where

$$
U_{ij} = \begin{cases} 0 & i < j, \\ 1 & i = j, \\ 2 & i > j. \end{cases}
$$

Setting $f(S, T) = \cos \theta(S, T)$ and $f(S, T) = \sin \theta(S, T)$ in turn, and using the fact that $\theta_0 = \alpha$, we obtain

$$
X(S_i, T) \approx \frac{\Delta S}{2} \left[\cos \alpha + \sum_{k=1}^{N-1} U_{ik} \cos \theta_k \right],
$$

$$
Y(S_i, T) \approx \frac{\Delta S}{2} \left[\sin \alpha + \sum_{k=1}^{N-1} U_{ik} \sin \theta_k \right], \quad i = 1, 2, \ldots, N-1.
$$

It follows that

$$
\left(\frac{\partial^2 X}{\partial T^2} + \upsilon\frac{\partial X}{\partial T}\right)\bigg|_{S=S_i} \approx -\frac{\Delta S}{2}\sum_{k=1}^{N-1}U_{ik}\left[\left(\frac{\mathrm{d}^2\theta_k}{\mathrm{d}T^2} + \upsilon\frac{\mathrm{d}\theta_k}{\mathrm{d}T}\right)\sin\theta_k + \left(\frac{\mathrm{d}\theta_k}{\mathrm{d}T}\right)^2\cos\theta_k\right],
$$

$$
\left(\frac{\partial^2 Y}{\partial T^2} + \upsilon\frac{\partial Y}{\partial T}\right)\bigg|_{S=S_i} \approx \frac{\Delta S}{2}\sum_{k=1}^{N-1}U_{ik}\left[\left(\frac{\mathrm{d}^2\theta_k}{\mathrm{d}T^2} + \upsilon\frac{\mathrm{d}\theta_k}{\mathrm{d}T}\right)\cos\theta_k - \left(\frac{\mathrm{d}\theta_k}{\mathrm{d}T}\right)^2\sin\theta_k\right].
$$

Substituting the above into (4.52), we may then approximate the force component N_X as (making use of $X(0,T)=0$)

$$
\begin{aligned}
N_X(S_i,T) &\approx P(T) + \frac{\Delta S}{2}\sum_{j=1}^{N-1}U_{ij}\left(\frac{\partial^2 X}{\partial T^2} + \upsilon\frac{\partial X}{\partial T}\right)\bigg|_{S=S_j}, \\
&\approx P(T) - \frac{\Delta S^2}{4}\sum_{j=1}^{N-1}U_{ij}\sum_{k=1}^{N-1}U_{jk}\left[\left(\frac{\mathrm{d}^2\theta_k}{\mathrm{d}T^2} + \upsilon\frac{\mathrm{d}\theta_k}{\mathrm{d}T}\right)\sin\theta_k + \left(\frac{\mathrm{d}\theta_k}{\mathrm{d}T}\right)^2\cos\theta_k\right].
\end{aligned}
$$

$$(4.54)$$

Similarly, using (4.53) and $Y(0,T)=0$, we have

$$
N_Y(S_i,T) \approx Q(T) + \frac{\Delta S^2}{4}\sum_{j=1}^{N-1}U_{ij}\sum_{k=1}^{N-1}U_{jk}\left[\left(\frac{\mathrm{d}^2\theta_k}{\mathrm{d}T^2} + \upsilon\frac{\mathrm{d}\theta_k}{\mathrm{d}T}\right)\cos\theta_k - \left(\frac{\mathrm{d}\theta_k}{\mathrm{d}T}\right)^2\sin\theta_k\right].
$$

$$(4.55)$$

We approximate the $\partial^2\theta/\partial S^2$ term appearing in the moment balance (4.43) using a second-order centered difference on the interior grid points. Upon substituting the approximations (4.54)–(4.55), and making use of the addition formulae for $\sin(\theta_i - \theta_k)$ and $\cos(\theta_i - \theta_k)$, equation (4.43) becomes, for $i = 1, 2, \ldots, N-1$,

$$
\begin{aligned}
&\frac{\theta_{i+1} - 2\theta_i + \theta_{i-1}}{\Delta S^2} - P\sin\theta_i + Q\cos\theta_i \\
&= -\frac{\Delta S^2}{4}\sum_{j=1}^{N-1}U_{ij}\sum_{k=1}^{N-1}U_{jk}\left[\left(\frac{\mathrm{d}^2\theta_k}{\mathrm{d}T^2} + \upsilon\frac{\mathrm{d}\theta_k}{\mathrm{d}T}\right)\cos(\theta_i - \theta_k) + \left(\frac{\mathrm{d}\theta_k}{\mathrm{d}T}\right)^2\sin(\theta_i - \theta_k)\right].
\end{aligned}
$$

$$(4.56)$$

The boundary conditions (4.44) give

$$
\theta_0 = \alpha, \quad \theta_N = 0. \tag{4.57}
$$

The imposed end-shortening $X(1,T) = 1 - \Delta L/L$ and $Y(1,T) = 0$ (recall (4.45)) leads to

the algebraic constraints

$$\frac{\Delta S}{2}\left[\cos\alpha + 1 + 2\sum_{k=1}^{N-1}\cos\theta_k\right] = 1 - \frac{\Delta L}{L},$$

$$\frac{\Delta S}{2}\left[\sin\alpha + 2\sum_{k=1}^{N-1}\sin\theta_k\right] = 0. \tag{4.58}$$

To write the system in matrix form, we introduce the column vectors of length $(N-1)$

$$\begin{aligned}
\boldsymbol{\Theta} &= (\theta_1, \theta_2, \ldots, \theta_{N-1})^{\mathrm{T}}, \\
\mathbf{s} &= (\sin\theta_1, \sin\theta_2, \ldots, \sin\theta_{N-1})^{\mathrm{T}}, \\
\mathbf{c} &= (\cos\theta_1, \cos\theta_2, \ldots, \cos\theta_{N-1})^{\mathrm{T}}, \\
\mathbf{e}_1 &= (1, 0, \ldots, 0)^{\mathrm{T}}.
\end{aligned}$$

We define the $(N-1)\times(N-1)$ upper triangular matrices $A = (A_{ij})$ and $B = (B_{ij})$ where

$$\begin{aligned}
A_{ij} &= \cos(\theta_i - \theta_j)(U^2)_{ij}, \\
B_{ij} &= \sin(\theta_i - \theta_j)(U^2)_{ij}.
\end{aligned}$$

We also define the $(N-1)\times(N-1)$ tridiagonal matrix

$$D = \frac{1}{\Delta S^2}\begin{pmatrix}
-2 & 1 & & & \\
1 & -2 & 1 & & \\
& \ddots & \ddots & \ddots & \\
& & 1 & -2 & 1 \\
& & & 1 & -2
\end{pmatrix}.$$

The system of equations (4.56) can then be written as

$$A\frac{\mathrm{d}^2\boldsymbol{\Theta}}{\mathrm{d}T^2} + \left[vA + B\,\mathrm{diag}\left(\frac{\mathrm{d}\boldsymbol{\Theta}}{\mathrm{d}T}\right)\right]\frac{\mathrm{d}\boldsymbol{\Theta}}{\mathrm{d}T} = \frac{4}{\Delta S^2}\left[P\mathbf{s} - Q\mathbf{c} - \frac{\alpha}{\Delta S^2}\mathbf{e}_1 - D\boldsymbol{\Theta}\right], \tag{4.59}$$

where we write diag($\mathbf{a}$) for the diagonal matrix whose diagonal entries are the entries of the vector $\mathbf{a}$. Together with the constraints (4.58), these equations constitute a system of differential algebraic equations (DAEs) since the unknown functions $P(T)$ and $Q(T)$ do not explicitly enter (4.58). It is convenient to reduce the index of the system by differentiating

(4.58) once, which can then be written in the form

$$\Delta S \, \mathbf{s}^{\mathrm{T}} \frac{\mathrm{d}\boldsymbol{\Theta}}{\mathrm{d}T} = 0,$$
$$\Delta S \, \mathbf{c}^{\mathrm{T}} \frac{\mathrm{d}\boldsymbol{\Theta}}{\mathrm{d}T} = 0.$$

The numerical solution then satisfies (4.58) (to within numerical tolerances) provided that the initial data are consistent with (4.58). Together with (4.59), the DAE system can then easily be written in mass-matrix form (with singular mass matrix) and integrated numerically using the MATLAB ODE solvers. We note that it is possible to obtain explicit expressions for the Lagrange multipliers P and Q (up to the solution of a linear system) and hence avoid a singular mass matrix (Ruhoff *et al.*, 1996); alternatively, using the impetus-striction method, the system can be rephrased as an unconstrained Hamiltonian system in which the constraints (4.58) are automatically satisfied (Dichmann & Maddocks, 1996). However, we found that the formulation here can be efficiently integrated using the routine `ode15s`, once the sparsity pattern of the mass matrix is specified (for example the matrix A is upper triangular); simulations using $N = 100$ typically complete in under a minute on a laptop computer. We also note that the matrices A and B can be efficiently constructed by applying the routine `meshgrid` to the vector $\boldsymbol{\Theta}$.

4.B.1 Equilibrium solutions

Setting the time derivatives to zero in (4.59) shows that equilibrium solutions satisfy

$$D\boldsymbol{\Theta} = P\mathbf{s} - Q\mathbf{c} - \frac{\alpha}{\Delta S^2}\mathbf{e}_1, \tag{4.60}$$

together with (4.58). We solve these algebraic equations in MATLAB using the routine `fsolve` to determine $\boldsymbol{\Theta}$ and the unknown force components P and Q. To obtain a response diagram as we vary the dimensionless end-shortening $\Delta L/L$, we implement the numerical solver into a continuation algorithm. Rather than controlling $\Delta L/L$, however, we instead control P and solve for the corresponding value of $\Delta L/L$ at each stage. This allows us to use a simple continuation algorithm that continues past the saddle-node bifurcation without any convergence issues (when controlling $\Delta L/L$, the bifurcation diagram exhibits a vertical fold near which a small change in $\Delta L/L$ produces a large change in the solution). In dealing with the different solution branches, we use the analytical solutions predicted by beam theory (derived in §4.3) as initial guesses, relating these to $\boldsymbol{\Theta}$, P and Q using (4.48).
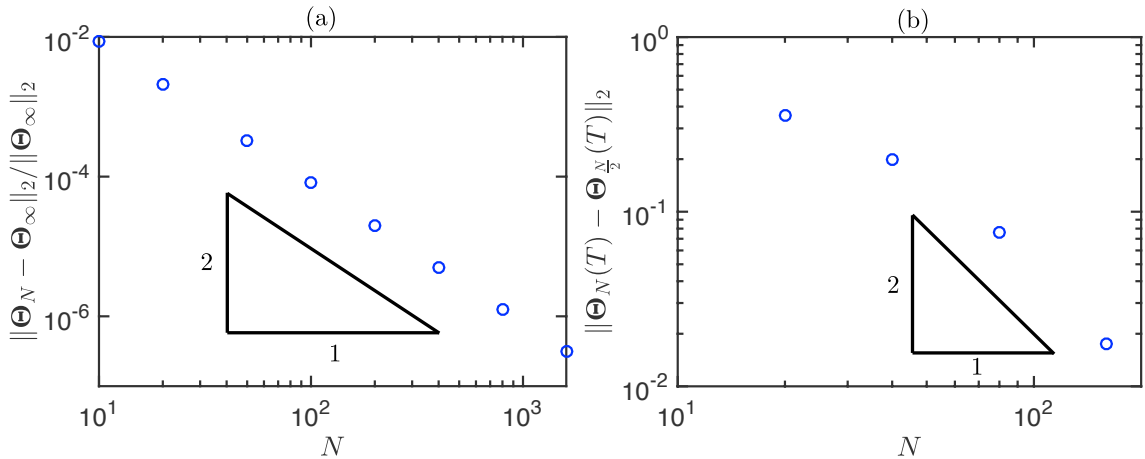
Figure 4.14: (a) Relative error between the solution to the steady problem using N grid points, $\mathbf{\Theta}_N$, and the 'exact' solution $\mathbf{\Theta}_\infty$ (obtained by solving the ODE boundary-value problem using `bvp4c`), as N is increased (here $\alpha = \pi/6$ and $\Delta L/L = 10^{-1}$). (b) Difference between successive approximations obtained by numerical integration up to dimensionless time $T = 1$ during snapping ($\alpha = \pi/6$, $\epsilon = 10^{-3}$, $\upsilon = 1$).

4.B.2 Convergence plots

We check convergence of our numerical scheme using two approaches. In the first approach, we solve the equilibrium problem at a fixed value of α and $\Delta L/L$ (using an error tolerance of 10^{-10} for `fsolve`). We denote the solution for $\mathbf{\Theta}$ using spacing $\Delta S = 1/N$ as $\mathbf{\Theta}_N$. We then compare these to the solution obtained by solving the steady elastica equations (i.e. the ODE (4.43), boundary conditions (4.44) and integral constraints (4.47)) directly in MATLAB using the solver `bvp4c`, which employs a collocation method (error tolerances 10^{-10}); we denote the corresponding solution evaluated on the grid points in our discretisation by $\mathbf{\Theta}_\infty$. The particular case $\alpha = \pi/6$ and $\Delta L/L = 10^{-1}$ is shown in figure 4.14a, which confirms that second-order accuracy is indeed obtained, with the relative error

$$\frac{||\mathbf{\Theta}_N - \mathbf{\Theta}_\infty||_2}{||\mathbf{\Theta}_\infty||_2} = O(N^{-2}) \quad \text{as} \quad N \to \infty.$$

(Similar convergence is observed in the force components.) Figure 4.14a also shows that using $N = 100$ results in a relative error that is around 10^{-4} (this is also observed with other values of α and $\Delta L/L$).

In the second test of convergence, we integrate the dynamic equations for fixed values of α, ϵ and υ up to a specified time T during the snapping motion. We denote the solution for $\mathbf{\Theta}$ using spacing $\Delta S = 1/N$ as $\mathbf{\Theta}_N(T)$. In the absence of an 'exact' solution in this case, we instead compare the differences between successive approximations as N is increased. A typical plot is shown in figure 4.14b (setting $\alpha = \pi/6$, $\epsilon = 10^{-3}$, $\upsilon = 1$ and $T = 1$),

which suggests that the differences $||\boldsymbol{\Theta}_N - \boldsymbol{\Theta}_{N/2}||_2$ form a Cauchy sequence with

$$||\boldsymbol{\Theta}_N(T) - \boldsymbol{\Theta}_{N/2}(T)||_2 = O(N^{-2}) \quad \text{as} \quad N \to \infty.$$

4.B.3 Solving for the indented shape

To solve for the indented arch shape, we must account for a point force at the arch midpoint $S = 1/2$. The magnitude of this force, F_{ind}, is unknown and must be determined as part of the solution, so that the imposed midpoint displacement

$$Y(1/2) = Y_{\text{fold}}(1/2),$$

is satisfied. Assuming the indentation force acts purely in the transverse direction, this introduces a jump in the force resultant N_Y of size F_{ind} at $S = 1/2$. The steady moment balance (4.43) then becomes

$$\frac{\partial^2 \theta}{\partial S^2} = \begin{cases} P \sin \theta - (Q - F_{\text{ind}}) \cos \theta & 0 < s < 1/2, \\ P \sin \theta - Q \cos \theta & 1/2 < s < 1, \end{cases}$$

for unknown P and Q, which is to be solved with the boundary conditions (4.44) and (4.47) and additional constraints

$$\int_0^{1/2} \sin \theta \, \mathrm{d}S = Y_{\text{fold}}(1/2), \quad \left[\theta\right]_{1/2-}^{1/2+} = \left[\frac{\partial \theta}{\partial S}\right]_{1/2-}^{1/2+} = 0.$$

The latter conditions ensure that θ and $\partial\theta/\partial S$ are continuous across $S = 1/2$, to avoid a corner (with infinite bending energy).

In our numerical scheme, considering N even, the midpoint of the arch corresponds to the grid point $i = N/2$ and the jump conditions above are automatically satisfied. The steady equations (4.60) then become

$$D\boldsymbol{\Theta} = P\mathbf{s} - Q\mathbf{c} - \frac{\alpha}{\Delta S^2}\mathbf{e}_1 + F_{\text{ind}} \begin{pmatrix} I_{N/2-1} & 0_{N/2-1,N/2} \\ 0_{N/2,N/2-1} & 0_{N/2} \end{pmatrix} \mathbf{c},$$

and we include the additional constraint

$$\frac{\Delta S}{2} \left[\sin \alpha + \sin \theta_{N/2} + 2 \sum_{k=1}^{N/2-1} \sin \theta_k \right] = (Y_{\text{fold}})_{N/2},$$

where $(Y_{\text{fold}})_{N/2}$ is the vertical displacement of the equilibrium solution at the fold, evaluated at the grid point $i = N/2$.

Appendix 4.C   Determining the snapping transition in experiments

The dimensional bifurcation diagram obtained by varying ΔL quasi-statically is shown in figure 4.15a. The bifurcation point, ΔL_{fold}, was never observed exactly: when we decreased ΔL, we introduced perturbations that caused snap-through slightly before the fold was reached. We determined ΔL_{fold} by fitting the data points close to the transition to a parabola (dotted curves in figure 4.15a). This best-fit parabola also predicted the corresponding midpoint position at the bifurcation point, $w_{\text{fold}}(L/2)$, which was then the midpoint displacement fixed by the indenter in experiments. Note that this fitting procedure only needed to be performed once for each strip.

In determining the bifurcation diagram experimentally, various errors were introduced in the measurement of the angle α and the end-shortening ΔL. To plot the dimensionless bifurcation diagram, we therefore allow the value of α to be varied (within the limits of experimental uncertainty, $\pm 2°$) so that the experimentally determined fold point is as close as possible to that predicted theoretically. The result, plotted in terms of $\mu = \alpha(\Delta L/L)^{-1/2}$, is compared with the result of beam theory in figure 4.15b. The fitted position of the fold, μ_{fold} (as predicted from the best-fit parabola), is displayed in each case (dotted vertical lines). Because the snapping dynamics depend sensitively on the size of $\Delta\mu = \mu - \mu_{\text{fold}}$, the theoretical value of μ_{fold} (≈ 1.7818) is not used to calculate $\Delta\mu$; instead, we use the shifted values of α, and the corresponding fitted values of μ_{fold}, since this is consistent with the observed behaviour of the strip prior to snapping. Throughout §4.6.2 we refer to the shifted value of α for each experiment.

Appendix 4.D   Measuring the snap-through dynamics

The montage in figure 4.11c begins before the indenter lost contact with the strip, and it is not clear from these plots *when* the snapping motion first occurs. This start of the motion is key to the snapping time, and so this point must be carefully determined. The values of $w(L/2, t_{\text{raw}})$ are determined from each montage, with t_{raw} denoting the raw time (measured from an arbitrary point in the montage). Figure 4.16a shows a typical set of trajectories obtained in this way for snap-through at different values of $\Delta L < \Delta L_{\text{fold}}$; these are plotted in terms of the change in midpoint position away from the value imposed by the indenter, $\Delta w_{\text{mid}} \equiv (w - w_{\text{fold}})|_{x=L/2}$. Even without the moment of release determined, a semi–log plot of Δw_{mid} would reveal a straight line if the initial growth of the instability were exponential (as predicted if a standard linear stability analysis were applicable). This plot (figure 4.16b) does not indicate such an exponential growth.
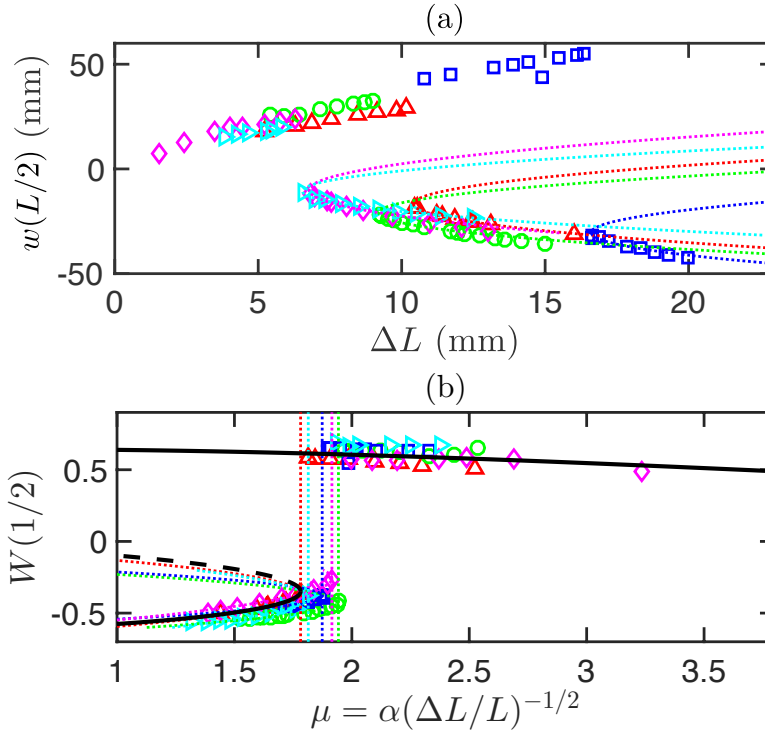
Figure 4.15: *(a) Midpoint position of equilibrium shapes as a function of the applied end-shortening, ΔL. Data is shown for PET strips with $L = 240$ mm (red upward-pointing triangles), $L = 290$ mm (green circles) and $L = 430$ mm (blue squares). Also plotted is data for steel strips with $L = 140$ mm (cyan right-pointing triangles) and $L = 280$ mm (magenta diamonds). The lower branches (i.e. with $w(L/2) < 0$) correspond to the inverted shape while the upper branches (i.e. with $w(L/2) > 0$) correspond to the natural shape after snap-through has occurred. In each case the best-fit (least-squares) parabola through the 6 points closest to the snapping transition is shown (dotted curves). (b) The same data plotted in dimensionless terms, where α has been chosen within the range of experimental uncertainty ($\pm 2°$) so that the fitted bifurcation points (vertical dotted lines) are close to the theoretical value $\mu_{\mathrm{fold}} \approx 1.7818$. The final points are $\mu_{\mathrm{fold}} \approx 1.7884$, $\alpha = 21.34°$ (red upward-pointing triangles), $\mu_{\mathrm{fold}} \approx 1.9452$, $\alpha = 19.85°$ (green circles), $\mu_{\mathrm{fold}} \approx 1.8800$, $\alpha = 21.17°$ (blue squares), $\mu_{\mathrm{fold}} \approx 1.8174$, $\alpha = 22.51°$ (cyan right-pointing triangles), and $\mu_{\mathrm{fold}} \approx 1.9236$, $\alpha = 17.14°$ (magenta diamonds). The prediction from beam theory (reproduced from figure 4.4a) is also shown (black curves). (Reprinted from Gomez et al. (2017a), DOI: https://doi.org/10.1038/nphys3915.)*
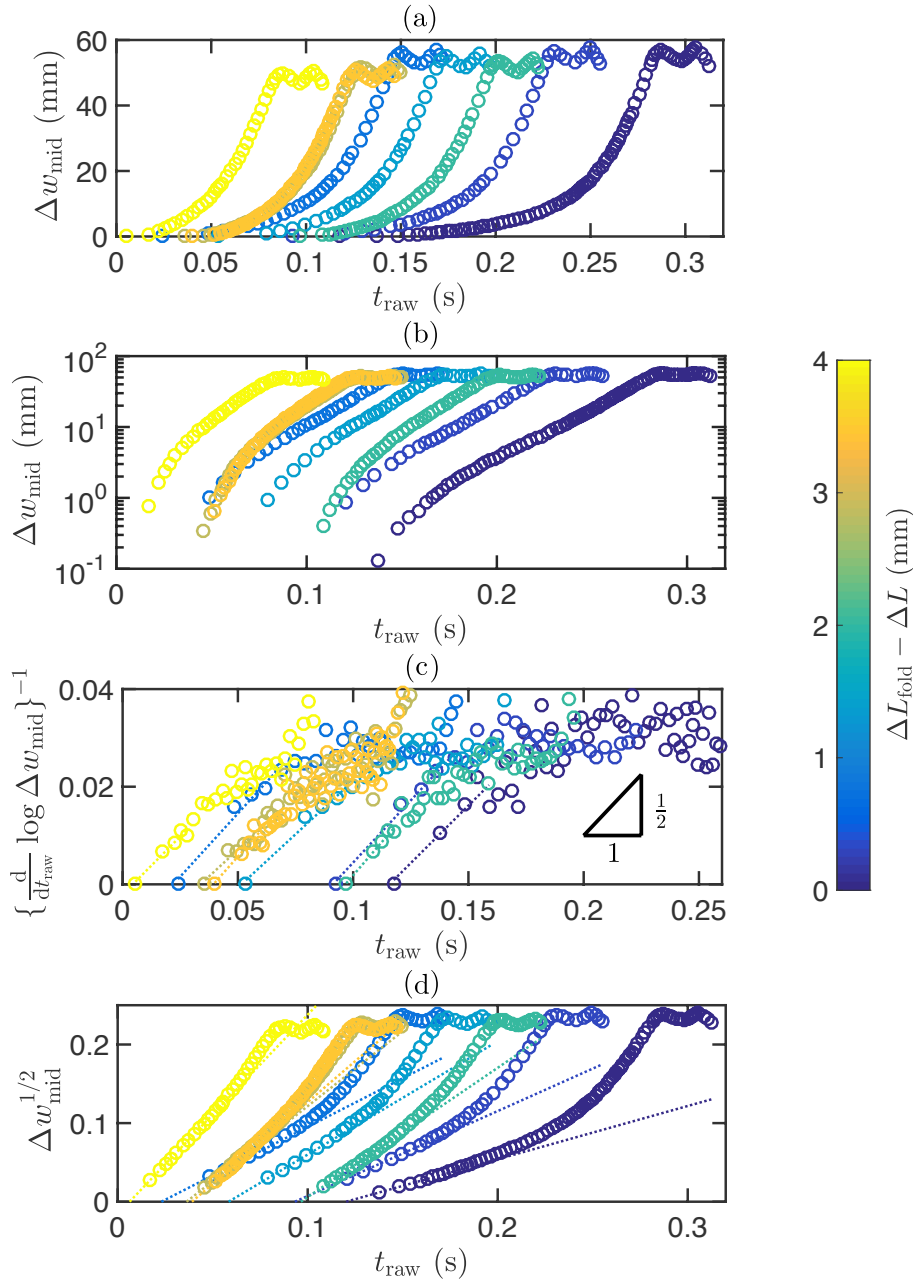
Figure 4.16: *Midpoint trajectories during snap-through (PET, $L = 290$ mm, $\alpha = 19.85°$, $\Delta L_{\mathrm{fold}} = 9.20$ mm, $w_{\mathrm{fold}}(L/2) = -20.95$ mm). (a) Evolution of the midpoint displacement from its initial value, $\Delta w_{\mathrm{mid}} = (w - w_{\mathrm{fold}})|_{x=L/2}$. For each end-shortening (given by the colourbar), the snapping motion begins at some time $t_{\mathrm{raw}} = t_0 > 0$ that is not known. (Note that data is plotted only until the strip begins to oscillate about the natural shape.) (b) The same data plotted on semi–log axes do not suggest the presence of a classical linear instability in the initial motion (which would be indicated by a phase of exponential growth). (c) Rescaling the data according to the right-hand side of (4.62) (numerical differentiation was performed using forward differences). A linear (least-squares) fit over the first 5 points in each case (dotted lines) gives the estimates $\beta \approx \{2.12, 1.96, 1.93, 2.29, 1.83, 2.29, 1.87, 2.10\}$ given in increasing order of $\Delta L_{\mathrm{fold}} - \Delta L$; these are all consistent with the expected quadratic growth, $\beta = 2$. (d) Rescaling the data according to the power-law (4.61) with $\beta = 2$, together with the best-fit line over the first 5 points in each case (dotted lines). This allows the start time of snapping, t_0, to be determined from the intercept with the horizontal axis. (Reprinted from Gomez et al. (2017a), DOI: https://doi.org/10.1038/nphys3915.)*

If we instead assume power-law growth of the form

$$\Delta w_{\mathrm{mid}} \propto (t_{\mathrm{raw}} - t_0)^{\beta}, \tag{4.61}$$

where t_0 is the time when contact is first lost and $\beta > 0$ is an (unknown) exponent, then

$$\frac{t_{\mathrm{raw}} - t_0}{\beta} = \left\{ \frac{\mathrm{d}}{\mathrm{d}t_{\mathrm{raw}}} \log \Delta w_{\mathrm{mid}} \right\}^{-1}. \tag{4.62}$$

A plot of the experimentally determined right-hand side of (4.62) as a linear function of t_{raw} is shown in figure 4.16c. Despite the noise in the plot (which is due to numerical differentiation of the logarithm of our experimental data, as in (4.62)), we see that our data is entirely consistent with $\beta = 2$, i.e. the strip deflection grows quadratically in time, as predicted by our bottleneck analysis in §4.4.

A further check that the growth is quadratic is to plot the square root of the midpoint displacement as a function of t_{raw} on linear axes (figure 4.16d). This confirms a linear behaviour at early times, and allows us to determine the start of the snap, t_0, from the intercept of the best-fit line with the horizontal axis. (We use the plotting procedure indicated in figure 4.16d to determine t_0 because this is less susceptible to noise than the approach used in figure 4.16c.)
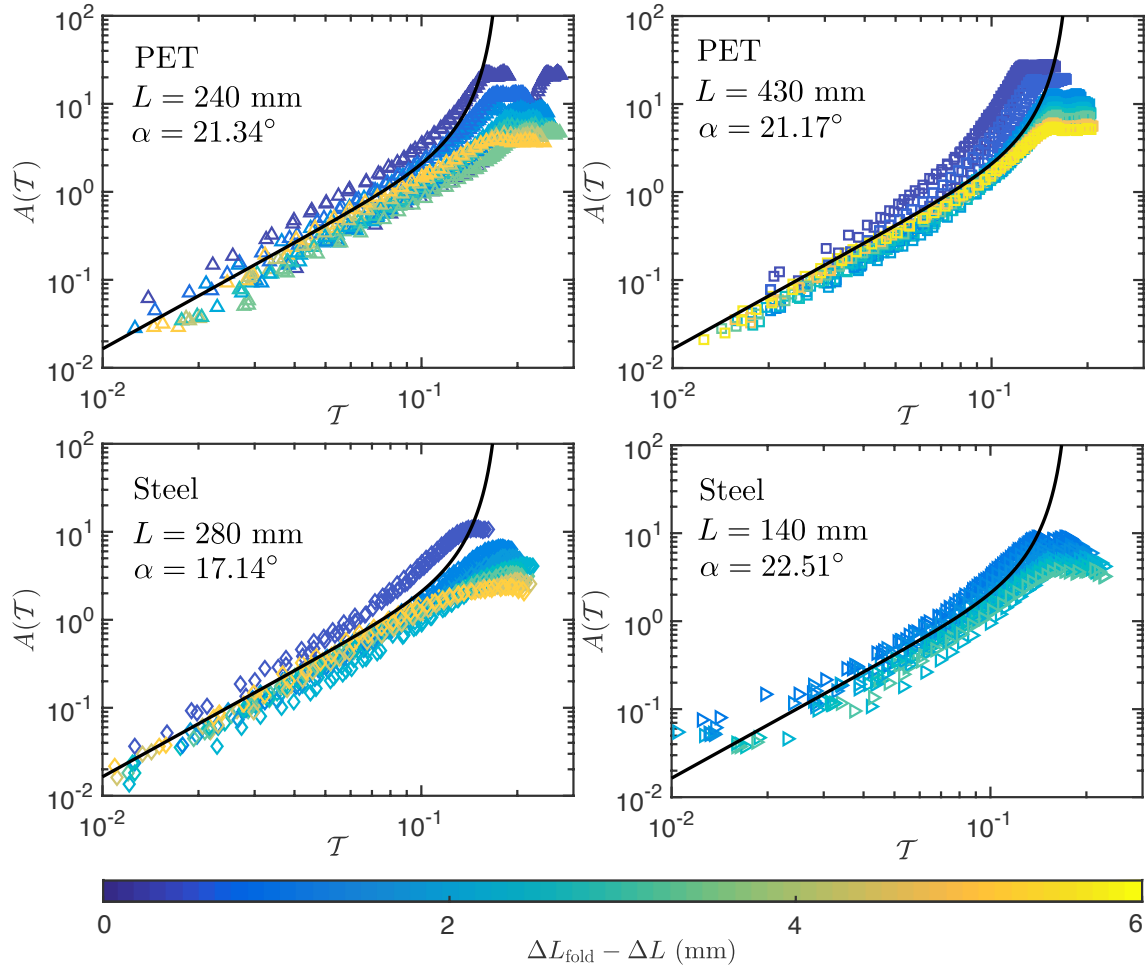
Figure 4.17: *Dimensionless midpoint trajectories during snapping for PET and steel strips of different natural length L than figure 4.12 in the main text. For each value of $\Delta L_{\text{fold}} - \Delta L$ (given by the colourbar), three runs are recorded and shown here. In each panel, we plot the amplitude variable $A(\mathcal{T})$ (defined in equation (4.50)) as a function of dimensionless time $\mathcal{T} = \Delta \mu^{1/4} t / t^*$. The solid black curves are the predicted asymptotic behaviour (4.27) in the underdamped limit from beam theory. (Reprinted from Gomez et al. (2017a), DOI: https://doi.org/10.1038/nphys3915.)*

Viscoelastic snap-through

Synopsis

We study the dynamics of snap-though when viscoelastic effects are present. To gain analytical insight we analyse a modified form of the Mises truss, a single-degree-of-freedom structure, which features an 'inverted' shape that snaps to a 'natural' shape. Motivated by the anomalously slow snap-through shown by spherical caps, we consider a theoretical experiment in which the truss is first indented to an inverted state and allowed to relax whilst a specified displacement is maintained, before the displacement constraint is removed. We first study the dynamics for the limit in which the timescale of viscous relaxation is much larger than the characteristic elastic timescale. Combining direct numerical solutions with a multiple-scales analysis, we show that two types of snap-through are possible: the truss immediately snaps back over the elastic timescale or it displays 'pseudo-bistability', in which it undergoes a slow creeping motion before rapidly accelerating. This pseudo-bistability occurs in a narrow parameter range near the snap-through bifurcation, and so is naturally susceptible to a saddle-node ghost. We then analyse the alternative limit in which the viscous timescale is much smaller than the elastic timescale, demonstrating that even a small amount of viscoelasticity significantly influences the bottleneck dynamics. This leads to an intricate asymptotic structure and new scaling laws for the snap-through time. Curiously, we find a regime in which increasing the viscosity has the effect of *decreasing* the snap-through time.

A preprint of a paper based on this chapter is available (Gomez *et al.*, 2018*b*).

5.1 Introduction

Many elastic systems that undergo snap-through exhibit some degree of energy dissipation. This is particularly true of biological systems such as the Venus flytrap, whose snapping leaves are saturated with water and may dissipate energy via internal fluid flow (Forterre *et al.*, 2005). Similarly, commercially available 'jumping popper' toys are composed of a rubbery polymer that may exhibit viscoelastic behaviour (Brinkmeyer *et al.*, 2012). In each of these systems, the speed of snap-through is much slower than what would be predicted by the naïve elastic timescale, so it is commonly assumed that the dissipation must be responsible for the observed timescale.

In the previous chapter we showed that this assumption need not be the case: surprisingly slow dynamics can in fact be obtained in systems with negligible dissipation. This time delay arises from the remnant or 'ghost' of the saddle-node bifurcation, and so requires no additional physics to be present. Nevertheless, a key feature of this slowing down is that the system needs to be very close to the snap-through bifurcation: the amount of delay that is experimentally attainable may in practice be small. Moreover, when dissipative effects are present, it is not clear what relative role dissipation and the saddle-node ghost may play. While we have previously considered the influence of external damping (e.g. due to air drag), viscoelastic behaviour is fundamentally different because it modifies the stability characteristics of structures. We are therefore interested in how material viscosity interacts with the critical slowing down phenomenon, and in characterising the snap-through times and parameter regimes in which each mechanism becomes dominant.

Unlike elastic solids, viscoelastic materials generally undergo stress relaxation when subject to a constant strain; this causes the effective stiffness of the structure to evolve in time. If a constant stress is imposed instead, the material may also exhibit a slow creeping motion (Howell *et al.*, 2009). Santer (2010) has demonstrated how these combined effects allow structures to exhibit 'temporary bistability' or 'pseudo-bistability' during snap-through. The idea of pseudo-bistability is that when a structure is held in a configuration that is near (but just beyond) a snap-through threshold, just as a popper toy may be held 'inside-out', the change in stiffness associated with stress relaxation can cause the structure to effectively become bistable. When the structure is released, the stiffness recovers during a creeping motion, until eventually this bistability is lost and rapid snap-through occurs. Similar to the phenomenon of creep buckling (Hayman, 1978), the total snap-through time is then governed by the relaxation timescale of the material and can be very large. This phenomenon may be useful in morphing devices that are required to cycle continuously between two distinct states; for example, dimples proposed for aircraft wings that buckle in response to the air flow to reduce skin friction (Dearing *et al.*, 2010;

Terwagne *et al.*, 2014), and ventricular assist devices which use snap-through of a spherical cap under a cyclic pneumatic load to generate blood flow (Gonçalves *et al.*, 2003). In these applications, pseudo-bistability means that the actuation needed to move the structure between different states can be applied for a shorter duration, which may lead to significant reduction in the energy consumed (Santer, 2010).

Using finite element simulations, Santer (2010) has demonstrated pseudo-bistability in a single-degree-of-freedom truss-like structure, as well as spherical caps reminiscent of jumping popper toys. The phenomenon has been observed experimentally in spherical caps (Madhukar *et al.*, 2014) and truncated conical shells (Urbach & Efrati, 2017), and generically appears to occur only in a narrow parameter range near the transition to bistability, i.e. the threshold at which snap-through no longer occurs. Brinkmeyer *et al.* (2012) performed a systematic study of the snap-through dynamics of viscoelastic spherical caps, using a combination of finite element simulations and experiments. Continuing this work, Brinkmeyer *et al.* (2013) studied the pseudo-bistable effect in viscoelastic arches. In these studies the phenomenon is found to have a number of common features, including (i) to obtain any time delay the structure needs to be held for a minimum amount of time before release; and (ii) the resulting snap-through time depends sensitively on the parameters of the system and appears to diverge near the bistability transition. However, these basic features are not well understood quantitatively despite having important implications for applications of pseudo-bistability. The sensitivity of the snap-through time, for instance, means the system needs to be precisely tuned to obtain a desired response time. For this reason direct comparison between experiments and finite element simulations has revealed large quantitative errors (Brinkmeyer *et al.*, 2012; 2013).

In addition, the simulations referred to above are all based on two key assumptions regarding the viscoelastic response: (i) the material behaves as though elastic with an effective stiffness that evolves in time, and (ii) the response during recovery is the reciprocal of the response during relaxation, i.e. once the structure is released, the stiffness smoothly recovers to its initial, fully unrelaxed, value. These assumptions mean that modelling the dynamics is relatively simple compared to more general viscoelastic models, and the resulting equations are more easily implemented in commercially-available finite element packages. Furthermore, the different dynamical regimes can often be inferred by considering the elastic response in which the stiffness is fully unrelaxed and fully relaxed, as the stiffness at any moment must be bounded between these two extremes (Santer, 2010). However, the validity of these assumptions, and whether they can be justified from first principles, remains unclear.

An alternative approach is to start from the constitutive law of a viscoelastic solid, and derive the equations of motion that couple the stress to the deformation of the structure.

While this approach is significantly more complicated, it eliminates the need to make any additional assumptions regarding the behaviour of the stiffness. Instead, the stiffness is an unknown that is solved for as part of the problem. This method has previously been used to obtain analytical expressions for the snap-through loads of simple viscoelastic structures (Nachbar & Huang, 1967), and the conditions under which creep buckling occurs (Hayman, 1978). More recently, Urbach & Efrati (2017) developed a general theoretical framework for modelling viscoelastic snap-through based on a metric description of the constitutive equations. However, due to the inherent complexity of viscoelastic effects an analytical understanding of the dynamics is still lacking, with previous approaches relying on experiments and direct numerical solutions. For example, it is unclear precisely when pseudo-bistable behaviour is obtained, and why the snap-through time appears to diverge near the snap-through transition. Are we simply observing another instance of a saddle-node ghost? These are the questions we address in this chapter.

5.1.1 A simple model system

While we are motivated by the slow dynamics shown by snapping shells (e.g. the leaves of the Venus flytrap), we study a much simpler model system to gain analytical insight. Due to the additional complexity of viscoelastic effects here, we follow Brinkmeyer *et al.* (2013) and consider a Mises truss (also referred to as a von Mises truss). In its simplest form, this single-degree-of-freedom structure features two central springs, assumed to be linearly elastic, that are pin-jointed at their ends. As shown in figure 5.1a, the springs are inclined at a non-zero angle to the horizontal in their natural state. To give the system inertia, we place a point mass where the springs meet, which is assumed to move only in the vertical direction.

The truss in its current form is bistable: as well as the undeformed or 'natural' state, the truss may be in equilibrium in a reflected state, where the length of each spring is unchanged from its rest length. This bistability may be modified by introducing an additional spring connected vertically to the point mass (figure 5.1b) (Krylov *et al.*, 2008; Panovko & Gubanova, 1987). As the stiffness of the vertical spring increases relative to the central springs, we expect the inverted state to eventually become unstable, since this state leads to a large increase in the length of the vertical spring. In an experiment where the truss is held fixed in an inverted position using an indenter, the truss will then immediately snap back to its natural state when the indenter is released, independently of how long it is held. This snap-through is reminiscent of a spherical cap (and the pre-buckled arch studied in Chapter 4), which features an analogous 'inverted' state that snaps back to a 'natural' state. In fact, we may consider the truss as a lumped model for a spherical cap. The central springs parameterise the membrane (stretching) stiffness
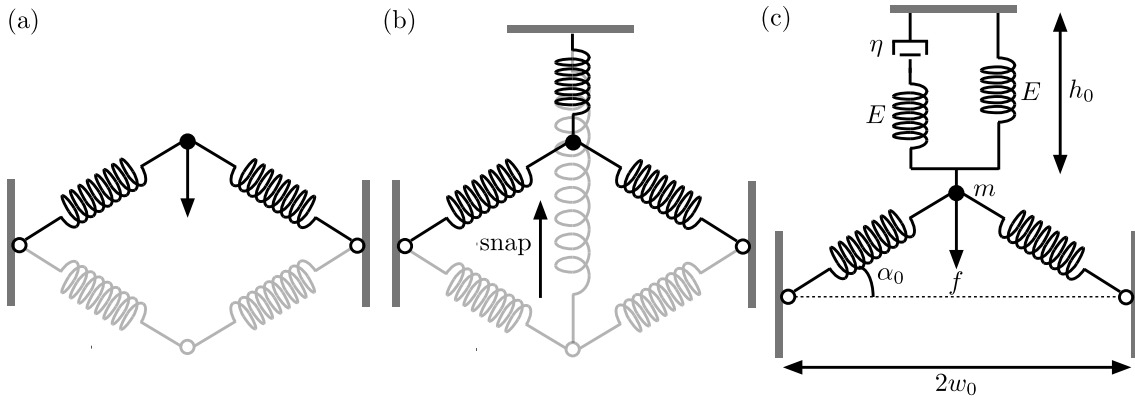
Figure 5.1: *(a) The simplest form of the Mises truss, which features bistable 'natural' (highlighted) and 'inverted' (lightly shaded) equilibrium states. (b) This bistability is lost when an additional, linearly elastic, spring of sufficient stiffness is attached vertically to the point mass. (c) Replacing the vertical spring by a viscoelastic element, modelled as a standard linear solid (SLS).*

of the shell, since these springs can be viewed as corresponding to the shell's midsurface. The vertical spring parameterises the bending stiffness: this spring penalises rotating the truss about its pin-jointed ends, which mimics bending the shell about its edges as it is turned inside-out.

Now suppose that the vertical spring is viscoelastic. Note that a typical snap-through experiment includes both displacement-control and force-control: during indentation we impose a given displacement, and releasing the truss corresponds to imposing zero indentation force. It is therefore insufficient to describe the viscoelastic response using a Maxwell or Kelvin-Voigt model, since these fail to capture both stress relaxation (under displacement-control) and creep (under force-control) behaviour. Instead, we use the constitutive law of a standard linear solid (SLS), which is the simplest model that describes both of these effects (Urbach & Efrati, 2017). Physically, the SLS model is equivalent to placing a linear spring in parallel with a Maxwell element that features a second spring and a dashpot in series; see figure 5.1c. When the structure is indented and held for a specified time, stress relaxation causes the effective stiffness of the SLS element to decrease, so that the behaviour upon release is no longer obvious: the truss may immediately snap back, or it may initially creep in an inverted state for a period of time. In particular, these regimes cannot be inferred by only considering the equilibrium states of the system.

In this chapter we analyse the dynamics of the truss system in figure 5.1c. Nachbar & Huang (1967) have analysed a similar truss using a Kelvin-Voigt model, and determined the onset of snap-through to an inverted state when a constant indentation force is suddenly applied. Here, we are interested in the dynamics of the snap-back when the indentation force is removed. The remainder of this chapter is organised as follows. We begin in §5.2 by deriving the equations governing the motion of the truss, assuming the SLS constitutive

law. We then discuss the equilibrium states of the system and the stress relaxation during indentation. In §5.3, we analyse the snap-through dynamics when the indenter is released, focussing on the limit when the timescale of viscous relaxation is much larger than the characteristic elastic timescale. Using direct numerical solutions, we identify the regimes in which the dynamics slow down considerably, and we explain this behaviour asymptotically using the method of multiple scales. We show that while pseudo-bistable behaviour can be obtained without critical slowing down, it occurs only in a narrow parameter range near the snap-through bifurcation. As a result, the snap-through time inherits the usual inverse square-root scaling law as the saddle-node bifurcation is approached, and we compare this prediction to experimental and numerical data reported in the literature. In §5.4, we consider the alternative limit in which the timescale of viscous relaxation is much smaller than the elastic timescale. We show that even a small amount of viscoelasticity can significantly modify the snap-through dynamics: the truss may snap when a purely elastic analysis would indicate it is stable, and the bottleneck dynamics depend delicately on the amount of stress relaxation that occurs during indentation. This allows us to build up a complete picture of the different bottleneck regimes, which we summarise later in figure 5.14. Finally, in §5.5, we summarise our findings and conclude.

5.2 Theoretical formulation

A schematic diagram of the truss is shown in figure 5.1c. In the natural state the central springs are assumed to be inclined at an angle $\alpha_0 > 0$ to the horizontal, and the springs are at their natural length; the distance between the pin joints at each base is $2w_0$. We assume that the central springs are linearly elastic with constant stiffness k. The natural length of the vertical SLS element is h_0, the dashpot has viscosity η, and we suppose that both upper springs have modulus E.

Let x be the downward displacement of the point mass m from the natural state, and write α for the corresponding inclination angle of the central springs. To obtain an equation of motion for x, we calculate the various forces exerted on the point mass. Writing Δl for the change in length of the central springs, simple geometry gives that

$$
\begin{aligned}
x &= w_0 \left(\tan \alpha_0 - \tan \alpha \right), \\
\Delta l &= w_0 \left(\frac{1}{\cos \alpha} - \frac{1}{\cos \alpha_0} \right).
\end{aligned}
$$

For simplicity, we assume that the truss remains shallow in shape, i.e. $\alpha_0 \ll 1$ and $|\alpha| \ll 1$.

Neglecting terms of $O(\alpha_0^3, \alpha^3)$, we then have

$$
\begin{aligned}
x &= w_0 \left(\alpha_0 - \alpha \right), \\
\Delta l &= \frac{w_0}{2} \left(\alpha^2 - \alpha_0^2 \right).
\end{aligned}
$$

The first equation shows that, for small angles, the vertical displacement x is proportional to the change in the inclination angle α. Hence, the vertical SLS element is analogous to a viscoelastic torsional spring at the base of each central spring, as was considered by Brinkmeyer *et al.* (2012). We also note that it is necessary to retain the quadratic non-linearity in the second equation above; this provides the geometric nonlinearity necessary to obtain bistability and snap-through behaviour. Combining these relations, we obtain

$$
\Delta l = \frac{x}{2w_0} \left(x - 2\alpha_0 w_0 \right).
$$

Because the central springs are linearly elastic, the corresponding force in each spring is $k\Delta l$. The vertical component of the total force exerted on the point mass (directed downwards) is then

$$
2k\Delta l \sin \alpha \approx \frac{kx}{w_0^2} \left(x - 2\alpha_0 w_0 \right) \left(\alpha_0 w_0 - x \right).
$$

The displacement x also leads to a strain in the upper SLS element of size $e = x/h_0$. The corresponding stress σ satisfies the constitutive law of a standard linear solid (Lakes, 1998) (with t denoting time)

$$
2\frac{\mathrm{d}e}{\mathrm{d}t} + \frac{E}{\eta}e = \frac{1}{E}\frac{\mathrm{d}\sigma}{\mathrm{d}t} + \frac{1}{\eta}\sigma. \tag{5.1}
$$

This leads to a vertical force $-A\sigma$ exerted on the point mass (directed downwards), where A is the cross-sectional area of each elastic element. If we also account for a downwards indentation force f, then conservation of momentum gives

$$
m\frac{\mathrm{d}^2 x}{\mathrm{d}t^2} = \frac{kx}{w_0^2} \left(x - 2\alpha_0 w_0 \right) \left(\alpha_0 w_0 - x \right) - A\sigma + f. \tag{5.2}
$$

Together with appropriate initial conditions specified below, the coupled ODEs (5.1)–(5.2) (and the relation $e = x/h_0$) provide a closed system to determine the trajectory $x(t)$ and stress $\sigma(t)$.

5.2.1 Non-dimensionalisation

To make the problem dimensionless, it is natural to scale the displacement with the initial height of the truss in the small-angle approximation, i.e. $x \sim \alpha_0 w_0$. The timescale of viscous relaxation comes from balancing the first two terms in (5.1), giving $t \sim \eta/E$. Balancing the remaining terms in (5.1)–(5.2), we therefore introduce the dimensionless variables

$$x = \alpha_0 w_0 X, \quad t = \frac{\eta}{E} T, \quad \sigma = \frac{E\alpha_0 w_0}{h_0} \Sigma, \quad f = k\alpha_0^3 w_0 F.$$

Inserting these scalings into (5.1), and eliminating the strain for the dimensionless displacement X, we obtain

$$2\frac{\mathrm{d}X}{\mathrm{d}T} + X = \frac{\mathrm{d}\Sigma}{\mathrm{d}T} + \Sigma. \tag{5.3}$$

The momentum equation (5.2) can be written as

$$\mathrm{De}^{-2}\frac{\mathrm{d}^2 X}{\mathrm{d}T^2} = X(X-2)(1-X) - \lambda\Sigma + F, \tag{5.4}$$

where we have introduced the dimensionless parameters

$$\mathrm{De} = \alpha_0 \frac{\eta/E}{\sqrt{m/k}}, \quad \lambda = \frac{AE}{kh_0\alpha_0^2}.$$

Here the Deborah number De measures the ratio of the timescale of viscous relaxation ($\sim \eta/E$) to the characteristic timescale of the experiment (Howell $et\ al.$, 2009); we take this to be the timescale of elastic oscillations ($\sim \alpha_0^{-1}\sqrt{m/k}$), which comes from balancing inertia and the force due to the central springs in (5.2). Note that in this non-dimensionalisation, the viscous timescale is $T = O(1)$ while the elastic timescale is $T = O(\mathrm{De}^{-1})$. We may interpret λ as the relative stiffness of the upper SLS element compared to the central springs. The cubic term on the right-hand side of (5.4) represents the dimensionless force due to the central springs. As expected, this vanishes in the undeformed state $X = 0$, the reflected state $X = 2$ (when the central springs are also at their natural length), and the intermediate displacement $X = 1$ when the springs are aligned horizontally — in this state they are compressed but do not contribute any vertical force.

5.2.2 Steady solutions

When the system is in equilibrium, the constitutive equation (5.3) is identical to that of an elastic solid, i.e. $\Sigma = X$. From (5.4), the indentation force F must balance the total force exerted by the central springs and the SLS element, which we label F_{eq}. In particular, the
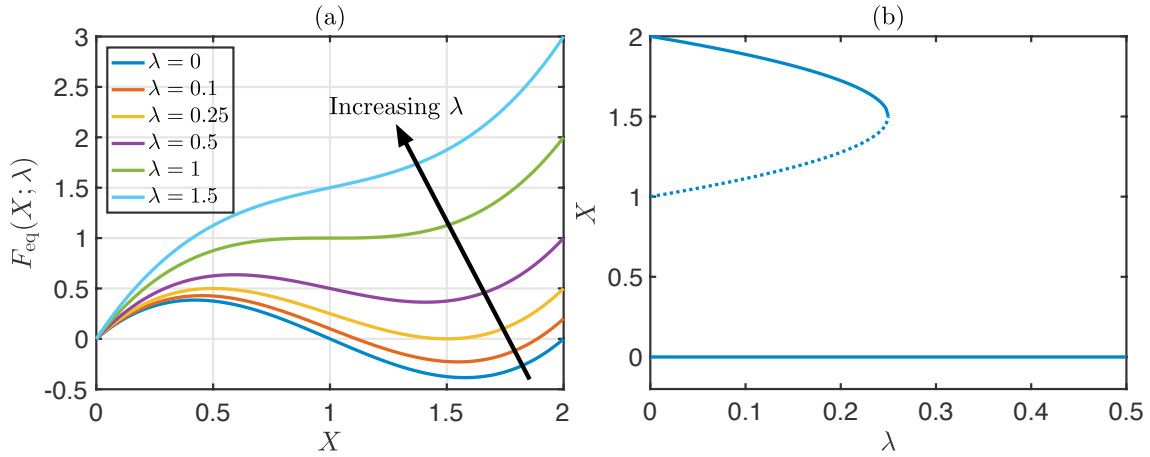
Figure 5.2: *(a) The force-displacement curve for a truss in equilibrium: plotting the indentation force required to impose a steady displacement X (coloured curves; see legend). At zero force, the truss is bistable for $\lambda < 1/4$ and monostable for $\lambda > 1/4$. (b) Response diagram for the steady roots of $F_{eq}(X; \lambda) = 0$ as λ varies. At the critical value $\lambda = \lambda_{fold} = 1/4$, the stable root away from zero (upper solid curve) meets an unstable root (dotted curve) and disappears at a saddle-node bifurcation.*

force associated with a steady displacement X is

$$F_{eq}(X; \lambda) \equiv -X(X - 2)(1 - X) + \lambda X.$$

When the indentation force is removed, the resulting dynamics depends on the solutions to $F_{eq} = 0$. This has roots

$$X = 0, \quad X = \frac{3 \pm \sqrt{1 - 4\lambda}}{2}.$$

For $\lambda < 1/4$, there are two real solutions away from $X = 0$, which coincide and disappear at a saddle-node bifurcation when $\lambda = \lambda_{fold} = 1/4$; the corresponding displacement at this point is $X = X_{fold} = 3/2$. For $\lambda > 1/4$, the only real solution is the undeformed state $X = 0$. This behaviour is apparent in figure 5.2a, which plots the force-displacement curve for different values of λ; we see that increasing λ (corresponding to a stiffer SLS element) acts to rotate the curve anti-clockwise about the origin, until eventually the turning point of the cubic lies above the line $F_{eq} = 0$. The corresponding behaviour of the roots to $F_{eq} = 0$ is shown in figure 5.2b. It can be shown that the roots in which $F'_{eq}(X; \lambda) > 0$ (solid branches on figure 5.2b) are linearly stable, while the root in which $F'_{eq}(X; \lambda) < 0$ (dotted branch) is linearly unstable (Panovko & Gubanova, 1987).

5.2.3 Indentation response

In a snap-through experiment, we imagine indenting the truss to an inverted state by imposing the constant displacement $X = X_{\text{ind}}$ where $X_{\text{ind}} \geq 1$. We also suppose this indentation occurs over the time interval $-T_{\text{ind}} < T < 0$ of duration $T_{\text{ind}} > 0$; for later convenience, we define $T = 0$ to be the time at which the indenter is released. To avoid introducing additional timescales into the problem, we suppose that the indentation is suddenly applied at $T = -T_{\text{ind}}$, i.e. over a timescale much faster than the viscous timescale η/E. We can then approximate the behaviour for $T < 0$ as

$$X = X_{\text{ind}} H(T + T_{\text{ind}}),$$

where $H(\cdot)$ is the Heaviside step function. Substituting into the constitutive equation (5.3), the stress in the upper SLS element satisfies

$$X_{\text{ind}} \left[2\delta(T + T_{\text{ind}}) + H(T + T_{\text{ind}}) \right] = \frac{\mathrm{d}\Sigma}{\mathrm{d}T} + \Sigma, \qquad T < 0,$$

where $\delta(\cdot)$ is the Dirac delta-function. The solution is

$$\Sigma = X_{\text{ind}} \left[1 + e^{-(T+T_{\text{ind}})} \right], \qquad -T_{\text{ind}} < T < 0.$$

This solution is classical in the literature and represents the stress relaxation of a standard linear solid under a step increase in strain (Lakes, 1998; Santer, 2010): the stress initially (i.e. at $T = -T_{\text{ind}}$) jumps instantaneously to a fully unrelaxed value $\Sigma = 2X_{\text{ind}}$ when the indentation is applied, and then exponentially decays to the fully relaxed value $\Sigma = X_{\text{ind}}$ associated with an elastic material.

Inspecting the momentum equation (5.4), we see that the effect of this relaxation is to give an effective value of λ that changes in time. The corresponding indentation force can be written as

$$F = F_{\text{eq}} \left(X_{\text{ind}}; \lambda \left[1 + e^{-(T+T_{\text{ind}})} \right] \right), \qquad -T_{\text{ind}} < T < 0.$$

Note in particular that the effective value of λ is given by $\lambda[1 + e^{-(T+T_{\text{ind}})}]$, which decreases from 2λ to λ during indentation. In terms of the force-displacement curve in figure 5.2a, this corresponds to rotating the curve *clockwise* as stress relaxation occurs, so that the indentation force decreases in time. From this picture, we anticipate that there are different dynamical regimes when the indenter is released, depending on the values of λ and T_{ind}. For $\lambda < 1/8$, the turning point on the cubic lies below the line $F_{\text{eq}} = 0$ in the fully unrelaxed state (since $2\lambda < \lambda_{\text{fold}}$), and moves further below this line as relaxation occurs. Hence the truss is bistable at the moment when the indenter is released, and we do not

expect snap-through to occur if the indentation displacement is sufficiently close to the stable root of $F_{\mathrm{eq}} = 0$ away from zero. Similarly, for $\lambda > 1/4$, the turning point lies above the line $F_{\mathrm{eq}} = 0$ when the structure is fully relaxed, and so the truss is always monostable; we expect snap-through occurs for any value of X_{ind}. For $1/8 < \lambda < 1/4$, the turning point lies above the line $F_{\mathrm{eq}} = 0$ when the structure is fully unrelaxed (since $2\lambda > \lambda_{\mathrm{fold}}$), but eventually decreases below this line as stress relaxation occurs. In particular, the truss is effectively bistable when the indenter is released (i.e. $T = 0$) provided that

$$\lambda \left(1 + e^{-T_{\mathrm{ind}}}\right) < \frac{1}{4}.$$

This can be re-arranged to

$$T_{\mathrm{ind}} > \log\left(\frac{\lambda}{1/4 - \lambda}\right). \tag{5.5}$$

We then expect that snap-through does not occur if the inequality (5.5) is satisfied, and does occur otherwise. We will show that while this naïve argument correctly accounts for different dynamical regimes, it fails to quantitatively predict when snap-through behaviour is obtained.

For later reference, we write F_{ind} for the value of F just before the indenter is released, i.e. at $T = 0-$. From above, this is given by

$$F_{\mathrm{ind}} = F_{\mathrm{eq}}\left(X_{\mathrm{ind}}; \lambda\left[1 + e^{-T_{\mathrm{ind}}}\right]\right). \tag{5.6}$$

5.2.4 Release dynamics

At $T = 0$, the indenter is suddenly released so that the indentation force

$$F = F_{\mathrm{ind}}\left[1 - H(T)\right].$$

We solve the momentum equation (5.4) for the corresponding stress Σ and substitute this into the constitutive equation (5.3). After re-arranging we obtain

$$\mathrm{De}^{-2}\left(\frac{\mathrm{d}^3 X}{\mathrm{d}T^3} + \frac{\mathrm{d}^2 X}{\mathrm{d}T^2}\right) + F'_{\mathrm{eq}}(X; 2\lambda)\frac{\mathrm{d}X}{\mathrm{d}T} + F_{\mathrm{eq}}(X; \lambda) = -F_{\mathrm{ind}}\left[\delta(T) + H(T) - 1\right],$$

where $' = \mathrm{d}/\mathrm{d}X$. Due to the presence of inertia, X and $\dot{X}$ must be continuous across $T = 0$ (writing $\dot{} = \mathrm{d}/\mathrm{d}T$), as a jump in either of these quantities would imply an infinite force. We therefore solve

$$\mathrm{De}^{-2}\left(\frac{\mathrm{d}^3 X}{\mathrm{d}T^3} + \frac{\mathrm{d}^2 X}{\mathrm{d}T^2}\right) + F'_{\mathrm{eq}}(X; 2\lambda)\frac{\mathrm{d}X}{\mathrm{d}T} + F_{\mathrm{eq}}(X; \lambda) = 0, \quad T > 0, \tag{5.7}$$

together with the jump conditions

$$X(0+) = X_{\text{ind}}, \quad \dot{X}(0+) = 0, \quad \text{De}^{-2}\ddot{X}(0+) = -F_{\text{ind}}. \tag{5.8}$$

The jump in acceleration here is necessary to balance the discontinuity in the applied indentation force.

Currently, we have four dimensionless parameters in the problem: these are the Deborah number De, the relative stiffness λ, the indentation depth X_{ind}, and the indentation time T_{ind} (together these quantities determine F_{ind}). Throughout this chapter, we restrict to indentation depths $1 \leq X_{\text{ind}} \leq 2$. As a baseline value we use $X_{\text{ind}} = X_{\text{fold}} = 3/2$, since the initial conditions (5.8) are then analogous to those used in Chapter 4 (recall the arch started at rest in a shape near the equilibrium shape at the saddle-node bifurcation). We therefore expect to recover similar behaviour here when the truss is purely elastic, corresponding to the limit De $\to$ 0. In particular, we expect that the dynamics are governed by the elastic timescale and only slow down considerably near the saddle-node bifurcation at $\lambda = \lambda_{\text{fold}}$. However, for larger values of De, it is not clear when the dynamics are instead governed by viscous relaxation. To gain insight, we analyse the dynamics in the limits De $\gg$ 1 and De $\ll$ 1 separately.

5.3 Snap-through dynamics: De $\gg$ 1

5.3.1 Numerical solution

We first consider the limit De $\gg$ 1, which corresponds to a relaxation timescale that is much slower than the elastic timescale. This is the relevant regime for many structures composed of rubbery polymers such as silicone-based elastomers (Brinkmeyer *et al.*, 2012; 2013; Urbach & Efrati, 2017). Typical dimensionless trajectories $X(T)$ in this limit are shown in figures 5.3a–c; here we have fixed $X_{\text{ind}} = X_{\text{fold}}$, De = 10 and varied λ between the different panels. We have obtained the trajectories by integrating the ODE (5.7) with initial conditions (5.8) numerically in MATLAB using the routine `ode45` (here and throughout we use error tolerances 10^{-10}).

Figure 5.3 shows that the initial jump in acceleration causes oscillations to occur on the fast elastic timescale $T = O(\text{De}^{-1})$; these oscillations persist due to the absence of external damping in our model. As anticipated from the discussion in §5.2.3, there are different regimes depending on the size of λ. For $\lambda \lesssim 1/8$, the truss appears to never snap and instead oscillates around an inverted state; see figure 5.3a. As $T \to \infty$, these oscillations decay and the displacement approaches the stable root of $F_{\text{eq}} = 0$ away from zero. For
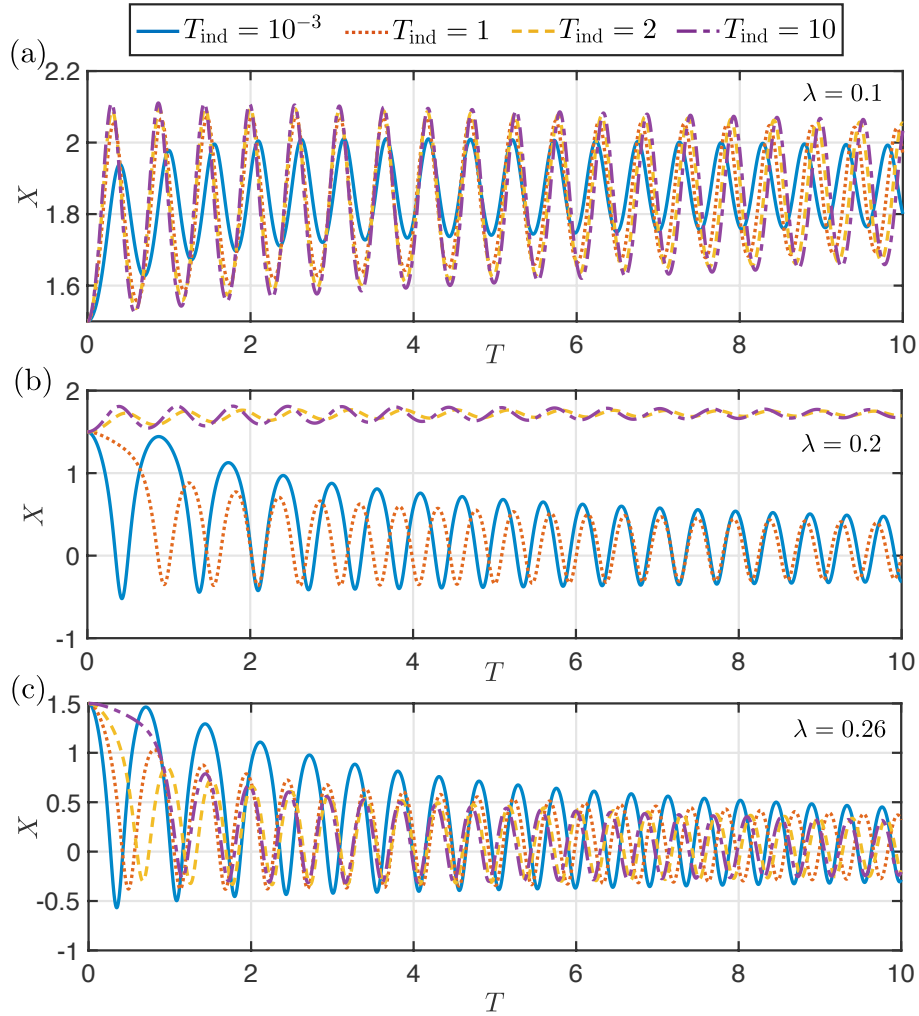
Figure 5.3: *Dimensionless trajectories obtained by numerical integration of* (5.7) *with initial conditions* (5.8) *(coloured curves). Here* $X_{\mathrm{ind}} = X_{\mathrm{fold}}$, $\mathrm{De} = 10$ *and data is shown for (a)* $\lambda = 0.1$, *(b)* $\lambda = 0.2$ *and (c)* $\lambda = 0.26$. *In each panel, trajectories associated with four different values of the indentation time* T_{ind} *(given in the upper legend) are shown. Note that the vertical scale varies between panels.*
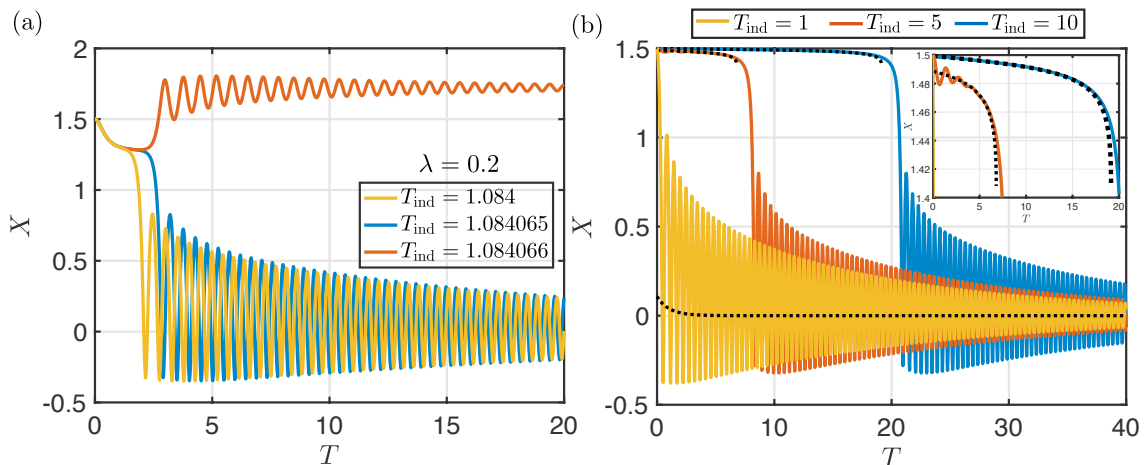
Figure 5.4: *Different regimes in which the snap-through dynamics slow down significantly (De = 10, $X_{ind} = X_{fold}$). (a) When $1/8 \lesssim \lambda \lesssim 1/4$, slowing down occurs when T_{ind} is just below the critical value at which snap-through no longer occurs (coloured curves; see legend). (b) A much slower snap-through is observed when $0 < \lambda - 1/4 \ll 1$ and T_{ind} is sufficiently large (coloured curves; see legend). (Note the range of times plotted is larger than panel (a).) Here $\lambda = 0.2501$ and for later reference the predictions from the multiple-scale analysis are shown (black dotted curves).*

$1/8 \lesssim \lambda \lesssim 1/4$, the truss does not snap if the indentation time T_{ind} is sufficiently large, in which case the behaviour is similar to $\lambda \lesssim 1/8$ (figure 5.3b). However, for smaller values of T_{ind} the truss instead snaps and oscillates around the natural state. For $\lambda \gtrsim 1/4$, the truss appears to snap for any value of T_{ind} (figure 5.3c). For larger values De $\gtrsim 10$, we observe similar behaviour though with faster oscillations (due to a faster elastic timescale).

We also find that the dynamics may slow down considerably near the threshold at which snap-through no longer occurs. For example, we can approach this boundary by fixing $1/8 \lesssim \lambda \lesssim 1/4$ and tuning the value of T_{ind} appropriately. However, as shown in figure 5.4a, we find that T_{ind} must be very close to a critical value to obtain significant slowing down. Much slower dynamics are more easily obtained by fixing $0 < \lambda - \lambda_{fold} \ll 1$ and choosing T_{ind} sufficiently large; see figure 5.4b. Here the oscillations are rapidly damped out, and the trajectory features an initial plateau before rapidly accelerating towards the natural configuration (highlighted in the inset of figure 5.4b). This behaviour is reminiscent of the bottleneck behaviour we have seen previously, which was caused by a saddle-node ghost.

To study this slowing down more systematically, we define the snap-through time, T_{snap}, as the time at which the displacement first crosses $X = 0$, i.e. the displacement corresponding to the natural configuration. (While this definition allows us to measure the dynamics in a consistent way, we note that the value is somewhat influenced by variations in the oscillations that occur on the $O(\mathrm{De}^{-1})$ timescale.) The computed snap-through times are shown on the (λ, T_{ind})-plane in figure 5.5a, where we have specified $X_{ind} = X_{fold}$ and

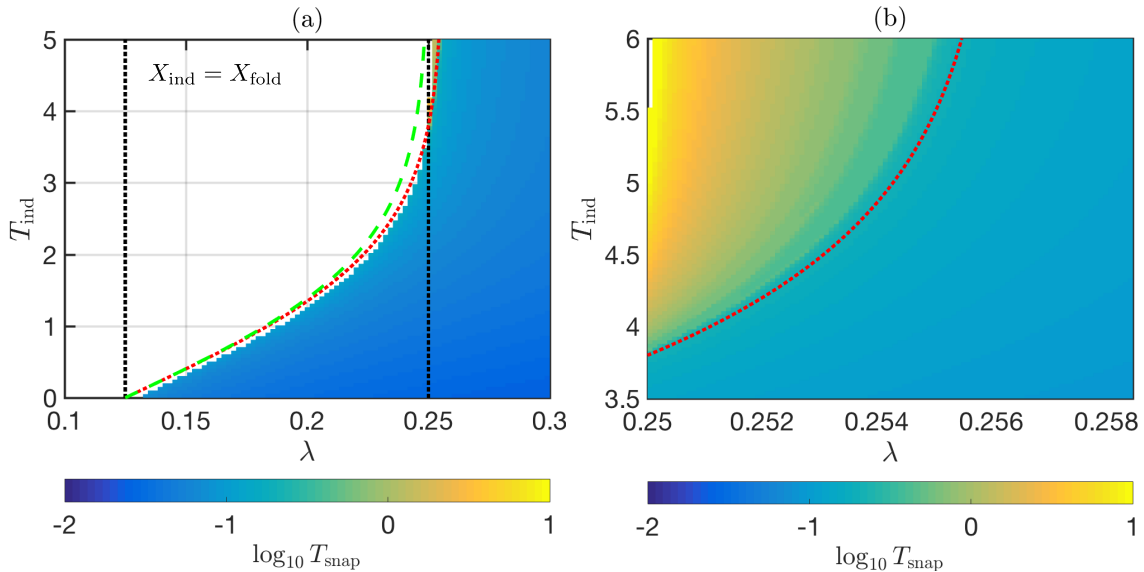**Figure 5.5:** *Snap-through times in the limit* De $\gg$ 1 *($X_{\mathrm{ind}} = X_{\mathrm{fold}}$, De = 100). (a) Numerical results obtained by integrating* (5.7)– (5.8) *until the point when $X = 0$ (see colourbar). Also shown is the boundary separating snap-through/no snap-through predicted by (5.5) (green dashed curve), and, for later reference, the boundary predicted by equation (5.23) in §5.3.2 (red dotted curve). (b) A close-up of the region where the dynamics slow down significantly. In each panel, the snap-through times have been computed on a 100×100 grid of equally spaced values in the region displayed.*

De = 100. The blank regions on the figure correspond to regions where snap-through does not occur (after integrating the equations up to a specified time, taken to be $T = 10$ here; due to the limited amount of slowing down in figure 5.5a, this was found to be sufficient). This confirms the different dynamical regimes and shows that the boundary at which snap-through no longer occurs with $1/8 \lesssim \lambda \lesssim 1/4$ is non-trivial. In particular, the critical value of T_{ind} increases nonlinearly as λ increases, and appears to approach a finite value $T_{\mathrm{ind}} \approx 3.5$ as $\lambda \to 1/4$. For comparison, we have also plotted the naïve prediction (5.5) based on whether the truss is effectively bistable at the moment when the indenter is released (green dashed curve). This provides a good approximation when $\lambda \approx 1/8$, but increasingly over-predicts the critical value of T_{ind} as λ increases, with the predicted value diverging as $\lambda \to 1/4$. (For later comparison, the boundary predicted by the multiple-scale analysis in §5.3.2 is shown as a red dotted curve).

Another key feature of figure 5.5a is that the snap-through time is very small throughout most of the parameter space. In fact, we will show that here the elastic oscillations cause the truss to immediately cross $X = 0$, so that $T_{\mathrm{snap}} = O(\mathrm{De}^{-1}) \ll 1$. This behaviour may be observed in the trajectories plotted in figures 5.3b–c. Figure 5.5a also confirms that the snap-through time only becomes $O(1)$ or larger in a very narrow region of the parameter space, where $0 < \lambda - 1/4 \ll 1$ and $T_{\mathrm{ind}} \gtrsim 3.5$. A zoom in on this region is provided in figure 5.5b, which shows that considerable slowing down can occur (here we
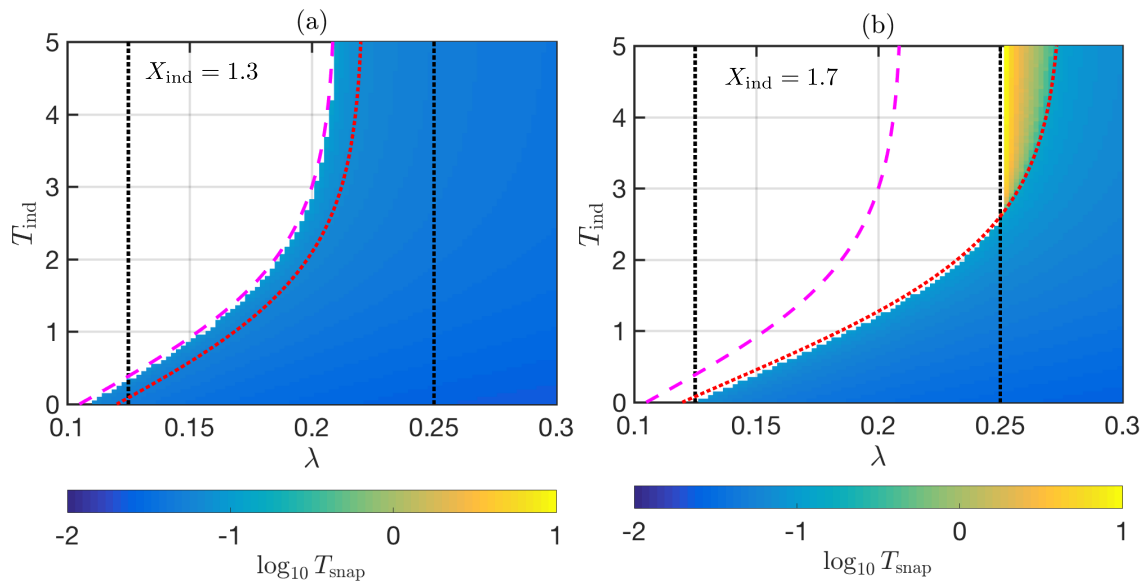
Figure 5.6: *Snap-through times when* $\mathrm{De} \gg 1$ *for different indentation depths. Numerical results are shown for (a)* $X_{\mathrm{ind}} = 1.3$ *and (b)* $X_{\mathrm{ind}} = 1.7$ *(De = 100). For later reference, also shown is the boundary predicted by equation (5.22) relevant for* $X_{\mathrm{ind}} < X_{\mathrm{fold}}$ *(magenta dashed curve), and the boundary predicted by equation (5.23) relevant for* $X_{\mathrm{ind}} \geq X_{\mathrm{fold}}$ *(red dotted curve). In each panel, the snap-through times have been computed on a* 100×100 *grid of equally spaced values. For ease of comparison the range of the colourbar is the same in both panels here and in figures 5.5a–b.*

now integrate up to a maximum time $T = 20$). In fact, the snap-through time appears to increase without bound as we take $\lambda \searrow 1/4$ in this region (the upper bound on figure 5.5b is due to the finite number of values used). We will show that this is precisely the pseudo-bistable regime: here the displacement initially oscillates around an inverted state and does not immediately cross $X = 0$. As with the trajectories in figure 5.4b, this inverted state also undergoes a slow creeping motion until the truss rapidly accelerates towards the natural state, so that $T_{\mathrm{snap}} \gtrsim O(1)$.

The computed snap-through times for different values of X_{ind} are shown in figures 5.6a–b. These show that the boundary at which snap-through no longer occurs is qualitatively different depending on whether $X_{\mathrm{ind}} < X_{\mathrm{fold}}$ or $X_{\mathrm{ind}} \geq X_{\mathrm{fold}}$. In the case $X_{\mathrm{ind}} < X_{\mathrm{fold}}$, the boundary appears to be shifted entirely to the left of the line $\lambda = 1/4$, and there is no longer a region where the dynamics slow down considerably (figure 5.6a). The truss also snaps at values $\lambda < 1/8$ when T_{ind} is sufficiently small. In contrast, for $X_{\mathrm{ind}} \geq X_{\mathrm{fold}}$ the boundary intercepts the line $\lambda = 1/4$ and the size of the pseudo-bistable region may be significantly larger compared to the case $X_{\mathrm{ind}} = X_{\mathrm{fold}}$ (figure 5.6b).

5.3.2 Multiple-scale analysis

To understand the above observations, we now perform a detailed analysis of the dynamics in the limit $\mathrm{De} \gg 1$. The trajectories in figures 5.3a–c indicate that the displacement undergoes fast oscillations (on an $O(\mathrm{De}^{-1})$ timescale) around a value that varies on an $O(1)$ timescale. This suggests that the dynamics can be understood asymptotically using the method of multiple scales (Hinch, 1991). We first introduce the fast timescale $\mathcal{T}$ defined by

$$T = \mathrm{De}^{-1}\mathcal{T}.$$

On this timescale, equation (5.7) becomes

$$\frac{\mathrm{d}^3 X}{\mathrm{d}\mathcal{T}^3} + \mathrm{De}^{-1}\frac{\mathrm{d}^2 X}{\mathrm{d}\mathcal{T}^2} + F'_{\mathrm{eq}}(X; 2\lambda)\frac{\mathrm{d}X}{\mathrm{d}\mathcal{T}} + \mathrm{De}^{-1}F_{\mathrm{eq}}(X; \lambda) = 0, \quad \mathcal{T} > 0, \tag{5.9}$$

while the initial conditions (5.8) modify to (subscripts denoting differentiation)

$$X(0+) = X_{\mathrm{ind}}, \quad X_{\mathcal{T}}(0+) = 0, \quad X_{\mathcal{T}\mathcal{T}}(0+) = -F_{\mathrm{ind}}. \tag{5.10}$$

Treating T and $\mathcal{T}$ as independent, the chain rule implies that

$$\frac{\mathrm{d}}{\mathrm{d}\mathcal{T}} = \frac{\partial}{\partial\mathcal{T}} + \mathrm{De}^{-1}\frac{\partial}{\partial T}. \tag{5.11}$$

We seek an asymptotic expansion of the solution in the form

$$X \sim X_0(\mathcal{T}, T) + \mathrm{De}^{-1}X_1(\mathcal{T}, T) + \dots. \tag{5.12}$$

Leading order problem

We insert the expansion (5.12) into the ODE (5.9). After Taylor expanding the force terms $F'_{\mathrm{eq}}(X; 2\lambda)$ and $F_{\mathrm{eq}}(X; \lambda)$ about X_0, and expanding the derivatives using (5.11), we obtain at leading order the homogeneous problem

$$\frac{\partial^3 X_0}{\partial\mathcal{T}^3} + F'_{\mathrm{eq}}(X_0; 2\lambda)\frac{\partial X_0}{\partial\mathcal{T}} = 0.$$

The initial conditions (5.10) remain unchanged in terms of X_0. The above equation may then be integrated with these conditions to give

$$\frac{\partial^2 X_0}{\partial\mathcal{T}^2} + F_{\mathrm{eq}}(X_0; 2\lambda) = \lambda X_{\mathrm{ind}}\left(1 - e^{-T_{\mathrm{ind}}}\right) + A(T), \tag{5.13}$$

where $A(0+) = 0$ and we have used the identity

$$-F_{\mathrm{ind}} + F_{\mathrm{eq}}(X_{\mathrm{ind}}; 2\lambda) = \lambda X_{\mathrm{ind}} \left(1 - e^{-T_{\mathrm{ind}}}\right),$$

which follows from the expression (5.6) for F_{ind}. Currently, the function $A(T)$ is unknown. As in our asymptotic analysis of the bottleneck dynamics in Chapters 3 and 4, we expect to determine $A(T)$ as a result of a solvability condition on a higher-order problem.

To reveal the role that $A(T)$ plays in the dynamics, we decompose the leading order solution into a "slow part" and a "fast part":

$$X_0(\mathcal{T}, T) = \mathcal{X}(T) + \mathscr{X}(\mathcal{T}, T). \tag{5.14}$$

We specify that $\mathcal{X}$ satisfies the "slow part" of the leading order equation (5.13), i.e.

$$F_{\mathrm{eq}}(\mathcal{X}; 2\lambda) = \lambda X_{\mathrm{ind}} \left(1 - e^{-T_{\mathrm{ind}}}\right) + A(T). \tag{5.15}$$

In terms of the "fast part" $\mathscr{X}$, equation (5.13) then becomes

$$\frac{\partial^2 \mathscr{X}}{\partial \mathcal{T}^2} + F_{\mathrm{eq}}'(\mathcal{X}; 2\lambda)\mathscr{X} + \frac{1}{2} F_{\mathrm{eq}}''(\mathcal{X}; 2\lambda)\mathscr{X}^2 + \frac{1}{6} F_{\mathrm{eq}}'''(\mathcal{X}; 2\lambda)\mathscr{X}^3 = 0. \tag{5.16}$$

(Higher order terms in the Taylor expansion vanish as F_{eq} is a cubic polynomial.) The initial conditions (5.10) imply that

$$\mathscr{X}(0+) = X_{\mathrm{ind}} - \mathcal{X}(0+), \quad \mathscr{X}_{\mathcal{T}}(0+) = 0, \quad \mathscr{X}_{\mathcal{T}\mathcal{T}}(0+) = -F_{\mathrm{ind}}.$$

Due to the nonlinear terms in (5.16), it is difficult to make analytical progress. We note that by multiplying by $\partial \mathscr{X}/\partial \mathcal{T}$ and integrating twice, it is possible to obtain an implicit equation for $\mathscr{X}$ (up to quadrature). However, each integration introduces a further unknown function of the slow timescale T, which requires a solvability condition to be determined. We therefore make the simplifying assumption that $|\mathscr{X}| \ll 1$, so that (5.16) is approximately

$$\frac{\partial^2 \mathscr{X}}{\partial \mathcal{T}^2} + F_{\mathrm{eq}}'(\mathcal{X}; 2\lambda)\mathscr{X} = 0. \tag{5.17}$$

Provided that $F_{\mathrm{eq}}'(\mathcal{X}; 2\lambda) > 0$ (an assumption we will later justify in Appendix 5.A), the solutions are periodic; we denote the period by L, which will vary on the slow timescale as $\mathcal{X}$ varies. Integrating the equation from $\mathcal{T} = 0$ to $\mathcal{T} = L$ then shows that for each T

$$\int_0^L \mathscr{X}\,\mathrm{d}\mathcal{T} = 0. \tag{5.18}$$

Returning to the way we decomposed the solution in (5.14), we see that $\mathcal{X}$ corresponds to

the mean value of X_0 that varies on the slow timescale T. This evolution is captured by the variable $A(T)$. The variable $\mathscr{X}$ describes the oscillations around this mean displacement that occur on the fast timescale $\mathcal{T}$; the property (5.18) guarantees that these oscillations do not influence the mean value if their amplitude is small. We now show that it is possible to obtain an evolution equation for $A(T)$ without requiring detailed knowledge of $\mathscr{X}$, using only the zero-mean property (5.18). While it is possible to obtain an analytical expression for $\mathscr{X}$ using the simplified equation (5.17) (after formulating a second solvability condition), we do not pursue this here — knowledge of $\mathcal{X}$ will be sufficient to determine when snap-through occurs and the associated snap-through time.

Before proceeding, we consider when the assumption $|\mathscr{X}| \ll 1$ is justified. From the initial conditions for $\mathscr{X}$, we expect this to be valid whenever $|X_{\text{ind}} - \mathcal{X}(0+)| \ll 1$ and $|F_{\text{ind}}| \ll 1$. Using the initial condition implied by (5.15), i.e.

$$F_{\text{eq}}(\mathcal{X}(0+); 2\lambda) = \lambda X_{\text{ind}} \left(1 - e^{-T_{\text{ind}}}\right) = -F_{\text{ind}} + F_{\text{eq}}(X_{\text{ind}}; 2\lambda), \qquad (5.19)$$

we expect that $X_{\text{ind}} \approx \mathcal{X}(0+)$ whenever $|F_{\text{ind}}| \ll 1$; hence, we simply require $|F_{\text{ind}}| \ll 1$ for validity. For example, in the particular case $X_{\text{ind}} = X_{\text{fold}} = 3/2$, this becomes (using the expression (5.6))

$$|F_{\text{ind}}| = \frac{3}{2} \left| \lambda - \frac{1}{4} + \lambda e^{-T_{\text{ind}}} \right| \ll 1.$$

For $\lambda \in [0, 1/4]$, we have that $F_{\text{ind}} \in [-3/8, 3/8]$ so the above approximation should be reasonably accurate (increasing in accuracy as $\lambda \to 1/4$ for $T_{\text{ind}} \gg 1$ and as $\lambda \to 1/8$ for $T_{\text{ind}} \ll 1$).

First order problem

At $O(\text{De}^{-1})$, the ODE (5.9) becomes

$$\frac{\partial^3 X_1}{\partial \mathcal{T}^3} + F_{\text{eq}}'(X_0; 2\lambda) \frac{\partial X_1}{\partial \mathcal{T}} + F_{\text{eq}}''(X_0; 2\lambda) \frac{\partial X_0}{\partial \mathcal{T}} X_1 = -\frac{\partial^2 X_0}{\partial \mathcal{T}^2} - 3 \frac{\partial^3 X_0}{\partial \mathcal{T}^2 \partial T}$$
$$-F_{\text{eq}}'(X_0; 2\lambda) \frac{\partial X_0}{\partial T} - F_{\text{eq}}(X_0; \lambda).$$

Re-writing the final two terms on the right-hand side using the leading order equation (5.13), this can be written as

$$\frac{\partial^3 X_1}{\partial \mathcal{T}^3} + \frac{\partial}{\partial \mathcal{T}} \left[F_{\text{eq}}'(X_0; 2\lambda) X_1 \right] = -2 \frac{\partial^3 X_0}{\partial \mathcal{T}^2 \partial T} + \lambda X_0 - \lambda X_{\text{ind}} \left(1 - e^{-T_{\text{ind}}}\right) - \frac{\mathrm{d}A}{\mathrm{d}T} - A.$$

This represents a linear, inhomogeneous problem for X_1. Setting the right-hand side to zero, we see that the homogeneous problem can be solved approximately whenever

$|\mathscr{X}| \ll 1$ by taking $X_1 = X_1(T)$, as $X_0 \approx \mathcal{X}(T)$ in this case and so all $\mathcal{T}$ derivatives vanish. This homogeneous solution is associated with the freedom we had to incorporate the function $A(T)$ in the leading order problem; recall that $A(T)$ entered when we integrated the problem once with respect to $\mathcal{T}$. We therefore expect to determine $A(T)$ from the solvability condition associated with the approximate homogeneous solution $X_1 = X_1(T)$. To formulate this condition, we simply integrate the first order problem from $\mathcal{T} = 0$ to $\mathcal{T} = L$. We assume that for each fixed T, the solution X_1 is also a periodic function with period L; this is reasonable, since X_1 is forced by the X_0 terms that have period L. It follows that all $\partial/\partial\mathcal{T}$ terms vanish in the integration and we are left with

$$\frac{\lambda}{L}\int_0^L X_0 \, \mathrm{d}\mathcal{T} - \lambda X_{\mathrm{ind}}\left(1 - e^{-T_{\mathrm{ind}}}\right) - \frac{\mathrm{d}A}{\mathrm{d}T} - A = 0.$$

Using the zero-mean property (5.18), the first term can be evaluated as $\lambda\mathcal{X}$. Eliminating $A(T)$ for $\mathcal{X}$ using the relation (5.15), we arrive at

$$F'_{\mathrm{eq}}(\mathcal{X}; 2\lambda)\frac{\mathrm{d}\mathcal{X}}{\mathrm{d}T} + F_{\mathrm{eq}}(\mathcal{X}; \lambda) = 0. \tag{5.20}$$

This equation is exactly our original ODE (5.7) when we set $\mathrm{De} = \infty$! This corresponds to neglecting the terms associated with inertia. This is perhaps not so surprising: when the zero-mean property (5.18) holds, the fast elastic oscillations 'cancel out' on the slow viscous timescale T and so do not affect the dynamics. However, the above analysis shows that the correct initial condition is *not* $\mathcal{X}(0+) = X_{\mathrm{ind}}$, as might be expected. Instead, from (5.19), $\mathcal{X}(0+)$ satisfies

$$F_{\mathrm{eq}}(\mathcal{X}(0+); 2\lambda) - F_{\mathrm{eq}}(X_{\mathrm{ind}}; 2\lambda) = -F_{\mathrm{ind}}.$$

This correction arises from the initial transient around $T = 0$ where inertia is always important; physically, the above equation states that the change in spring force in moving from X_{ind} to $\mathcal{X}(0+)$ (when the SLS element is fully unrelaxed with effective stiffness 2λ) must balance the discontinuity in the indentation force. When viewed on the slow timescale, the mean value $\mathcal{X}$ then appears to change discontinuously from the indentation displacement X_{ind}.

To check our multiple-scale analysis, we numerically integrate the simplified ODE (5.20) with initial condition (5.19). In figure 5.4b solutions are superimposed (as black dotted curves) onto the trajectories obtained by integrating the full ODE (5.7) when $X_{\mathrm{ind}} = X_{\mathrm{fold}}$ and $\mathrm{De} = 10$. We see that the agreement is excellent, with the multiple-scale solution indeed capturing the average behaviour of the displacement during snap-through (see inset). (We observe slight disagreement when the mean value changes rapidly on a timescale comparable to $\mathcal{T}$, in which case the multiple-scale analysis is no longer applicable.) Figure

5.4b also shows that the initial value $\mathcal{X}(0+)$ may be both larger or smaller than X_{ind}, and the value changes rapidly as the indentation time T_{ind} increases: compare the initial value predicted for $T_{\mathrm{ind}} = 1$ (yellow curve), which is very close to zero, with that for $T_{\mathrm{ind}} = 5$ (orange curve), which is close to X_{ind}. We postpone a detailed analysis of $\mathcal{X}(0+)$ to the section below and Appendix 5.A.

Snap-through dynamics

We have shown that while the amplitude of the oscillations is small compared to the mean displacement, the leading order behaviour is given by

$$X \sim \mathcal{X}(T) \quad \text{where} \quad \frac{\mathrm{d}\mathcal{X}}{\mathrm{d}T} = -\frac{F_{\mathrm{eq}}(\mathcal{X}; \lambda)}{F'_{\mathrm{eq}}(\mathcal{X}; 2\lambda)}, \tag{5.21}$$

subject to the initial condition (5.19). Since (5.21) represents a first-order autonomous ODE for $\mathcal{X}$, the dynamics can be understood by considering the $(\mathcal{X}, \mathrm{d}\mathcal{X}/\mathrm{d}T)$ phase plane; see figure 5.7. Moreover, (5.21) implies that the qualitative features of the phase plane are determined by the roots of $F_{\mathrm{eq}}(\mathcal{X}; \lambda) = 0$ and $F'_{\mathrm{eq}}(\mathcal{X}; 2\lambda) = 0$. In particular, the roots of $F_{\mathrm{eq}}(\mathcal{X}; \lambda) = 0$ correspond to stationary points, $\mathrm{d}\mathcal{X}/\mathrm{d}T = 0$. For $\lambda < 1/4$, there are two distinct stationary points away from zero, which correspond to the stable and unstable roots of $F_{\mathrm{eq}}(\mathcal{X}; \lambda) = 0$; for $\lambda > 1/4$, the only stationary point is the zero solution, $\mathcal{X} = 0$. The roots of $F'_{\mathrm{eq}}(\mathcal{X}; 2\lambda) = 0$ correspond to vertical asymptotes where $|\mathrm{d}\mathcal{X}/\mathrm{d}T| = \infty$. Denoting these roots by $\mathcal{X}_{\pm}$, we find that

$$\mathcal{X}_{\pm} = 1 \pm \left(\frac{1 - 2\lambda}{3}\right)^{1/2}, \quad F_{\mathrm{eq}}(\mathcal{X}_{\pm}; 2\lambda) = 2\lambda \mp 2\left(\frac{1 - 2\lambda}{3}\right)^{3/2}.$$

These roots are real and distinct if and only if $\lambda < 1/2$, in which case the phase plane features two vertical asymptotes; otherwise the trajectories smoothly approach the origin.

In Appendix 5.A, we show that the initial value $\mathcal{X}(0+)$ must satisfy either $\mathcal{X}(0+) < \mathcal{X}_{-}$ or $\mathcal{X}(0+) > \mathcal{X}_{+}$, i.e. the solution always starts outside the interval between the two vertical asymptotes (for this reason we have lightly shaded this region in figure 5.7). Focussing on $\lambda \leq 1/2$, we deduce that there are three possibilities depending on where the solution starts in the phase plane:

- If $\mathcal{X}(0+) > \mathcal{X}_{+}$ and $\lambda < 1/4$, then the mean value starts to the right of both vertical asymptotes and approaches the stationary point away from zero (as with the orange curve in figure 5.7). This point corresponds to the stable root of $F_{\mathrm{eq}}(\mathcal{X}; \lambda) = 0$. Because $\mathcal{X}_{+} > 1$, the truss starts in an inverted position and there is no snap-through.
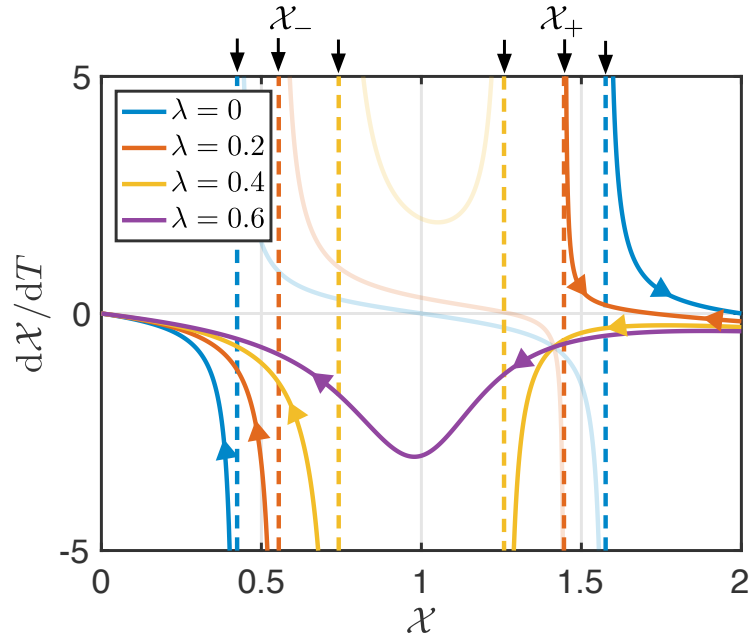
Figure 5.7: *Phase plane of the simplified ODE (5.21) for different values of λ (coloured curves; see legend). Arrows indicate the direction of motion. The initial value $\mathcal{X}(0+)$ is determined by the transient around $T = 0$ in which inertia is important, and is the solution of the cubic (5.19).*

- If $\mathcal{X}(0+) > \mathcal{X}_+$ and $\lambda > 1/4$, then the mean value starts to the right of both vertical asymptotes. It then decreases to the vertical asymptote at $\mathcal{X}_+$ where rapid snap-through occurs (yellow curve in figure 5.7) and inertial effects again become significant — because this approach to the asymptote occurs on the slow timescale T, the total time taken to snap-through is at least $O(1)$. This regime corresponds to pseudo-bistable behaviour, in which the snap-through time is governed by the timescale of viscous relaxation.

- If $\mathcal{X}(0+) < \mathcal{X}_-$, then the mean value starts to the left of the vertical asymptotes and smoothly decays to zero. Because $\mathcal{X}_- < 1$, the truss immediately snaps back to near its natural configuration during the initial transient where inertia is important. The amplitude of the elastic oscillations will therefore be large compared to the mean value in this case, and our assumption $|\mathscr{X}| \ll 1$ is no longer valid; nevertheless, we expect the truss to pass $X = 0$ on an $O(\mathrm{De}^{-1})$ timescale so that $T_{\mathrm{snap}} = O(\mathrm{De}^{-1})$.

The final task is to determine when the initial value satisfies $\mathcal{X}(0+) > \mathcal{X}_+$. This is not obvious because (5.19) implies that $\mathcal{X}(0+)$ is the root of a cubic polynomial, for which there may be multiple real solutions. The relevant solution can be found by analysing the phase portrait of equation (5.13): setting $A(T) = 0$, this equation governs the elastic behaviour of the truss at very early times, and hence determines which root of (5.19) the solution approaches. When viewed on the slow timescale, this root corresponds to the

relevant value of $\mathcal{X}(0+)$. The full analysis is provided in Appendix 5.A. The key result is that if $1 \leq X_{\text{ind}} < X_{\text{fold}}$, then $\mathcal{X}(0+) > \mathcal{X}_+$ if and only if $F_{\text{ind}} < 0$; otherwise we have $\mathcal{X}(0+) < \mathcal{X}_-$. Physically, this states that the indentation force needs to be adhesive for the truss to remain in an inverted state. This is intuitive: if the truss has to be 'pulled' upwards to the imposed indentation depth, it should move further downwards (increasing X) when the indenter is released. Using the expression (5.6) for F_{ind}, the condition $F_{\text{ind}} < 0$ can be expressed as

$$\mathcal{X}(0+) > \mathcal{X}_+ \iff T_{\text{ind}} > \log\left[\frac{\lambda X_{\text{ind}}}{-F_{\text{eq}}(X_{\text{ind}}; \lambda)}\right]. \tag{5.22}$$

In the alternative case $X_{\text{fold}} \leq X_{\text{ind}} \leq 2$, the condition $F_{\text{ind}} < 0$ turns out to no longer be relevant. Instead, in Appendix 5.A we show that

$$\mathcal{X}(0+) > \mathcal{X}_+ \iff T_{\text{ind}} > \log\left[\frac{\lambda X_{\text{ind}}}{\lambda X_{\text{ind}} - F_{\text{eq}}(X^*; 2\lambda)}\right], \tag{5.23}$$

where

$$X^* = -\frac{1}{3}(X_{\text{ind}} - 4) + \frac{\sqrt{2}}{3}\sqrt{3 - 6\lambda - (X_{\text{ind}} - 1)^2}.$$

Physically, this condition arises from bounding the amplitude of the elastic oscillations at very early times, so that these do not 'push' the truss sufficiently far from the inverted state and cause an immediate snap-back.

Combining this with the phase-plane discussion above, the different dynamical regimes are shown schematically in figure 5.8. This explains how the qualitative features of the dynamics are very different in the two cases $X_{\text{ind}} < X_{\text{fold}}$ and $X_{\text{ind}} \geq X_{\text{fold}}$. When $X_{\text{ind}} < X_{\text{fold}}$, it may be shown that the boundary predicted by (5.22) reaches a vertical asymptote on the $(\lambda, T_{\text{ind}})$-plane when $\lambda < 1/4$. For values T_{ind} below the boundary we have $\mathcal{X}(0+) < \mathcal{X}_-$, and the above discussion implies that the truss immediately snaps with $T_{\text{snap}} = O(\text{De}^{-1})$ (shaded blue in figure 5.8). Above the boundary, $\mathcal{X}(0+) > \mathcal{X}_+$ and, because $\lambda < 1/4$ here, the truss does not snap-through. Pseudo-bistable behaviour therefore cannot be obtained when $X_{\text{ind}} < X_{\text{fold}}$. Conversely, when $X_{\text{fold}} \leq X_{\text{ind}} \leq 2$, the boundary predicted by (5.23) reaches a vertical asymptote when $\lambda > 1/4$. Hence, there is a region where $\mathcal{X}(0+) > \mathcal{X}_+$ and $\lambda > 1/4$, in which pseudo-bistable behaviour occurs (shaded red). We deduce that $T_{\text{snap}} \gtrsim O(1)$ precisely when

$$X_{\text{fold}} \leq X_{\text{ind}} \leq 2, \quad \lambda > 1/4, \quad T_{\text{ind}} > \log\left[\frac{\lambda X_{\text{ind}}}{\lambda X_{\text{ind}} - F_{\text{eq}}(X^*; 2\lambda)}\right].$$
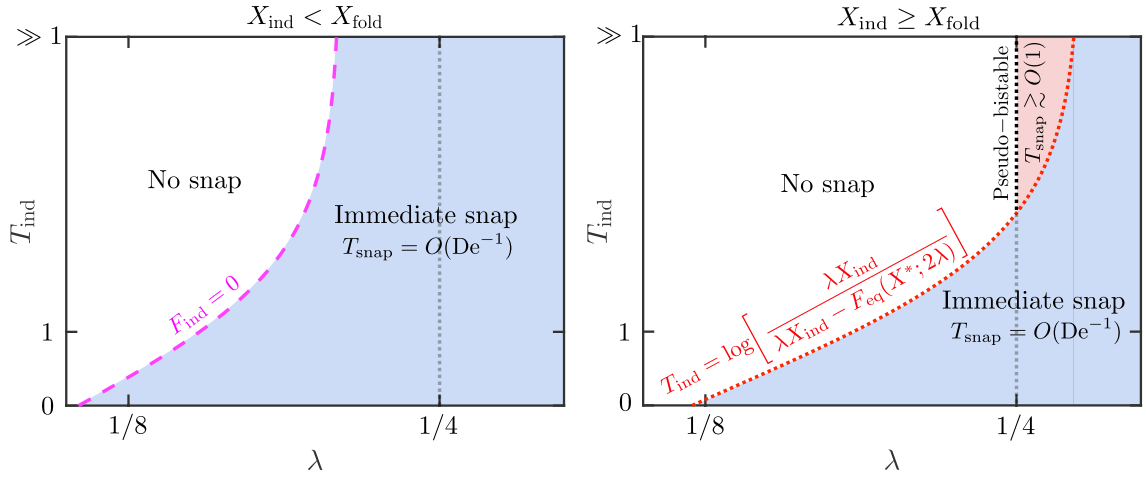
Figure 5.8: *The different dynamical regimes in the limit* $\mathrm{De} \gg 1$ *predicted by multiple-scale analysis: we combine the phase plane in figure 5.7 with the analysis of* $\mathcal{X}(0+)$ *in Appendix 5.A.*

As $\lambda \to 1/4$, the critical value of T_{ind} approaches the $O(1)$ value

$$T_{\mathrm{ind}} = \log \left[\frac{-27 X_{\mathrm{ind}}}{20 X_{\mathrm{ind}}^3 - 60 X_{\mathrm{ind}}^2 + 15 X_{\mathrm{ind}} + 52 - 2 \left[3 - 2(X_{\mathrm{ind}} - 1)^2 \right]^{3/2}} \right].$$

Figure 5.8 explains many basic features of pseudo-bistability that have been observed previously in experiments and numerical simulations (Santer, 2010; Brinkmeyer *et al.*, 2012; 2013; Madhukar *et al.*, 2014; Urbach & Efrati, 2017). We see that pseudo-bistability occurs only in a narrow parameter range, near the threshold at which snap-through no longer occurs (i.e. $\lambda = \lambda_{\mathrm{fold}} = 1/4$ here); the width of the pseudo-bistable region grows as the amount of stress relaxation increases, i.e. increasing T_{ind}; and pseudo-bistable behaviour is not obtained if T_{ind} is too small, nor if the indentation depth X_{ind} is below a critical value. In addition, the phase-plane in figure 5.7 explains how the truss initially creeps in an inverted state before abruptly accelerating upwards; this difference in timescales is considered to be a distinguishing feature of pseudo-bistable behaviour (Brinkmeyer *et al.*, 2012; 2013). We emphasise that the analytical understanding of these features presented here is, to the best of our knowledge, new.

To check the validity of the picture presented in figure 5.8, we have superimposed the boundaries predicted by (5.22)–(5.23) (red dotted curves, magenta dashed curves) onto the numerical snap-through times in figures 5.5–5.6. We observe that the agreement with the numerics is excellent, despite the fact that the assumption $|F_{\mathrm{ind}}| \ll 1$ made in the multiple-scale analysis is not formally valid throughout the range of values shown. We now consider the detailed snap-through times in the pseudo-bistable regime.

Snap-through time in the pseudo-bistable regime

Another key feature of the dynamics is that the snap-through time increases considerably as $\lambda \searrow 1/4$ in the pseudo-bistable regime, becoming much larger than $O(1)$ (figure 5.5b). This slowing down does not require $X_{\mathrm{ind}} \approx X_{\mathrm{fold}}$ but can be observed when $X_{\mathrm{ind}} = 1.7$ (figure 5.6b). The phase plane in figure 5.7 suggest this slowing down is due to a saddle-node ghost: when $\lambda > 1/4$ the stationary point away from zero no longer exists, but as $\lambda \searrow 1/4$ the trajectory passes increasingly close to the line $\mathrm{d}\mathcal{X}/\mathrm{d}T = 0$ at $\mathcal{X} \approx X_{\mathrm{fold}}$. Because the velocity becomes very small but non-zero, this will lead to a slow passage through a bottleneck.

To analyse this slowing down in detail, we set

$$\lambda = \frac{1}{4} + \epsilon, \quad \mathcal{X} = X_{\mathrm{fold}} - \epsilon^{1/2}\chi, \tag{5.24}$$

where $0 < \epsilon \ll 1$ and $|\chi| \ll \epsilon^{-1/2}$. Based on previous chapters, we anticipate an $\epsilon^{1/2}$ scaling for the change in displacement during the bottleneck phase (we have also introduced a minus sign since we expect the displacement to decrease during snap-through). We expand

$$
\begin{aligned}
F_{\mathrm{eq}}(\mathcal{X}; \lambda) &= \frac{3}{2}\epsilon\left(1 + \chi^2\right) + O(\epsilon^{3/2}\chi, \epsilon^{3/2}\chi^3), \\
F'_{\mathrm{eq}}(\mathcal{X}; 2\lambda) &= \frac{1}{4} + O(\epsilon, \epsilon^{1/2}\chi).
\end{aligned}
\tag{5.25}
$$

The neglected terms here are small compared to at least one retained term provided $|\chi| \ll \epsilon^{-1/2}$. Inserting these expansions into the simplified ODE (5.21), we obtain

$$\frac{\mathrm{d}\chi}{\mathrm{d}T} \sim 6\epsilon^{1/2}\left(1 + \chi^2\right), \tag{5.26}$$

i.e. we recover the normal form for overdamped dynamics near a saddle-node bifurcation. The solution is

$$\chi \sim \tan\left[6\epsilon^{1/2}T + \arctan\chi(0+)\right],$$

where

$$\chi(0+) = \epsilon^{-1/2}\left[X_{\mathrm{fold}} - \mathcal{X}(0+)\right].$$

We now show that it is often possible to approximate the snap-through time without detailed knowledge of $\mathcal{X}(0+)$, which would require solving the cubic equation (5.19). The snap-through time is dominated by the time spent passing through the bottleneck, T_b, which can be determined by finding the time when χ first reaches $O(\epsilon^{-1/2})$; after this point, we no longer have $\mathcal{X} \approx X_{\mathrm{fold}}$ and so the truss is moving rapidly. Using the expansion

$\tan x \sim (\pi/2 - x)^{-1}$ as $x \to \pi/2$, we have that $\chi = O(\epsilon^{-1/2})$ when

$$T_b = \frac{\pi}{12}\epsilon^{-1/2} - \frac{1}{6}\epsilon^{-1/2}\arctan\chi(0+) + O(1).$$

It follows that there are three distinguished limits, depending on the size and sign of $\chi(0+)$:

- If $|X_{\text{fold}} - \mathcal{X}(0+)| \ll \epsilon^{1/2}$, the argument of the arctan function is much smaller than unity. The asymptotic behaviour $\arctan x \sim x$ for $x \ll 1$ then implies that

$$\chi \sim \tan\left[6\epsilon^{1/2}T + \chi(0+)\right], \quad T_b = \frac{\pi}{12}\epsilon^{-1/2} + O\left(\epsilon^{-1/2}\chi(0+), 1\right).$$

  Here the truss starts in the immediate neighbourhood of the fold displacement X_{fold}, i.e. in the middle of the bottleneck. We recover the usual inverse square-root scaling law for an overdamped saddle-node ghost, with the bottleneck duration independent of T_{ind}.

- If $|X_{\text{fold}} - \mathcal{X}(0+)| \gg \epsilon^{1/2}$ and $\mathcal{X}(0+) < X_{\text{fold}}$, the argument of the arctan function is positive and much larger than unity. Using the expansion $\arctan x \sim \pi/2 - 1/x$ as $x \to \infty$, we obtain

$$\chi \sim \frac{1}{6}\epsilon^{-1/2}\left(\frac{1}{6\epsilon^{1/2}\chi(0+)} - T\right)^{-1}, \quad T_b = \frac{1}{6\epsilon^{1/2}\chi(0+)} + O(1) \ll \epsilon^{-1/2}.$$

  In this case the truss starts away from the immediate vicinity of X_{fold} and the quadratic term in the normal form is initially large compared to the $O(\epsilon)$ term. The truss never passes X_{fold} and simply accelerates out of the bottleneck. The dynamics are therefore limited by the initial value $\mathcal{X}(0+)$ and hence the value of T_{ind}.

- If $|X_{\text{fold}} - \mathcal{X}(0+)| \gg \epsilon^{1/2}$ and $\mathcal{X}(0+) > X_{\text{fold}}$, the argument of the arctan function is very large and negative. Using the expansion $\arctan x \sim -\pi/2 + 1/x$ as $x \to -\infty$, we obtain

$$\chi \sim \tan\left[6\epsilon^{1/2}T - \frac{\pi}{2} + \frac{1}{\chi(0+)}\right], \quad T_b = \frac{\pi}{6}\epsilon^{-1/2} + O\left(\frac{1}{\epsilon^{1/2}\chi(0+)}, 1\right).$$

  Here the displacement starts away from X_{fold} but passes X_{fold} during snap-through. The bottleneck duration is therefore twice the value compared to the case $|X_{\text{fold}} - \mathcal{X}(0+)| \ll \epsilon^{1/2}$.

Because we have assumed $\mathcal{X}(0+) \approx X_{\text{ind}}$ in our multiple-scale analysis (needed for $|\mathcal{X}| \ll 1$), we expect the final case is relevant whenever X_{ind} is not close to X_{fold}, e.g. when $X_{\text{ind}} = 1.7$. This is confirmed in figure 5.9a, which shows that the computed snap-through
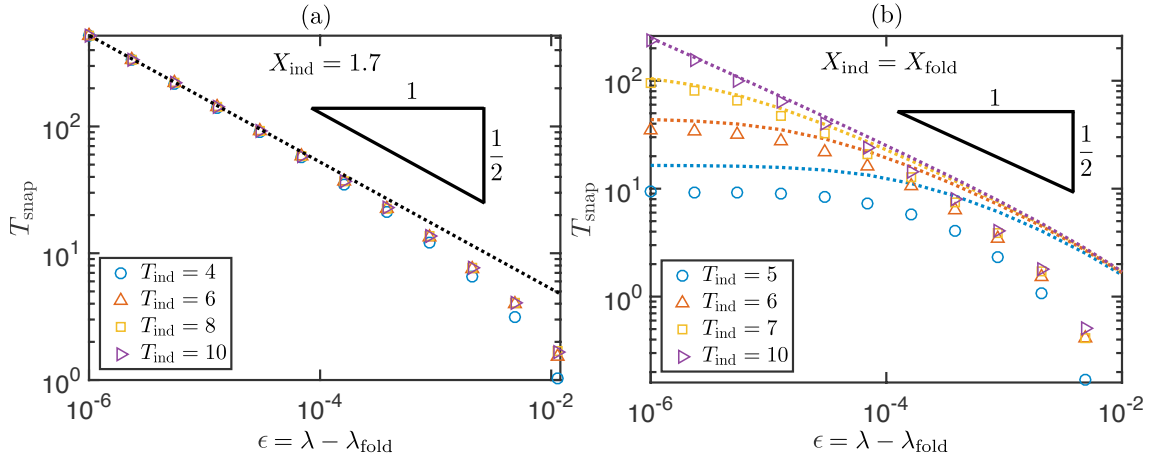
Figure 5.9: *Snap-through times in the pseudo-bistable regime (*De = 100*). (a) Numerical results for (a) $X_{\mathrm{ind}} = 1.7$ and (b) $X_{\mathrm{ind}} = X_{\mathrm{fold}} = 3/2$ (symbols; see legend). Also shown for comparison is the asymptotic prediction $T_{\mathrm{snap}} \sim (\pi/6)\epsilon^{-1/2}$ (black dotted curve) valid for $X_{\mathrm{ind}} \not\approx X_{\mathrm{fold}}$, and the predictions (5.28) (coloured dotted curves) valid for $X_{\mathrm{ind}} = X_{\mathrm{fold}}$.*

times (obtained by numerically integrating (5.7)–(5.8)) collapse onto the prediction $T_{\mathrm{snap}} \sim (\pi/6)\epsilon^{-1/2}$.

The case when $X_{\mathrm{ind}} \approx X_{\mathrm{fold}}$ is much more delicate as we require detailed knowledge of $\mathcal{X}(0+)$ to determine the relative sizes of $|X_{\mathrm{fold}} - \mathcal{X}(0+)|$ and $\epsilon^{1/2}$, and hence the relevant distinguished limit. For example, setting $X_{\mathrm{ind}} = X_{\mathrm{fold}}$, we insert the expansions (5.24) into the initial condition (5.19). Upon neglecting terms quadratic in ϵ and $e^{-T_{\mathrm{ind}}}$ (from figure 5.5b we have $T_{\mathrm{ind}} \gtrsim 3.5$ in the pseudo-bistable regime, so that $e^{-T_{\mathrm{ind}}} \lesssim 0.03 \ll 1$), we obtain

$$\chi(0+) \sim 6\epsilon^{1/2} + \frac{3}{2}\epsilon^{-1/2}e^{-T_{\mathrm{ind}}}. \tag{5.27}$$

The above expression for the bottleneck duration then becomes

$$T_b = \frac{\pi}{12}\epsilon^{-1/2} - \frac{1}{6}\epsilon^{-1/2}\arctan\left(6\epsilon^{1/2} + \frac{3}{2}\epsilon^{-1/2}e^{-T_{\mathrm{ind}}}\right) + O(1). \tag{5.28}$$

The distinguished limits now correspond to $\epsilon^{-1/2}e^{-T_{\mathrm{ind}}} \ll 1$ and $\epsilon^{-1/2}e^{-T_{\mathrm{ind}}} \gg 1$, and we obtain

$$T_b = \begin{cases} \frac{\pi}{12}\epsilon^{-1/2} + O(\epsilon^{-1}e^{-T_{\mathrm{ind}}}, 1) & \text{if} \quad T_{\mathrm{ind}} \gg \log\left(\epsilon^{-1/2}\right), \\ \frac{1}{9}e^{T_{\mathrm{ind}}} + O(1) & \text{if} \quad T_{\mathrm{ind}} \ll \log\left(\epsilon^{-1/2}\right). \end{cases} \tag{5.29}$$

Figure 5.9b shows that the prediction (5.28) approximates the numerical snap-through times reasonably well, with the data indeed obeying the $\epsilon^{-1/2}$ scaling law when T_{ind} is sufficiently large compared to $\log\left(\epsilon^{-1/2}\right)$. However, the $O(1)$ error in (5.28) becomes significant if $T_{\mathrm{ind}} \lesssim 5$ or $\epsilon \gtrsim 10^{-4}$ is only moderately small. While it is possible to obtain the $O(1)$ correction analytically by integrating the ODE (5.21) directly, we do not compute

this here.

5.3.3 Data comparison

We have shown that in the pseudo-bistable regime, the dynamics slow down considerably due to the ghost of the saddle-node bifurcation at $\lambda = \lambda_{\text{fold}}$. The snap-through time then inherits the inverse square-root scaling law for overdamped dynamics, i.e.

$$T_{\text{snap}} = \frac{t_{\text{snap}}}{\eta/E} \propto \epsilon^{-1/2} \qquad \text{where} \qquad \epsilon = \lambda - \lambda_{\text{fold}},$$

valid when $0 < \epsilon \ll 1$ and T_{ind} is sufficiently large. As discussed in §5.1.1, we may consider the truss as a lumped model for more complex structures such as spherical caps: here we regard the central springs as parameterising the membrane stiffness of the shell, and the vertical SLS spring as parameterising the bending stiffness. Because the dimensionless parameter λ measures the ratio of the stiffnesses of these springs, λ is analogous to the Föppl-von-Kármán number, which measures the ratio of bending and stretching energies for spherical caps (Brodland & Cohen, 1987). The parameter λ is also the analogue of the μ parameter we discussed in Chapter 4, which measures this ratio in the context of pre-buckled elastic arches. Hence, we expect that the above scaling law may hold more generically and explain the slowing down that is observed in these systems.

To test this hypothesis, we examine data for the snap-through times of various viscoelastic structures reported in the literature. As in our truss model, each structure is held in an inverted state for a duration t_{ind}, before being instantaneously released from rest. The snap-through time is measured to be the time taken between release and when the structure rapidly accelerates towards its natural state. We focus on results in which the indentation time t_{ind} is fixed, while the analogue of λ is varied between each snapping experiment. In all cases examined, the structure exhibits pseudo-bistability so that the snap-through times are easily measured. Where data is only available graphically, we have extracted the values using the WebPlotDigitizer (arohatgi.info/WebPlotDigitizer).

The first set of data we consider is that of Brinkmeyer *et al.* (2012), who study the snap-through of viscoelastic spherical caps using finite element simulations (performed in ABAQUS). In their viscoelastic model, Brinkmeyer *et al.* (2012) use a Prony series expansion for the Young's modulus, which assumes that the modulus can be written as a sum of exponentially decaying modes. The coefficients in the sum and the relaxation timescales are then fitted to experimental data for the relaxation of Sylgard 182, a rubbery polymer. The thickness of the shell and its depth are varied between different simulations, keeping all other parameters fixed. We also analyse the snap-through times of elastic arches reported by Brinkmeyer *et al.* (2013). Similar to the problem we discussed at

the beginning of Chapter 4, the arch is subject to an end-shortening and its ends are clamped at equal angles to the horizontal. Brinkmeyer *et al.* (2013) perform finite element simulations (again using a Prony series expansion for the Young's modulus) in which the end-shortening and clamp angle are varied, as well as experiments on arches fabricated from Sylgard 182. The final data set we examine is the snap-through times of truncated conical shells simulated by Urbach & Efrati (2017); similar to spherical caps, these feature an 'inside-out' state that snaps back to a natural shape when released. In their simulations, Urbach & Efrati (2017) model the viscoelastic behaviour using a SLS model, implemented using a metric description. The inertia of the shell is neglected and its thickness is varied between simulations.

A summary of the conditions for each of these data is provided in table 5.1. Here we have separated the data so that only a single parameter is varying within each data set (corresponding to a particular row in the table), indicated by a unique symbol shape, while different references are distinguished using different colours. We have provided the relevant parameter values for each data set. These are the shell/arch thickness h, the relevant horizontal lengthscale l (defined to be the base diameter of the shell/natural length of the arch), Young's modulus E, Poisson ratio ν, material density ρ_s, viscous timescale $[t]_{\mathrm{vis}}$, elastic timescale t^*, and the indentation time t_{ind}. (Where a parameter varies within a data set, the range of values is provided, and we use the average to compute t^*.) For the data reported by Brinkmeyer *et al.* (2012; 2013), there is no single viscous timescale due to the multiple terms in the Prony series expansion. We therefore estimate $[t]_{\mathrm{vis}}$ by the timescale that appears in the dominant term of the Prony series (i.e. the term with the largest coefficient). To estimate the elastic timescale, we recall from Chapter 4 that a balance between inertial forces and bending forces for a shell/arch yields

$$t^* \sim \left(\frac{\rho_s h l^4}{B} \right)^{1/2},$$

where l is the horizontal lengthscale defined above, and B is the bending stiffness (in particular $B = Eh^3/[12(1 - \nu^2)]$ for a shell, and $B = Eh^3/12$ for an arch). (In Urbach & Efrati (2017) inertia of the shell is neglected so we do not know the value of ρ_s or t^*.) Table 5.1 shows that for all data sets, the viscous timescale $[t]_{\mathrm{vis}}$ is an order of magnitude larger than the elastic timescale t^*, so these systems are effectively in the large Deborah number limit. The indentation times t_{ind} are also much larger than $[t]_{\mathrm{vis}}$, so that the dimensionless indentation times $T_{\mathrm{ind}} = t_{\mathrm{ind}}/[t]_{\mathrm{vis}}$ are large. Hence, the pseudo-bistability observed in these systems occurs in an analogous parameter range to that in our truss model.

For each data set it is found that as the analogue of λ varies, the snap-through time increases rapidly and appears to diverge near a critical value. Beyond this transition no

Table 5.1: *Summary of previous data for pseudo-bistable snap-through times reported in the literature.*

Reference	System	Data type	Varying	h (mm)	l (mm)	E (MPa)	ν	ρ_s (kgm^{-3})	$[t]_{\text{vis}}$ (s)	t^* (s)	t_{ind} (s)	Fitted exponent	Legend
Brinkmeyer et al. (2012)	Spherical shell	Simulation	Thickness	(5.16, 5.25)	54.16	0.935	0.469	1030	0.634*	0.0572	10	−1.08	●
Brinkmeyer et al. (2012)	Spherical shell	Simulation	Thickness†	(5.16, 5.72)	54.16	0.935	0.469	1030	0.634*	0.0548	10	−3.38	■
Brinkmeyer et al. (2012)	Spherical shell	Simulation	Depth	5.2	(54.1, 54.2)	0.935	0.469	1030	0.634*	0.0573	10	−1.22	▶
Brinkmeyer et al. (2013)	Buckled arch	Simulation	End-shortening	2.5	100	0.935	0.469	1035	3.66*	0.461	10	−0.500	▼
Brinkmeyer et al. (2013)	Buckled arch	Simulation	Clamp angle	2.5	100	0.935	0.469	1035	3.66*	0.461	10	−0.502	★
Brinkmeyer et al. (2013)	Buckled arch	Experiment	Clamp angle	2.5	100	0.935	0.469	1035	3.66*	0.461	10	−0.537	◀
Urbach & Efrati (2017)	Conical shell	Simulation	Thickness	(5.36, 5.76)	50	2.5	0.47	N/A	0.1	N/A	60	−0.519	◆

N/A, not applicable.

* Estimated from the dominant term of the Prony series expansion.

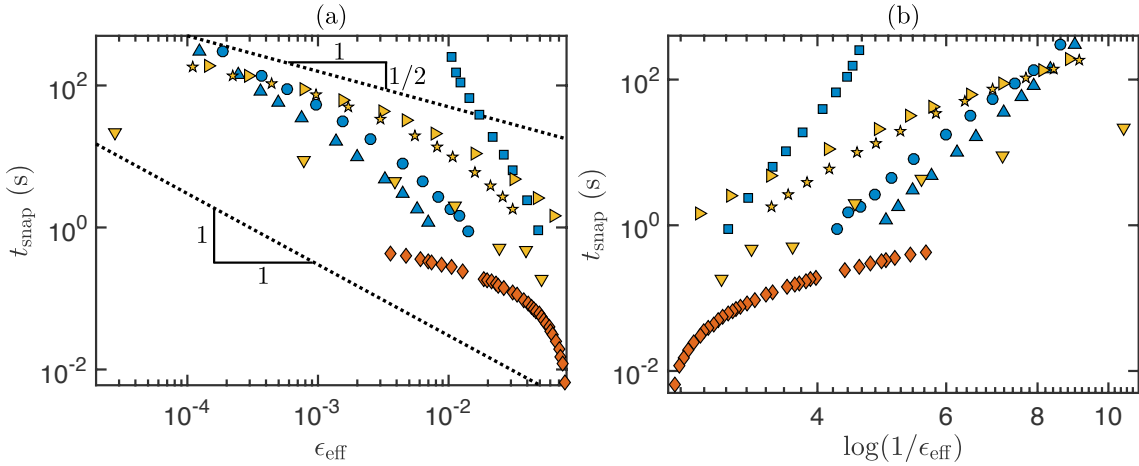† Using a larger material relaxation in the Prony series.

Figure 5.10: *(a) Snap-through times of viscoelastic arches and shells reported in the literature to exhibit pseudo-bistability. For a legend and the parameters used in each data set, see table 5.1. (b) Plotting the same data as a function of* $\log(1/\epsilon_{\mathrm{eff}})$*.*

snap-through occurs. This transition therefore appears to be the saddle-node bifurcation at which the inverted arch/shell becomes bistable. (For the inverted arch, we discussed at the start of Chapter 4 how the bifurcation is a subcritical pitchfork if the ends are clamped at equal angles; however, we expect this to 'unfold' to a saddle-node bifurcation in the presence of material imperfections, in a similar way to other buckling instabilities; see Hayman, 1978; Bushnell, 1981, for example.) We use the critical value that is reported to compute the normalised distance to the bifurcation, which we denote by ϵ_{eff}. For example, if the thickness h is varied and h_c is the critical value when snap-through no longer occurs, then we define

$$\epsilon_{\mathrm{eff}} = \left| \frac{h - h_c}{h_c} \right|,$$

and similarly when other parameters are varied. The dimensional snap-through times are plotted as a function of ϵ_{eff} on logarithmic axes in figure 5.10a. Here we observe the characteristic signs of a saddle-node ghost: as $\epsilon_{\mathrm{eff}} \to 0$ the snap-through time increases systematically, varying by over two orders of magnitude within a very narrow range of ϵ_{eff}.

The key observation is that the data of Brinkmeyer *et al.* (2013) (yellow symbols) and Urbach & Efrati (2017) (orange symbols) are roughly consistent with an inverse square-root scaling law, i.e. $t_{\mathrm{snap}} \propto \epsilon_{\mathrm{eff}}^{-1/2}$ as $\epsilon_{\mathrm{eff}} \to 0$. To be more quantitative, we fit each data set to a power law of the form $t_{\mathrm{snap}} \propto \epsilon_{\mathrm{eff}}^{\beta}$ using least squares. (For the data of Brinkmeyer *et al.* (2012; 2013) we fit the six points closest to bifurcation, while for Urbach & Efrati (2017) there is more data available so we instead fit the closest ten points). The best-fit exponents are provided in table 5.1 and confirm that $\beta \approx -0.5$ for the data reported by Brinkmeyer *et al.* (2013) and Urbach & Efrati (2017). While the data of Urbach & Efrati (2017) deviate significantly from the square–root scaling for moderately small values

$\epsilon_{\mathrm{eff}} \gtrsim 10^{-2}$, this is similar to the behaviour we have seen in our truss model, in which the error of the asymptotic prediction becomes significant if ϵ is not too small (compare to figures 5.9a–b).

In contrast, the snap-through times reported by Brinkmeyer *et al.* (2012) (blue symbols) do not appear to follow the square-root scaling, with the best-fit exponents $\beta \lesssim -1$. In particular, one data set (blue squares) appears to curve upwards for small ϵ_{eff}, suggesting that this discrepancy may be due to the sensitivity to the precise value of the bifurcation point (small shifts in ϵ_{eff} can cause such variations when plotted on logarithmic axes). However, when we plot t_{snap}^{-2} as a function of ϵ_{eff} on linear axes for these data (to eliminate this sensitivity), we do not observe a linear relationship, suggesting that these data obey a different scaling law. We note that this discrepancy may not be physical, but rather a direct consequence of the viscoelastic model used by Brinkmeyer *et al.* (2012), which assumes that the stiffness decays back to its fully unrelaxed value when the indenter is released. When we make this assumption in our truss model, we obtain $t_{\mathrm{snap}} \propto \log(1/\epsilon)$ rather than the $\epsilon^{-1/2}$ scaling when this assumption is not made; see Appendix 5.B. There is some evidence that the data of Brinkmeyer *et al.* (2012) indeed follow this logarithmic scaling; see figure 5.10b, which shows that these data exhibit a slightly more linear relationship when t_{snap} is plotted as a function of $\log(1/\epsilon_{\mathrm{eff}})$ compared to figure 5.10a. However, it is not clear why the logarithmic scaling is not found in the data of Brinkmeyer *et al.* (2013) (yellow symbols), despite the fact that these simulations are based on a similar assumption for the stiffness. In any case, in the absence of more experimental data, it is not possible to conclude that the square-root scaling holds generically for pseudo-bistable snap-through.

5.4 Snap-through dynamics: $\mathrm{De} \ll 1$

5.4.1 Numerical solution

In this section we consider the limit $\mathrm{De} \ll 1$, i.e. the relaxation timescale is much faster than the elastic timescale. This is the relevant limit for "glassy" polymers that possess a high degree of crystallinity, such as polyethylene terephthalate (PET) (Demirel *et al.*, 2011; Yilmazer *et al.*, 2000), as well as composite laminates reinforced by additives such as glass fibres (Brinkmeyer *et al.*, 2013). For simplicity, we focus on the case $X_{\mathrm{ind}} = X_{\mathrm{fold}} = 3/2$. Because the SLS element will generally behave as an elastic solid when viewed over the timescale of snap-through, we expect to recover similar dynamics to that presented in Chapter 4. However, we will show that when bottleneck behaviour occurs, this expectation is only correct when the indentation time is sufficiently large.

Typical numerically-determined trajectories in the small-De limit are shown in figures 5.11a–d (for De $= 10^{-2}$). Here the truss exhibits oscillations on the elastic timescale $T = O(\text{De}^{-1}) \gg 1$, which become damped on a much slower timescale (in fact, balancing terms in (5.7) shows that this damping timescale is $T = O(\text{De}^{-2})$). As we saw in the limit De $\gg$ 1, there are different dynamical regimes as the bifurcation parameter λ is varied. When $\lambda < \lambda_{\text{fold}} = 1/4$, it appears that the truss does not snap and oscillates around a mean value away from zero. Here viscous relaxation plays an insignificant role as the trajectories are indistinguishable for different indentation times T_{ind} (figure 5.11a). Surprisingly, as $\lambda \nearrow 1/4$ the truss may snap if the indentation time is sufficiently small (figure 5.11b). This behaviour must be due to viscous effects at very early times: if the truss were purely elastic, we would expect it to remain in the neighbourhood of the stable root of $F_{\text{eq}} = 0$ away from zero (since the truss starts near this root when $X_{\text{ind}} = X_{\text{fold}}$ and $\lambda \approx 1/4$). Finally, when $\lambda > 1/4$ the truss appears to snap for any value of T_{ind}. As $\lambda \searrow 1/4$ the motions evidently slow down in a bottleneck whose duration depends strongly on T_{ind} (figure 5.11c). At larger values $\lambda > 1/4$, the dependence on T_{ind} decreases (figure 5.11d).

These regimes are confirmed when we plot the computed snap-through times on the $(\lambda, T_{\text{ind}})$-plane. Figure 5.12a shows that the boundary at which snap-through no longer occurs is roughly located at $\lambda = 1/4$, and slowing down is only obtained when $\lambda \approx 1/4$. (No snap-through is observed for $\lambda < 1/4$ in figure 5.12a due to the resolution of the grid on which the snap-through times are computed.) In contrast to the pseudo-bistable behaviour discussed in §5.3, it appears that this slowing down still occurs when the indentation time is small. This slowing down is more clearly visible in figure 5.12b, which shows a close-up of the region $0 < 1/4 - \lambda \ll 1$ in which snap-through occurs. Consistent with being caused by viscous effects, we find that this region only exists for small, but non-zero, De — this region decreases in size for smaller values De $\lesssim 10^{-2}$.

5.4.2 Bottleneck analysis

We now perform a detailed asymptotic analysis of the dynamics in the limit De $\ll$ 1, focussing on the bottleneck behaviour when

$$\lambda = \frac{1}{4} + \epsilon,$$

where $0 < \epsilon \ll 1$. To understand how viscous effects may influence the snap-through dynamics, we consider the evolution at early times when $X \approx X_{\text{fold}}$. When De is sufficiently small, we expect that the bottleneck duration obeys the underdamped scaling derived in Chapter 4, i.e. $T = O(\text{De}^{-1}\epsilon^{-1/4})$ (the factor of De^{-1} is because this bottleneck occurs on

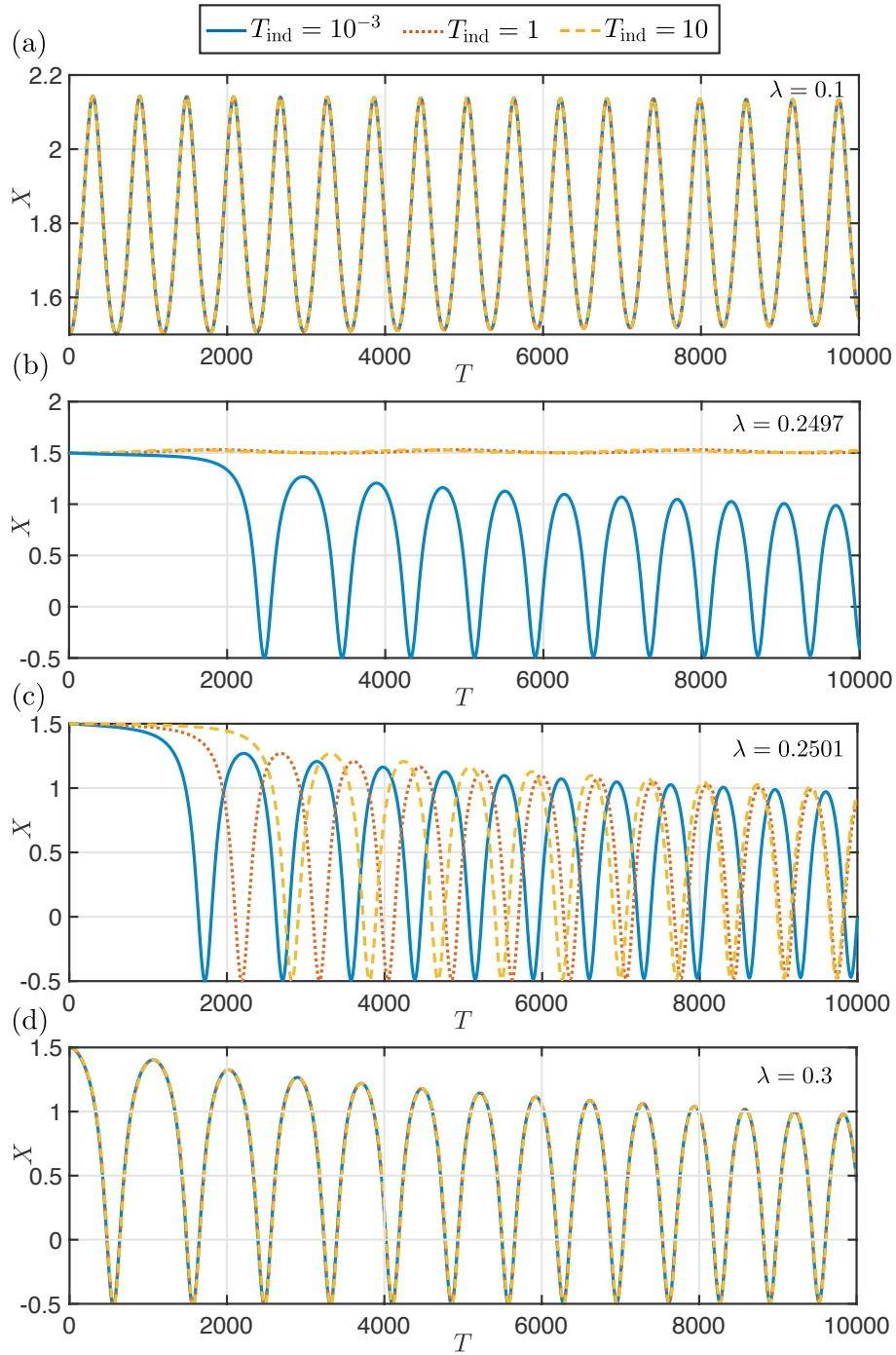**Figure 5.11:** *Dimensionless trajectories in the small Deborah number limit ($X_{\mathrm{ind}} = X_{\mathrm{fold}} = 3/2$, De = 10^{-2}). Numerical results are shown for (a) $\lambda = 0.1$, (b) $\lambda = 0.2497$, (c) $\lambda = 0.2501$ and (d) $\lambda = 0.3$ using three different values of T_{ind} (given in the upper legend). Note that the vertical scale varies between panels.*
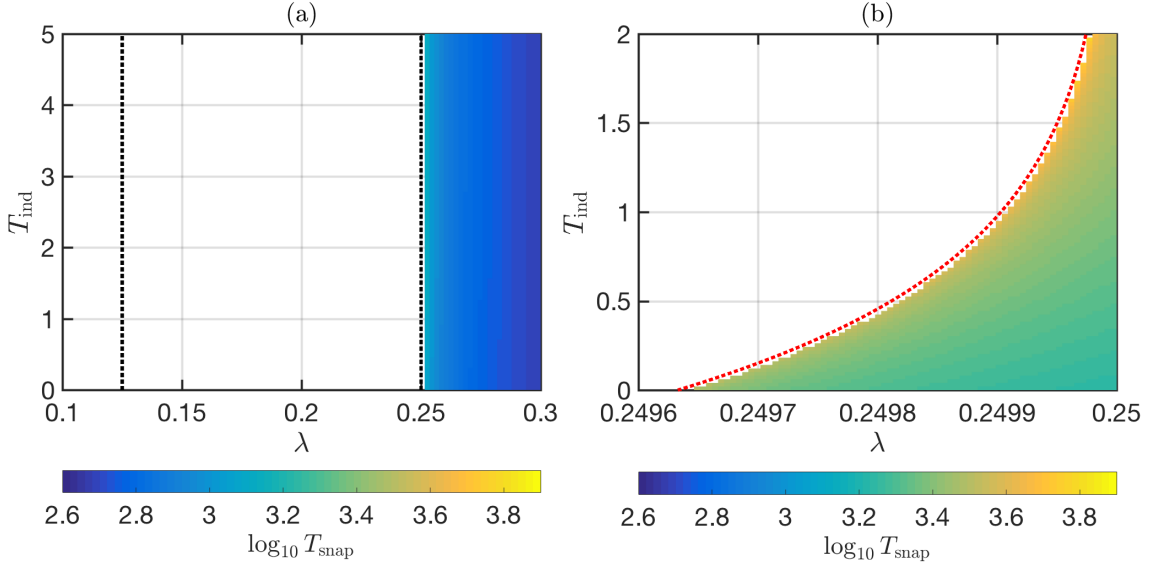
Figure 5.12: *Snap-through times in the limit* De $\ll$ 1 ($X_{\mathrm{ind}} = X_{\mathrm{fold}}$, De $= 10^{-2}$). *(a) Numerical results obtained by integrating* (5.7)–(5.8) *numerically (see colourbar). (b) A close-up of the region where* $0 < 1/4 - \lambda \ll 1$. *For later reference, the boundary separating snap-through/no snap-through predicted by equation* (5.42) *is shown (red dotted curve).*

the elastic timescale, rather than the viscous timescale which was used to make times dimensionless). Re-scaling the displacement as in §5.3.2, and inferred by the elastic analysis of Chapter 4, we set

$$
\begin{aligned}
X &= X_{\mathrm{fold}} - \epsilon^{1/2}\chi, \\
T &= \mathrm{De}^{-1}\epsilon^{-1/4}\tau.
\end{aligned}
$$

While $|\chi| \ll \epsilon^{-1/2}$, the force terms can be expanded in a similar way to (5.25). Inserting these expansions into the ODE (5.7), we obtain

$$
\epsilon^{1/2}\mathcal{D}\frac{\mathrm{d}^3\chi}{\mathrm{d}\tau^3} + \frac{\mathrm{d}^2\chi}{\mathrm{d}\tau^2} + \frac{1}{4}\mathcal{D}\frac{\mathrm{d}\chi}{\mathrm{d}\tau} = \frac{3}{2}\left(1 + \chi^2\right), \tag{5.30}
$$

where we have introduced

$$
\mathcal{D} = \mathrm{De}\,\epsilon^{-1/4}.
$$

Here $\mathcal{D}$ measures the importance of the viscous terms compared to the inertia term in the bottleneck phase. This is analogous to the Λ parameter we defined in Chapter 4: recall that for our elastic arch, $\Lambda = \upsilon\Delta\mu^{-1/4}$ where υ was the dimensionless damping coefficient and $\Delta\mu$ the normalised 'distance' to the snap-through bifurcation. The idea is that as the snap-through transition is approached in both systems (i.e. $\epsilon \to 0$ or $\Delta\mu \to 0$), the motions are slowed down sufficiently for the dynamics to become overdamped, even if the external viscosity/damping is small.

The initial conditions (5.8) are written in terms of χ as

$$\chi(0+) = 0, \quad \chi_\tau(0+) = 0, \quad \chi_{\tau\tau}(0+) = \frac{F_{\text{ind}}}{\epsilon}. \tag{5.31}$$

Since $\epsilon \ll 1$, it appears that we can simply neglect the third-order derivative in (5.30) in favour of the first-order derivative. However, using the expression (5.6) for F_{ind}, we expand

$$\frac{F_{\text{ind}}}{\epsilon} = \frac{3}{2} + \frac{3}{2}\epsilon^{-1}e^{-T_{\text{ind}}}\left(\frac{1}{4} + \epsilon\right) \sim \frac{3}{2} + \frac{3}{8}\epsilon^{-1}e^{-T_{\text{ind}}}. \tag{5.32}$$

Neglecting the third-order derivative in (5.30) would instead imply that $\mathrm{d}^2\chi/\mathrm{d}\tau^2 \sim 3/2$ initially, which is incompatible with the initial data (5.31) and (5.32) if $\epsilon^{-1}e^{-T_{\text{ind}}}$ is not small. This suggests that all terms in (5.30) may be important at early times. To make analytical progress, we therefore consider the behaviour when $\chi \ll 1$ so that we can linearise the right-hand side of the ODE (5.30). The leading order solution is

$$\chi \sim 6\mathcal{D}^{-1}\left(\tau + \frac{e^{m_-\tau} - e^{m_+\tau}}{m_+ - m_-}\right) + 4\left(\epsilon^{-1/2}F_{\text{ind}} - 6\mathcal{D}^{-2}\right)\left(1 + \frac{m_-e^{m_+\tau} - m_+e^{m_-\tau}}{m_+ - m_-}\right), \tag{5.33}$$

where we define

$$m_\pm = \frac{-1 \pm \sqrt{1 - \epsilon^{1/2}\mathcal{D}^2}}{2\epsilon^{1/2}\mathcal{D}}.$$

Because $\epsilon^{1/2}\mathcal{D}^2 = \text{De}^2 \ll 1$, we can expand the square root term in $m_\pm$ to obtain

$$m_+ \sim -\frac{\mathcal{D}}{4} - \frac{\epsilon^{1/2}\mathcal{D}^3}{16}, \quad m_- \sim -\epsilon^{-1/2}\mathcal{D}^{-1} + \frac{\mathcal{D}}{4} + \frac{\epsilon^{1/2}\mathcal{D}^3}{16}.$$

Furthermore, while $\tau \ll \mathcal{D}^{-1}$ we have $m_+\tau \ll 1$ so we may expand the exponential term $e^{m_+\tau}$ for small arguments. Upon inserting the above expansions for F_{ind} and m_+, the solution to leading order reduces to

$$\chi \sim \frac{3}{8}e^{-T_{\text{ind}}}\mathcal{D}^2\left(e^{m_-\tau} - 1\right) + \frac{3}{8}\epsilon^{-1/2}e^{-T_{\text{ind}}}\mathcal{D}\tau + \frac{3}{64}\left(16 - \epsilon^{-1/2}e^{-T_{\text{ind}}}\mathcal{D}^2\right)\tau^2$$
$$- \frac{\mathcal{D}}{256}\left(16 - \epsilon^{-1/2}e^{-T_{\text{ind}}}\mathcal{D}^2\right)\tau^3. \tag{5.34}$$

It may be verified that the neglected terms in this solution are indeed smaller than at least one retained term provided $\text{De} \ll 1$ and $\tau \ll \mathcal{D}^{-1}$; we have retained some higher order terms (such as the cubic term) to allow us to evaluate derivatives to leading order later.

The linearised solution (5.34) breaks down when χ reaches $O(1)$ and the χ^2 term in the ODE (5.30) is no longer negligible. Note that when $m_-\tau = O(1)$, i.e. $\tau = O(\epsilon^{1/2}\mathcal{D}) \ll \mathcal{D}^{-1}$, the solution implies that $\chi = O(e^{-T_{\text{ind}}}\mathcal{D}^2, \epsilon\mathcal{D}^2)$. This suggests that χ is already larger than $O(1)$ by this time if $\mathcal{D}$ is sufficiently large. We therefore consider the cases $\mathcal{D} \ll 1$

and $\mathcal{D} \gg 1$ separately, determining the different leading order balances the solution passes through before χ eventually reaches $O(\epsilon^{-1/2})$ and leaves the bottleneck phase. This will enable us to calculate the bottleneck duration to leading order, and hence approximate the total time taken to snap-through.

The case $\mathcal{D} \ll 1$

We first assume that $\mathcal{D} \ll 1$. Because $\mathcal{D}$ scales weakly with ϵ (due to the $1/4$ power), this assumption is violated only for very small values of ϵ that are unlikely to be experimentally attainable; for example, when $\mathrm{De} = 10^{-1}$ attaining $\mathcal{D} \geq 1$ requires $\epsilon \leq 10^{-4}$, with smaller values of ϵ required as De decreases. With the assumption $\mathcal{D} \ll 1$, we also have $e^{-T_{\mathrm{ind}}}\mathcal{D}^2 \ll 1$ and so from the above discussion $\chi \ll 1$ while $\tau = O(\epsilon^{1/2}\mathcal{D})$. Focussing instead on the interval $\epsilon^{1/2}\mathcal{D} \ll \tau \ll \mathcal{D}^{-1}$, the exponential term $e^{m-\tau}$ in the solution (5.34) is exponentially small. Keeping only the dominant terms for $\tau \ll \mathcal{D}^{-1}$, we then have

$$\chi \sim \frac{3}{8}\epsilon^{-1/2}e^{-T_{\mathrm{ind}}}\mathcal{D}\tau + \frac{3}{4}\tau^2.$$

We see that as well as quadratic growth due to inertia, the solution also has a linear part associated with viscous effects. This linear growth is a consequence of the SLS element not being completely relaxed when the indenter is released: as $T_{\mathrm{ind}} \to \infty$, this term becomes negligible and we are left with the usual quadratic growth we have previously seen for underdamped bottleneck dynamics (Chapter 4). The ratio of the linear and quadratic terms is measured by the dimensionless parameter

$$\Psi \equiv \epsilon^{-1/2}e^{-T_{\mathrm{ind}}}\mathcal{D} = \mathrm{De}\,\epsilon^{-3/4}e^{-T_{\mathrm{ind}}}.$$

(Note that both $\Psi \ll 1$ and $\Psi \gg 1$ are possible for any value of $\mathcal{D}$, depending on the relative sizes of ϵ and T_{ind}.) We then expect to recover the underdamped scaling $T = O(\mathrm{De}^{-1}\epsilon^{-1/4})$ for the bottleneck duration when $\Psi \ll 1$, corresponding to sufficiently small De/large T_{ind}; we will show that when $\Psi \gtrsim 1$ this scaling breaks down. Before proceeding, we use (5.34) to evaluate the solution components when $\epsilon^{1/2}\mathcal{D} \ll \tau \ll \mathcal{D}^{-1}$ as

$$\begin{aligned}
\chi &\sim \frac{3}{8}\Psi\tau + \frac{3}{4}\tau^2, \\
\frac{\mathrm{d}\chi}{\mathrm{d}\tau} &\sim \frac{3}{8}\Psi + \frac{3}{2}\tau, \\
\frac{\mathrm{d}^2\chi}{\mathrm{d}\tau^2} &\sim \frac{3}{32}\left(16 - \mathcal{D}\Psi\right), \\
\frac{\mathrm{d}^3\chi}{\mathrm{d}\tau^3} &\sim -\frac{3\mathcal{D}}{128}\left(16 - \mathcal{D}\Psi\right).
\end{aligned} \tag{5.35}$$

The sub-case $\Psi \ll 1$

Consider first the sub-case $\mathcal{D} \ll 1$ and $\Psi \ll 1$, i.e. when the linear growth due to an unrelaxed stiffness is dominated by the quadratic growth. It follows from (5.35) that $\chi = O(1)$ when $\tau = O(1)$ (which satisfies $\epsilon^{1/2}\mathcal{D} \ll \tau \ll \mathcal{D}^{-1}$ when $\mathcal{D} \ll 1$, as assumed above). To determine the updated balance in the ODE at this stage, we evaluate the size of the different terms in (5.30). With the assumptions $\Psi \ll 1$ and $\mathcal{D} \ll 1$, the expressions in (5.35) imply that when $\tau = O(1)$

$$\mathcal{D}\frac{\mathrm{d}\chi}{\mathrm{d}\tau} = O(\mathcal{D}) \ll 1, \quad \frac{\mathrm{d}^2\chi}{\mathrm{d}\tau^2} = O(1), \quad \epsilon^{1/2}\mathcal{D}\frac{\mathrm{d}^3\chi}{\mathrm{d}\tau^3} = O(\epsilon^{1/2}\mathcal{D}^2) = O(\mathrm{De}^2) \ll 1,$$

so that the viscous terms are both negligible compared to the inertia term. The updated balance in (5.30) is therefore

$$\frac{\mathrm{d}^2\chi}{\mathrm{d}\tau^2} \sim \frac{3}{2}\left(1 + \chi^2\right), \tag{5.36}$$

i.e. we recover the normal form for underdamped dynamics near a saddle-node bifurcation (discussed in Chapter 4), as we anticipated. Multiplying by $\mathrm{d}\chi/\mathrm{d}\tau$ and integrating twice, the solution matching back to the quadratic growth for $\chi \ll 1$ is given implicitly by

$$\tau \sim \int_0^\chi \frac{\mathrm{d}\xi}{\sqrt{\xi^3 + 3\xi}}.$$

The bottleneck duration, τ_b, is obtained by setting $\chi = O(\epsilon^{-1/2})$. As in Chapter 4, we may evaluate the resulting integral to leading order by replacing the upper limit by ∞; the error in doing so is $O(\epsilon^{1/4})$. In the original dimensionless variables, $T = \mathrm{De}^{-1}\epsilon^{-1/4}\tau$, this gives the bottleneck duration, T_b, as

$$T_b \sim \mathrm{De}^{-1}\epsilon^{-1/4}\int_0^\infty \frac{\mathrm{d}\xi}{\sqrt{\xi^3 + 3\xi}}.$$

The integral can be evaluated to yield

$$T_b \sim \frac{\Gamma\left(\frac{1}{4}\right)^2}{2 \cdot 3^{1/4}\sqrt{\pi}}\mathrm{De}^{-1}\epsilon^{-1/4} \approx 2.82\,\mathrm{De}^{-1}\epsilon^{-1/4}. \tag{5.37}$$

The sub-case $\Psi \gtrsim 1$

Suppose instead that $\mathcal{D} \ll 1$ and $\Psi \gtrsim 1$, i.e. the linear growth due to viscous effects is significant. We now have that $\chi = O(1)$ first when $\tau = O(\Psi^{-1})$ (again, we may verify that $\epsilon^{1/2}\mathcal{D} \ll \tau \ll \mathcal{D}^{-1}$ at this point when $\mathcal{D} \ll 1$). Using the expressions in (5.35), at

this point we evaluate

$$\mathcal{D}\frac{\mathrm{d}\chi}{\mathrm{d}\tau} = O(\mathcal{D}\Psi), \quad \frac{\mathrm{d}^2\chi}{\mathrm{d}\tau^2} = O(1, \mathcal{D}\Psi), \quad \epsilon^{1/2}\mathcal{D}\frac{\mathrm{d}^3\chi}{\mathrm{d}\tau^3} = O(\epsilon^{1/2}\mathcal{D}^2, \epsilon^{1/2}\mathcal{D}^3\Psi). \qquad (5.38)$$

Provided that $\mathcal{D}\Psi \ll 1$, i.e. the linear growth is not too large, the viscous terms are again negligible compared to the inertia term when $\chi = O(1)$, and the updated balance is unchanged from (5.36). The implicit solution matching back into $\chi \ll 1$ modifies to

$$\tau \sim \int_0^\chi \frac{\mathrm{d}\xi}{\sqrt{\xi^3 + 3\xi + (3\Psi/8)^2}}, \qquad (5.39)$$

i.e. the integrand now has an $O(\Psi^2)$ correction due to the linear growth. The bottleneck duration in original dimensionless time is then

$$T_b \sim \mathrm{De}^{-1}\epsilon^{-1/4} \int_0^\infty \frac{\mathrm{d}\xi}{\sqrt{\xi^3 + 3\xi + (3\mathrm{De}\,\epsilon^{-3/4}e^{-T_{\mathrm{ind}}}/8)^2}}. \qquad (5.40)$$

As expected, this expression reduces to (5.37) in the limit $\Psi \ll 1$ (this can be justified by decomposing the interval of integration, and showing that the contribution when the Ψ^2 term is comparable to the other terms, around $\xi = 0$, is negligible).

If $\Psi \gg 1$, however (which is possible while maintaining $\mathcal{D}\Psi \ll 1$ because $\mathcal{D}$ is assumed small), we can uniformly approximate the integrand in (5.40) by ignoring the ξ term: if $\xi \ll \Psi^{2/3}$ then both ξ and ξ^3 terms are negligible compared to the Ψ^2 term, and if $\xi \gtrsim \Psi^{2/3} \gg 1$ then the ξ term is negligible compared to the ξ^3 term. We deduce that when $\Psi \gg 1$

$$T_b \sim \mathrm{De}^{-1}\epsilon^{-1/4} \int_0^\infty \frac{\mathrm{d}\xi}{\sqrt{\xi^3 + (3\mathrm{De}\,\epsilon^{-3/4}e^{-T_{\mathrm{ind}}}/8)^2}}.$$

Evaluating the integral, we obtain

$$T_b \sim \frac{4\Gamma\left(\frac{1}{3}\right)\Gamma\left(\frac{7}{6}\right)}{3^{1/3}\sqrt{\pi}}\mathrm{De}^{-4/3}e^{T_{\mathrm{ind}}/3} \approx 3.89\,\mathrm{De}^{-4/3}e^{T_{\mathrm{ind}}/3}, \qquad (5.41)$$

so that the bottleneck duration is independent of ϵ. This regime corresponds to the linear growth dominating the quadratic growth due to inertia: as χ reaches $O(1)$, the truss has a significant velocity that consequently limits the time taken to leave the bottleneck. Hence, critical slowing down does not occur as ϵ decreases.

Note that the $\mathrm{De}^{-4/3}$ scaling in (5.41) gives a bottleneck duration that scales as a combination of both viscous and elastic timescales:

$$t_{\mathrm{snap}} \propto \left(\frac{\eta}{E}\right)^{-1/3}\left(\sqrt{\frac{m}{k}}\right)^{4/3}\exp\left(\frac{t_{\mathrm{ind}}}{3\eta/E}\right).$$

Particularly surprising here is that increasing the viscosity (keeping all other parameters constant) *decreases* the snapping time. This is due to both the negative exponent of η in t_{snap} and the inverse dependence within the exponential. Physically, this result is because increasing the viscosity (while t_{ind} is fixed) decreases the dimensionless indentation time $T_{\mathrm{ind}} = t_{\mathrm{ind}}/(\eta/E)$, and so the destabilising effect of the unrelaxed stiffness at early times becomes more significant.

We arrived at the expression (5.40) by assuming that $\mathcal{D}\Psi \ll 1$. If instead $\mathcal{D}\Psi \gtrsim 1$, (5.38) implies that the linear growth is sufficient to cause the first-order viscous term to now balance the inertia term when χ reaches $O(1)$. The updated balance (5.36) is then no longer valid. However, further analysis (provided in Appendix 5.C) shows that the ODE ultimately reduces to a balance between the inertia term and the χ^2 term before the truss leaves the bottleneck, and we recover the same implicit solution (5.39) when we neglect the ξ term in the integrand. To leading order, the bottleneck duration is therefore unchanged from (5.41).

Summary for $\mathcal{D} = \mathrm{De}\,\epsilon^{-1/4} \ll 1$

We have shown that the bottleneck duration to leading order is given by the integral (5.40), which remains uniformly valid for $0 < \epsilon \ll 1$ and $\mathcal{D} \ll 1$, i.e. $\mathrm{De} \ll \epsilon^{1/4}$. In particular, we have the distinguished limits

$$
T_b \sim \begin{cases} \frac{\Gamma\left(\frac{1}{4}\right)^2}{2 \cdot 3^{1/4}\sqrt{\pi}}\mathrm{De}^{-1}\epsilon^{-1/4} & \text{if} \quad \Psi = \mathrm{De}\,\epsilon^{-3/4}e^{-T_{\mathrm{ind}}} \ll 1, \\ \frac{4\Gamma\left(\frac{1}{3}\right)\Gamma\left(\frac{7}{6}\right)}{3^{1/3}\sqrt{\pi}}\mathrm{De}^{-4/3}e^{T_{\mathrm{ind}}/3} & \text{if} \quad \Psi = \mathrm{De}\,\epsilon^{-3/4}e^{-T_{\mathrm{ind}}} \gg 1. \end{cases}
$$

The prediction (5.40) agrees well with the computed snap-through times — see figure 5.13, where we have fixed $\mathrm{De} = 10^{-2}$ and varied ϵ in the range where $\mathcal{D} \ll 1$ (the maximum value is $\mathcal{D} \approx 0.3$ when $\epsilon = 10^{-6}$). As expected, the data collapse onto the predicted $\epsilon^{-1/4}$ scaling only when T_{ind} is sufficiently large to ensure $\Psi \ll 1$. We delay verifying the dependence of the snap-through times on the Deborah number De until we have considered the dynamics when $\mathcal{D} \gtrsim 1$.

The case $\mathcal{D} \gtrsim 1$

To build up a complete picture of the different dynamical regimes, we now consider the case when $\mathrm{De} \ll 1$ and $\mathcal{D} \gtrsim 1$, i.e. $\epsilon^{1/4} \lesssim \mathrm{De} \ll 1$. It turns out that determining the different leading order balances the solution passes through once χ reaches $O(1)$ is more complicated, requiring more intermediate intervals. However, the analysis in Appendix
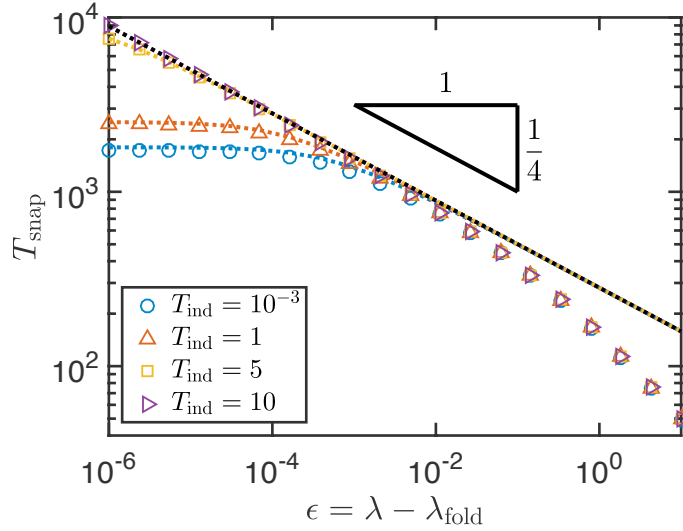
Figure 5.13: *Snap-through times in the limit $\mathcal{D} = \mathrm{De}\,\epsilon^{-1/4} \ll 1$ ($X_{\mathrm{ind}} = X_{\mathrm{fold}}$, $\mathrm{De} = 10^{-2}$). Numerical results are shown (symbols; see legend) together with the asymptotic predictions using (5.40), evaluated using quadrature (dotted curves), which are valid for $0 < \epsilon \ll 1$ and $\mathcal{D} \ll 1$. These collapse onto the limiting form (5.37) (black dotted line) when T_{ind} is sufficiently large.*

5.C suggests that the ODE (5.30) ultimately reduces to a balance between the χ^2 term and either the inertia term or the first-order viscous term, and that only this balance is relevant for finding when χ leaves the bottleneck. We therefore determine when this balance occurs and ignore the different proceeding balances. This approach is also justified by noting that while the inertia or viscous terms dominate the χ^2 term, the solution of the linearised ODE is still asymptotically valid. This is because when χ is larger than $O(1)$, these terms will also dominate the constant term, so that linearising the ODE has no effect on the leading order solution.

Recall from the linearised solution (5.34), expanded for times $\tau \ll \mathcal{D}^{-1}$, that $\chi = O(e^{-T_{\mathrm{ind}}}\mathcal{D}^2, \epsilon\mathcal{D}^2)$ by the time $\tau = O(\epsilon^{1/2}\mathcal{D})$. Using this solution, it may be shown that χ^2 is always small compared to the viscous and inertia terms by this stage. Hence, we again focus on the interval $\epsilon^{1/2}\mathcal{D} \ll \tau \ll \mathcal{D}^{-1}$ when the solution components are given by the expressions (5.35).

Consider first the case when Ψ is sufficiently large that the linear part of χ dominates the quadratic part. The expressions (5.35) imply that the first-order viscous and inertia terms are both $O(\mathcal{D}\Psi) \gg 1$ (the third-order viscous term is a factor of De^2 smaller). It follows that χ^2 first becomes comparable to these terms when $\tau = O(\mathcal{D}^{1/2}\Psi^{-1/2})$; to ensure this occurs while $\tau \ll \mathcal{D}^{-1}$, we then require $\Psi \gg \mathcal{D}^3 \gtrsim 1$ (we also verify this occurs while $\chi \ll \epsilon^{-1/2}$). With the assumption $\Psi \gg \mathcal{D}^3 \gtrsim 1$, the updated balance is then

$$\frac{\mathrm{d}^2\chi}{\mathrm{d}\tau^2} + \frac{1}{4}\mathcal{D}\frac{\mathrm{d}\chi}{\mathrm{d}\tau} \sim \frac{3}{2}\chi^2.$$

Together with the matching requirement $\chi \sim (3/8)\Psi\tau$ for $\tau \ll \mathcal{D}^{1/2}\Psi^{-1/2}$, this is precisely the problem considered in Appendix 5.C when $\mathcal{D}$ was assumed small. We deduce that the bottleneck duration is again given by (5.41) to leading order. This is not surprising: because the destabilising effect of the linear growth is limiting the dynamics, the bottleneck duration is insensitive to the values of $\mathcal{D}$ and ϵ, and so is unchanged from the case $\mathcal{D} \ll 1$. We also note the requirement $\Psi \gg \mathcal{D}^3$ is equivalent to

$$T_{\text{ind}} \ll \log(\text{De}^{-2}).$$

Suppose instead that $\Psi \lesssim \mathcal{D}^3$. In this case we expect that the χ^2 term will remain small compared to the remaining terms while $\tau \ll \mathcal{D}^{-1}$. This can be verified directly using the expressions (5.35) and the fact that $\mathcal{D} \gtrsim 1$. Moreover, assuming $\mathcal{D} \gg 1$, this also holds when $\tau = O(\mathcal{D}^{-1})$. This allows us to consider the linearised solution at times $\tau \gg \mathcal{D}^{-1}$, when both exponential terms in (5.33) are negligible. Inserting the expansion (5.32) for F_{ind}, at leading order the solution reduces to

$$\chi \sim \mathcal{D}^{-1}\left(6\tau + \frac{3}{2}\Psi\right).$$

This breaks down when $\tau = O(\mathcal{D})$ and both the χ^2 term and the first-order viscous term are $O(1)$. Because the higher order derivatives are exponentially small, the updated balance is

$$\frac{1}{4}\mathcal{D}\frac{\mathrm{d}\chi}{\mathrm{d}\tau} \sim \frac{3}{2}\left(1 + \chi^2\right),$$

i.e. we now obtain the normal form associated with overdamped dynamics. In the original dimensionless time, this becomes

$$\frac{\mathrm{d}\chi}{\mathrm{d}T} = 6\epsilon^{1/2}\left(1 + \chi^2\right).$$

Matching backwards requires

$$\chi \sim 6\epsilon^{1/2}T + \frac{3}{2}\epsilon^{-1/2}e^{-T_{\text{ind}}}.$$

This is almost exactly the problem we considered in the limit De $\gg 1$ using multiple-scale analysis; recall equations (5.26)–(5.27) in §5.3.2. In a similar way, we calculate the bottleneck duration to be

$$T_b = \frac{\pi}{12}\epsilon^{-1/2} - \frac{1}{6}\epsilon^{-1/2}\arctan\left(\frac{3}{2}\epsilon^{-1/2}e^{-T_{\text{ind}}}\right).$$

To leading order, this coincides with the expressions (5.29) in the distinguished limits $\epsilon^{-1/2}e^{-T_{\text{ind}}} \ll 1$ and $\epsilon^{-1/2}e^{-T_{\text{ind}}} \gg 1$: if $\epsilon^{-1/2}e^{-T_{\text{ind}}} \ll 1$ we have $T_b \sim (\pi/12)\epsilon^{-1/2}$, while

if $\epsilon^{-1/2}e^{-T_{\mathrm{ind}}} \gg 1$ critical slowing down does not occur with $T_b \sim e^{T_{\mathrm{ind}}}/9$.

In summary, we have shown that when $0 < \epsilon \ll 1$ and $\epsilon^{1/4} \ll \mathrm{De} \ll 1$, the bottleneck duration has the distinguished limits

$$
T_b \sim \begin{cases} \frac{4\Gamma\left(\frac{1}{3}\right)\Gamma\left(\frac{7}{6}\right)}{3^{1/3}\sqrt{\pi}}\mathrm{De}^{-4/3}e^{T_{\mathrm{ind}}/3} & \text{if} \quad T_{\mathrm{ind}} \ll \log(\mathrm{De}^{-2}), \\ \frac{1}{9}e^{T_{\mathrm{ind}}} & \text{if} \quad \log(\mathrm{De}^{-2}) \lesssim T_{\mathrm{ind}} \ll \log(\epsilon^{-1/2}), \\ \frac{\pi}{12}\epsilon^{-1/2} & \text{if} \quad T_{\mathrm{ind}} \gg \log(\epsilon^{-1/2}). \end{cases}
$$

We only recover the usual inverse square-root scaling associated with an overdamped saddle-node ghost when T_{ind} is sufficiently large.

Complete regime diagram

We are now able to present the complete picture of the dynamical regimes during the bottleneck phase. This is shown schematically on the $(\mathrm{De}, T_{\mathrm{ind}})$-plane in figure 5.14. Here we have combined the results of the above analysis, valid for $\mathrm{De} \ll 1$, with the regions predicted by the multiple-scales analysis in §5.3.2 when $\mathrm{De} \gg 1$. In each case, we have plotted the boundaries that separate different distinguished limits for the bottleneck duration. These should be interpreted only in an order-of-magnitude sense, so that generally the scaling laws for the snap-through time are valid away from these boundaries. We have also plotted the minimum value of T_{ind} needed for pseudo-bistable behaviour when $\mathrm{De} \gg 1$ (yellow line; recall equation (5.23)). While our analysis is not valid for $\mathrm{De} = O(1)$, we found that the scaling laws may be identical in the cases $\mathrm{De} \gg 1$ and $\mathrm{De} \ll 1$ for certain values of T_{ind}. We have therefore not plotted the boundary $\mathrm{De} = O(1)$ in these cases.

To further illustrate the different regimes, we have plotted the computed snap-through times as a function of De in figure 5.15a (specifying $\epsilon = 10^{-6}$ to clearly distinguish the different regimes). Here we have fixed T_{ind} in each data set, so that different symbols correspond to taking different horizontal slices through the regime diagram. Figure 5.15a confirms that when T_{ind} is smaller than unity, the snap-through times follow a De^{-1} scaling when De is large, before switching to the predicted $\mathrm{De}^{-4/3}$ scaling for values $\mathrm{De} \lesssim 1$ (blue circles, red upward-pointing triangles, yellow squares). As T_{ind} increases past $O(1)$, pseudo-bistable behaviour is obtained when $\mathrm{De} \gg 1$, in which the snap-through time is independent of De; as De decreases, both $\mathrm{De}^{-4/3}$ and De^{-1} scaling laws may be observed in succession (purple right-pointing triangles), corresponding to crossing multiple boundaries in the regime diagram (i.e. the blue and red boundaries in figure 5.14). When T_{ind} is larger than unity, the results for $\mathrm{De} \gg 1$ collapse onto the $O(\epsilon^{-1/2})$ prediction in the pseudo-bistable regime, while only the De^{-1} scaling is observed as De decreases (green diamonds, cyan upward-pointing triangles).
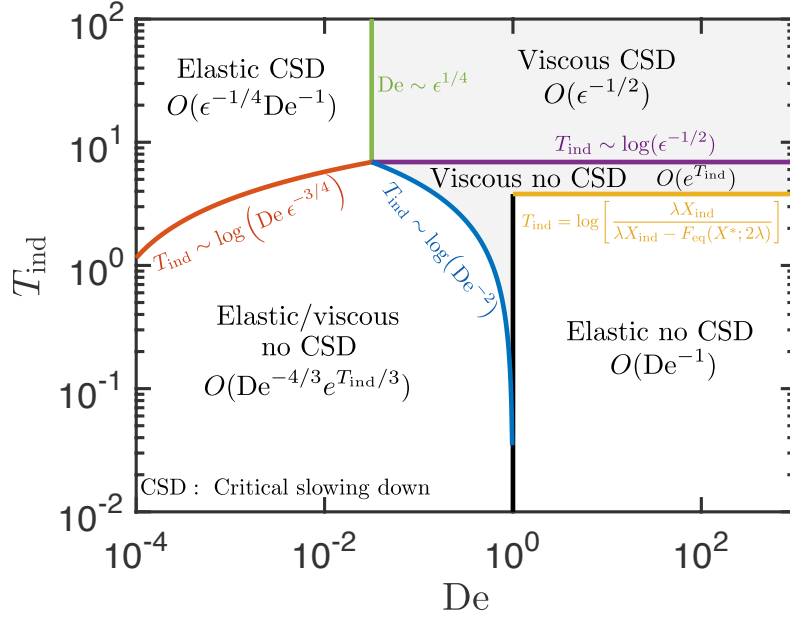
Figure 5.14: *Regime diagram for the snap-through dynamics when $0 < \lambda - \lambda_{\mathrm{fold}} \ll 1$ and $X_{\mathrm{ind}} = X_{\mathrm{fold}}$ (here $\epsilon = \lambda - \lambda_{\mathrm{fold}} = 10^{-6}$). Results for the dimensionless snap-through time T_{snap} are shown in each region. The pseudo-bistable regime, in which the snap-through time is governed by the timescale of viscous relaxation, is lightly shaded.*
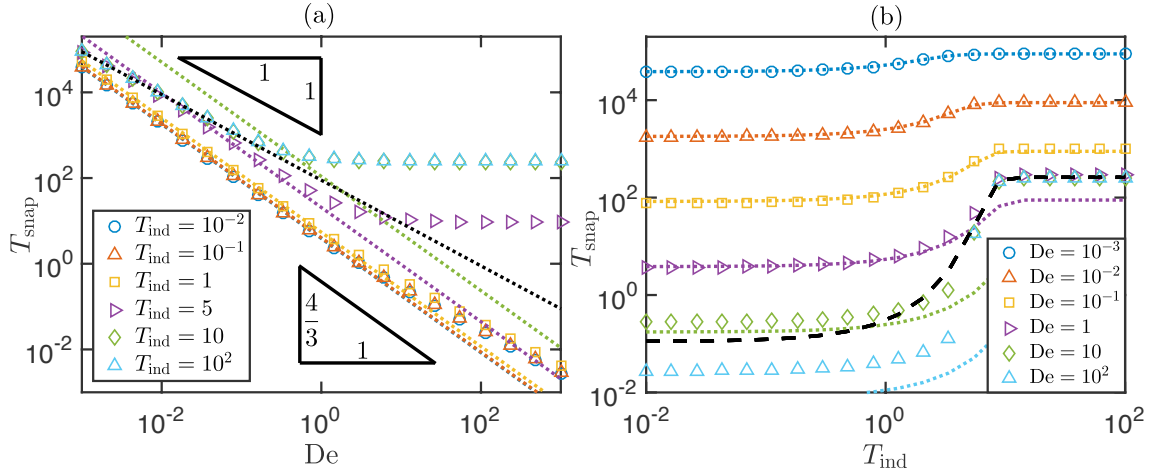
Figure 5.15: *Snap-through times when $0 < \lambda - \lambda_{\mathrm{fold}} \ll 1$ ($X_{\mathrm{ind}} = X_{\mathrm{fold}}$, $\epsilon = \lambda - \lambda_{\mathrm{fold}} = 10^{-6}$). (a) Computed snap-through times as a function of De for fixed T_{ind} (symbols; see legend), together with the asymptotic predictions $T_{\mathrm{snap}} \approx 3.89 \mathrm{De}^{-4/3} e^{T_{\mathrm{ind}}/3}$ (coloured dotted lines) and the prediction $T_{\mathrm{snap}} \approx 2.82 \, \mathrm{De}^{-1} \epsilon^{-1/4}$ (black dotted line). (b) Computed times as a function of T_{ind} for fixed De. We have also plotted the asymptotic predictions (5.40) (coloured dotted curves) and (5.28) (black dashed curve), which move between the different distinguished limits on figure 5.14 as T_{ind} is varied.*

We have also plotted the computed snap-through times as a function of T_{ind} while De is fixed; see figure 5.15b. We again find that the results are consistent with taking different slices through the regime diagram in figure 5.14, now in the vertical direction. Remarkably, the asymptotic prediction (5.40) (dotted curves) agrees excellently with the numerics when $\text{De} = O(1)$ and T_{ind} is sufficiently small, even though this result is formally valid only for $\text{De} \ll 1$. This suggests that it may be possible to generalise the above bottleneck analysis to incorporate values $\text{De} = O(1)$, though we do not pursue this here.

5.4.3 Premature snap-through behaviour ($\lambda < \lambda_{\text{fold}}$)

The above analysis allowed us to calculate the bottleneck duration, and hence approximate the total time taken to snap-through. However, it does not explain when snap-through behaviour is observed. Recall from figure 5.12b that viscous effects cause premature snap-through when $\lambda < \lambda_{\text{fold}}$, i.e. when a purely elastic truss would instead be stable. In particular, the boundary at which snap-through no longer occurs on the $(\lambda, T_{\text{ind}})$-plane is located at $0 < 1/4 - \lambda \ll 1$ and depends on De. In this final section, we briefly modify the bottleneck analysis to determine this boundary.

We now set

$$\lambda = \frac{1}{4} - \epsilon,$$

where $0 < \epsilon \ll 1$, and we introduce the re-scaled variables χ and τ as before. The expansions for the force terms are now

$$
\begin{aligned}
F_{\text{eq}}(X; \lambda) &= \frac{3}{2}\epsilon \left(\chi^2 - 1\right) + O(\epsilon^{3/2}\chi, \epsilon^{3/2}\chi^3), \\
F_{\text{eq}}'(X; 2\lambda) &= \frac{1}{4} + O(\epsilon, \epsilon^{1/2}\chi).
\end{aligned}
$$

The re-scaled ODE (5.30) modifies to

$$\epsilon^{1/2}\mathcal{D}\frac{\mathrm{d}^3\chi}{\mathrm{d}\tau^3} + \frac{\mathrm{d}^2\chi}{\mathrm{d}\tau^2} + \frac{1}{4}\mathcal{D}\frac{\mathrm{d}\chi}{\mathrm{d}\tau} = \frac{3}{2}\left(\chi^2 - 1\right),$$

so that the sign of the constant term is flipped compared to (5.30). The initial conditions (5.31) remain unchanged, though the expansion for F_{ind} becomes

$$\chi_{\tau\tau}(0+) = \frac{F_{\text{ind}}}{\epsilon} \sim -\frac{3}{2} + \frac{3}{8}\epsilon^{-1}e^{-T_{\text{ind}}} = -\frac{3}{2} + \frac{3}{8}\epsilon^{-1/2}\frac{\Psi}{\mathcal{D}},$$

i.e. the constant term also changes sign here. It follows that we recover the same problem we considered earlier (i.e. when $\lambda > 1/4$) by flipping the sign of the constant terms in the

ODE and the expression for $\chi_{\tau\tau}(0+)$. When the χ^2 term is negligible, this can be achieved by sending

$$\chi \to -\chi, \quad \Psi \to -\Psi.$$

We deduce that the solution of the linearised ODE is found by applying the above transformation to our previous solution for $\lambda > 1/4$. In particular, when $\epsilon^{1/2}\mathcal{D} \ll \tau \ll \mathcal{D}^{-1}$, the solution (5.35) becomes

$$\chi \sim \frac{3}{8}\Psi\tau - \frac{3}{4}\tau^2.$$

Assuming that $\mathcal{D} \ll 1$ and $\mathcal{D}\Psi \ll 1$, we can similarly show that when χ first reaches $O(1)$ the viscous terms are negligible in the updated balance, which here modifies to

$$\frac{\mathrm{d}^2\chi}{\mathrm{d}\tau^2} \sim \frac{3}{2}\left(\chi^2 - 1\right).$$

The solution matching back into $\chi \ll 1$ satisfies

$$\left(\frac{\mathrm{d}\chi}{\mathrm{d}\tau}\right)^2 \sim \chi^3 - 3\chi + \left(\frac{3}{8}\Psi\right)^2.$$

For the truss to never leave the bottleneck and simply oscillate in an inverted state, the right-hand side must be zero at a positive value of χ. Since this is a cubic function of χ, the smallest value of T_{ind} when this occurs corresponds to when the graph of the cubic has a turning point that coincides with the horizontal axis; below this value (corresponding to larger Ψ), the turning point lies above the horizontal axis and the velocity is always positive for $\chi \geq 0$. This turning point is located at $\chi = 1$, so the critical value of T_{ind} satisfies

$$-2 + \left(\frac{3}{8}\Psi\right)^2 = 0.$$

This can be re-arranged to

$$T_{\text{ind}} = \log\left[\frac{3\sqrt{2}}{16}\mathrm{De}\,\epsilon^{-3/4}\right]. \tag{5.42}$$

This prediction is superimposed (red dotted curve) onto the numerical snap-through times in figure 5.12b, where we observe excellent agreement. Note that in the purely elastic limit $\mathrm{De} \to 0$, the critical value of T_{ind} is always exceeded and the boundary will approach the line $\lambda = 1/4$, as expected. Because $\Psi = O(1)$ at the critical value, we also verify that the earlier assumption $\mathcal{D}\Psi \ll 1$ is valid whenever $\mathcal{D} \ll 1$, which in turn is violated only for extremely small values of ϵ.

5.5 Summary and discussion

In this chapter, we have analysed the dynamics of snap-through when viscoelastic effects are present. We re-emphasise that such effects are fundamentally different to external damping such as viscous drag: viscoelasticity modifies the bistability characteristics and hence can change when snap-through occurs. Moreover, in an experiment where we first indent a structure to a particular configuration, the resulting dynamics depend on the history of stress relaxation during the indentation phase. Previous approaches have dealt with this complexity by modelling the structure as being elastic with an effective stiffness that evolves according to a Prony series ansatz (Santer, 2010; Brinkmeyer *et al.*, 2012; 2013). Here, we have presented an alternative approach that derives the equations of motion from first principles using the constitutive law of a standard linear solid. This enables us to capture both stress relaxation and creep phenomena without making any additional assumptions regarding the dynamic behaviour.

To gain analytical insight we studied a modified form of the Mises truss, a simple and commonly used model system that exhibits bistability and snap-through (Panovko & Gubanova, 1987; Krylov *et al.*, 2008; Brinkmeyer *et al.*, 2013). By introducing an additional vertical spring and a point mass in our formulation, the truss becomes a more realistic lumped model for more complex structures such as spherical shells and arches. Using a small-angle approximation, we were able to reduce the number of dimensionless parameters in our problem to four. These are the Deborah number De, measuring the importance of inertia compared to viscosity; the relative stiffness λ, which acts as a bifurcation parameter and determines the bistability characteristics of the truss; and the details of the indentation stage are specified by the indentation displacement X_{ind} and time duration T_{ind}. Regarding the truss as a lumped model, we then expect that analogous parameters will control the dynamics in elastic shells and arches; for example, λ may be compared to the Föppl-von-Kármán number for spherical shells.

We began by considering the dynamics when De is large. Using direct numerical solutions, we showed that the onset of snap-through cannot be inferred by whether or not the truss is effectively bistable at the moment the indenter is released. Instead, we turned to a detailed asymptotic analysis of the snap-through dynamics using the method of multiple scales. This analysis showed that the leading-order dynamics generally obey the equations of motion when we neglect the terms associated with inertia, as expected. However, immediately after the indenter is released, inertial effects become important, as the displacement moves rapidly to a new value to balance the jump in the applied force. It is this purely elastic behaviour at early times that determines whether the truss then creeps in an inverted state or immediately jumps back to near its natural configuration. In this way, we were able to build up a complete picture of the different dynamical regimes and

determine precisely when pseudo-bistable behaviour is obtained (figure 5.8). Our analysis describes many features of pseudo-bistability that have been reported previously in experiments and numerical simulations, such as why a minimum indentation depth X_{ind} and duration T_{ind} are needed to obtain any creep behaviour. Both of these features are readily observed in a commercially available popper toy: this needs to be turned sufficiently far 'inside-out', and held for some seconds, to be placed on a surface without immediately jumping upwards.

In the pseudo-bistable regime, the truss undergoes a creeping motion until a rapid snap-back occurs. In our leading-order description of the dynamics, this snapping event is associated with an infinite velocity, implying that inertial effects must become important again. This is very similar to the analysis of creep buckling, in which an infinite velocity is used as a criterion to determine the onset of instability (Hayman, 1978). Nevertheless, the snap-back considered here is considerably more complicated compared to classical creep buckling under a constant applied load. Due to the initial indentation stage in our experiment, both the history of stress relaxation and inertial effects at early times must be accounted for.

As well as being characterised by overdamped dynamics, a key feature of the pseudo-bistable regime is that it occurs in a narrow parameter range at the transition between bistability and monostability. This corresponds to the saddle-node bifurcation at $\lambda = \lambda_{\mathrm{fold}}$. As a direct consequence of this fact, the snap-through dynamics are susceptible to slowing down due to the saddle-node ghost. Provided T_{ind} is sufficiently large, we showed that the snap-through time t_{snap} inherits the usual inverse square-root scaling law, i.e. we have $t_{\mathrm{snap}} \propto (\eta/E)\epsilon^{-1/2}$ where η/E is the viscous timescale and $\epsilon = \lambda - \lambda_{\mathrm{fold}}$. In analysing data from experiments and numerical simulations reported in the literature, we found that this slowing down explains the sensitivity of the snap-through time in the pseudo-bistable regime, and there is some evidence of an inverse square-root scaling law (figure 5.10). While the snap-through times reported by Brinkmeyer *et al.* (2012) appear to follow a different scaling, this may be due to the Prony series ansatz used in their finite element simulations. However, the lack of experimental data means that it is not possible to draw firm conclusions. In future work, it would be interesting to perform further experiments and determine whether the square-root scaling indeed holds more generically, as we were able to conclude for the pull-in instabilities studied in Chapter 2.

We then considered the limit of small Deborah number. By focussing on the indentation displacement $X_{\mathrm{ind}} = X_{\mathrm{fold}}$, i.e. the displacement associated with the saddle-node bifurcation, our analysis becomes a natural extension to the elastic snap-through we studied in Chapter 4. Away from the saddle-node bifurcation, the dynamics are largely independent of T_{ind} and the truss behaves as though it were purely elastic. However, we showed that

this conclusion is no longer valid when the system is near the saddle-node bifurcation. When T_{ind} is small, the stiffness is largely unrelaxed when the indenter is released, which causes the displacement to initially grow linearly rather than quadratically. If $\lambda < \lambda_{\mathrm{fold}}$, this can induce snap-through when a purely elastic truss would be stable.

If $\lambda > \lambda_{\mathrm{fold}}$, this linear growth interferes with the bottleneck dynamics during snap-through. Because the bottleneck depends sensitively on ϵ, and the linear growth acts like an 'extra' perturbation, this results in a bottleneck time that depends delicately on the value of T_{ind}. If T_{ind} is sufficiently large, the Deborah number simply enters as a viscous damping coefficient, and we obtain the usual underdamped/overdamped bottleneck scalings depending on the value of $\mathcal{D} = \mathrm{De}\,\epsilon^{-1/4}$; this is analogous to the dynamics we studied in Chapter 4. However, as T_{ind} decreases, we showed that the regime diagram features two further asymptotic regions while $\mathrm{De} \ll 1$ (figure 5.14). In particular, we identified a regime in which the snap-through time scales as $t_{\mathrm{snap}} \propto (\eta/E)^{-1/3}(\sqrt{m/k})^{4/3}$, which we believe has not been reported previously. It remains an interesting possibility as to whether this scaling may be found in more complex structures.
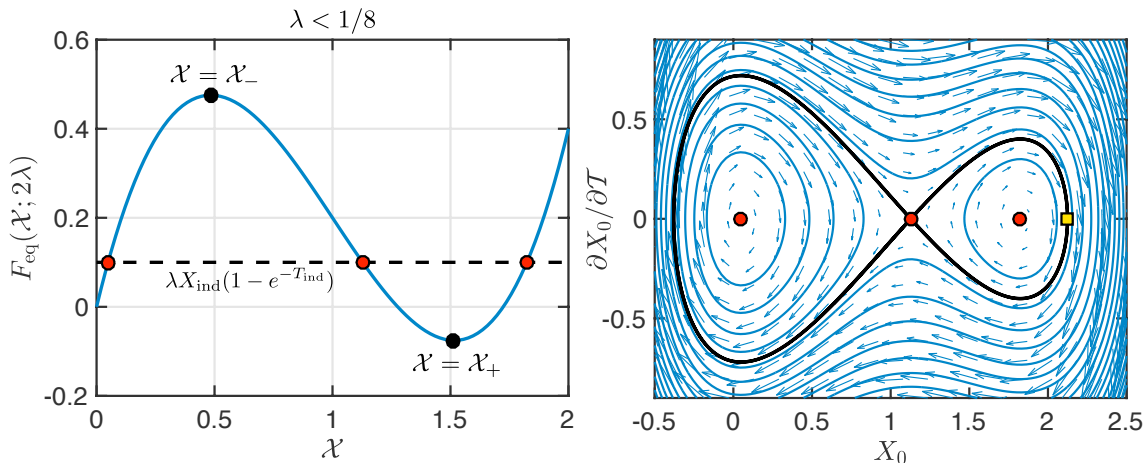
Figure 5.16: *A typical force-displacement curve in the case $\lambda < 1/8$ (left panel), and the corresponding phase plane of the first-order system (5.43) (right panel). In this regime (5.19) has three distinct real roots (labelled as red circles), corresponding to three critical points on the phase plane.*

Appendix 5.A   Determining $\mathcal{X}(0+)$

In this appendix we consider the solution $\mathcal{X}(0+)$ of the cubic equation (5.19). This provides the initial value of the "slow part" of the displacement, and so determines whether the truss initially creeps in an inverted position or immediately snaps to its natural state.

5.A.1   The case $\lambda < 1/8$

We first consider the case $\lambda < 1/8$. Here $2\lambda < \lambda_{\text{fold}}$, so that the turning point $\mathcal{X}_+$ on the force-displacement curve $F_{\text{eq}}(\mathcal{X}; 2\lambda)$ lies below the horizontal axis, i.e. $F_{\text{eq}}(\mathcal{X}_+; 2\lambda) < 0$. Furthermore, restricting to $X_{\text{ind}} \leq 2$, it is possible to show that

$$\lambda X_{\text{ind}} \left(1 - e^{-T_{\text{ind}}}\right) < F_{\text{eq}}(\mathcal{X}_-; 2\lambda).$$

Hence, when $\lambda < 1/8$, the line of height $\lambda X_{\text{ind}}(1 - e^{-T_{\text{ind}}})$ always lies between the two turning points on the force-displacement curve — there are three distinct real roots of equation (5.19). This is illustrated in the left panel of figure 5.16, which highlights the roots as red circles. However, it is not immediately clear which root is the relevant one.

To determine the relevant root, we return to equation (5.13), i.e. the leading order problem in the multiple-scale analysis. Recall that in our multiple-scale analysis, we first re-scaled the ODE in terms of the fast elastic timescale $\mathcal{T}$. Setting $A(T) = 0$, equation (5.13) then governs the dynamics of the truss at very early times, before viscous relaxation

of the SLS element becomes important. Defining $V_0 = \partial X_0 / \partial \mathcal{T}$, this equation can be written as the first-order system

$$
\begin{aligned}
\frac{\partial X_0}{\partial \mathcal{T}} &= V_0, \\
\frac{\partial V_0}{\partial \mathcal{T}} &= \lambda X_{\mathrm{ind}} \left(1 - e^{-T_{\mathrm{ind}}} \right) - F_{\mathrm{eq}}(X_0; 2\lambda),
\end{aligned}
\tag{5.43}
$$

with initial data $(X_0, V_0) = (X_{\mathrm{ind}}, 0)$ at $\mathcal{T} = 0+$. The significance here comes from the fact that the critical points of this system are precisely the solutions of (5.19), and hence correspond to the possible values of $\mathcal{X}(0+)$. The relevant value is then determined by which critical point the solution oscillates around on the phase plane, when we follow the trajectory emerging from $(X_0, V_0) = (X_{\mathrm{ind}}, 0)$ — these oscillations correspond to the "fast part" of the solution, $\mathscr{X}$, as opposed to the slowly varying mean. For later reference, we also note that (5.43) is Hamiltonian with conserved energy

$$
\frac{1}{2} \left(\frac{\partial X_0}{\partial \mathcal{T}} \right)^2 + \int_{X_{\mathrm{ind}}}^{X_0} F_{\mathrm{eq}}(\xi; 2\lambda) \, \mathrm{d}\xi = \lambda X_{\mathrm{ind}} \left(1 - e^{-T_{\mathrm{ind}}} \right) (X_0 - X_{\mathrm{ind}}).
\tag{5.44}
$$

A typical phase plane of (5.43) in the case $\lambda < 1/8$ is shown in the right panel of figure 5.16. Here the three real roots of equation (5.19) give rise to three critical points. By considering the Jacobian of (5.43), we find that the two roots where $F'_{\mathrm{eq}}(\mathcal{X}; 2\lambda) > 0$ correspond to centres, while the intermediate root where $F'_{\mathrm{eq}}(\mathcal{X}; 2\lambda) < 0$ is associated with a saddle point. Figure 5.16 also shows that there are two homoclinic orbits that emerge from the saddle point (black solid curves). These orbits act as separatrices: all trajectories that oscillate around the left centre are enclosed in the homoclinic orbit to the left of the saddle point, while all trajectories that oscillate around the right centre are enclosed in the right orbit. We therefore expect that $\mathcal{X}(0+)$ corresponds to one of the centres rather than the saddle point, depending on whether the solution starts to the left or the right of the saddle point on the phase plane. Moreover, because $F'_{\mathrm{eq}}(\mathcal{X}; 2\lambda) > 0$ at the centres, and $F'_{\mathrm{eq}}(\mathcal{X}; 2\lambda) < 0$ when $\mathcal{X} \in (\mathcal{X}_-, \mathcal{X}_+)$ (as seen from the force-displacement curve), we must have $\mathcal{X}(0+) < \mathcal{X}_-$ or $\mathcal{X}(0+) > \mathcal{X}_+$. (In addition, because we expect the solution to oscillate around these centres as T increases and $A \neq 0$, this verifies our earlier assumption that $F'_{\mathrm{eq}}(\mathcal{X}; 2\lambda) > 0$, which we made immediately after equation (5.17).)

Suppose that $1 \leq X_{\mathrm{ind}} < 3/2$. From the force-displacement curve in figure 5.16, we see that X_{ind} lies to the right of the saddle point if and only if $F_{\mathrm{eq}}(X_{\mathrm{ind}}; 2\lambda) < \lambda X_{\mathrm{ind}}(1 - e^{-T_{\mathrm{ind}}})$ (since this is where $F_{\mathrm{eq}}(\mathcal{X}; 2\lambda)$ is monotonically decreasing on the diagram). Using the expression (5.6) for F_{ind}, this is precisely the statement

$$
F_{\mathrm{ind}} = F_{\mathrm{eq}} \left(X_{\mathrm{ind}}; \lambda \left[1 + e^{-T_{\mathrm{ind}}} \right] \right) < 0.
$$

This is equivalent to

$$T_{\text{ind}} > \log\left[\frac{\lambda X_{\text{ind}}}{-F_{\text{eq}}(X_{\text{ind}}; \lambda)}\right]. \tag{5.45}$$

When this is satisfied the relevant solution is the right centre with $\mathcal{X}(0+) > \mathcal{X}_+$; otherwise we have $\mathcal{X}(0+) < \mathcal{X}_-$.

Suppose instead that $X_{\text{ind}} \geq 3/2$. In this case, X_{ind} always lies to the right of the saddle point (the force-displacement curve illustrates how the intermediate root is smaller than $3/2$ when $\lambda < 1/8$). However, it is also possible that X_{ind} is large enough to fall outside the homoclinic orbit to the right of the saddle point. If this occurs, the phase plane in figure 5.16 shows how the amplitude of the oscillations becomes very large, with the trajectory enclosing both centre points. In particular, the trajectory crosses the horizontal axis again near the origin, and so the truss will immediately snap in this regime. If this occurs, we consider the relevant solution to be the left centre, i.e. $\mathcal{X}(0+) < \mathcal{X}_-$.

Now imagine that λ and X_{ind} are fixed, while the indentation time T_{ind} is varied. As T_{ind} increases, the value of $\lambda X_{\text{ind}}\left(1 - e^{-T_{\text{ind}}}\right)$ increases, and so both the right centre and the homoclinic orbit are shifted further to the right on the phase plane. There will be a critical value of T_{ind} for which the initial point $(X_{\text{ind}}, 0)$ lies exactly where the homoclinic orbit crosses the horizontal axis (highlighted as a yellow square on figure 5.16). Only when T_{ind} is larger than this value does the initial point fall inside the separatrix and we have $\mathcal{X}(0+) > \mathcal{X}_+$. This change in behaviour is an instance of a homoclinic bifurcation (Strogatz, 2014), which has been observed in other dynamic snap-through (Nachbar & Huang, 1967) and pull-in instabilities (Krylov, 2007).

To determine this critical value, we note that there is a discontinuous change in where the trajectory starting from $(X_{\text{ind}}, 0)$ later crosses the horizontal axis. Setting $\partial X_0/\partial \mathcal{T} = 0$ in (5.44), the value of X_0 at this point satisfies

$$\int_{X_{\text{ind}}}^{X_0} F_{\text{eq}}(\xi; 2\lambda)\,\mathrm{d}\xi = \lambda X_{\text{ind}}\left(1 - e^{-T_{\text{ind}}}\right)(X_0 - X_{\text{ind}}).$$

At the critical value of T_{ind}, the trajectory starts on the homoclinic orbit and later crosses the axis at the saddle point, so that we also have

$$F_{\text{eq}}(X_0; 2\lambda) = \lambda X_{\text{ind}}\left(1 - e^{-T_{\text{ind}}}\right).$$

It follows that

$$\int_{X_{\text{ind}}}^{X_0} F_{\text{eq}}(\xi; 2\lambda)\,\mathrm{d}\xi = (X_0 - X_{\text{ind}})\,F_{\text{eq}}(X_0; 2\lambda),$$

which can be re-arranged to

$$-\frac{1}{4}\left(X_0 - X_{\text{ind}}\right)^2\left[3X_0^2 + 2(X_{\text{ind}} - 4)X_0 + (X_{\text{ind}} - 2)^2 + 4\lambda\right] = 0.$$
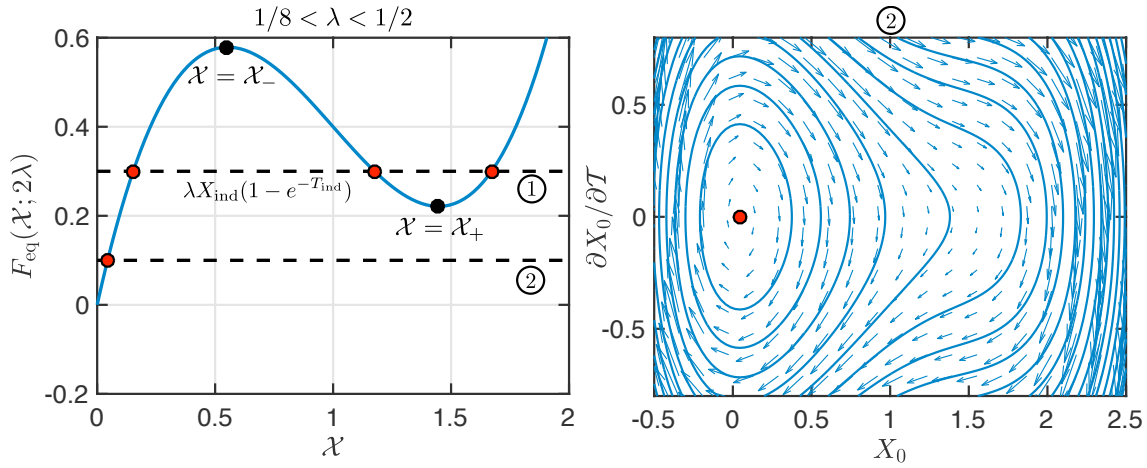
Figure 5.17: *A typical force-displacement curve in the case $1/8 < \lambda \leq 1/2$ (left panel), and the corresponding phase plane of equation* (5.43) *(right panel). In this regime equation* (5.19) *may have three distinct real roots (labelled as case* ① *) or a single real root (case* ② *).*

The solution corresponding to the saddle point is

$$X^* = -\frac{1}{3}\left(X_{\mathrm{ind}} - 4\right) + \frac{\sqrt{2}}{3}\sqrt{3 - 6\lambda - (X_{\mathrm{ind}} - 1)^2}.$$

Hence, the critical value of T_{ind} satisfies

$$\lambda X_{\mathrm{ind}}\left(1 - e^{-T_{\mathrm{ind}}}\right) = F_{\mathrm{eq}}(X^*; 2\lambda).$$

Solving for T_{ind}, we conclude that when $X_{\mathrm{ind}} \geq 3/2$, we have $\mathcal{X}(0+) > \mathcal{X}_+$ if and only if

$$T_{\mathrm{ind}} > \log\left[\frac{\lambda X_{\mathrm{ind}}}{\lambda X_{\mathrm{ind}} - F_{\mathrm{eq}}(X^*; 2\lambda)}\right]. \tag{5.46}$$

5.A.2 The case $1/8 < \lambda \leq 1/2$

When $1/8 < \lambda \leq 1/2$, both turning points on the force-displacement curve $F_{\mathrm{eq}}(\mathcal{X}; 2\lambda)$ lie above the horizontal axis; see the left panel of figure 5.17. We deduce that there are two possibilities. If the line of height $\lambda X_{\mathrm{ind}}\left(1 - e^{-T_{\mathrm{ind}}}\right)$ lies below the turning point at $\mathcal{X}_+$, i.e. if

$$\lambda X_{\mathrm{ind}}\left(1 - e^{-T_{\mathrm{ind}}}\right) < F_{\mathrm{eq}}(\mathcal{X}_+; 2\lambda),$$

then there is a single real root of equation (5.19) that corresponds to a centre on the phase plane. This is labelled as case ② on figure 5.17, and a typical phase plane is shown in the right panel of the figure. We therefore always have $\mathcal{X}(0+) < \mathcal{X}_-$ in this case.

If instead

$$\lambda X_{\mathrm{ind}}\left(1 - e^{-T_{\mathrm{ind}}}\right) > F_{\mathrm{eq}}(\mathcal{X}_+; 2\lambda), \tag{5.47}$$

then there are three distinct real roots of equation (5.19) (labelled as case ① on figure 5.17). (The third possibility, that the line $\lambda X_{\mathrm{ind}}\left(1 - e^{-T_{\mathrm{ind}}}\right)$ lies above both turning points, cannot occur when $X_{\mathrm{ind}} \leq 2$ and $\lambda \leq 1/2$.) The analysis then proceeds in a similar way to the case $\lambda < 1/8$. In particular, if $1 \leq X_{\mathrm{ind}} < 3/2$ the relevant root has $\mathcal{X}(0+) > \mathcal{X}_+$ if and only if T_{ind} satisfies (5.45), otherwise $\mathcal{X}(0+) < \mathcal{X}_-$; while if $X_{\mathrm{ind}} \geq 3/2$, we have $\mathcal{X}(0+) > \mathcal{X}_+$ if and only if T_{ind} satisfies (5.46), otherwise $\mathcal{X}(0+) < \mathcal{X}_-$.

Finally, it may be shown (e.g. by graphical considerations) that the conditions (5.45)–(5.46) are always stronger than (5.47), i.e. the critical value of T_{ind} required is larger. Because $\mathcal{X}(0+) < \mathcal{X}_-$ whenever (5.47) is not satisfied, we conclude that necessary and sufficient conditions that determine whether $\mathcal{X}(0+) < \mathcal{X}_-$ or $\mathcal{X}(0+) > \mathcal{X}_+$ are given by equations (5.45)–(5.46), both for $\lambda < 1/8$ and $1/8 < \lambda \leq 1/2$.

Appendix 5.B   Assumption of an evolving stiffness

In the approach of Santer (2010), later adopted by Brinkmeyer *et al.* (2012; 2013), the viscoelastic response is modelled as an elastic structure with an effective stiffness that changes in time. The evolution is specified by a Prony series, which assumes that the stiffness can be expressed as a sum of decaying exponential functions. For example, if $E(t)$ is the Young's modulus at time t, and $E_0 = E(0)$ is the initial modulus, this can be written as (Brinkmeyer *et al.*, 2012)

$$E(t) = E_0 \left[1 - \sum_{j=1}^{N} K_j \left(1 - e^{-t/\tau_j} \right) \right], \tag{5.48}$$

where $N \geq 1$ is an integer; the coefficients K_j and timescales τ_j are specified parameters that can be fitted to experimental data from relaxation tests. In the case of a step increase in strain applied at $t = 0$, this model is physically equivalent to a superposition of SLS elements, with each term corresponding to the stress relaxation of a particular element (Kim *et al.*, 2010; Brinkmeyer *et al.*, 2012); the value E_0 corresponds to the fully unrelaxed modulus, i.e. just after the strain is applied. As $t \to \infty$, the modulus $E(t)$ decays to the fully relaxed value

$$E_\infty = E_0 \left[1 - \sum_{j=1}^{N} K_j \right].$$

To apply this model when the indenter is released, Santer (2010) and Brinkmeyer *et al.* (2012; 2013) assume that the evolution during recovery is the reciprocal of the behaviour during indentation, and that there is no jump in the value of the stiffness. The stiffness

is also allowed to fully relax before the indenter is released. With $t = 0$ now denoting the point when the indenter is released, this corresponds to setting

$$E(t) = E_0 \left[1 - \sum_{j=1}^{N} K_j e^{-t/\tau_j} \right],$$

for $t > 0$. Thus $E(t = 0+) = E_\infty$, and $E(t)$ decays to the fully unrelaxed value E_0 as $t \to \infty$. If instead the stiffness is only allowed to relax for a time duration t_{ind} before the indenter is released, as in our truss experiment, this modifies to

$$E(t) = E_0 \left[1 - \sum_{j=1}^{N} K_j e^{-t/\tau_j} \left(1 - e^{-t_{\text{ind}}/\tau_j} \right) \right], \tag{5.49}$$

since when $t = 0+$ this corresponds to (5.48) evaluated at $t = t_{\text{ind}}$.

To understand this assumption within the framework of our truss model, we recall from §5.2.3 that in response to an indentation displacement X_{ind} suddenly applied at $T = -T_{\text{ind}}$, the dimensionless stress is

$$\Sigma = X_{\text{ind}} \left[1 + e^{-(T+T_{\text{ind}})} \right], \qquad -T_{\text{ind}} < T < 0.$$

Since X is the strain in the SLS element, the effective stiffness is therefore

$$\frac{\Sigma}{X} = 1 + e^{-(T+T_{\text{ind}})}.$$

This corresponds to the Prony series (5.48) when we identify

$$E(t) = [\sigma] \frac{\Sigma}{X}, \quad E_0 = 2[\sigma], \quad N = 1, \quad K_1 = 1/2, \quad \tau_1 = \eta/E, \quad \frac{t}{\tau_1} = T + T_{\text{ind}},$$

for some pressure scale $[\sigma]$. Hence, when the indenter is released, the above assumption (5.49) would be equivalent to specifying for $T > 0$

$$\frac{\Sigma}{X} = 2 \left[1 - \frac{1}{2} e^{-T} \left(1 - e^{-T_{\text{ind}}} \right) \right].$$

(Here we instead identify $t/\tau_1 = T$.) Setting $F = 0$ in the momentum equation (5.4), and substituting the effective stiffness above, the trajectory $X(T)$ would then obey

$$\text{De}^{-2} \frac{\mathrm{d}^2 X}{\mathrm{d}T^2} = -F_{\text{eq}} \left(X(T); 2\lambda \left[1 - \frac{1}{2} e^{-T} \left(1 - e^{-T_{\text{ind}}} \right) \right] \right), \tag{5.50}$$

for $T > 0$, together with

$$X(0+) = X_{\text{ind}}, \quad \dot{X}(0+) = 0. \tag{5.51}$$

To understand how the behaviour of (5.50) differs to the model we consider in the main text when $\text{De} \gg 1$, we neglect the inertia term in a first approximation to obtain

$$F_{\text{eq}}\left(X(T); 2\lambda\left[1 - \frac{1}{2}e^{-T}\left(1 - e^{-T_{\text{ind}}}\right)\right]\right) = 0, \qquad T > 0.$$

The dynamics can therefore be determined by considering the force-displacement curve (figure 5.2a) as λ varies. Recall that indentation corresponds to rotating the curve clockwise as stress relaxation occurs. Because of the assumption that the response during recovery is the reverse of relaxation, it follows that the graph rotates *anticlockwise* as soon as the indenter is released. In particular, the effective value of λ increases from $\lambda(1 + e^{-T_{\text{ind}}})$ to 2λ as $T \to \infty$. For each value of λ, the displacement is found as the value of X at which the force-displacement curve crosses the horizontal axis. If $\lambda < 1/8$ (so $2\lambda < \lambda_{\text{fold}}$), the truss is bistable in the fully unrelaxed state, and so is bistable during recovery — provided the truss is indented near the stable root of $F_{\text{eq}} = 0$ away from zero, snap-through does not occur and the truss remains at this root. If $\lambda > 1/4$, the truss is monostable when the indenter is released, and so remains monostable during recovery — to satisfy $F_{\text{eq}} = 0$ the solution must immediately jump to $X = 0$ and the snap-through time is governed by inertia. If $1/8 < \lambda < 1/4$ the truss is temporarily bistable when the indenter is released if and only if

$$\lambda\left(1 + e^{-T_{\text{ind}}}\right) < \frac{1}{4}. \tag{5.52}$$

In this case, rapid snap-through occurs as soon as the anticlockwise rotation is enough to put the turning point on the force-displacement curve above the line $F_{\text{eq}} = 0$; the snap-through time is therefore $O(1)$. In fact, since the turning point intersects the horizontal axis at $X = X_{\text{fold}} = 3/2$, the snap-through time satisfies

$$F_{\text{eq}}\left(\frac{3}{2}; 2\lambda\left[1 - \frac{1}{2}e^{-T_{\text{snap}}}\left(1 - e^{-T_{\text{ind}}}\right)\right]\right) = 0.$$

This can be re-arranged to

$$T_{\text{snap}} = \log\left[\frac{\lambda\left(1 - e^{-T_{\text{ind}}}\right)}{2(\lambda - 1/8)}\right].$$

If instead $\lambda\left(1 + e^{-T_{\text{ind}}}\right) > 1/4$, the truss is initially monostable and so immediately snaps, similarly to the case $\lambda > 1/4$.

Comparing this picture with figure 5.8 in the main text, we conclude that this model exhibits very different behaviour compared to that derived without making assumptions regarding the behaviour of the stiffness during recovery: both the regions where snap-
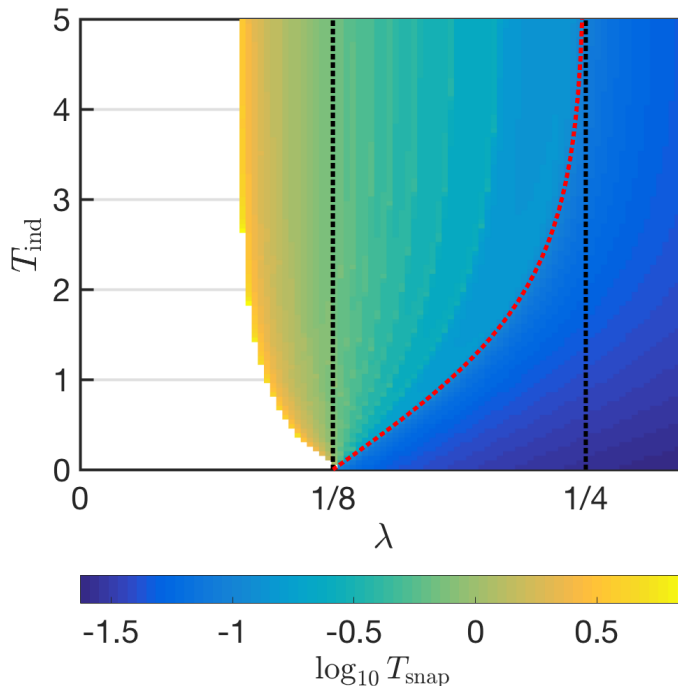
Figure 5.18: *Snap-through times obtained by integrating* (5.50)–(5.51) *numerically until the point when* $X = 0$ *(see colourbar), which assumes that the stiffness during recovery reverses back to its fully unrelaxed value* ($X_{\mathrm{ind}} = X_{\mathrm{fold}}$, De = 100). *Also shown is the boundary above which pseudo-bistable behaviour is obtained predicted by* (5.52) *(red dotted curve).*

through and pseudo-bistability occur differ significantly between the two models. Moreover, the expression above implies that in the pseudo-bistable regime the snap-through time diverges according to

$$T_{\mathrm{snap}} \sim \log\left[\frac{1}{\lambda - 1/8}\right] \quad \text{as} \quad \lambda \searrow 1/8,$$

i.e. we obtain a *logarithmic* scaling rather than an inverse square-root scaling law. This conclusion also holds when we account for the effects of inertia and directly solve the ODE (5.50) with initial conditions (5.51); see figure 5.18, which plots the computed snap-through times on the $(\lambda, T_{\mathrm{ind}})$-plane for $X_{\mathrm{ind}} = X_{\mathrm{fold}}$ and De $= 10^2$. This shows that the region where snap-through occurs is roughly in agreement with the above analysis (contrast this to figure 5.8), though the boundary is shifted slightly to the left of the line $\lambda = 1/8$ due to the de-stabilising effects of inertia. Analysing the slowing down near this boundary confirms that a logarithmic scaling is indeed obtained. We then suggest that the snap-through times reported by Brinkmeyer *et al.* (2012) may exhibit a similar logarithmic scaling, due to the Prony series ansatz used in their finite element simulations of spherical caps.

Appendix 5.C   Bottleneck analysis for $\mathcal{D} \ll 1$, $\mathcal{D}\Psi \gtrsim 1$

In this appendix we extend the bottleneck analysis of §5.4.2 to consider the case $\mathcal{D} \ll 1$ and $\mathcal{D}\Psi \gtrsim 1$. Unlike the case $\mathcal{D}\Psi \ll 1$, the order-of-magnitude estimates in (5.38) imply that the first-order viscous term balances the inertia term at the point when χ reaches $O(1)$ (the third-order derivative is again negligible).

In particular, when $\Psi = O(\mathcal{D}^{-1})$, both terms are $O(1)$ and the updated balance is

$$\frac{\mathrm{d}^2\chi}{\mathrm{d}\tau^2} + \frac{1}{4}\mathcal{D}\frac{\mathrm{d}\chi}{\mathrm{d}\tau} \sim \frac{3}{2}\left(1 + \chi^2\right). \tag{5.53}$$

Multiplying by $\mathrm{d}\chi/\mathrm{d}\tau$ and integrating, the solution matching back into $\chi \ll 1$ satisfies

$$\left(\frac{\mathrm{d}\chi}{\mathrm{d}\tau}\right)^2 \sim \chi^3 + 3\chi + \left(\frac{3}{8}\Psi\right)^2 - \frac{1}{2}\mathcal{D}\int_0^\tau \left(\frac{\mathrm{d}\chi}{\mathrm{d}\tau}\right)^2 \mathrm{d}\xi.$$

Due to the integral on the right-hand side (arising from the viscous term), it is not clear how to make further analytical progress. However, when χ grows sufficiently large, we expect that the inertia term will dominate the viscous term and (5.53) will reduce to the underdamped dynamics we have previously considered. To show this, we note that the integral on the right-hand side is positive, so we can bound the velocity by

$$\frac{\mathrm{d}\chi}{\mathrm{d}\tau} \leq \sqrt{\chi^3 + 3\chi + \left(\frac{3}{8}\Psi\right)^2} = O(\chi^{3/2}, \Psi).$$

From (5.53), we calculate the ratio of the viscous term to the inertia term:

$$\frac{\mathcal{D}\frac{\mathrm{d}\chi}{\mathrm{d}\tau}}{\frac{\mathrm{d}^2\chi}{\mathrm{d}\tau^2}} \sim \frac{\mathcal{D}\frac{\mathrm{d}\chi}{\mathrm{d}\tau}}{\frac{3}{2}\left(1 + \chi^2\right) - \frac{1}{4}\mathcal{D}\frac{\mathrm{d}\chi}{\mathrm{d}\tau}}.$$

This ratio becomes small when $\chi^2 \gg \mathcal{D}(\mathrm{d}\chi/\mathrm{d}\tau)$. Using the above bound for the velocity, this is satisfied when $\chi \gg (\mathcal{D}\Psi)^{1/2} = O(1)$. (This occurs before χ reaches $O(\epsilon^{-1/2})$ and leaves the bottleneck.) The solution then reduces to

$$\left(\frac{\mathrm{d}\chi}{\mathrm{d}\tau}\right)^2 \sim \chi^3 + \left(\frac{3}{8}\Psi\right)^2.$$

Integrating again, we recover the implicit solution (5.39) when we neglect the ξ term in the integrand. To leading order, the bottleneck duration is therefore identical to the case $1 \ll \Psi \ll \mathcal{D}^{-1}$, i.e. equation (5.41). The only difference when $\Psi = O(\mathcal{D}^{-1})$ is a further transient that involves a different leading order balance, before the same underdamped dynamics are recovered at later times.

A similar picture also occurs if $\Psi \gg \mathcal{D}^{-1}$. The inertia and viscous terms are now much larger than unity when $\chi = O(1)$, so the updated balance modifies to

$$\frac{\mathrm{d}^2\chi}{\mathrm{d}\tau^2} \sim -\frac{1}{4}\mathcal{D}\frac{\mathrm{d}\chi}{\mathrm{d}\tau}.$$

The solution matching backwards is

$$\chi \sim \frac{3}{2}\frac{\Psi}{\mathcal{D}}\left(1 - e^{-\mathcal{D}\tau/4}\right).$$

While $\tau \ll \mathcal{D}^{-1}$, we have $\chi \sim (3/8)\Psi\tau$ and the viscous and inertia terms are both $O(\mathcal{D}\Psi)$. The χ^2 term then becomes comparable when $\tau = O(\mathcal{D}^{1/2}\Psi^{-1/2})$, at which point we solve

$$\frac{\mathrm{d}^2\chi}{\mathrm{d}\tau^2} + \frac{1}{4}\mathcal{D}\frac{\mathrm{d}\chi}{\mathrm{d}\tau} \sim \frac{3}{2}\chi^2.$$

The solution matching backwards satisfies

$$\left(\frac{\mathrm{d}\chi}{\mathrm{d}\tau}\right)^2 \sim \chi^3 + \left(\frac{3}{8}\Psi\right)^2 - \frac{1}{2}\mathcal{D}\int_0^\tau \left(\frac{\mathrm{d}\chi}{\mathrm{d}\tau}\right)^2 \mathrm{d}\xi.$$

Similar to the case $\Psi = O(\mathcal{D}^{-1})$, it is possible to show that the viscous term becomes negligible before the end of the bottleneck phase, so the bottleneck duration is unaffected.

Epilogue

6.1 Summary of the thesis

This thesis has been dedicated to understanding the dynamics of snap-through. In particular, we have explored how the mathematical structure underlying snap-through controls the timescale of instability, and the precise role played by energy dissipation in obtaining surprisingly slow dynamics.

We began in Chapter 2 by analysing the dynamics of pull-in instabilities in micro-electromechanical systems (MEMS). This provided a context in which to understand the dynamics of overdamped snap-through. Because the equilibrium away from collapse disappears at a saddle-node bifurcation, a standard linear stability analysis fails to yield any information about the dynamics. Using a lumped-parameter model with a single degree of freedom, we showed that the bottleneck phenomenon reported near the pull-in transition is a type of critical slowing down, in which the displacement grows linearly rather than exponentially. As a result, the pull-in time, t_{PI}, inherits an inverse square-root scaling law: we have $t_{\mathrm{PI}} \propto \epsilon^{-1/2}$ as $\epsilon \to 0$, where ϵ is the normalised difference between the applied voltage and the pull-in voltage. This new realisation unifies previous experimental and simulation results, as well as providing a useful design rule for micro-accelerometers and pressure sensors that use pull-in time as a sensing mechanism.

Building on this work, in Chapter 3 we presented the pull-in dynamics of MEMS microbeams. We extended the lumped-parameter approach of Chapter 2 to explicitly consider the geometry of the beam, modelled using the dynamic beam equation with viscous damping. Because this constitutes a PDE in space and time, the associated dynamical system is infinite dimensional. To make progress, we developed a perturbation method that exploits the proximity to the pull-in transition to systematically reduce the PDE to the normal form for a saddle-node bifurcation — hence the ghost phenomenon is immediately inherited by the elastic continuum. In this way, we were able to obtain a simple expression for the pull-in time in terms of the beam parameters, which agrees well with numerical simulations and experiments. We also explored the accuracy of a single-mode approximation of the microbeam equations, showing that this method can provide a viable alternative to our perturbation approach by yielding quantitatively similar results with much less effort.

In Chapter 4, we studied the dynamics of macroscopic snap-through caused by varying geometric confinement (rather than external loading). To understand the influence of viscous damping, we focussed on a shallow elastic arch as a simple and common structural prototype. Using a beam model, we showed that the steady problem may be entirely characterised by the single geometrical parameter μ, analogous to the Föppl-von-Kármán number for shallow spherical caps. We then modified the perturbation method of Chapter 3 to show that two bottleneck regimes are possible, depending delicately on the importance of external damping compared to the distance to bifurcation in parameter space. In particular, we showed that critical slowing down is still possible in the underdamped limit, and determined a new scaling law for the snap-through time that was confirmed by dynamic elastica simulations and experiments. This provides a fresh perspective on the various factors that limit the speed of snap-through in applications, and suggests a new tool for controlling dynamic responses.

Finally, in Chapter 5, we investigated the effect of viscoelasticity on the dynamics of snap-through. To make analytical progress we considered a Mises truss, a single-degree-of-freedom structure that can be regarded as a lumped model for more complex systems, such as spherical caps and arches. We focussed on a theoretical experiment in which the truss is first allowed to relax in a specified shape before being released. When the timescale of viscous relaxation is much larger than the elastic timescale, we showed that only two types of snap-through are possible: the truss either immediately snaps on the elastic timescale, or it first undergoes a slow creeping motion governed by the viscous timescale. This creeping motion may be very slow indeed, as we found that the snap-through time is still subject to critical slowing down in this regime. In the limit when the viscous timescale is smaller than the elastic timescale, we determined how viscoelasticity interacts with the bottleneck phenomenon near the snap-through transition. We discovered that even a small amount

of viscosity modifies the dynamics we saw in Chapter 4, leading to new dynamical regimes and associated scaling laws for the snap-through time.

In summary, while snap-through generates fast motions on a global scale, it is generally caused by a loss of stability at a local bifurcation. We have exploited this fact to show that anomalously slow dynamics in macroscopic snap-through, as well as electrostatic pull-in, can result from being close to a bifurcation in parameter space, in a similar manner to the critical slowing down observed in other areas of physics (Strogatz & Westervelt, 1989; Chaikin & Lubensky, 1995; Scheffer *et al.*, 2009). This is a generic property of dynamical systems near bifurcation that does not require an additional physical mechanism. Nevertheless, we have found that material viscoelasticity may significantly enhance the slowing down effect. By developing the machinery to understand the bifurcation structure, we have been able to obtain expressions for the snap-through time that are in good agreement with direct numerical solutions and experiments.

6.2 Future work

6.2.1 Spherical caps and dynamic loading

The perturbation method we developed in Chapters 3 and 4 depends only on the mathematical structure underlying the saddle-node bifurcation, and so can be applied to study the dynamics of other snap-through problems. An obvious candidate for future work in this direction is the snap-through of a spherical cap, which more closely resembles the jumping popper toy that first motivated our studies of snap-through. Because we chose the boundary conditions of our arch system in Chapter 4 to recreate the morphology of a spherical cap, many features of the shell problem work analogously. For example, the stability characteristics of a spherical cap are completely characterised by the geometric parameter (Huang, 1964; Fitch, 1968)

$$\lambda_d = [12(1 - \nu^2)]^{1/4} \left(\frac{2H}{h} \right)^{1/2},$$

together with the Poisson ratio ν; here H is the rise of the apex above the base diameter, and h is the shell thickness. (The related parameter $\gamma = \lambda_d^4$ is sometimes referred to as the Föppl-von-Kármán number for spherical caps, as opposed to complete shells.) Just like the μ parameter, λ_d can be interpreted as the ratio of bending to stretching energies so the dependence on the Young's modulus cancels out (Brinkmeyer *et al.*, 2012).

When λ_d is large, corresponding to relatively thin/deep caps, the shell can be turned 'inside-out' and the everted shape is also stable; as λ_d is decreased, this shape eventually

becomes unstable at a saddle-node bifurcation, and the shell snaps back to its natural shape (Brodland & Cohen, 1987). This is similar to varying μ in our arch setup, and varying the relative stiffness λ in the Mises truss (Chapter 5). Starting from the equations of force balance and compatibility of strains for a shallow spherical shell, this suggests that a similar asymptotic analysis may be performed near the snap-through transition. If the material is viscoelastic, it would also be interesting to see whether the different scaling laws for the bottleneck duration, predicted in Chapter 5, can be observed. Due to the complexity of the shallow shell equations (Gomez *et al.*, 2016), and the possibility of non-axisymmetric deformations (Seffen & Vidoli, 2016), few analytical results concerning their snap-through dynamics are available; such scaling laws would provide an analytical basis for tuning the dynamic response in morphing applications.

The snap-through of spherical caps also provides a context in which to understand the effects of dynamic loading. We briefly discussed at the end of Chapter 4 how our asymptotic analysis does not apply in these scenarios, since we assumed that the system is quasi-statically placed beyond the snap-through transition. Experimentally this was achieved in our arch setup by an indenter that is suddenly removed before snap-through occurs. In many real systems, however, the stimulus that causes snap-through smoothly evolves in time, so the system gradually approaches the snap-through transition. For example, the leaf of the Venus flytrap swells with water when stimulated by an insect, causing a gradual change in natural curvature that makes the 'open' equilibrium unstable (Forterre *et al.*, 2005). Similarly, in many systems the stimulus is driven by mass transport meaning that changes occur on a diffusion-limited timescale; for example, the snap-through of colloidal particles under changes in pH (resulting from absorption of a chemical) (Epstein *et al.*, 2015), and hydrogels upon solvent uptake (Lee *et al.*, 2010). In low-dimensional systems, previous work has demonstrated how dynamic loading can delay the onset of instability and modify the scaling law describing critical slowing down (Tredicce *et al.*, 2004; Majumdar *et al.*, 2013) — a so-called delayed bifurcation. It would be interesting to understand how such effects influence the dynamics of snap-through, which may yield new insights into how systems such as the Venus flytrap behave near critical transitions.

6.2.2 Effects of noise

In our analysis of snap-through dynamics, we have neglected the effects of noise (thermal or mechanical). One type of mechanical 'noise', material imperfections, is discussed in the next section. However, in nanoscale systems thermal noise becomes significant and may interact with elastic instabilities to produce new types of dynamical behaviour. In particular, a natural question to ask is how does noise interact with the slowing down phenomenon we have studied in macroscopic snap-through?
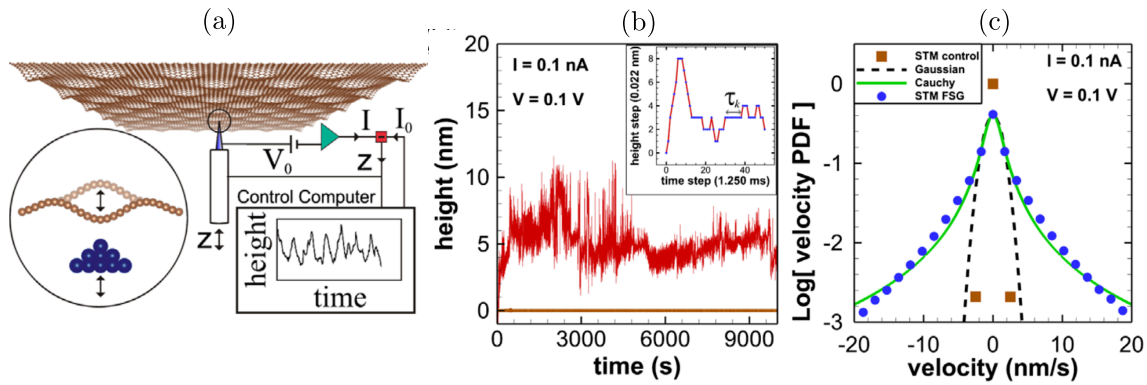
Figure 6.1: *(a) Experimental setup used by Ackerman* et al. *(2016) to measure the dynamics of a freestanding graphene membrane. (b) Time series of the out-of-plane displacement measured using a scanning tunneling microscope (red curve). For comparison, the time series for a rigid sample is also shown (lower brown curve). (c) The distribution of measured velocities (blue circles) extracted from the time series in (b), together with the best-fit Cauchy-Lorentz (green curve) and Gaussian (black dashed curve) distributions. (Reprinted figures with permission from [M. L. Ackerman, P. Kumar, M. Neek-Amal, P. M. Thibado, F. M. Peeters and S. Singh. Physical Review Letters. 117 (12), 126801 (2016). DOI: https://doi.org/10.1103/PhysRevLett.117.126801]. Copyright 2016 by the American Physical Society.)*

This question is inspired by recent experiments on graphene membranes — atom-thick sheets of carbon atoms arranged in a hexagonal lattice. When a graphene membrane is freestanding and not bonded to a substrate, it is constantly in motion due to thermal fluctuations. These fluctuations mean that the membrane is not planar but is rippled. Using a scanning tunneling microscope, Ackerman *et al.* (2016) have measured the out-of-plane displacement of a single point on such a membrane over an extended time interval; see figure 6.1a. This generates a time series of the displacement (figure 6.1b), from which a probability density function of the velocities can be extracted (figure 6.1c, blue circles). Experimentally, it is observed that the membrane occasionally exhibits large jumps between different positions, so that the velocity distribution has anomalously long tails away from usual Brownian motion. Classical models that couple membrane elasticity to thermal fluctuations predict a Gaussian distribution, which does not account for these tails (the best-fit Gaussian is plotted as a black dashed curve). Instead, the long tails are much better fitted by a Cauchy-Lorentz distribution (green curve), which decays algebraically rather than exponentially. Molecular dynamics simulations performed by Ackerman *et al.* (2016) suggest that the large jumps correspond to local snapping events: a portion of the rippled membrane spontaneously becomes doubly curved, resembling part of a spherical shell, which snaps through and reverses its curvature. However, it is not yet clear how these snapping events interact with the thermal fluctuations, and lead to the velocity distribution that is observed.

Similar anomalous dynamics have also been reported in optomechanical buckling transi-
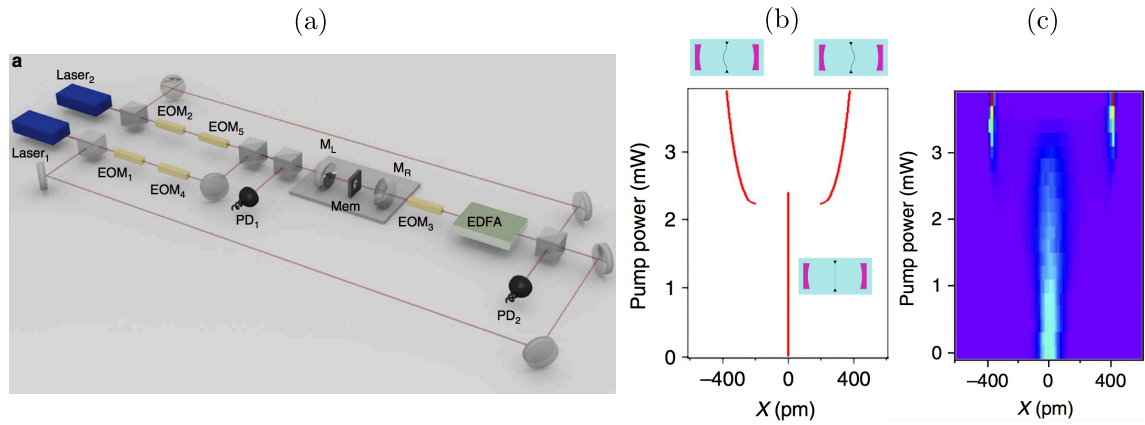
Figure 6.2: *(a) Experimental setup used by Xu* et al. *(2017) to investigate radiation pressure-induced buckling of a dielectric membrane (thickness* 258 nm*). (b) The predicted displacement of steady equilibrium states as a function of laser power. (c) Histogram of measured membrane positions, coloured as a heat-map according to dwell times at each laser power. (Reprinted from [H. Xu, U. Kemiktarak, J. Fan, S. Ragole, J. Lawall and J. M. Taylor. Nature Communications. 8, 14481 (2017). DOI: https://doi.org/10.1038/ncomms14481] under a Creative Commons Attribution 4.0 International License [https://creativecommons.org/licenses/by/4.0/].)*

tions. In recent experiments performed by Xu *et al.* (2017), an ultra-thin membrane is held under tension and subject to radiation pressure inside an optical cavity. This radiation pressure is controlled by adjusting the power of two pump lasers; see figure 6.2a. When a critical laser power is exceeded, it is observed that the straight membrane suddenly breaks symmetry and buckles out-of-plane. Using an optical spring model, Xu *et al.* (2017) show that in a certain parameter range this corresponds to a subcritical pitchfork bifurcation: the straight configuration loses stability to two remote buckled states, similar to a snap-through instability (figure 6.2b). In experiments, the membrane fluctuates around these states due to mechanical noise; a histogram of the measured positions is shown in figure 6.2c. As expected, at low laser powers the membrane fluctuates in a narrow band of positions around the straight configuration, the only stable equilibrium; at high powers, the fluctuations are restricted to near the two buckled states. Interestingly, at powers just beyond the buckling transition, the distribution widens significantly and the membrane spends a large proportion of its time near the straight configuration, even when this is no longer the minimum energy state. This is reminiscent of the bottleneck phenomena we have studied in snap-through, in which the dynamics are slowed by the remnant of the equilibrium shape at the snap-through bifurcation. We also note that the widening of the distribution in figure 6.2c causes the system to become highly sensitive to external forces, and so has important implications for sensing applications of optomechanical devices.

In both of these examples, there are tantalising hints that the observed anomalous dynamics may be connected to the slowing down we have studied in macroscopic snap-through. If a system driven by noise is near a snap-through transition, it is conceivable
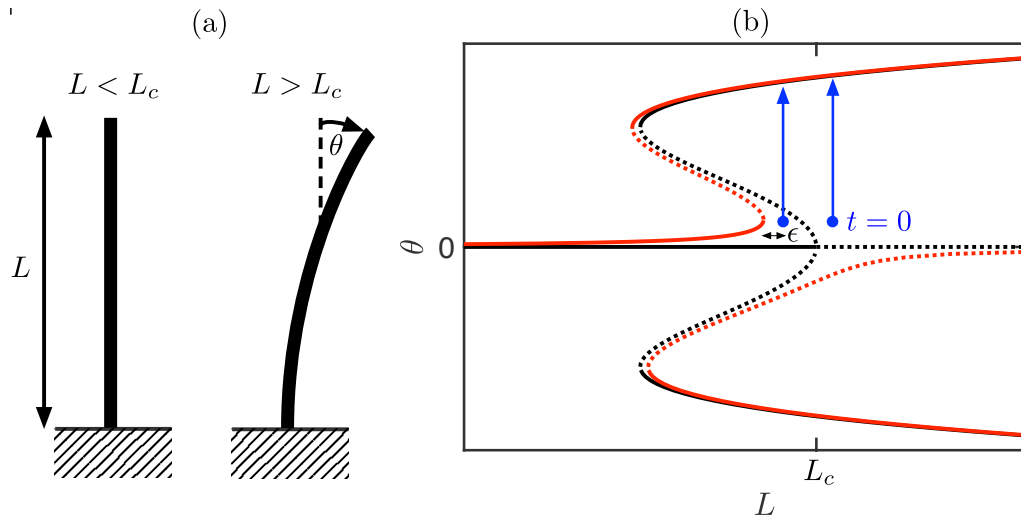
Figure 6.3: *(a) Schematic of a cantilever beam buckling due to self-weight. (b) A typical response diagram of the cantilever when the moment-curvature relationship exhibits softening behaviour. Here collapse occurs at a subcritical pitchfork bifurcation (black curves), which becomes a saddle-node bifurcation in the presence of small imperfections (red curves). In both cases, solid branches correspond to stable equilibrium modes, while dotted branches correspond to unstable modes.*

that this slowing down effect could modify the dynamics, causing the system to spend long periods of time in the tails of the distribution. It remains an intriguing possibility as to whether this mechanism could explain the observed dynamics in systems such as graphene, and if it is possible to make quantitative predictions about the form of the velocity distribution. This is a technical challenge due to qualitatively different physical effects present in these systems compared to those we have previously studied: as well as the importance of noise, inertia forces are unlikely to play a significant role.

6.2.3 Effects of imperfections

Another effect that has been neglected throughout this thesis is the influence of material imperfections. By focussing on snap-through caused by a saddle-node bifurcation, this is partly justified: this type of bifurcation is imperfection insensitive in the sense that it generally does not change type in the presence of small imperfections. However, other types of bifurcation may qualitatively change type when imperfections are present, and the critical load may be significantly reduced (Hayman, 1978). This has been well documented in many examples of buckling instabilities (Bushnell, 1981), though the full consequences of this fact for the dynamics (particularly when there is a bottleneck) are unclear. Because we have shown that such phenomena are controlled by the underlying mathematical structure, we anticipate that the dynamics will depend delicately on the size of the imperfection.

As a more concrete example, consider a heavy cantilever beam that is clamped vertically at its base while the upper end is freely suspended. If the beam is linearly elastic, it is

well known that it buckles due to self-weight when a critical height is exceeded (Wang, 1986); see figure 6.3a. Similar to classical Euler buckling, this corresponds to a supercritical pitchfork bifurcation. If instead the material is non-linearly elastic with a softening property, i.e. its stiffness decreases when subject to bending, the bifurcation at collapse becomes subcritical: any small increase in length causes the beam to abruptly droop to one side, similar to a snap-through instability (figure 6.3b, black curves). This experiment may readily be performed using a piece of ordinary curtain wire, which possesses such a softening property (Fraser & Champneys, 2002). Virgin & Plaut (2004) have shown how the presence of imperfections then changes this to a saddle-node bifurcation (figure 6.3b, red curves). Now imagine an experiment in which the beam is held near the straight position before being released, as illustrated in figure 6.3b. There is the curious possibility of observing different dynamical regimes depending on the excess length ϵ beyond bifurcation. If ϵ is sufficiently large compared to the imperfection size, the system only 'sees' a perfect diagram in the initial state, and so the displacement should grow exponentially (as would be predicted by a standard linear stability analysis about the unstable branch); for smaller ϵ, i.e. 'zooming in' on the bifurcation, the fold structure becomes apparent and so we expect the growth to instead be algebraic. It should therefore be possible to move between these two behaviours within a single experimental system.

6.2.4 Other mechanical instabilities

In fact, there is nothing special about snap-through in the perturbation method we developed in Chapters 3 and 4. The reduction to the normal form for a saddle-node bifurcation showed that there are only three fundamental ingredients: the nonlinearity giving rise to the saddle-node bifurcation, the perturbation to the bifurcation parameter, and inertia and/or damping. This suggests that we can adopt our method to study a whole host of other mechanical instabilities that feature similar delay phenomena.

In conclusion, some of the features that make snap-through difficult to analyse are generic to elastic instabilities. Because of this fact, previous approaches are mainly computational or experimental in nature. However, the general techniques developed in this thesis promise to be applicable more broadly, and may lead to new analytical frameworks for understanding the dynamics of such instabilities in a quantitative way.

Bibliography

ACKERMAN, M. L., KUMAR, P., NEEK-AMAL, M., THIBADO, P. M., PEETERS, F. M. & SINGH, S. 2016 Anomalous dynamical behavior of freestanding graphene membranes. *Phys. Rev. Lett.* **117** (12), 126801.

ARANSON, I. S., MALOMED, B. A., PISMEN, L. M. & TSIMRING, L. S. 2000 Crystallization kinetics and self-induced pinning in cellular patterns. *Phys. Rev. E* **62** (1), R5–R8.

AUDOLY, B. & POMEAU, Y. 2010 *Elasticity and geometry: from hair curls to the nonlinear response of shells*. Oxford University Press, Oxford.

BATRA, R. C., PORFIRI, M. & SPINELLO, D. 2007 Review of modeling electrostatically actuated microelectromechanical systems. *Smart Mater. Struct.* **16** (6), R23–R31.

BATRA, R. C., PORFIRI, M. & SPINELLO, D. 2008 Vibrations of narrow microbeams predeformed by an electric field. *J. Sound Vib.* **309** (3), 600–612.

BAXTER, G. J., DOROGOVTSEV, S. N., LEE, K.-E., MENDES, J. F. F. & GOLTSEV, A. V. 2015 Critical dynamics of the k-core pruning process. *Phys. Rev. X* **5** (3), 031017.

BAZANT, Z. & CENDOLIN, L. 1991 *Stability of Structures: Elastic, Inelastic, Fracture, and Damage Theories*. Oxford University Press, Oxford.

BLECH, J. J. 1983 On isothermal squeeze films. *J. Lubrication Tech.* **105** (4), 615–620.

BOISSEAU, S., DESPESSE, G., MONFRAY, S., PUSCASU, O. & SKOTNICKI, T. 2013 Semi-flexible bimetal-based thermal energy harvesters. *Smart Mater. Struct.* **22** (2), 025021.

BRINKMEYER, A., PIRRERA, A., SANTER, M. & WEAVER, P. M. 2013 Pseudo-bistable pre-stressed morphing composite panels. *Int. J. Solids Struct.* **50** (7), 1033–1043.

BRINKMEYER, A., SANTER, M., PIRRERA, A. & WEAVER, P. M. 2012 Pseudo-bistable self-actuated domes for morphing applications. *Int. J. Solids Struct.* **49** (9), 1077–1087.

BRODLAND, G. W. & COHEN, H. 1987 Deflection and snapping of spherical caps. *Int. J. Solids Struct.* **23** (10), 1341–1356.

BUSHNELL, D. 1981 Buckling of shells—pitfall for designers. *AIAA J.* **19** (9), 1183–1226.

CARR, J. 2012 *Applications of Centre Manifold Theory*. Springer-Verlag, Berlin.

CASSAK, P. A. 2006 Catastrophe model for the onset of fast magnetic reconnection. PhD thesis, University of Maryland.

CASTANER, L. M. & SENTURIA, S. D. 1999 Speed-energy optimization of electrostatic actuators based on pull-in. *J. Microelectromech. Syst.* **8** (3), 290–298.

CHAIKIN, P. M. & LUBENSKY, T. C. 1995 *Principles of condensed matter physics*. Cambridge University Press, Cambridge.

CHATERJEE, S. & POHIT, G. 2009 A large deflection model for the pull-in analysis of electrostatically actuated microcantilever beams. *J. Sound Vib.* **322** (4), 969–986.

CHEN, J.-S. & HUNG, S.-Y. 2011 Snapping of an elastica under various loading mechanisms. *Eur. J. Mech. A Solids* **30** (4), 525–531.

DAS, K. & BATRA, R. C. 2009 Pull-in and snap-through instabilities in transient deformations of microelectromechanical systems. *J. Micromech. Microeng.* **19** (3), 035008.

DEARING, S. S., MORRISON, J. F. & IANNUCCI, L. 2010 Electro-active polymer (EAP) "dimple" actuators for flow control: Design and characterisation. *Sens. Actuators A Phys.* **157** (2), 210–218.

DEMIREL, B., YARAŞ, A. & ELÇIÇEK, H. 2011 Crystallization behavior of PET materials. *BAÜ Fen Bil. Enst. Dergisi Cilt* **13** (1), 26–35.

DENG, P., WANG, N., CAI, F. & CHEN, L. 2017 A high-force and high isolation metal-contact RF MEMS switch. *Microsyst. Technol.* **23**, 4699–4708.

DESAI, A. V., TICE, J. D., APBLETT, C. A. & KENIS, P. J. A. 2012 Design considerations for electrostatic microvalves with applications in poly (dimethylsiloxane)-based microfluidics. *Lab Chip* **12** (6), 1078–1088.

DIAS, R. A., ALVES, F. S., COSTA, M., FONSECA, H., CABRAL, J., GASPAR, J. & ROCHA, L. A. 2015 Real-time operation and characterization of a high-performance time-based accelerometer. *J. Microelectromech. Syst.* **24** (6), 1703–1711.

DIAS, R. A., CRETU, E., WOLFFENBUTTEL, R. & ROCHA, L. A. 2011 Pull-in-based μg-resolution accelerometer: Characterization and noise analysis. *Sens. Actuators A Phys.* **172** (1), 47–53.

DICHMANN, D. J. & MADDOCKS, J. H. 1996 An impetus-striction simulation of the dynamics of an elastica. *J. Nonlinear Sci.* **6** (3), 271–292.

DUDTE, LEVI H., VOUGA, E., TACHI, T. & MAHADEVAN, L. 2016 Programming curvature using origami tessellations. *Nature Mater.* **15**, 583–588.

EPSTEIN, E., YOON, J., MADHUKAR, A., HSIA, K. J. & BRAUN, P. V. 2015 Colloidal particles that rapidly change shape via elastic instabilities. *Small* **11** (45), 6051–6057.

FARGETTE, A., NEUKIRCH, S. & ANTKOWIAK, A. 2014 Elastocapillary snapping: Capillarity induces snap-through instabilities in small elastic beams. *Phys. Rev. Lett.* **112** (13), 137802.

FITCH, J. R. 1968 The buckling and post-buckling behavior of spherical caps under concentrated load. *Int. J. Solids Struct.* **4** (4), 421–446.

FLORES, G., MERCADO, G. A. & PELESKO, J. A. 2003 Dynamics and touchdown in electrostatic MEMS. In *Proc. ASME Design Engineering Technical Conf. and Computers and Information in Engineering Conf. and 19th Biennial Conf. on Mechanical Vibration and Noise (Chicago, IL, 2–6 September 2003)*, , vol. 5, pp. 1807–1814. American Society of Mechanical Engineers.

FONTICH, E. & SARDANYÉS, J. 2007 General scaling law in the saddle–node bifurcation: a complex phase space study. *J. Phys. A* **41** (1), 015102.

FORTERRE, Y., SKOTHEIM, J. M., DUMAIS, J. & MAHADEVAN, L. 2005 How the Venus flytrap snaps. *Nature* **433**, 421–425.

FRASER, W. B. & CHAMPNEYS, A. R. 2002 The 'Indian rope trick' for a parametrically excited flexible rod: nonlinear and subharmonic analysis. *Proc. R. Soc. A* **458** (2022), 1353–1373.

GANO, S. E., RENAUD, J. E., BATILL, S. M. & TOVAR, A. 2003 Shape optimization for conforming airfoils. In *Proc. 44th AIAA/ASME/ASCE/AHS Structures, Structural Dynamics, and Materials Conference (SDM), AIAA*, , vol. 1579, pp. 7–10.

GO, J. S., CHO, Y.-H., KWAK, B. M. & PARK, K. 1996 Snapping microswitches with adjustable acceleration threshold. *Sens. Actuators A Phys.* **54** (1-3), 579–583.

GOMEZ, M., MOULTON, D. E. & VELLA, D. 2016 The shallow shell approach to Pogorelov's problem and the breakdown of 'mirror buckling'. *Proc. R. Soc. A* **472**, 20150732.

GOMEZ, M., MOULTON, D. E. & VELLA, D. 2017*a* Critical slowing down in purely elastic 'snap-through' instabilities. *Nat. Phys.* **13**, 142–145.

GOMEZ, M., MOULTON, D. E. & VELLA, D. 2017*b* Passive control of viscous flow via elastic snap-through. *Phys. Rev. Lett.* **119**, 144502.

GOMEZ, M., MOULTON, D. E. & VELLA, D. 2018*a* Delayed pull-in transitions in over-damped MEMS devices. *J. Micromech. Microeng.* **28**, 015006.

GOMEZ, M., MOULTON, D. E. & VELLA, D. 2018*b* Dynamics of viscoelastic snap-through. *arXiv preprint arXiv:1807.05978 [cond-mat.soft]* .

GOMEZ, M., VELLA, D. & MOULTON, D. E. 2018*c* Pull-in dynamics of overdamped microbeams. *J. Micromech. Microeng.* **28**, 115002.

GONÇALVES, P. B., PAMPLONA, D., TEIXEIRA, P. B. C., JERUSALMI, R. L. C., CESTARI, I. A. & LEIRNER, A. A. 2003 Dynamic non-linear behavior and stability of a ventricular assist device. *Int. J. Solids Struct.* **40**, 5017–5035.

GRÉTILLAT, M.-A., YANG, Y.-J., HUNG, E. S., RABINOVICH, V., ANANTHASURESH, G. K., DE ROOIJ, N. F. & SENTURIA, S. D. 1997 Nonlinear electromechanical behaviour of an electrostatic microrelay. In *Proc. Int. Conf. on Solid State Sensors and Actuators (Transducers 1997, Chicago, IL)*, , vol. 2, pp. 1141–1144. IEEE.

GUCKENHEIMER, J. & HOLMES, P. J. 2013 *Nonlinear oscillations, dynamical systems, and bifurcations of vector fields*. Springer Science & Business Media, Berlin.

GUPTA, R. K., HUNG, E. S., YANG, Y.-J., ANANTHASURESH, G. K. & SENTURIA, S. D. 1996 Pull-in dynamics of electrostatically-actuated beams. In *Proc. Solid State Sensor and Actuator Workshop*, pp. 1–2.

GUPTA, R. K. & SENTURIA, S. D. 1997 Pull-in time dynamics as a measure of absolute pressure. In *Proc. IEEE. Int. Workshop on MEMS (Nagoya, Jan. 1997)*, pp. 290–294. IEEE.

HAN, J. S., KO, J. S. & KORVINK, J. G. 2004 Structural optimization of a large-displacement electromagnetic Lorentz force microactuator for optical switching applications. *J. Micromech. Microeng.* **14** (11), 1585.

HARVEY, P. S. & VIRGIN, L. N. 2015 Coexisting equilibria and stability of a shallow arch: Unilateral displacement-control experiments and theory. *Int. J. Solids Struct.* **54**, 1–11.

HAYMAN, B. 1978 Aspects of creep buckling I. The influence of post-buckling characteristics. *Proc. R. Soc. A* **364**, 393–414.

HINCH, E. J. 1991 *Perturbation methods*. Cambridge University Press, Cambridge.

HOLMES, D. P. & CROSBY, A. J. 2007 Snapping surfaces. *Adv. Mater.* **19** (21), 3589–3593.

HOWELL, P., KOZYREFF, G. & OCKENDON, J. 2009 *Applied Solid Mechanics*. Cambridge University Press, Cambridge.

HU, N. & BURGUEÑO, R. 2015 Buckling-induced smart applications: recent advances and trends. *Smart Mater. Struct.* **24** (6), 063001.

HUANG, N.-C. 1964 Unsymmetrical buckling of thin shallow spherical shells. *J. Appl. Mech.* **31** (3), 447–457.

HUNG, E. S. & SENTURIA, S. D. 1999 Generating efficient dynamical models for microelectromechanical systems from a few finite-element simulation runs. *J. Microelectromech. Syst.* **8** (3), 280–289.

IJNTEMA, D. J. & TILMANS, H. A. C. 1992 Static and dynamic aspects of an air-gap capacitor. *Sens. Actuators A Phys* **35** (2), 121–128.

JOGLEKAR, M. M. & PAWASKAR, D. N. 2011 Estimation of oscillation period/switching time for electrostatically actuated microbeam type switches. *Int. J. Mech. Sci.* **53** (2), 116–125.

JOHNSTON, B. G. 1983 Column buckling theory: historic highlights. *J. Struct. Eng.* **109** (9), 2086–2096.

JONES, R. M. 2006 *Buckling of bars, plates, and shells*. Bull Ridge Publishing, Blacksburg, VA.

KACEM, N., HENTZ, S., PINTO, D., REIG, B. & NGUYEN, V. 2009 Nonlinear dynamics of nanomechanical beam resonators: improving the performance of NEMS-based sensors. *Nanotechnology* **20** (27), 275501.

KEENER, J. P. 1988 *Principles of Applied Mathematics*. Addison-Wesley, Boston, MA.

KIM, J., LEE, H. S. & KIM, N. 2010 Determination of shear and bulk moduli of viscoelastic solids from the indirect tension creep test. *J. Eng. Mech.* **136** (9), 1067–1075.

Knoche, S. 2014 Instabilities and shape analyses of elastic shells. PhD thesis, Universitätsbibliothek Dortmund.

Krieger, K. 2012 Buckling down. *Nature* **488** (7410), 146.

Krylov, S. 2007 Lyapunov exponents as a criterion for the dynamic pull-in instability of electrostatically actuated microstructures. *Int. J. Non-Linear Mech.* **42** (4), 626–642.

Krylov, S. & Dick, N. 2010 Dynamic stability of electrostatically actuated initially curved shallow micro beams. *Continuum Mech. Thermodyn.* **22** (6), 445–468.

Krylov, S., Ilic, B. R., Schreiber, D., Seretensky, S. & Craighead, H. 2008 The pull-in behavior of electrostatically actuated bistable microstructures. *J. Micromech. Microeng.* **18** (5), 055026.

Krylov, S. & Maimon, R. 2004 Pull-in dynamics of an elastic beam actuated by continuously distributed electrostatic force. *J. Vib. Acoust.* **126** (3), 332–342.

Kuder, I. K., Arrieta, A. F., Raither, W. E. & Ermanni, P. 2013 Variable stiffness material and structural concepts for morphing applications. *Prog. Aerosp. Sci.* **63**, 33–55.

Kuehn, C. 2008 Scaling of saddle-node bifurcations: degeneracies and rapid quantitative changes. *J. Phys. A* **42** (4), 045101.

Lachenal, X., Daynes, S. & Weaver, P. M. 2013 Review of morphing concepts and materials for wind turbine blade applications. *Wind Energy* **16** (2), 283–307.

Lakes, R. S. 1998 *Viscoelastic Solids*. CRC press, Boca Raton, FL.

Landau, L. D. & Lifshitz, E. M. 1986 *Theory of elasticity*. Butterworth-Heinemann, Oxford.

LaRose, R. P. & Murphy, K. D. 2010 Impact dynamics of MEMS switches. *Nonlinear Dyn.* **60** (3), 327–339.

Lee, H., Xia, C. & Fang, N. X. 2010 First jump of microgel; actuation speed enhancement by elastic instability. *Soft Matter* **6** (18), 4342–4345.

Leus, V. & Elata, D. 2008 On the dynamic response of electrostatic MEMS switches. *J. Microelectromech. Syst.* **17** (1), 236–243.

Lin, R. M. & Wang, W. J. 2006 Structural dynamics of microsystems—current state of research and future directions. *Mech. Sys. Signal Process* **20** (5), 1015–1043.

LOH, O. Y. & ESPINOSA, H. D. 2012 Nanoelectromechanical contact switches. *Nat. Nanotechnol.* **7** (5), 283–295.

LOUKAIDES, E. G., SMOUKOV, S. K. & SEFFEN, K. A. 2014 Magnetic actuation and transition shapes of a bistable spherical cap. *Int. J. Smart Nano Mater.* **5** (4), 270–282.

MADDOCKS, J. H. 1987 Stability and folds. *Arch. Rational Mech. Anal.* **99** (4), 301–328.

MADHUKAR, A., PERLITZ, D., GRIGOLA, M., GAI, D. & HSIA, K. J. 2014 Bistable characteristics of thick-walled axisymmetric domes. *Int. J. Solids Struct.* **51** (14), 2590–2597.

MAJUMDAR, A., OCKENDON, J., HOWELL, P. & SUROVYATKINA, E. 2013 Transitions through critical temperatures in nematic liquid crystals. *Phys. Rev. E* **88** (2), 022501.

MAURINI, C., POUGET, J. & VIDOLI, S. 2007 Distributed piezoelectric actuation of a bistable buckled beam. *Eur. J. Mech. A Solids* **26** (5), 837–853.

MCCARTHY, B., ADAMS, G. G., MCGRUER, N. E. & POTTER, D. 2002 A dynamic model, including contact bounce, of an electrostatically actuated microswitch. *J. Microelectromech. Syst.* **11** (3), 276–283.

MCMILLEN, T. & GORIELY, A. 2003 Whip waves. *Physica D* **184** (1), 192–225.

MISSOFFE, A., JUILLARD, J. & AUBRY, D. 2008 A reduced-order model of squeeze-film damping for deformable micromechanical structures including large displacement effects. *J. Micromech. Microeng.* **18** (3), 035042.

NACHBAR, W. & HUANG, N. C. 1967 Dynamic snap-through of a simple viscoelastic truss. *Q. Appl. Math.* **25** (1), 65–82.

NAYFEH, A. H., YOUNIS, M. I. & ABDEL-RAHMAN, E. M. 2005 Reduced-order models for MEMS applications. *Nonlinear Dyn.* **41** (1), 211–236.

NAYFEH, A. H., YOUNIS, M. I. & ABDEL-RAHMAN, E. M. 2007 Dynamic pull-in phenomenon in MEMS resonators. *Nonlinear Dyn.* **48** (1-2), 153–163.

NEUKIRCH, S., FRELAT, J., GORIELY, A. & MAURINI, C. 2012 Vibrations of post-buckled rods: the singular inextensible limit. *J. Sound Vib.* **331** (3), 704–720.

NGUYEN, C. T.-C., KATEHI, L. P. B. & REBEIZ, G. M. 1998 Micromachined devices for wireless communications. *Proc. IEEE* **86** (8), 1756–1768.

NIELSON, G. N. & BARBASTATHIS, G. 2006 Dynamic pull-in of parallel-plate and torsional electrostatic MEMS actuators. *J. Microelectromech. Syst.* **15** (4), 811–821.

Nijhuis, M. H. H., Basten, T. G. H., Wijnant, Y. H., Tijdeman, H. & Tilmans, H. A. C. 1999 Transient non-linear response of 'pull-in MEMS devices' including squeeze film effects. *Proc. Eurosensors XIII (The Hague, The Netherlands, 1999)* pp. 729–732.

Osterberg, P. M. & Senturia, S. D. 1997 M-TEST: a test chip for MEMS material property measurement using electrostatically actuated test structures. *J. Microelectromech. Syst.* **6** (2), 107–118.

Overvelde, J. T. B., Kloek, T., Dhaen, J. J. A. & Bertoldi, K. 2015 Amplifying the response of soft actuators by harnessing snap-through instabilities. *Proc. Natl. Acad. Sci. U.S.A.* **112** (35), 10863–10868.

Pandey, A., Moulton, D. E., Vella, D. & Holmes, D. P. 2014 Dynamics of snapping beams and jumping poppers. *Europhys. Lett.* **105** (2), 24001.

Panovko, Ya. G. & Gubanova, I. I. 1987 *Stability and Oscillations of Elastic Systems: Advanced Concepts, Paradoxes, and Errors*. Nauka, Moscow.

Patricìo, P., Adda-Bedia, M. & Ben Amar, M. 1998 An elastica problem: instabilities of an elastic arch. *Physica D* **124** (1-3), 285–295.

Pelesko, J. A. & Bernstein, D. H. 2002 *Modeling MEMS and NEMS*. CRC press, Boca Raton, FL.

Plaut, R. H. 2009 Snap-through of shallow elastic arches under end moments. *J. Appl. Mech.* **76** (1).

Qiu, J., Lang, J. H. & Slocum, A. H. 2004 A curved-beam bistable mechanism. *J. Microelectromech. Syst.* **13** (2), 137–146.

Ramachandran, V., Bartlett, M. D., Wissman, J. & Majidi, C. 2016 Elastic instabilities of a ferroelastomer beam for soft reconfigurable electronics. *Extreme Mech. Lett.* **9**, 282–290.

Rega, G. & Troger, H. 2005 Dimension reduction of dynamical systems: methods, models, applications. *Nonlinear Dyn.* **41** (1), 1–15.

Reis, P. M. 2015 A perspective on the revival of structural (in)stability with novel opportunities for function: From buckliphobia to buckliphilia. *J. Appl. Mech.* **82** (11), 111001.

Roa, M. A. D., Copelli, M., Kinouchi, O. & Caticha, N. 2007 Scaling law for the transient behavior of type-ii neuron models. *Phys. Rev. E* **75** (2), 021911.

ROCHA, L. A., CRETU, E. & WOLFFENBUTTEL, R. F. 2004a Behavioural analysis of the pull-in dynamic transition. *J. Micromech. Microeng.* **14** (9), S37.

ROCHA, L. A., CRETU, E. & WOLFFENBUTTEL, R. F. 2004b Pull-in dynamics: analysis and modeling of the transitional regime. In *Proc. MEMS'04 (Maastricht, The Netherlands, 25–29 January 2004)*, pp. 249–252. IEEE.

ROCHUS, V., RIXEN, D. J. & GOLINVAL, J.-C. 2005 Electrostatic coupling of MEMS structures: transient simulations and dynamic pull-in. *Nonlinear Anal. Theory Methods Appl.* **63** (5), e1619–e1633.

RUHOFF, P. T., PRAESTGAARD, E. & PERRAM, J. W. 1996 Efficient algorithms for simulating complex mechanical systems using constraint dynamics. *Proc. R. Soc. A.* **452** (1948), 1139–1165.

SANTER, M. 2010 Self-actuated snap back of viscoelastic pulsing structures. *Int. J. Solids Struct.* **47** (24), 3263–3271.

SARDANYÉS, J. & SOLÉ, R. V. 2006 Ghosts in the origins of life? *Int. J. Bifurc. Chaos* **16** (09), 2761–2765.

SARDANYÉS, J. & SOLÉ, R. V. 2007 Delayed transitions in non-linear replicator networks: about ghosts and hypercycles. *Chaos Soliton. Fract.* **31** (2), 305–315.

SCHEFFER, M., BASCOMPTE, J., BROCK, W. A., BROVKIN, V., CARPENTER, S. R., DAKOS, V., HELD, H., VAN NES, E. H., RIETKERK, M. & SUGIHARA, G. 2009 Early-warning signals for critical transitions. *Nature* **461** (7260), 53.

SEFFEN, K. A. & VIDOLI, S. 2016 Eversion of bistable shells under magnetic actuation: a model of nonlinear shapes. *Smart Mater. Struct.* **25** (6), 065010.

SHANKAR, M. R., SMITH, M. L., TONDIGLIA, V. P., LEE, K. M., MCCONNEY, M. E., WANG, D. H., TAN, L.-S. & WHITE, T. J. 2013 Contactless, photoinitiated snap-through in azobenzene-functionalized polymers. *Proc. Natl. Acad. Sci. U.S.A.* **110** (47), 18792–18797.

SILVERBERG, J. L., NA, J.-H., EVANS, A. A., LIU, B., HULL, T. C., SANTANGELO, C. D., LANG, R. J., HAYWARD, R. C. & COHEN, I. 2015 Origami structures with a critical transition to bistability arising from hidden degrees of freedom. *Nature Mat.* **14**, 389–393.

SKOTHEIM, J. M. & MAHADEVAN, L. 2005 Physical limits and design principles for plant and fungal movements. *Science* **308**, 1309–1310.

SMITH, M. L., YANEGA, G. M. & RUINA, A. 2011 Elastic instability model of rapid beak closure in hummingbirds. *J. Theor. Biol.* **282**, 41–51.

SOBOTA, P. M. & SEFFEN, K. A. 2017 Effects of boundary conditions on bistable behaviour in axisymmetrical shallow shells. *Proc. R. Soc. A* **473** (2203), 20170230.

STROGATZ, S. H. 2014 *Nonlinear Dynamics and Chaos*. Westview Press, Boulder, CO.

STROGATZ, S. H. & WESTERVELT, R. M. 1989 Predicted power laws for delayed switching of charge-density waves. *Phys. Rev. B* **40** (15), 10501–10508.

TERWAGNE, D., BROJAN, M. & REIS, P. M. 2014 Smart morphable surfaces for aerodynamic drag control. *Adv. Mater.* **26** (38), 6608–6611.

TREDICCE, J. R., LIPPI, G. L., MANDEL, P., CHARASSE, B., CHEVALIER, A. & PICQUÉ, B. 2004 Critical slowing down at a bifurcation. *Am. J. Phys.* **72** (6), 799–809.

TRICKEY, S. T. & VIRGIN, L. N. 1998 Bottlenecking phenomenon near a saddle-node remnant in a Duffing oscillator. *Phys. Lett. A* **248** (2), 185–190.

URBACH, E. Y. & EFRATI, E. 2017 Delayed instabilities in viscoelastic solids through a metric description. *arXiv preprint arXiv:1711.09491* .

VEIJOLA, T., KUISMA, H., LAHDENPERÄ, J. & RYHÄNEN, T. 1995 Equivalent-circuit model of the squeezed gas film in a silicon accelerometer. *Sens. Actuators A Phys.* **48** (3), 239–248.

VENTSEL, E. & KRAUTHAMMER, T. 2001 *Thin Plates and Shells*. Marcel Dekker, New York, NY.

VIRGIN, L. N. & PLAUT, R. H. 2004 Postbuckling and vibration of linearly elastic and softening columns under self-weight. *Int. J. Solids Struct.* **41** (18), 4989–5001.

WANG, C. Y. 1986 A critical review of the heavy elastica. *Int. J. Mech. Sci.* **28** (8), 549–559.

WIEBE, R. 2012 Nonlinear dynamics of discrete and continuous mechanical systems with snap-through instabilities. PhD thesis, Duke University.

WIGGINS, S. 2003 *Introduction to Applied Nonlinear Dynamical Systems and Chaos*. Springer Science & Business Media, Berlin.

XU, H., KEMIKTARAK, U., FAN, J., RAGOLE, S., LAWALL, J. & TAYLOR, J. M. 2017 Observation of optomechanical buckling transitions. *Nat. Commun.* **8**, 14481.

XU, P., NEEK-AMAL, M., BARBER, S. D., SCHOELZ, J. K., ACKERMAN, M. L., THIBADO, P. M., SADEGHI, A. & PEETERS, F.M. 2014 Unusual ultra-low-frequency fluctuations in freestanding graphene. *Nature Comm.* **5**, 3720.

YILMAZER, U., XANTHOS, M., BAYRAM, G. & TAN, V. 2000 Viscoelastic characteristics of chain extended/branched and linear polyethylene terephthalate resins. *J. Appl. Polym. Sci.* **75** (11), 1371–1377.

YOUNIS, M. I., ABDEL-RAHMAN, E. M. & NAYFEH, A. 2003 A reduced-order model for electrically actuated microbeam-based MEMS. *J. Microelectromech. Syst.* **12** (5), 672–680.

YOUNIS, M. I. & ALSALEEM, F. 2009 Exploration of new concepts for mass detection in electrostatically-actuated structures based on nonlinear phenomena. *J. Comput. Nonlin. Dyn.* **4** (2), 021010.

ZAITSEV, S., SHTEMPLUCK, O., BUKS, E. & GOTTLIEB, O. 2012 Nonlinear damping in a micromechanical oscillator. *Nonlinear Dyn.* **67** (1), 859–883.

ZHANG, W.-M., YAN, H., PENG, Z.-K. & MENG, G. 2014 Electrostatic pull-in instability in MEMS/NEMS: A review. *Sens. Actuators A Phys.* **214**, 187–218.